

Atoms in intense ultrashort laser pulses and the absolute phase

Dissertation der Fakultät für Physik
der Ludwig-Maximilians-Universität München

vorgelegt von
Fabrizio Lindner
aus Mailand (Italien)

München, April 2004

Erster Gutachter: PROF. DR. H. WALTHER

Zweiter Gutachter: PROF. DR. D. HABS

Tag der mündlichen Prüfung: 30.06.2004

Abstract

The subject of this work is the experimental investigation of atomic processes under the influence of intense, ultrashort laser pulses. Emphasis is given to the twin effects of high-order harmonic generation (HHG) and above-threshold ionization (ATI). In particular, the latter is explored in detail here for the case of few-cycle laser pulses. While the generation of light pulses of duration below 5 fs is today routine, a complete control of the constituting electric-field waveform was so far not possible. This is here achieved with the first unambiguous measurement of the absolute phase of the laser pulses. The precision and reliability of the measurement permitted to establish a new approach for active phase stabilization, which will presumably play a major role in future research. The experiments described here address also general optical properties such as the Gouy phase anomaly showing up in a focused wave, being precisely measured for the first time. Finally, it is shown how ATI with few-cycle laser pulses can be regarded not only as a powerful tool for phase diagnostics, but also as a novel method for studying the interaction of atoms with light with unprecedented sub-fs time resolution.

Zusammenfassung

Diese Arbeit beschäftigt sich mit der experimentellen Analyse atomarer Prozesse in intensiven ultrakurzen Laserpulsen. Der Schwerpunkt liegt hierbei bei den Zwillingseffekten der Erzeugung hoher Harmonischer (“high-order harmonic generation”, HHG) und der Ionisation über Zustände im Kontinuum (“above-threshold ionization”, ATI). Besonders letzterer Effekt wird detailliert in Verbindung mit der Wechselwirkung mit Laserpulsen von nur wenigen Zyklen Länge untersucht. Während es heutzutage Routine ist solche Pulse von weniger als 5 fs zu erzeugen, war die vollständige Kontrolle über das zugrundeliegende elektrische Feld bisher noch nicht möglich. Dies wurde in dieser Arbeit durch die erste eindeutige Messung der den Laserpuls charakterisierenden “absoluten Phase” erreicht. Die Genauigkeit und Zuverlässigkeit dieser Messung erweist sich als hinreichend, um eine neue Methode der aktiven Phasenstabilisierung einzuführen, welche voraussichtlich eine tragende Rolle in zukünftigen phasenstabilisierten Lasersystemen spielen wird. Die beschriebenen Experimente widmen sich zudem auch allgemeinen optischen Effekten, wie beispielsweise der Gouy’schen Phasen-anomalie in einem fokussierten Strahl, welche hier erstmals im optischen Bereich und über den gesamten Fokusbereich gemessen wurde. Schließlich wird gezeigt, wie ATI in Verbindung mit Wenig-Zyklen-Laserpulsen nicht nur als leistungsfähiges Werkzeug zur Phasendiagnostik genutzt werden kann, sondern auch einen neuen Zugang zur Untersuchung der Wechselwirkung von Atomen und Licht mit bis dato unerreichter Zeitauflösung bietet.

That which is static and repetitive is boring. That which is dynamic and random is confusing. In between lies art.

John A. Locke (1632-1704)

Contents

Introduction	1
1 Atoms in strong laser fields	5
1.1 Strong-field approximation (SFA) and the two-step model	6
1.2 First step: ionization	8
1.2.1 Tunneling and multiphoton limits	8
1.2.2 Ionization yields and saturation	11
1.3 Second step: free electron evolution	12
1.4 High-order harmonic generation (HHG)	13
1.4.1 Single-atom response	14
1.4.2 Macroscopic response: phase-matching	17
1.5 Above-threshold ionization (ATI)	20
1.5.1 Single-atom response	21
1.5.2 Macroscopic response: volume effects	22
1.6 Non-sequential double ionization (NSDI)	24
2 High-order harmonic generation at a repetition rate of 100 kHz	25
2.1 The laser system	26
2.2 The XUV spectrometer	28
2.3 Experimental results	30
2.3.1 Longitudinal dependence	30
2.3.2 Quantum path separation	32
2.3.3 Active spectral reshaping	35
3 Determination of the absolute phase of few-cycle laser pulses	39
3.1 The absolute phase	39
3.1.1 Absolute phase stabilization	41
3.1.2 Absolute phase and nonlinear phenomena	43
3.2 The laser system	45
3.3 The stereo-ATI spectrometer	45
3.3.1 Sensitivity of the spectrometer	47
3.4 Experimental results	48
3.5 Theoretical analysis	52
3.5.1 Semiclassical model	53

3.5.2	Strong-field approximation	55
3.5.3	Numerical integration of the Schrödinger equation	58
4	A new stabilization scheme for the absolute phase	59
4.1	The stereo-ATI as a phase meter	59
4.2	Phase stabilization	62
4.2.1	Basic idea	62
4.2.2	Experimental results	64
4.2.3	A first application: ATI and NSDI in parallel	67
4.3	Future developments	68
5	Full spatiotemporal characterization of the absolute phase	71
5.1	Spatial dependence: the Gouy effect	72
5.1.1	Physical picture	72
5.1.2	Gouy phase measurement	74
5.2	Intensity dependence	80
5.2.1	Ionization yield	80
5.2.2	ATI spectra	83
5.3	Pulse duration dependence	86
5.3.1	Ionization yield	86
5.3.2	ATI spectra	89
6	Quantum mechanics in ATI with few-cycle pulses	91
6.1	Electron interference in ATI	92
6.2	The double-slit experiment	94
6.2.1	Experimental evidence	94
6.2.2	Semiclassical description	98
6.3	Beyond the classical model: classically forbidden trajectories	101
6.4	Heisenberg's uncertainty principle	106
	Conclusion	109
	List of publications	111
	Bibliography	147

Introduction

This work deals with elementary processes occurring when exposing atoms to very intense laser fields. Since the early developments, lasers have been used for studying the behavior of matter under strong electromagnetic radiation. Progress in laser technology has been enormous: today, table-top laser systems delivering intensities up to $\sim 10^{15}$ W/cm² at high repetition rates (1 kHz and more) are commercially available.

Such intensities are by no means the highest obtainable with lasers. Indeed, peak intensities exceeding 10^{20} W/cm² can be produced (at repetition rates < 1 Hz) in various large-scale laser facilities. At these regimes, relativistic effects are highly dominant in laser-matter interaction; in addition, any material at these intensities is fully ionized, and any experiment must cope with collective behavior of the ionized medium (*plasma* physics).

The experiments presented here consisted in ionizing dilute gas media by focusing laser pulses in the non-relativistic range (intensities below $\sim 10^{15}$ W/cm²). Under these conditions the physics of laser-matter interaction can be studied in a clean and elegant way at unprecedented high intensities while remaining in the field of *atomic* physics. In other words, all elementary processes studied and described in the following can be understood and explained in the simple frame of *one* atom exposed to a strong oscillating electric field (magnetic field effects play a significant role only at higher intensities). Collective behavior can only occur through interference of the elementary processes, not through mutual interactions. All physical processes in this context are also referred to as *multiphoton* processes, since the typical energy of a single photon ($\sim 1,5$ eV) is not sufficient to ionize an atom through the well-known photoeffect.

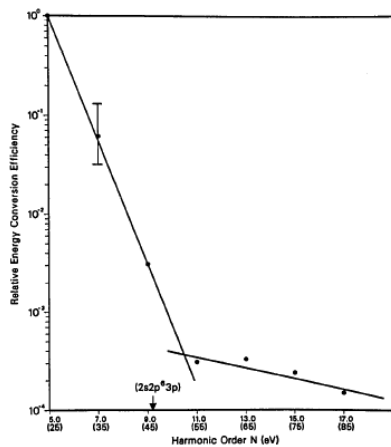
The most known of these processes is probably high-order harmonic generation (HHG), first presented in 1987 [McPherson87, Ferray88]. It consists of efficient coherent radiation emission at frequencies that are odd multiples of the laser frequency, occurring when exposing atoms to intense laser fields. For this effect, it was discovered that the initial decrease of harmonic yield was followed by a flat annex, i.e. the harmonic intensity was roughly independent of its order. This plateau-like feature ends with a sharp cutoff (Fig. 1). The complete disagreement with standard perturbation theory suggests the presence of different underlying mechanisms.

Less known currently but in fact older than HHG, above-threshold ionization (ATI) was discovered in 1979 by Agostini et al. [Agostini79]. Its discovery marked the begin-

Studies of multiphoton production of vacuum-ultraviolet radiation in the rare gases

A. McPherson, G. Gibson, H. Jara, U. Johann, T. S. Luk, I. A. McIntyre, K. Boyer, and C. K. Rhodes
Department of Physics, University of Illinois at Chicago, P.O. Box 4348, Chicago, Illinois 60680

Received November 1, 1986; accepted December 18, 1986



LETTER TO THE EDITOR

Multiple-harmonic conversion of 1064 nm radiation in rare gases

M Ferray, A L'Huilier, X F Li, L A Lompré, G Mainfray and C Manus
Service de Physique des Atomes et des Surfaces, 91191 Gif sur Yvette, Cédex, France

Received 2 November 1987

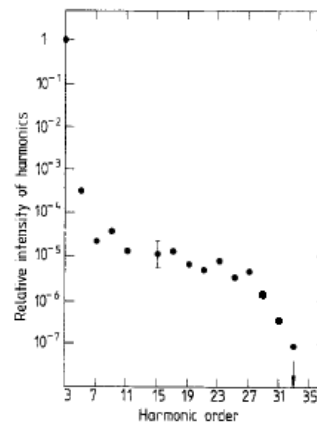


Figure 1: Discovery of high-order harmonic generation (HHG). After the initial exponential decrease of yield with increasing harmonic order, a flat annex (plateau) not explainable within perturbation theory was found. From [McPherson87] (left) and [Ferray88] (right).

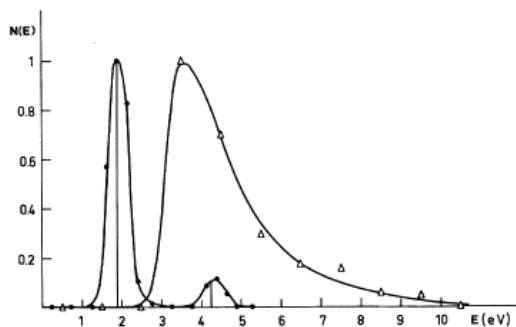
Free-Free Transitions Following Six-Photon Ionization of Xenon Atoms

P. Agostini, F. Fabre, G. Mainfray, and G. Petite
Centre d'Etudes Nucleaires de Saclay, Service de Physique Atomique, 91190 Gif-sur-Yvette, France

and

N. K. Rahman
Laboratorio di Chimica Quantistica ed Energetica Molecolare del
Consiglio Nazionale delle Ricerche, 35100 Pisa 35, Italy

(Received 20 January 1979)



Plateau in Above Threshold Ionization Spectra

G. G. Paulus,¹ W. Nicklich,¹ Hualie Xu,⁴ P. Lambropoulos,^{1,3} and H. Walther^{1,2}
¹Max-Planck-Institut für Quantenoptik, 85748 Garching, Germany
²Station Physik der Universität München, Germany

³Foundation for Research and Technology-Hellas, Institute of Electronic Structure and Laser, P.O. Box 1527, Heraklion 71110, Crete and Department of Physics, University of Crete, Greece
⁴Department of Physics, University of Southern California, Los Angeles, California 90089-0484

(Received 20 October 1993)

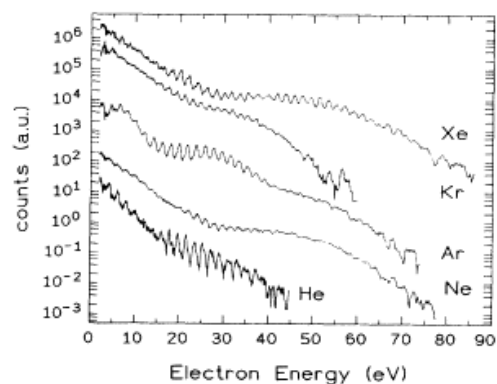


Figure 2: (left) Discovery of above-threshold ionization (ATI). The photoelectron spectrum shows two maxima separated by the laser photon energy, indicating the absorption of one photon more than necessary to overcome the ionization potential barrier. From [Agostini79]. (right) Discovery of the plateau in ATI. These results suggested that the physical mechanism at the basis of ATI and HHG is the same. From [Paulus94b].

ning of the investigation of extreme highly nonlinear phenomena in the visible spectral region. ATI is photoionization in intense laser fields such that an atom absorbs more photons than necessary for reaching the ionization threshold. This can be seen by inspection of the photoelectron kinetic energy spectra which consist of a series of peaks separated by the photon energy (Fig. 2). Generally, the peak heights decrease as the order is increased. In 1994 [Paulus94b] a phenomenon with similar appearance as the HHG plateau was measured for ATI (Fig. 2). Today, it is a well established fact that ATI and HHG are strongly connected.

The interest in these studies is far from being a merely academic one. Indeed, understanding the physics underlying these atomic processes has led in the last years to significant innovations. On the one hand, HHG represents a unique source of high brightness coherent radiation extending into the vacuum ultraviolet and soft X-ray spectral ranges. Applications of such light sources are naturally in the field of spectroscopy, holography and photobiology. On the other hand, ATI has recently attracted considerable interest in connection with ultrashort laser pulse generation. Indeed, the production of ever shorter light pulses (< 5 fs in the infrared) has caught the attention of the - even non-specialized - scientific community, for its potentiality of studying physical processes with unprecedented attosecond ($1 \text{ as} = 10^{-18} \text{ s}$) time resolution. In 2001 ATI proved [Paulus01b] to be an essential tool for investigating and controlling the so-called *absolute* phase (Fig. 3), a critical aspect in view of all applications of ultrashort pulses. A major part of the present work is devoted to exploit these potentialities of ATI, which have now reached a degree of completeness hardly conceivable only two years ago.

letters to nature

Absolute-phase phenomena in photoionization with few-cycle laser pulses

G. G. Paulus*, F. Grasbon†, H. Walther*, P. Villoresi‡, M. Nisoli§, S. Stagino, E. Priori† & S. De Silvestri§

*Max-Planck-Institut für Quantenoptik, Hans-Kopfermann-Straße 1, 85748 Garching bei München, Germany
†INFN and IZT—University of Padova, Via Gradenigo 6/a, 35131 Padova, Italy
‡INFN, Dipartimento di Fisica, Politecnico di Milano, Piazza L. da Vinci 32, 20133 Milan, Italy

Received 27 July; accepted 17 September 2001.

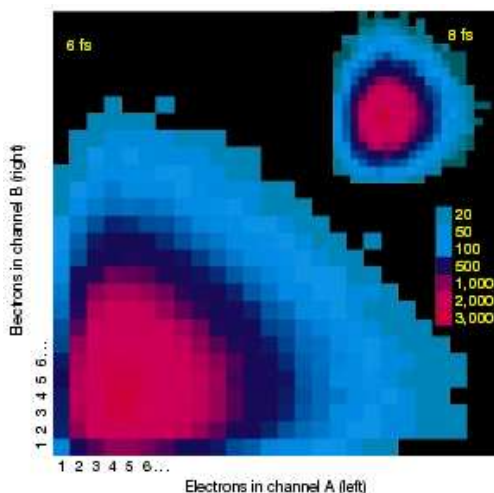


Figure 3: By ionizing krypton atoms with intense few-cycle laser pulses directional anticorrelation in the electron yield is measured. This constituted the first evidence of the absolute phase influence on nonlinear phenomena driven with ultrashort laser pulses. From [Paulus01b].

This work is organized as follows. Chapter 1 will describe the physics of light-matter interaction at the intensity range typical of the experiments described in the following. After a brief introduction in the framework of quantum mechanics, it will be shown that a semiclassical approach allows explaining all the essential features of HHG and ATI in an intuitive and simple way.

Chapter 2 will present experimental results of HHG performed with a laser system working at 100 kHz repetition rate. To date, this is by far the highest repetition rate at which HHG has ever been reported. The price for high repetition rate is low pulse energy, which makes generation and detection of the harmonic radiation challenging. Particular emphasis will be given to the spectral features of the harmonic comb, a very important issue in terms of both the theoretical understanding of the generation process and of possible applications.

Chapter 3 will introduce the concept of the carrier-envelope (CE) or absolute phase, a quantity of critical importance for few-cycle pulses (i.e. laser pulses consisting of only a few electromagnetic oscillations). Although it is unanimously recognized that the absolute phase plays a major role in a number of physical processes, in particular in attosecond pulse generation, its complete control (in particular the determination of its value) had not been achieved. Experimental results on ATI conducted with a laser delivering 5-fs pulses will be described. These conclusively solved the problem of determining the CE phase value: ATI can be used as a phase meter.

Chapter 4 will describe a very powerful technical application of ATI in the frame of a completely new absolute phase stabilization scheme. In particular, it will be shown that long-term (essentially unlimited) phase stability was achieved, allowing performing experiments hitherto not possible. The technical limits and future perspectives will also be discussed.

Chapter 5 will characterize absolute phase effects with respect to change in pulse duration, intensity and spatial position in the laser focus. In particular, the latter is strictly connected with the well-known *Gouy* phase anomaly. By means of the ATI phase meter it was possible for the first time to measure the phase variation during the pulse propagation in the focal region. This is of critical importance not only for the theoretical understanding but also for different applications, in particular for HHG and attosecond pulse generation performed with few-cycle pulses.

Finally, Chapter 6 will be dedicated to the study of interference patterns in ATI with few-cycle laser pulses of controlled and known phase. Comparisons with predictions from the semiclassical model will show the power and the limits of a semiclassical description. Furthermore, it will be shown that the information contained in the ATI spectra presents elegant analogies with the Young's double-slit experiment with electrons and permits to follow the ionization process in real time with unprecedented attosecond time resolution.

Chapter 1

Atoms in strong laser fields

The interaction of an atom exposed to a short, intense laser field, in principle, is a simple quantum-mechanical problem. However, analytical solutions of the Schrödinger equation are known only for the limiting cases of an electron in the Coulomb potential of the nucleus in the absence of an external oscillating field (hydrogen-like atom) and of an electron exposed to a laser field in the absence of the atom (Volkov eigenfunctions). Both solutions are clearly inadequate to describe the physics of nonlinear processes driven by femtosecond lasers. The standard method used in quantum mechanics to take into account more complex systems is perturbation theory. However, the condition for its applicability is the existence of a *strong* potential, determining the unperturbed solution, and of a *weak* perturbation. This condition is not fulfilled in the interaction of strong laser fields with atoms, since the electric field of a laser pulse can reach, and in fact even exceed, the inner-atomic Coulomb field. A useful formula in this context is:

$$E[\text{V/cm}] \sim 27.4 \cdot \sqrt{I[\text{W/cm}^2]} \quad (1.1)$$

where E is the electric field in the laser pulse and I the corresponding intensity. At an intensity of 10^{15} W/cm^2 , easily accessible experimentally, the electric field is already more than 30% of that of the nucleus on the first Bohrian radius. Hence, the laser field cannot be considered a *weak* perturbation.

In this chapter, a possible approach to study the problem will be presented. First, it will be shown how a suitable approximation of the Schrödinger equation gives a lot of insight into the physical processes involved. Then, a semiclassical model following the lines of the more rigorous quantum-mechanical approach will be discussed. This semiclassical model has attracted considerable interest in recent years, due to its simplicity and its surprising predictive power. Finally, the model will be used to describe a few remarkable features of high-order harmonic generation (HHG) and above-threshold ionization (ATI).

1.1 Strong-field approximation (SFA) and the two-step model

The time-dependent Schrödinger equation for an electron in the Coulomb potential exposed to a strong laser field reads¹:

$$i\frac{\partial|\Psi(t)\rangle}{\partial t} = \hat{H}(t)|\Psi(t)\rangle = \hat{H}_0|\Psi(t)\rangle + \hat{V}(t)|\Psi(t)\rangle \quad (1.2)$$

where \hat{H}_0 is the field-free hamiltonian and $\hat{V}(t)$ describes the interaction with the laser field. The formal solution to this equation is:

$$|\Psi(t)\rangle = e^{-i\int_{t_i}^t \hat{H}(t')dt'} |\Phi_i\rangle \quad (1.3)$$

where $|\Phi_i\rangle$ is the state of the system at some initial time t_i , thus independent of time. Let us look for a solution in the form:

$$|\Psi(t)\rangle = e^{-i\hat{H}_0 t} |C(t)\rangle \quad (1.4)$$

where the trial function $|C(t)\rangle$ has to be found by plugging Eq. (1.4) into Eq. (1.2). After routine mathematics and projecting the state $|\Psi(t)\rangle$ onto a final state $\langle\Phi_f|$ of the field-free system, one can write the transition amplitude as:

$$a_{fi}(t_f \leftarrow t_i) = -i \int_{t_i}^{t_f} dt' \langle\Phi_f| e^{-i\hat{H}_0(t_f-t')} \hat{V}(t') e^{-i\int_{t_i}^{t'} \hat{H}(t'')dt''} |\Phi_i\rangle. \quad (1.5)$$

By making use of the property of the Schrödinger equation of being symmetric with respect to time reversal and performing identical mathematics as outlined above, one can rewrite Eq. (1.5) in a slightly different form:

$$a_{fi}(t_f \leftarrow t_i) = -i \int_{t_i}^{t_f} dt' \langle\Phi_f| e^{-i\int_{t'}^{t_f} \hat{H}(t'')dt''} \hat{V}(t') e^{-i\hat{H}_0(t'-t_i)} |\Phi_i\rangle. \quad (1.6)$$

The physics behind this last (still exact) expression is very meaningful. The system starts in the initial state $|\Phi_i\rangle$ (usually, the ground state). During the time-interval before some time t' it evolves without interacting with the laser field and only accumulating a phase due to its energy. This quiet evolution ends at a moment t' when the system is kicked by the instantaneous interaction $V(t')$. Then, from the moment t' to the moment of observation t_f , when the wavefunction is projected onto the final state of interest, the evolution is under the action of the full Hamiltonian, including both the laser field and the field-free potential.

The essence of the so-called strong-field approximation (SFA) is now the following: instead of using the exact propagator $\exp[-i\int_{t'}^{t_f} \hat{H}(t'')dt'']$, one considers an approxi-

¹Atomic units are used throughout this chapter, i.e. $e = 1$, $m_e = 1$, $\hbar = 1$.

mate propagator that fully includes the laser field but completely ignores the field-free potential (i.e. the atomic potential). One reason to make such an approximation is that the problem of a free electron in a laser field has a known analytical solution. The eigenfunctions are called Volkov states $|\mathbf{p}\rangle$ and describe the oscillations of a free electron under the action of the laser field. The Volkov propagator is

$$e^{-i \int_{t'}^{t_f} \hat{H}(t'') dt''} = e^{-i \int_{t'}^{t_f} E(t'') dt''} \quad (1.7)$$

where $E(t)$ is the energy of the electron during the oscillations in the continuum. The main features of the free oscillations, their dependence on the initial condition and on the driving laser pulse will be discussed in detail semiclassically in Sec. 1.3. Now one can finally write the SFA expression for the probability amplitude to find the system in the state $|\mathbf{p}\rangle$ at the moment t_f . By assuming that the system has started at the moment t_i in the ground state $|g\rangle$ with the energy $-I_p$ (ionization potential of the atom), one obtains

$$a_{\mathbf{p}}(t_f) = -i \int_{t_i}^{t_f} dt' e^{-i \int_{t'}^{t_f} E(t'') dt''} e^{+i I_p(t'-t_i)} \langle \mathbf{p}(t') | \hat{V}(t') | g \rangle. \quad (1.8)$$

This result is highly intuitive. The electron sits in the ground state until t' when it makes a transition (ionization) into the continuum (the details of this instantaneous transition will be discussed in the next section). Then the electron moves in the laser field *without feeling the atomic potential* and accumulates a phase given by the integral of its energy, performed between the moment of birth t' and the moment of observation t_f . Finally, the electron is detected (observed) with the final kinetic momentum \mathbf{p} . Obviously, the result is integrated over all possible ionization times t' .

In this way the problem is splitted into two independent parts. First, ionization takes place; second, the free electron oscillates driven by the laser, possibly re-interacting with the ionized atom. This semiclassical interpretation [vLvdH88, Kulander93, Corkum93, Paulus94b] represented a breakthrough in the theoretical understanding of the physics of strong laser fields. Today, this approach is referred to as *two-step model* or, due to its simplicity, *simple man's model*. The next two sections will illustrate in details some interesting consequences of this intuitive picture.

The solution of the SFA expression (1.8), though already simplified with respect to the complete form (1.6), can be further approximated by making use of the so-called saddle point method. In short, the main contribution to the integral arises from those points where the phase factor $\exp[-i \int_{t'}^{t_f} E(t'') dt'']$ is stationary, all the others being canceled due to rapid oscillation during integration. Hence, the integral reduces to a sum of a few relevant points (or quantum paths). This idea is simply a formulation of the more general Feynman's path integral approach [Feynman65, Salières01], and allows fast and precise computational methods.

Note that there are some major problems with the result of the SFA, all originating from the main approximation of the theory, namely neglecting the Coulomb potential

of the atom. In particular, the Coulomb potential is expected to influence the ionization amplitude, the phase acquired by the electron during its evolution and, more drastically, the subsequent interaction of the electron with the atomic core. A partial justification of this approach is the much shorter range of the Coulomb potential compared to the laser potential, which implies that the electron can be significantly affected only at locations in the vicinity of the parent ion. One can therefore expect that during the major part of the electron's trajectory the Coulomb potential indeed be negligible. This is the physical justification of the SFA.

1.2 First step: ionization

Several theories of ionization in strong laser fields have been proposed to date [Delone94]. In the following, the main features characterizing this first step of the simple man's model will be discussed.

1.2.1 Tunneling and multiphoton limits

The origin of ionization is the perturbation induced by the strong oscillating laser field on the unperturbed Coulomb potential of the atom. A simple way to study this problem is the so-called adiabatic (or quasi-static) approximation. In the quasi-static limit, the electron in the ground state is subject at each time to a potential barrier originating from the sum of the atomic potential and the instantaneous potential of the laser's field (Fig. 1.1). The ionization rate (i.e. tunneling probability per unit time) can then be calculated [Landau65]:

$$W_{QS}(t) = 4 \frac{(2I_p)^{5/2}}{E(t)} \exp \left[-\frac{2(2I_p)^{3/2}}{3E(t)} \right] \quad (1.9)$$

where I_p is the ionization potential of the atom, $E(t)$ the laser's electric field, and the suffix QS stands for quasi-static. The ionization rate has a highly nonlinear dependence on the instantaneous value of the electric field. At the zero-crossings of the oscillating laser field, no potential barrier is created, hence the ionization rate is zero [Fig. 1.2(a)]. Other treatments based on the quasi-static limit have been proposed, yielding results similar to Eq. (1.9). Most known are the rates derived by Keldysh [Keldysh65] and Ammosov, Delone and Krainov (ADK) [Ammosov87]: they all share with Eq. (1.9) the exponential factor, which gives the strongest dependence on the electric field, but differ in the preexponential factor, which may include a weak dependence on the initial state (defined by its quantum numbers). In the following, Eq. (1.9) will be used as representative of quasi-static models.

The adiabatic assumption is only justified if the tunneling time (i.e. the time *spent* by the electron while overcoming the barrier) is significantly smaller than the laser

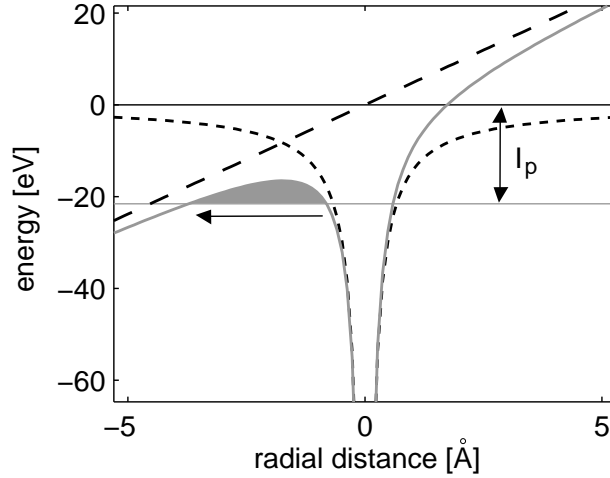


Figure 1.1: The oscillating electric potential of the laser (long dashed line) perturbs at each instant the atomic potential (short dashed line). This gives rise to a potential barrier (shaded area) that the electron in the ground state can overcome. The probability is expected to strongly depend on the instantaneous value of the electric field and on the ionization potential I_p of the atom.

period. This situation is known as *tunneling ionization*. In the pioneering paper by Keldysh [Keldysh65] it was shown that this condition is fulfilled, provided the *Keldysh* parameter $\gamma = \sqrt{I_p/2U_p}$ is smaller than 1. Here, $U_p = E^2/4\omega^2$ (ω is the laser's angular frequency) is the quiver energy of the electron, i.e. the average kinetic energy acquired by the electron in the laser field². When $\gamma > 1$ the tunneling time exceeds the laser period, i.e. ionization takes place during several oscillations of the electric field, and a quasi-static approach is clearly not correct. This situation is referred to as *multiphoton ionization*. Experimentally, one is typically dealing with intermediate values of the Keldysh parameter (Fig. 1.3).

An analytical expression for arbitrary values of γ has been recently derived by Yudin and Ivanov [Yudin01]. Their analysis allows to explicitly distinguish between tunneling and multiphoton contributions to the total ionization probability. In the tunneling limit ($\gamma < 1$) the ionization rate $W_{NA}(t)$ of [Yudin01] (the suffix NA stands for nonadiabatic) reproduces the quasi-static limit (1.9), while in the multiphoton limit ($\gamma > 1$) the ionization probability no longer depends on the instantaneous value of the electric field. In particular, nonzero ionization probability is predicted even at the zero-crossing of the laser field [Fig. 1.2(b)]. In general, however, it is common practice to use the more known quasi-static rates even for intermediate values of the Keldysh parameter ($\gamma \sim 1$).

If the laser field is very strong, the potential well of the ground state can be so perturbed that the electron is (in one direction) virtually in the continuum (Fig. 1.1).

² U_p is also known as ponderomotive energy. It is often used also as scaled intensity of a laser. In this context, a useful formula is $U_p[\text{eV}] = 0.09337 I[\text{W}/\text{cm}^2] \lambda^2[\text{m}]$.

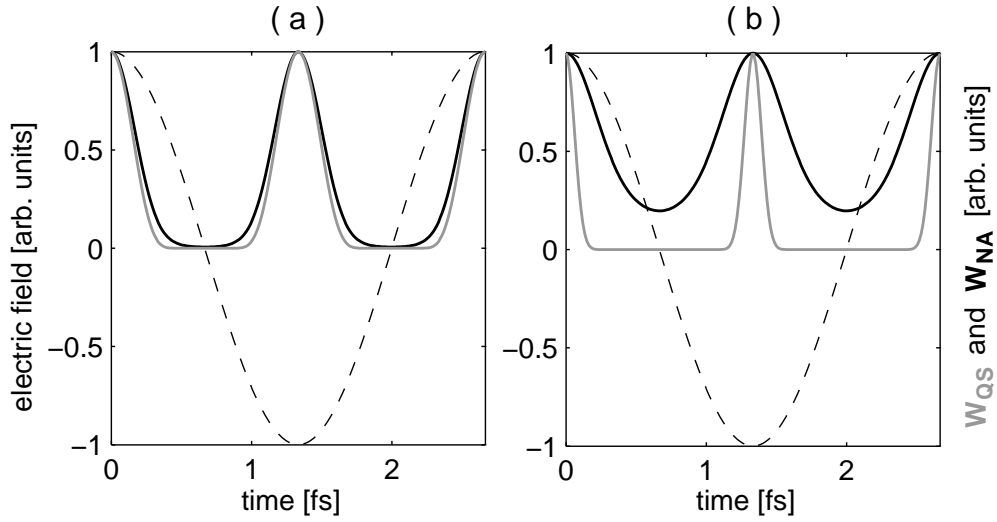


Figure 1.2: Periodic electric field (dashed line) and corresponding instantaneous ionization rates in argon ($I_p = 15.76$ eV) for a peak intensity of 3×10^{14} W/cm² (a) and 1×10^{13} W/cm² (b). Both the rates calculated with the static model [(1.9), gray solid line] and the nonadiabatic model [[Yudin01], black solid line] are shown. In (a) the quasi-static approach is justified ($\gamma \sim 0.5$), in (b) the nonadiabatic model is more suitable ($\gamma \sim 4$).

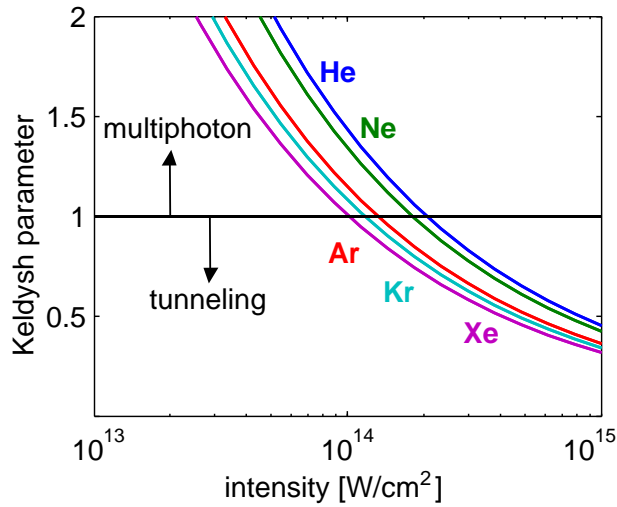


Figure 1.3: Keldysh parameter $\gamma = \sqrt{I_p/2U_p}$ as a function of the laser intensity for different atomic species. Depending on the atom and the intensity used, either multiphoton or tunneling limits may be valid.

This situation is known as *barrier-suppression* regime, and it occurs at threshold intensities dependent on the atomic potential. For instance, typical values for Ne, Ar and Kr are approximately 10^{15} W/cm^2 , $4 \times 10^{14} \text{ W/cm}^2$, and $3 \times 10^{14} \text{ W/cm}^2$ respectively. Obviously, any tunneling ionization theory fails at higher intensities, simply because the electron has no longer a barrier to overcome. Different approaches are then necessary to calculate the ionization rate, the most fundamental being numerical integration of the time-dependent Schrödinger equation (see [Bauer99] and references therein).

1.2.2 Ionization yields and saturation

Once a suitable ionization *rate* $W(t)$ is assumed [typically the quasi-static limit (1.9) is used], the integrated ionization *yield* can be calculated as:

$$\Lambda(t) = 1 - \exp \left[- \int_{-\infty}^t W(t') dt' \right]. \quad (1.10)$$

The saturation intensity (defined, e.g., as the intensity at which 50% of the atoms are ionized) depends on the ionization potential and on the duration of the laser pulse. A weak, long pulse can eventually lead to a fully ionized gas medium. Conversely, a strong, extremely short pulse, though characterized by much higher ionization rates, may not have sufficient time to significantly ionize [Fig. 1.4(a)].

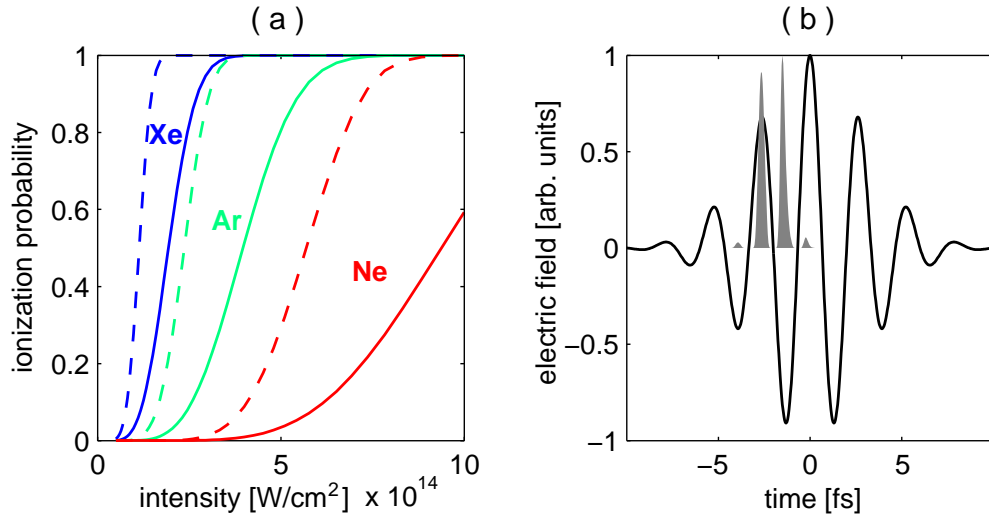


Figure 1.4: (a) Ionization probability as a function of the laser intensity for different atomic species and pulse durations of 5 fs (solid line) and 50 fs (dashed line). (b) Instantaneous ionization rate (shaded area) in Xe for a 5-fs pulse at $5 \times 10^{14} \text{ W/cm}^2$. Ionization takes place mainly in the leading edge.

Note that when ionization is saturated, the instantaneous ionization rates decrease accordingly, due to the ground-state depletion. In other words, the majority of the atoms is already ionized before the pulse is over³: thus, ionization takes place only in the leading edge of the pulse [Fig. 1.4(b)].

1.3 Second step: free electron evolution

The electron ejected into the continuum evolves, according to the SFA, under the action of the laser field only (the Coulomb potential is neglected). This problem can be treated very accurately with a classical approach. Consider the electric field of a linearly polarized laser:

$$\vec{E}(t) = \vec{E}_0 a(t) \cos(\omega t + \phi) \quad (1.11)$$

where \vec{E}_0 defines the peak intensity and the laser polarization, $a(t)$ is the pulse envelope (normalized to 1) and defines the pulse shape and duration, ω is the laser's angular frequency, and ϕ is the so called *absolute phase*, a quantity of critical importance for very short pulses (see Chapter 3). The electron appears in the continuum at some time t_0 with the initial conditions $x(t_0) = 0$ (defined as the location of the ion core) and $\dot{x}(t_0) = 0$. The subsequent evolution under the action of the quasi-periodic driving force $-e\vec{E}(t)$ is a simple classical problem. It can be solved numerically, graphically [Paulus95] and, for a periodic field (i.e. in the limit of a very long pulse), analytically [Corkum89].

The trajectory of the electron is the sum of an oscillation with time-dependent amplitude [proportional to the value of the envelope $a(t)$] and a drift term (Fig. 1.5). The latter is entirely determined by the initial time t_0 . This can be understood as follows. The Newton equation $m_e \partial \dot{x} / \partial t = -e\vec{E}(t)$ (m_e is the electron's mass), together with $\vec{E}(t) = -\partial \vec{A}(t) / \partial t$ [$\vec{A}(t)$ is the vector potential] implies that the *canonical momentum*

$$\vec{p}_{can} = m_e \dot{\vec{x}}(t) - e\vec{A}(t) \quad (1.12)$$

is constant during the electron's motion⁴. Therefore, since the initial velocity is assumed to be zero, the remaining velocity [$\dot{\vec{x}}(t \rightarrow \infty)$] when the pulse is over [$\vec{A}(t \rightarrow \infty) = 0$] is given by $(-e/m_e)\vec{A}(t_0)$. Thus, the initial time t_0 determines both the ionization probability [through $\vec{E}(t_0)$] and the drift velocity [through $\vec{A}(t_0)$].

For some initial times t_0 , the electron trajectory revisits the ion core (Fig. 1.5). In these cases, neglecting the Coulomb potential of the atom is a poor approximation.

³The argument applies also for a single atom. In this case, the probability amplitude of finding the electron in the ground state decreases, while the probability amplitude of finding the electron in the continuum increases, i.e. the ground state is depleted.

⁴This argument requires the choice of a particular gauge for the vector potential, namely the Coulomb gauge $\vec{\nabla} \cdot \vec{A} = 0$. It can be shown that this is consistent with the assumed initial condition $\dot{\vec{x}}(t_0) = 0$.

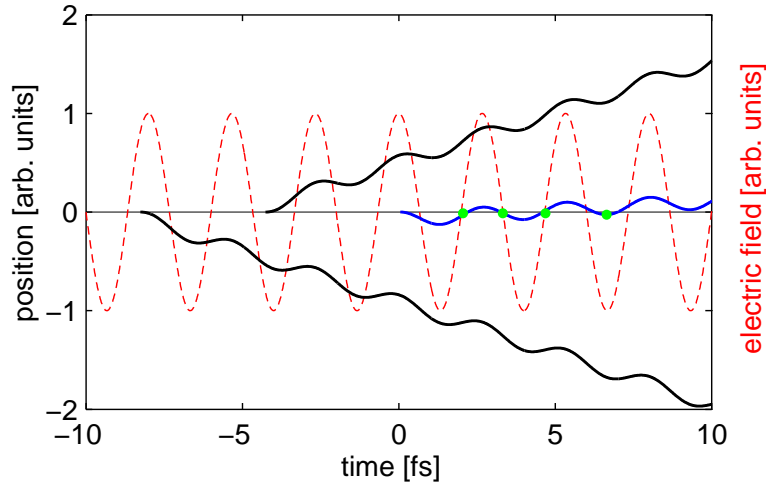


Figure 1.5: Periodic electric field (red dashed line) and possible electron trajectories (solid lines) as a function of time. The contribution of each orbit scales with the ionization rate $W(t_0)$. Depending on the initial time t_0 the trajectory leads to a drift in the positive or negative direction. For some initial times, the electron reencounters the ion core (position = 0) one or several times (blue line).

Indeed, the most interesting effects of strong laser physics arise from such an additional interaction of the returning electron with the parent ion. This gives rise to different possible scenarios:

- the electron may recombine, which leads to the emission of a photon with an energy equal to the electron's kinetic energy plus the ionization energy of the atom. This process is responsible for high-order harmonic generation (HHG, Sec. 1.4);
- the electron may scatter off the ion. In this case, the electron is further accelerated by the electric field, leading to a high-energetic photoelectron. This process is responsible for the plateau observed in above-threshold ionization (ATI, Sec. 1.5);
- the electron may kick out another electron and thus ionize the ion. This process is known as non-sequential double ionization (NSDI, Sec. 1.6).

1.4 High-order harmonic generation (HHG)

HHG, experimentally discovered in 1987 [McPherson87, Ferray88], consists of efficient, coherent radiation emission at frequencies that are odd multiples of the fundamental. One of the most peculiar feature of this process is the shape of the harmonic spectrum: it falls off for the first few orders, then exhibits a *plateau* where all the harmonics

have approximately the same strength, and ends up with a rather sharp *cutoff*. Any attempt of explaining this behavior in the frame of perturbative nonlinear optics failed, while the proposal of the two-step model [Kulander93, Corkum93] opened the way to a complete understanding of the physics of HHG. A fully and exhaustive quantum mechanical model in the frame of the SFA followed short afterwards [Lewenstein94]. Today, it is unanimously accepted that the physical mechanism at the basis of HHG is, as outlined in the last section, recombination of the electron interacting with its parent ion after free evolution. As a consequence, one photon of energy $\hbar\omega = E_{kin} + I_p$ is emitted. For a recent review of HHG, see [Salières99].

1.4.1 Single-atom response

Since HHG originates from recombination, the electron trajectories of interest are those returning to the ion core (Fig. 1.5). Numerical, graphical and analytical methods can be used for their determination. The basic results are the following⁵:

- the electron returns to the parent ion only if tunneling ionization takes place at given time *windows*, namely those characterized by an initial phase $\varphi_0 = \omega t_0 \in [0 + n\pi, \pi/2 + n\pi]$ [for an electric field of the form $E(t) \propto \cos(\omega t)$]⁶;
- the maximum kinetic energy of the returning electron is proportional to the laser intensity, and is given by $E_{max} = 3.17 U_p$, U_p being the ponderomotive potential. It occurs for trajectories starting at an initial phase $\varphi_0 = 1.88$ rad;
- for energies lower than $3.17 U_p$, there are two trajectories (for each laser cycle) leading to the same kinetic energy of the returning electron. They are characterized by a different *traveling* time (i.e. the time interval between the ionization instant t_0 and the recombination instant t_1), and they are therefore referred to as short and long trajectories⁷.

Figure 1.6 summarizes these results by showing the kinetic energy of the returning electron as a function of the initial time t_0 . A cutoff energy for the harmonic photon is then predicted at $3.17 U_p + I_p$ (I_p is the ionization potential of the atom), in agreement with experimental observations [Krause92, L’Huillier93]. Note that the photon

⁵These results are rigorously valid only in the case of an infinitely long pulse (i.e. of a periodic electric field). However, significant modifications only occur for pulses consisting of few optical cycles (Chapter 3).

⁶As can be seen in Fig. 1.5, the electron trajectory can reencounter more than once the ion core, giving rise to recombination probabilities at different times. In reality, due to wave-packet dispersion, the recombination cross section for the first return time is highly dominant in most cases.

⁷In particular, trajectories that started earlier ($\varphi_0 < 1.88$ rad) will return later. The picture suggests similarities with a classical projectile motion, the launch angle with the vertical being replaced by the phase of the electric field.

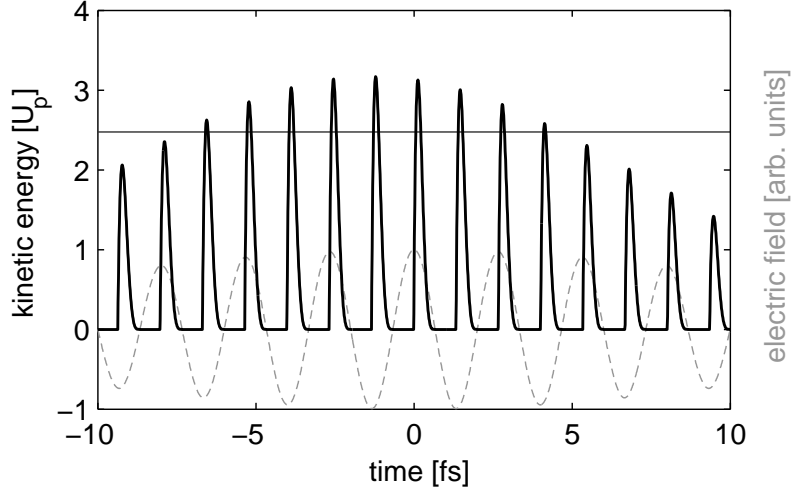


Figure 1.6: Laser’s electric field (dashed gray line) and kinetic energy of the electron returning to the ion core (solid black line) as a function of the initial time t_0 . The pulse duration considered here is 20 fs FWHM. For energies lower than the cutoff, several couples of short and long trajectories exist (e.g. 9 couples at $E_{kin} = 2.5 U_p$).

emission is spatially and spectrally not discrete. In other words, it occurs in a random direction and is not characterized by a peak structure.

For electron energies lower than $3.17 U_p$, photons of the same energy can be emitted at many instants. Hence, the resulting radiation field is given, at each energy, by the coherent sum of all elementary emission processes. The amplitude of these is given by the ionization rate at the time t_0 , while, according to the quantum-mechanical model of HHG [Lewenstein94, Lewenstein95], the phase is given by:

$$\theta = -\frac{1}{\hbar} \int_{t_0}^{t_1} [p^2(t)/2m_e + I_p] dt + q\omega t_1 \quad (1.13)$$

where t_0 is the tunneling time, t_1 the recombination time, p the electron’s classical momentum, m_e the electron mass, I_p the ionization potential of the atom, q the harmonic order (here any positive real number) and ω the laser’s angular frequency. Equation (1.13) has the following intuitive interpretation. During the motion (between t_0 and t_1) the electron acquires, at each small time interval dt , a phase given by $\omega_{el}(t)dt$, where $\omega_{el}(t) = E_{kin}(t)/\hbar$. The effect of the binding potential appears through the dependence on I_p . Finally, since recombinations take place at different times t_1 , all phases must be referred to a common time axis ($+q\omega t_1$).

Due to the shape of the pulse envelope and to the focusing geometry, the intensity of the fundamental laser is strongly varying both temporally and spatially. Therefore, it is particularly interesting to investigate the dependence of the phase of the emitted radiation on the intensity. Figure 1.7(a) shows the contour plot of the phase θ as a function of the ponderomotive energy U_p and the traveling time $\tau = t_1 - t_0$. This

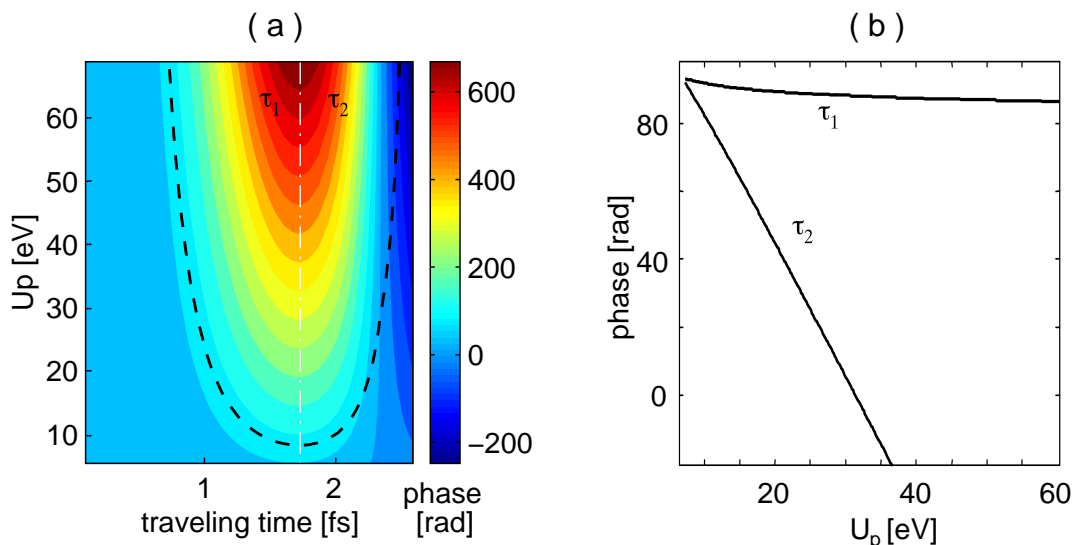


Figure 1.7: (a) Contour plot of the phase of the emitted radiation field (in argon) as a function of the laser ponderomotive energy U_p and the traveling time τ . The dashed line corresponds to the 25th harmonic. (b) Corresponding intensity dependence of the phase of the 25th harmonic (in argon) for the short (τ_1) and long (τ_2) trajectories.

allows to explicitly distinguish the behavior of the short (τ_1) and long (τ_2) trajectories. The dashed line connects all points giving rise to an harmonic photon of equal energy [e.g. the 25th harmonic in Fig. 1.7(a)]. Short trajectories (left-hand side of the plot) are characterized by a small variation of the phase along the line, while long trajectories (right-hand side of the plot) experience a remarkable variation of the phase. It turns out that the dependence is almost linear:

$$\theta = -\eta U_p \quad (1.14)$$

where η only depends on the type of trajectory followed by the electron⁸. Typical values are $\eta = -0.11$ rad/eV for the short trajectory and $\eta = -3.9$ rad/eV for the long trajectory [Fig. 1.7(b)].

Figure 1.8 shows the *single-atom* spectrum resulting from the coherent sum of all elementary emission processes. It is instructive to separate the short and long trajectories. Both are characterized by a peak structure⁹. The long trajectory (black line) shows broader peaks and a much more irregular behavior as compared to the short trajectory (gray line). This is due to the temporal intensity change and the corresponding stronger phase modulation (1.14), which directly translates into a spectral

⁸In fact, the coefficient η depends also on the ionization potential of the atom and on the harmonic order. However, this dependence is very weak.

⁹The more terms contribute to the coherent sum, the sharper the peaks. This is a fundamental property of Fourier transforms, with several examples in different fields of physics. For instance, the diffracted orders of a grating get better defined by increasing the number of lines.

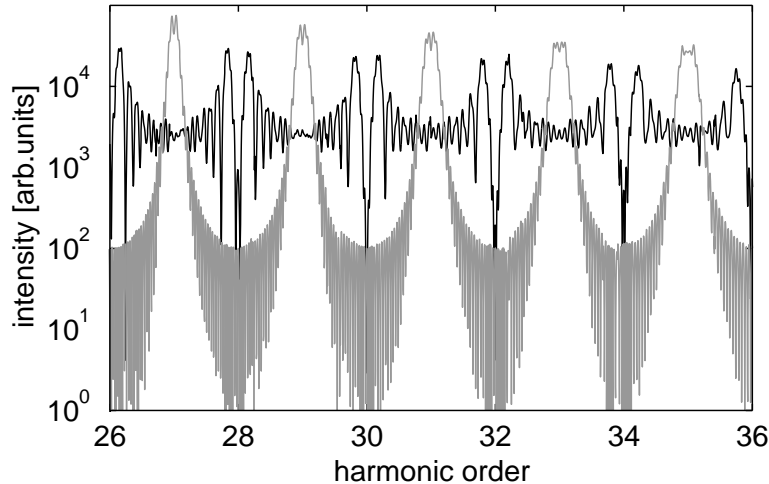


Figure 1.8: Single-atom spectrum (semi-logarithmic scale) of argon for short (gray) and long (black) trajectories. The laser pulse considered here has a duration of 60 fs FWHM and a peak intensity of $4 \times 10^{14} \text{ W/cm}^2$. Due to the different phase modulation, the characteristic peak structure is very different for the long and short trajectories. Note that for the higher orders (right-hand side) the peaks become broader, since fewer elementary emission processes are involved.

modulation $[\omega(t) = -\partial\theta(t)/\partial t]$ ¹⁰.

The fact that harmonic emission occurs at odd multiples of the fundamental frequency can thus be understood in terms of phase-matching (for a single atom) in time domain: arbitrary frequencies are rapidly washed out, while odd harmonics grow from cycle to cycle and give a nonzero net contribution. Not surprisingly, the spacing between the harmonic peaks is given by twice the photon energy. Indeed, photon emission takes place every half optical cycle, i.e. it is a periodic process with a time periodicity given by half the laser period ($\Delta t = \pi/\omega$; see Fig. 1.6). From the Fourier relation $\Delta t \Delta\omega = 2\pi$, it is thus clear that the frequency spacing of the spectrum must be $\Delta\omega = 2\omega$ (ω being the fundamental angular frequency).

1.4.2 Macroscopic response: phase-matching

Section 1.4.1 described the spectral properties of the radiation emitted (in a random direction) by each atom. Since a large number of atoms is involved in HHG, the macroscopic response will depend on how the elementary processes act together. The initial and final states of each elementary process coincide (one atom and one photon); hence, the conditions for interference are fulfilled. As the atom cloud consists of a large number of particles randomly positioned, constructive interference can only occur in

¹⁰Indeed, the details of the modulation are strictly connected with the pulse duration and temporal shape. Here and in the following, a Gaussian envelope is assumed.

the direction of the generating fundamental laser beam. Emission in different directions is completely washed out by the arbitrary phase relation between the elementary harmonic fields¹¹.

The efficiency of the harmonic build-up process strongly depends on how the phases match (*phase-matching*). This is one of the main issues in HHG experiments, in particular with respect to possible application of the generated coherent radiation. There are three main contributions to the phase of the harmonics:

- the *atomic* phase contribution θ_{atomic} (1.14). This term scales linearly with the laser intensity and strongly depends on the trajectory followed by the electron (Sec. 1.4.1);
- the *geometrical* phase due to the phase shift in the focus of a Gaussian beam [Svelto98]. For the fundamental this term reads:

$$\theta_{geom}(r, z) = -\arctan\left(\frac{z}{z_R}\right) + \frac{\pi r^2}{\lambda R(z)} \quad (1.15)$$

where r and z are the radial and longitudinal coordinates respectively, z_R is the Rayleigh distance of the focus, λ the wavelength of the fundamental, and $R(z)$ the radius of curvature (dependent on the longitudinal position z). At the wavelength of the q -th order harmonics $\lambda_q = \lambda/q$, this term will contribute as $q\theta_{geom}$;

- the *dispersion* phase due to neutral atoms, free electrons and ions. This term plays a role at intensities causing significant ionization and is usually dominated by the free electrons' contribution, which reads:

$$\theta_{disp}(r, z) = \frac{q\lambda e^2}{4\pi\epsilon_0 m_{el} c^2} N_{el}(r, z) z \quad (1.16)$$

where e is the electron charge, ϵ_0 the dielectric constant of vacuum, m_{el} the electron's mass, c the speed of light, and N_{el} the electrons' density (dependent on the local intensity and thus on r and z).

The harmonic field builds up efficiently only if the phases match over a significant volume. In other words, the algebraic sum $\theta_{atomic} + q\theta_{geom} + \theta_{disp}$ should remain constant. Note that both the geometrical and the dispersion phase have odd symmetry in the propagation direction around the focus, while the atomic phase, being simply proportional to the intensity, has even symmetry. Hence, the sum of the three terms is expected to be asymmetric.

Figure 1.9 represents the resulting phase (here, for the 35th harmonics in argon) for the short (a) and long (b) trajectories. For simplicity, only the atomic and geometrical

¹¹For the same reason, light propagates in a straight line in a dielectric medium.

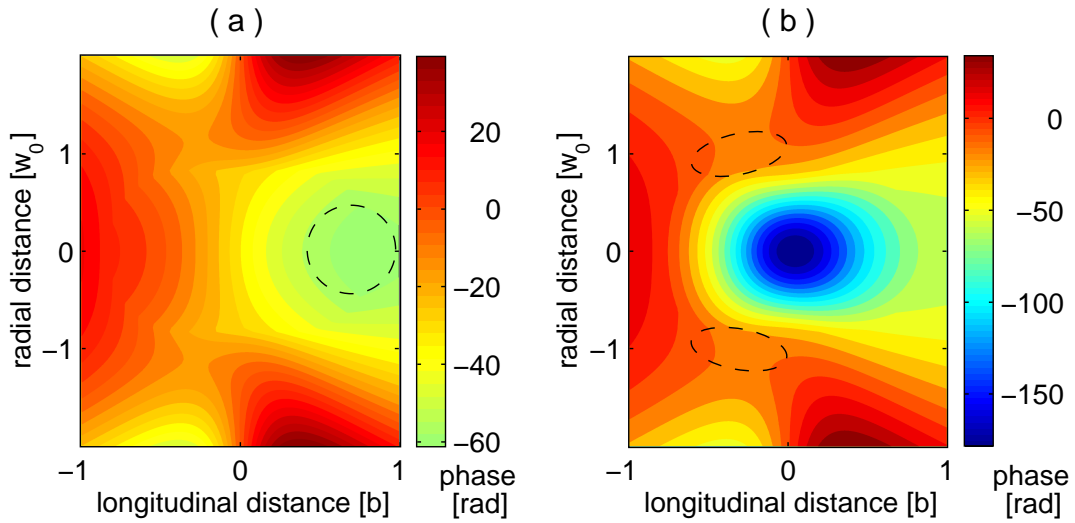


Figure 1.9: Contour map of the phase of the 35th harmonic in argon for the short (a) and long (b) trajectories. The longitudinal distance is indicated in units of the confocal parameter b , the radial distance in units of the beam waist w_0 . The peak intensity of the laser pulse is $5 \times 10^{14} \text{ W/cm}^2$. The emitted radiation builds up efficiently where the phases of the elementary processes match over a significant area (dashed lines).

phases are considered. The analysis can be easily and without any loss of generality extended to include dispersion effects. A striking difference appears in phase-matching conditions for short and long trajectories. The latter gives rise to a rapidly varying phase, with only a small *off-axis* annular region of good phase-matching *before* the focus. On the other hand, short-trajectory-generated harmonics show a quite flat phase, with a large *on-axis* region of very good phase-matching *after* the focus.

A more fundamental approach for studying phase-matching consists in generalizing the semiclassical model used to calculate single-atom spectra (Sec. 1.4.1, Fig. 1.8) to reproduce macroscopic effects. For each atom, a single-atom calculation is performed as described in Sec. 1.4.1. According to the position of the atom, a weight function is used to allow spatial variations of the gas pressure, and the generating electric field of the pulse is phase-shifted to take into account the geometrical term of the phase [Eq. (1.15)]. Finally, all contributions are coherently summed in the far field.

Figure 1.10 shows the intensity of the resulting radiation field as a function of the harmonic order and of the longitudinal position of the gas source in the laser focus. Efficient, sharp peaks can be observed after the focus, while spectrally modulated peaks are generated before the focus. A closer analysis reveals that the latter are due to phase-matching *off-axis* of harmonics generated through the long trajectories, while the first correspond to phase-matching *on-axis* of harmonics generated through the short trajectories. This is completely consistent with the descriptive analysis of Fig. 1.9. These remarkable differences are recognizable in the experimental results (Chapter 2).

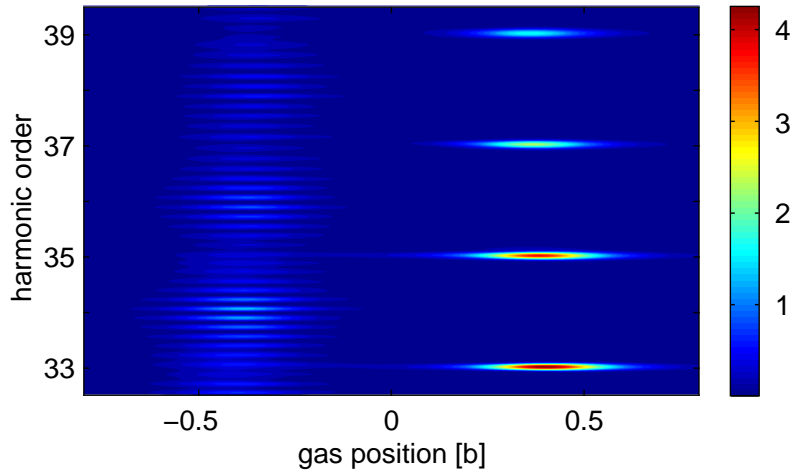


Figure 1.10: Intensity of the generated harmonic radiation in argon as a function of the harmonic order and of the longitudinal position (in units of the confocal parameter b) of the gas density maximum. The peak intensity of the laser pulse is $5 \times 10^{14} \text{ W/cm}^2$, the pulse duration 40 fs. The gas density considered here is a Lorentzian of width $b/2$. The sharp peaks after the focus correspond to short trajectories, the modulated structure before the focus to long trajectories.

In conclusion, the *spatial* outcome of HHG experiments is largely dominated by the *phase-matching* conditions (i.e. by the *spatial* variation of the laser pulse). Those critically depend on the type of trajectory followed by the electron, and permit in fact to macroscopically separate the contributions from the short and long trajectories. On the other hand, the *spectral* characteristics of the emitted radiation also differ for the two contributions, but are mainly determined by the *single-atom* response (i.e. by the *temporal* variation of the laser pulse). This behavior has been pointed out in previous work [Salières95, Balcou97] by means of quantum-mechanical calculations in the frame of the SFA. The semiclassical model developed here (Sec. 1.4.1 and 1.4.2) reproduces all the essential features of HHG remarkably well.

1.5 Above-threshold ionization (ATI)

ATI has been discovered experimentally in 1979 [Agostini79]. It denotes photoionization in intense laser fields such that an atom absorbs more photons than necessary for its ionization. This can be seen by measuring the photoelectron kinetic energy spectra, which consist of a series of peaks separated by the photon energy. The peak heights decrease as the order is increased. In 1994 [Paulus94b] it was discovered that the initial decrease of electron yield is followed by a flat annex (ATI *plateau*), very similar to the feature observed for HHG. All these characteristics are now understood in the framework of the semiclassical model. For a recent review of ATI, see [Becker02].

1.5.1 Single-atom response

In Sec. 1.3 it has been shown that, after ionization has occurred, the electron undergoes free oscillations along the polarization axis until the laser pulse is over. The *drift* momentum of the electron is given by $-e\vec{A}(t_0)$, $\vec{A}(t_0)$ being the vector potential at the tunneling time t_0 . An immediate consequence is that the drift energy shows a maximum at $2U_p$ [Paulus94a]. This maximum occurs when ionization takes place at a zero-crossing of the electric field, thus with very low probability. Conversely, the drift energy approaches zero when ionization takes place at a maximum of the electric field. Hence, the resulting electron spectrum for these *direct* electrons (i.e. without rescattering) is expected to decrease monotonically from $0U_p$ to $2U_p$. Note that, since electrons are emitted in both directions of the polarization axis, the drift momentum is either positive or negative.

For electrons returning to the ion core during their evolution (Fig. 1.5), elastic back-scattering can occur [i.e. $\vec{x}(t)$ changes its sign at the return time $t = t_1$]. In this case, the initial conditions of the electron's motion are changed such that the electric field of the pulse accelerates the electron further instead of decelerating it, as it is the case without rescattering. This leads to high-energetic photoelectrons. By numerically solving the equation of motion of the electron, the maximal kinetic energy for the *rescattered* electrons is calculated to be $10U_p$ [Paulus94a]¹². Today, this elastic rescattering process is recognized as being responsible for the ATI plateau [Paulus94b].

Figure 1.11 summarizes these results by showing the drift energy of the electrons as a function of the initial time t_0 . Note that the electron emission can occur in two opposite directions. Direct electrons (gray solid line) show a cutoff energy at $2U_p$, rescattered electrons (black solid line) at $10U_p$. In principle, there are no drift energies favored in this process, so that the electron emission is not characterized by a peak structure.

For energies lower than the cutoff, however, electrons of the same drift energy can be emitted at many instants. As in the case of HHG, there is no possibility to distinguish between the different elementary processes. Hence, quantum interference takes place between the electrons' wave-packets. The amplitude of these is given by the ionization rate at the time t_0 , while the phase is given by:

$$\theta = -\frac{1}{\hbar} \int_{t_0}^{\infty} [p^2(t)/2m_e] dt \quad (1.17)$$

where t_0 is the tunneling time, p the electron's classical momentum and m_e the electron's mass. Equation (1.17) simply states that during its motion the electron wave-packet acquires, at each small time interval dt , a phase given by $\omega_{el}(t)dt$, where $\omega_{el}(t) = E_{kin}(t)/\hbar$.

¹²This value, as well as the cutoff value of $2U_p$ for the direct electrons, is rigorously valid only in the case of an infinitely long pulse (i.e. of a periodic electric field). The differences occurring at short pulse durations will be extensively discussed in Chapter 3.

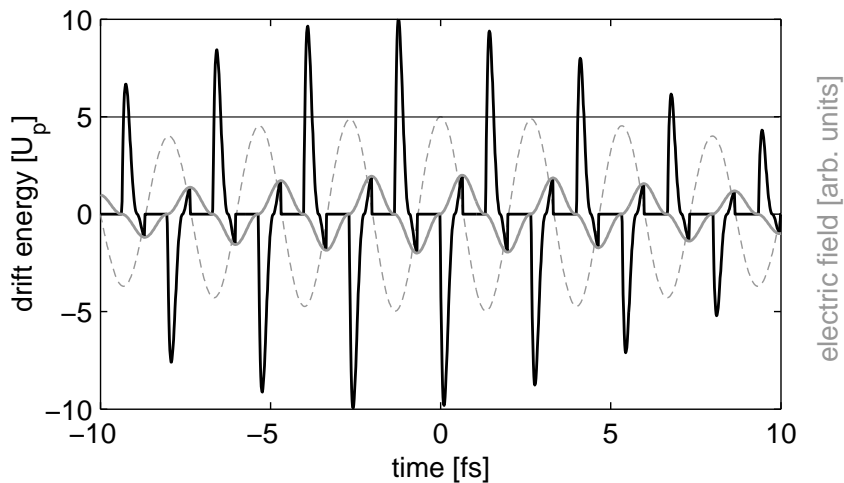


Figure 1.11: Laser’s electric field (dashed gray line) and drift energy of the electrons (solid lines) as a function of the initial time t_0 . The pulse duration considered here is 20 fs FWHM. Direct electrons (gray) show a cutoff at $2 U_p$, rescattered electrons (black) at $10 U_p$. Note that the electron emission can occur in two opposite directions (here indicated with positive and negative energies). For energies lower than the cutoff, several possible trajectories exist (e.g. 7 couples at $E_{drift} = +5 U_p$).

Figure 1.12 shows the ATI spectrum calculated by coherently adding all contributions. It is useful to introduce the *ATI order*, defined as $E_{kin,el}/\hbar\omega$, ω being the angular frequency of the laser. The spacing of the characteristic ATI peaks corresponds to one photon, thus half of the spacing observed in HHG. This is not surprising, since the time periodicity of ATI is twice that of HHG (cf. Figs. 1.6 and 1.11)¹³.

1.5.2 Macroscopic response: volume effects

As in HHG experiments, a large number of atoms contribute to the measured ATI signal. However, the size of the electrons’ wave-packets is several orders of magnitude smaller than that of the photons emitted in HHG. In addition, typical ATI experiments are done at very low target pressures ($< 10^{-3}$ mbar vs. > 1 mbar for HHG). As a consequence, even considering wave-packet dispersion in the free space before reaching the detector, the size of the electrons’ wave-packets remains well below the mean inter-atomic distance. Thus, interference between electrons emitted from *different* atoms do not occur.

The absence of a coherent macroscopic effect as in HHG means that the outcome of ATI experiments is given by the single-atom response. However, all atoms ionized in the focus still contribute (*incoherently*). As in HHG, the spatial variation of the intensity in the focal volume influences the measured signal significantly. This can be

¹³It is worth emphasizing that only electrons emitted in the same direction (e.g. positive energy in Fig. 1.11) can interfere.

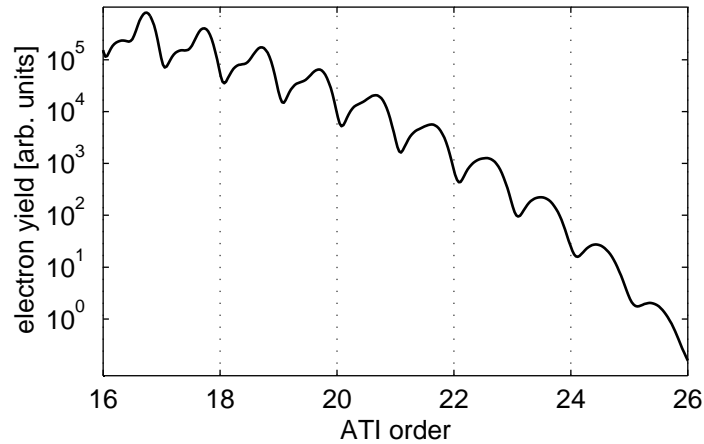


Figure 1.12: Electron yield (semi-logarithmic scale) in argon as a function of the ATI order. The laser pulse considered here has a duration of 30 fs FWHM and a peak intensity of $4 \times 10^{14} \text{ W/cm}^2$. The energy interval plotted corresponds to the range $[U_p, 2U_p]$. At these energies, the main contribution is from direct electrons (note the typical exponential decay). The characteristic peak structure is due to electrons' interference.

understood in the framework of the multiphoton description of ATI, where the position of the peaks is given by:

$$E_{peak} = n\hbar\omega - (I_p + U_p), \quad (1.18)$$

where n is an integer, I_p is the ionization potential of the atom, and U_p the ponderomotive energy. The latter acts as an additional potential barrier for the electron. Indeed, based on energy conservation arguments, the electron absorbs an integer number of photons ($n\hbar\omega$) and has to overcome the barrier (I_p) and to quiver (U_p).

Since the intensity (and thus U_p) is not constant in the focal volume, the overall effect is a broadening of the ATI peaks. In order to estimate the contribution of each intensity to the signal, one has to consider the larger number of atoms at low intensities (outer part of the focus) and the increase of the ionization rate at high intensities. For the latter, an often used rule-of-thumb is the following: Yield $\propto U_p^N$, where N is the minimum number of photons necessary to subdue the ionization potential¹⁴. As a result, the majority of the electrons originate from an annular region close (but not coincident) to the beam axis, where the intensity is maximum.

Figure 1.13 shows a few ATI peaks for three different peak intensities. Here, a constant background pressure is assumed, but the model can be easily extended to account spatial variations of the target gas pressure. The clear peak structure at low intensity is completely washed out at higher intensities. Nevertheless, very often peak structure is observed even at high intensities. The reason is that the light-shifts of atomic levels can lead, in specific regions of the laser focus, to particularly efficient ionization¹⁵.

¹⁴For instance, at 800 nm ($\hbar\omega = 1.55 \text{ eV}$) in xenon ($I_p = 12.13 \text{ eV}$), one has $N = 8$.

¹⁵One example is resonantly enhanced ionization induced by the ponderomotive shift [Freeman87].

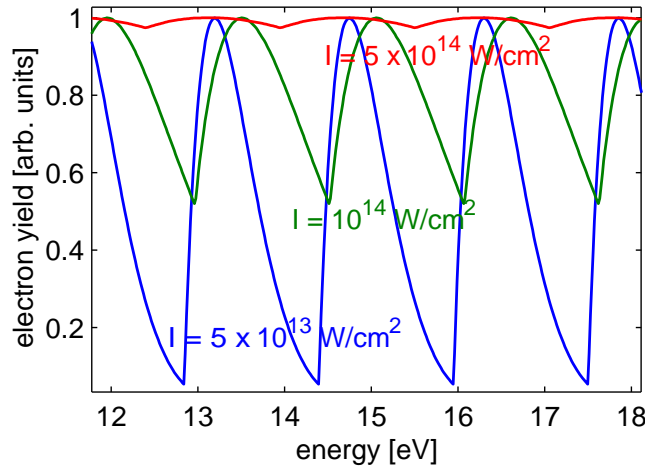


Figure 1.13: ATI peaks in xenon at intensities of $5 \times 10^{13} \text{ W/cm}^2$ (blue), 10^{14} W/cm^2 (green), and $5 \times 10^{14} \text{ W/cm}^2$ (red). The peak spacing is the photon energy, here for a wavelength of 800 nm (1.55 eV). At high intensity the peak structure is smeared out.

1.6 Non-sequential double ionization (NSDI)

The typical scenario for sequential multiple ionization is the following. By increasing the laser intensity, the ion yield scales with some high power of the laser intensity, as mentioned in Sec. 1.5.2, till the saturation point, where the whole interaction volume is ionized, is reached. From there on the ion yield roughly scales with the 3/2 power of the intensity, according to the geometrical increase of the saturation volume. Further increase of the intensity leads to ionization of ions, i.e. doubly charged ions are created. Again, this first scales with some high power of the intensity before saturating, and so on.

In 1983, unexpectedly high double ionization yields were measured [L’Huillier83], showing that the above *sequential* scheme was not exhaustive. Double ionization was found to proceed in a *non-sequential* way. The mechanism has to be traced back to the high kinetic energy of the electrons returning to the ion core (Sec. 1.4.1). If this energy exceeds the ionization potential I_p^+ of the ion core, non-sequential double ionization (NSDI) can occur through impact ionization.

The currently best experimental technique to study NSDI is based on correlated ion and electron momentum spectroscopy [Ullrich97]. In recent experiments performed with the 100-kHz laser system described in Sec. 2.1, NSDI at and below threshold for impact ionization has been investigated. The results strongly suggest that, within the quasi-static model (Sec. 1.2.1), the electric field of the light wave reduces the instantaneous ionization potential of the singly charged ion core at the instant of rescattering [Eremina03].

Chapter 2

High-order harmonic generation at a repetition rate of 100 kHz

Femtosecond laser systems normally used in HHG experiments have typical repetition rates up to 5 kHz. The corresponding energies are around 1 mJ, or even considerably higher for very low repetition rates. The main advantage of having a high pulse energy is the possibility of reaching the required high intensity with a loose focusing geometry. In this way, the increased interaction volume can lead to very high conversion efficiency into the harmonic comb [Hergott02].

Conversely, a very high repetition rate can be highly desirable in situations where space charge effects can play a critical role or for coincidence experiments. Another important issue of high repetition rates laser systems is the correspondingly large spacing of the modes constituting the spectrum. Thus, the modes are well defined and separated, which makes it interesting for applications in spectroscopy and frequency metrology¹. Since the modes are up-converted in the HHG process, using a high repetition rate can provide a source of high-brightness radiation in the VUV very suitable for potential spectroscopic applications.

In this chapter, experimental results of HHG at 100 kHz will be presented [Lindner03]. This is by far the highest repetition rate ever reported for HHG. After a brief description of the laser system used [Lindner02], the XUV spectrometer will be illustrated. Generation and detection of the harmonic radiation is very challenging, due to the very low pulse energy characterizing the laser system. The experimental results confirm the theoretical analysis of Sec. 1.4. In particular, it is shown that the position of the gas jet with respect to the laser focus can select a single quantum trajectory followed by the electron. Finally, a simple and intuitive method for spectral reshaping of the harmonics is proposed.

¹For such applications, active stabilization of the mode spacing (repetition rate) and of the carrier-envelope offset (CEO, Chapter 3) is necessary.

2.1 The laser system

The laser system [Lindner02] used in these experiments is an 800-nm Ti:sapphire regenerative amplifier system delivering pulses of $7 \mu\text{J}$ at a repetition rate of 100 kHz. It consists of a femtosecond oscillator, a commercial regenerative amplifier (RegA 9050, Coherent), a prism compressor and a liquid-crystals phase modulator in a 4f setup (Fig. 2.1).

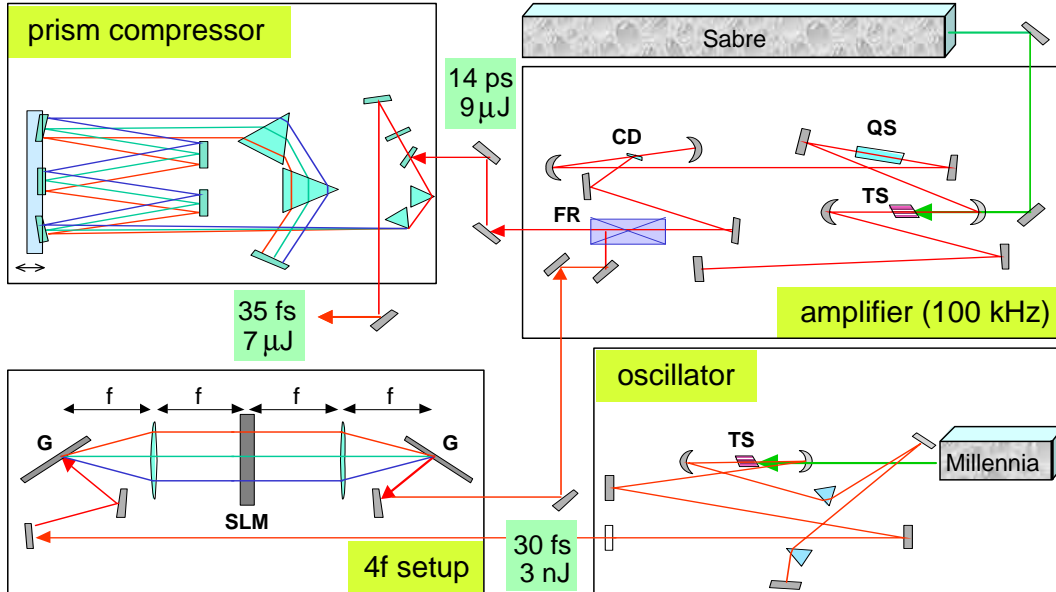


Figure 2.1: Scheme of the laser system. TS - Ti:Sapphire crystal; G - grating; SLM - spatial light modulator; FR - Faraday isolator; QS - Q-switch; CD - cavity dumper. The output pulses are characterized by a typical energy of $7 \mu\text{J}$ and a duration of 35 fs.

To avoid Kerr lens induced self-focusing and other detrimental nonlinear effects, the standard technique for amplifying femtosecond pulses is the so-called chirped pulse amplification (CPA) [Maine88], consisting in temporally stretching the pulses before amplification and recompressing them afterwards. Typically, a dedicated stretcher stage is used. Our laser, however, simply relies on the fact that sufficient broadening of the pulses naturally occurs due to the accumulated dispersion during the amplification process. This large amount of dispersion is peculiar to our system, since the high repetition rate prevents the use of a pulsed pump laser and, therefore, requires a Q-switch in the amplifier to reach the desired inversion in the gain medium (Fig. 2.1). The 30-fs pulses generated in the oscillator are broadened already to 700 fs after the first round trip in the regenerative amplifier, and to almost 14 ps before cavity dumping (taking place after 18 round trips). This makes nonlinear effects negligible.

The huge amount of dispersion accumulated in the amplification stage is compensated with a prism compressor. This choice presents two main advantages as compared to a standard grating compressor. First, the efficiency is much higher ($\sim 90\%$

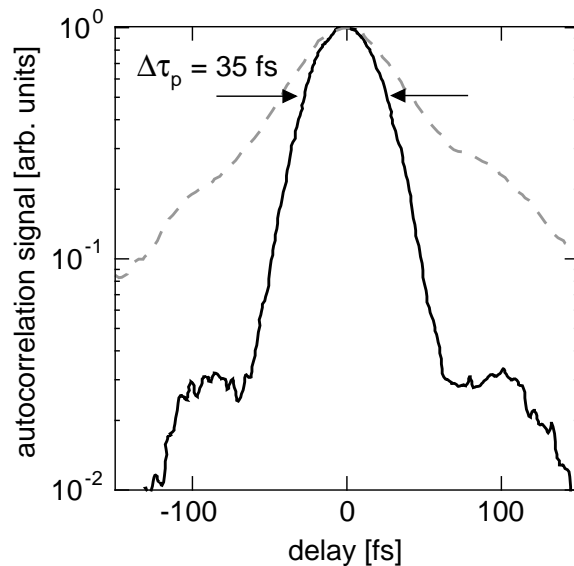


Figure 2.2: Noncollinear autocorrelation (semi-logarithmic scale) of the amplified and compressed pulses (solid black line). For comparison, the autocorrelation without SLM in operation is also shown (dashed gray line). Removing the higher orders of dispersion considerably shortens the pulse, for a typical value of 35 fs (a Gaussian envelope is assumed for determination of the pulse duration).

vs. $\sim 60\%$), particularly attractive for an already low-pulse-energy laser system. Second, a prism compressor permits better control and compensation of higher orders dispersion², essential for shortening the pulses down to the Fourier limit.

To achieve dispersion compensation in all orders, a spatial light modulator (SLM 128, CRI) is used before amplification. The SLM is placed in the Fourier plane of a 4f setup [Weiner00], where optimum spatial separation of the spectral components of the laser radiation occurs (Fig. 2.1). Each pixel ($N=128$) can independently influence the phase of the respective spectral component by means of an applied voltage. The overall phase distribution is chosen by adjusting the voltage values in an optimization loop [Zeidler00]. The second harmonic (SH) signal from a nonlinear crystal can be typically used as feedback. This allows shortening the pulse duration down to 35 fs, i.e. nearly to the bandwidth limit (Fig. 2.2). This is the shortest pulse duration reported at this very high repetition rate (100 kHz) for amplified fs-pulses. If a feedback directly related to the peak intensity at a given experiment is available, it is possible to make the pulse shortest in the experimental environment itself, making the system very flexible if optical elements are added. In addition, the use of the SLM allows performing experiments with pulses characterized by a precisely controlled chirp (Sec. 2.3.3).

²Optical materials are characterized by positive second-order dispersion (SOD) and third-order dispersion (TOD), prism compressors by negative SOD and TOD. Conversely, grating compressors are characterized by negative SOD but positive TOD. While both compressors compensate the positive SOD of optical materials, only a prism compressor can balance, at least partly, also the positive TOD of optical materials.

2.2 The XUV spectrometer

As any standard HHG setup, the XUV spectrometer (Fig. 2.3) consists of three parts: (i) an interaction region, where the nonlinear process takes place; (ii) a dispersive system, where the different wavelengths are separated; (iii) a detector. A detailed description can be found in [Zacher98].

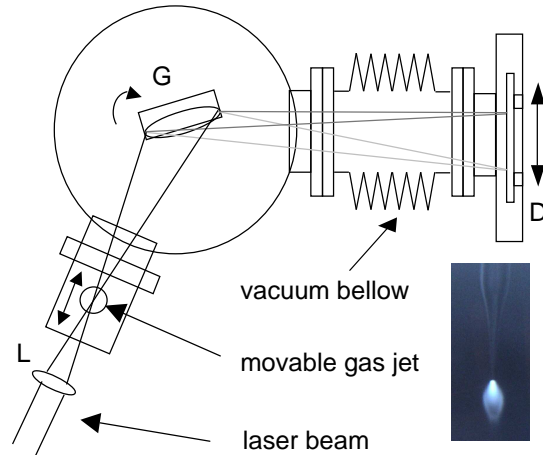


Figure 2.3: The XUV spectrometer for high-order harmonic generation and detection. L - Fraunhofer achromat ($f = 60$ mm); G - flat-field toroidal grating; D - pn-CCD detector. The whole system is in ultrahigh vacuum to prevent reabsorption of the generated VUV radiation. Inset: photograph of the gas jet illuminated by the focused fs laser. The shape of the characteristic fluorescence can be conveniently used for alignment.

The relatively low pulse energy (Sec. 2.1) requires a tight focusing geometry in order to reach the high intensities necessary for driving the nonlinear process. The beam is expanded and focused (f-number 8) with an achromatic lens ($f = 60$ mm, B. Halle Nachfl., Berlin) into a rare gas jet. Intensities of up to 3×10^{14} W/cm² are reached in the focus ($U_p = 18$ eV). However, since the interaction volume is extremely small (confocal parameter ~ 100 μ m), the conversion efficiency into the harmonics comb is $< 10^{-9}$, i.e. lower than normally reported in HHG experiments. The detection of the light field is therefore particularly challenging. With respect to this, advantage can also be taken of the very high repetition rate of the laser. The gas pressure before the effusive nozzle (diameter 100 μ m) is usually kept between 100 and 300 mbar. The nozzle position can be finely adjusted in all directions. On the basis of gas flow measurements, one can estimate a pressure in the interaction volume not exceeding 5-10 mbar. At these low pressures the absorption length ($L_{abs} = 1/\sigma\rho$, where ρ is the gas density and σ is the ionization cross-section [Chan92]) for, for example, the 25th harmonic generated in argon is a few millimeters, i.e. much larger than the medium length. Therefore, in this particular focusing geometry reabsorption does not play any role³.

³Differential pumping is used in order to keep very low pressure ($< 10^{-5}$ mbar) in the rest of the

2.2 The XUV spectrometer

The high harmonics generated are incident on a gold-coated flat-field toroidal grating (1800 grooves/mm, Jobin-Yvon Instruments, S.A.). This separates and focuses the harmonics in a plane at a focal distance of approximately 35 cm. The reflectivity in the energy of interest ($\sim 20\text{-}70\text{ eV}$) is 30% and the resulting spectral dispersion at the focal plane is $8\text{ \AA}/\text{mm}$.

The detector consists of a backside illuminated pn-CCD chip [Strüder00] of very high quantum efficiency (20-70%) in the range 15-70 eV. The detector length is 30 mm (64×200 pixels), which yields a spectral resolution of approximately $1\text{ \AA}/\text{pixel}$. The chip is cooled to liquid nitrogen temperature during operation. Since the CCD is sensitive not only to the XUV spectral range, but also to the visible and infrared, a thin (2000 \AA) aluminum filter in front of the detector is used to remove scattered light from the fundamental beam (800 nm). This restricts the sensitivity of the spectrometer to wavelengths above 18 nm (harmonic order < 45)⁴.

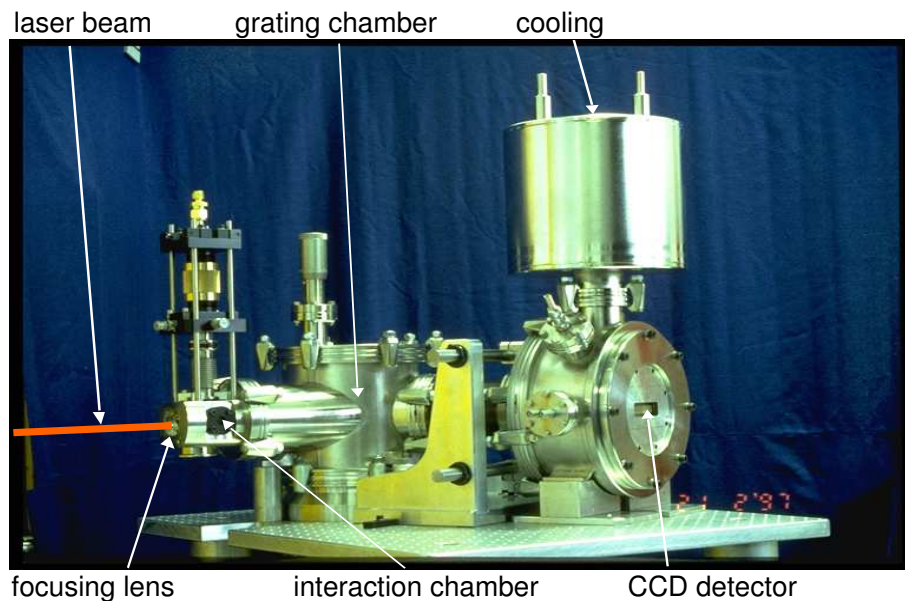


Figure 2.4: The XUV spectrometer.

vacuum chamber, so that any reabsorption can only take place in the interaction volume itself.

⁴In the experiments described here this does not represent a limitation, since the intensities used do not permit generation of harmonics of higher order. When higher intensities are available, however, different metal filters must be used.

2.3 Experimental results

2.3.1 Longitudinal dependence

In Sec. 1.4.2 it was shown that the most critical parameter for phase-matching (PM) in HHG is the position of the gas jet with respect to the laser focus. In order to probe the spatial dependence of PM, one has to systematically shift their relative positions. Ideally, one would need a gas jet of much smaller size than the focal volume. In our experiments this is not possible, due to the tight focusing geometry (confocal parameter $\sim 100 \mu\text{m}$). However, testing of the position dependence of PM is still possible owing to the thin nozzle used (cross-section $\sim 100 \mu\text{m}$) and to the density profile of the gas. The relative position between nozzle and focus can be easily estimated by the shape of the characteristic gas fluorescence induced by the laser (cf. Fig. 2.3). The nozzle position is then adjustable in all directions with translation stages.

Fig. 2.5 shows the measured intensity of different harmonic peaks as a function of the nozzle longitudinal position with respect to the focus. The target gases are argon (a,b) and krypton (c,d). Both sets of measurements show systematic behaviors: (i) The harmonic emission is characterized by a clear peak structure; (ii) The maximum of the efficiency is located after the focus; (iii) The maximum of the efficiency approaches the center of the focus for increasing harmonic order. Points (i) and (ii) strongly suggest, in agreement with the theoretical analysis (cf. Sec. 1.4.2 and Fig. 1.10 on page 20), that the HHG process is dominated by the electrons having followed the short trajectory. In the next section this will be discussed further. Point (iii) is a consequence of the cutoff law $\hbar\omega_{max} = 3.17 U_p + I_p$ (Sec. 1.4.1) according to which the highest orders are generated where the laser intensity is highest. Note also that in argon (a,b) slightly higher orders than in krypton (c,d) can be observed, due to the difference in ionization potential. On the other hand, a lower ionization potential implies that ionization (and hence the HHG process) can take place at lower intensities. For this reason the maximum efficiency for krypton is found even more shifted to the outer part of the focus with respect to argon.

Other effects producing asymmetries, such as reabsorption in the atomic gas, would lead to a maximum on the opposite side of the focus. Hence, what is observed is clearly a phase-matching effect. The observed asymmetry also indicates, as already outlined in Sec. 1.4.2, that phase terms of different symmetry [i.e. the atomic and Gouy phases, Eqs. (1.14) and (1.15) on page 18] compensate each other. Note that, since in our experiments we deal with low pressures ($< 10 \text{ mbar}$) and very tight focusing geometry (f-number 8), dispersion effects [Eq. (1.16)] don't play a crucial role. Even in the (nonrealistic) case of complete ionization of the atomic medium, the coherence length (i.e. the length over which the phase slippage is π) associated with the dispersion of the free electrons is of the order of the laser confocal parameter. In this range, the variation of the Gouy phase is much larger. Therefore, all dispersion effects can be neglected.

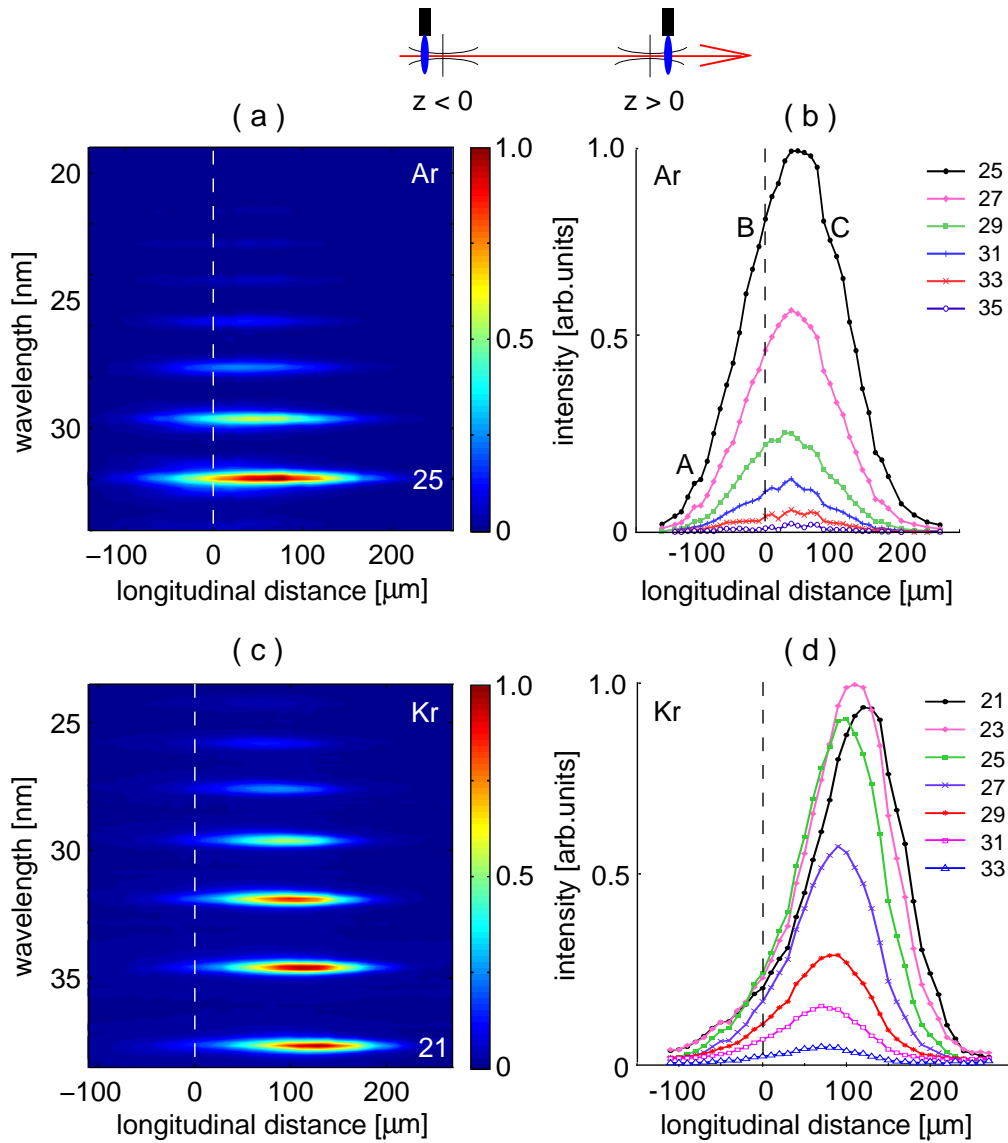


Figure 2.5: Measured HHG spectra (arb. units) in argon (a) and krypton (c) as a function of the relative position between gas jet and laser focus. The conversion efficiency into the different HHG orders (b,d) is calculated by integration of the relative peaks.

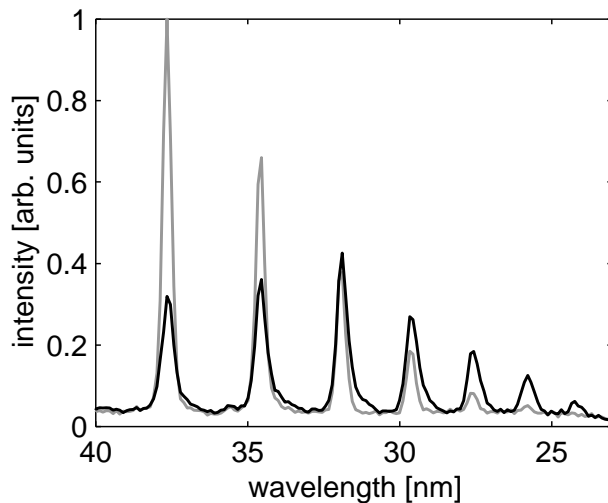


Figure 2.6: Measured HHG spectra in krypton (same measurement as Fig. 2.5) for a gas jet located in the focus ($z = 0$, black line) and after the focus ($z = +180 \mu\text{m}$, gray line). The qualitative difference is due to the different phase-matching conditions.

Finally, Fig. 2.6 compares the HHG spectrum measured in krypton for a gas jet located in the focus ($z = 0$, black line) and after the focus ($z = +180 \mu\text{m}$, gray line). The latter is characterized by good phase-matching but low laser intensity. Hence, the harmonics comb shows very pronounced peaks but low cutoff energy. Conversely, when the gas jet is positioned in the focus, the laser intensity is maximum (high cutoff energy) but the harmonic field does not build up efficiently, due to the poor PM conditions.

2.3.2 Quantum path separation

The phase of the emitted radiation varies linearly with the laser intensity [Eq. (1.14), $\theta = -\eta U_p$]. This phase modulation has interesting consequences on the spectral characteristics of the high harmonics generated. Since we are dealing with short pulses and high peak intensities, the rapid time variation of the intensity results in modulation of the instantaneous harmonic frequency:

$$\delta\omega = -\frac{\partial\theta}{\partial t} = +\eta\frac{\partial U_p}{\partial t}, \quad (2.1)$$

and therefore in broadening of the spectrum. In particular, the leading edge of the harmonic pulse is blue-shifted, and the trailing edge is red-shifted. In other words, the generated harmonic carries a negative chirp which depends on the peak intensity, the pulse duration and the slope (η) of the atomic phase. This phenomenon is similar to self-phase modulation of an intense laser pulse in a medium with negative Kerr index [Shen84]. Figure 2.7 shows the calculated instantaneous wavelength of the 25th

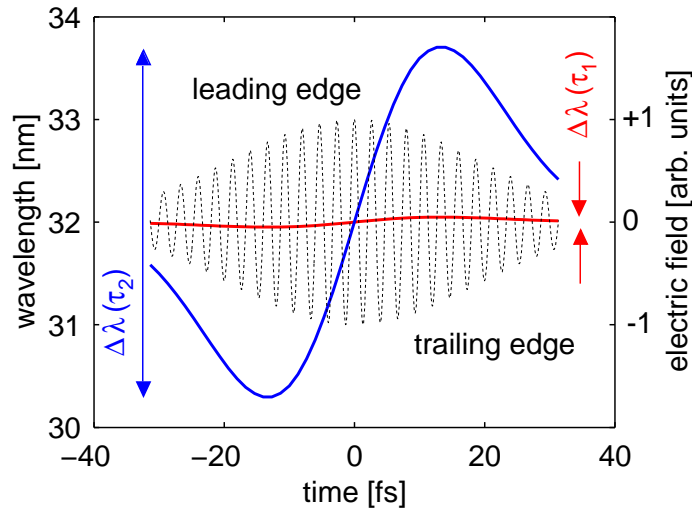


Figure 2.7: Laser’s electric field (dotted line) and instantaneous wavelength of the 25th harmonics generated in argon as a function of time for the short (red line) and long (blue line) trajectory. The peak intensity is 3×10^{14} W/cm², the pulse duration 35 fs. The harmonic pulse is characterized by a negative chirp that depends on the laser parameters and on the type of trajectory.

harmonic in argon for the parameters of our experiment. The type of trajectory followed determines the spectral width of the harmonic peak (cf. Sec. 1.4.1). Short trajectories (τ_1) are then characterized by a narrow spectrum (small η), while the opposite applies for long trajectories (τ_2 , large η).

If one trajectory is dominating, the spectral width is determined by the peak intensity of the laser. The maximum spectral broadening should be observed at the laser focus, where the temporal derivative of U_p is largest. Figure 2.8 shows the spectrum of the 25th harmonic in argon for two different positions of the gas jet [B and C in Fig. 2.5(b)]. For both positions the conversion efficiency (represented by the integral of the harmonic peak) is the same, i.e. the number of photons generated is equal. As expected, when the gas jet is located exactly in the focus (black line), the larger phase modulation experienced results in a broader peak than in case C (gray line), where the peak intensity is lower.

More interestingly, one can compare the spectra corresponding to two symmetric positions of the nozzle with respect to the focus [Fig. 2.9, corresponding to positions A and C in Fig. 2.5(b)]. The peak intensity of the fundamental is now the same in the two cases, and differences in the spectra must be explained in terms of the coefficient η in Eq. (2.1). The peak observed in C is relatively sharp, confirming that when the gas jet is positioned after the focus the HHG process is dominated by electrons that have followed the short trajectory. On the other hand, the peak in A is broader and suggests a double structure. Indeed, the position A corresponds [cf. Fig. 1.9(b) on page 19] to a region before the focus where the harmonics can be efficiently generated off-axis from electrons that have followed the long trajectory. In

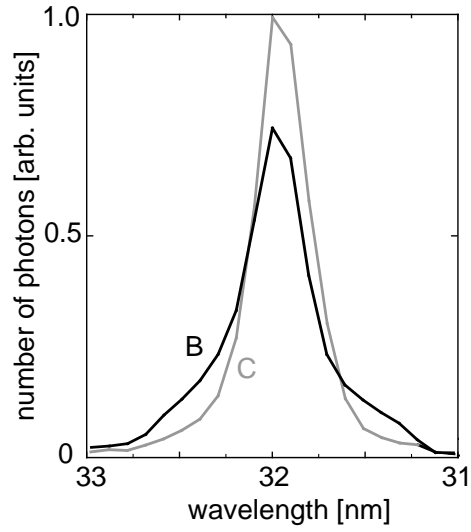


Figure 2.8: Spectrum of the 25th harmonic peak in argon for the gas jet positions B and C of Fig. 2.5(b). The conversion efficiency (represented by the integral of the peak) in B and C is identical. The spectral width is larger when the gas jet is positioned in the focus (black line), due to the higher peak intensity [Eq. (2.1)].

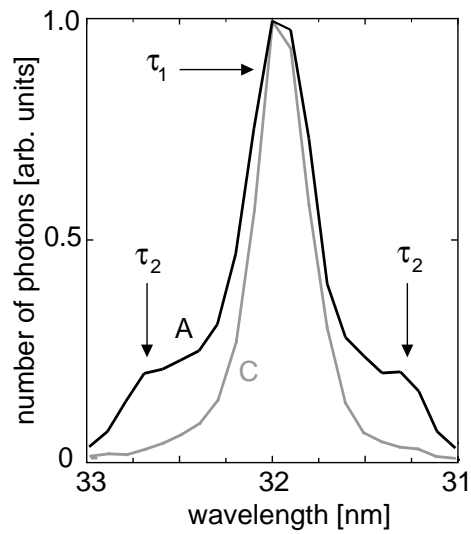


Figure 2.9: Spectrum of the 25th harmonic peak in argon for the gas jet positions A and C of Fig. 2.5(b). Since the conversion efficiency in A is lower than in C, suitable normalization is necessary for the sake of clarity. After the focus (gray line) the short trajectory (τ_1) dominates. Before the focus (black line) also the long trajectory (τ_2) plays a role.

fact, the spectrum in A consists of two superimposed contributions, one from the short trajectory (with phase-matching almost degraded) giving rise to the central peak, the other from the long trajectory (with increasingly good phase-matching) leading to the observed wings in the spectrum. The harmonic pulse is thus characterized by different generation processes, and therefore by regions of different spatial and temporal coherence [Bellini98, Gaarde99].

Adjusting the gas jet position allows to macroscopically separate the contributions of the different quantum paths. This effect, predicted [Gaarde99] and observed [Salières01], is here confirmed under qualitatively different experimental conditions. It should be noted that not only is separation of the harmonic field into the two τ_1 and τ_2 components a significant result from the point of view of theoretically understanding the HHG process, it also represents a way of providing XUV radiation with desired spatial and spectral characteristics. The latter, in particular, can also be tailored by adjusting the laser chirp.

2.3.3 Active spectral reshaping

The chirp of the harmonics induced by the rapid phase variation can, in principle, be controlled by an appropriate chirp on the fundamental laser pulse [Salières98]. The idea is illustrated in Fig. 2.10. When the laser pulse is not chirped, the generated harmonics are negatively chirped [Eq. (2.1)]. If the fundamental beam carries a positive chirp, the *red* frequencies on the leading edge of the pulse will be blue-shifted, and the *blue* frequencies on the trailing edge will be red-shifted. The resulting spectrum will thus appear quite narrow and will be limited by the natural bandwidth of the harmonic pulse. On the other hand, for a negative chirp on the fundamental one should observe enhanced spectral broadening.

Simple numerical estimates based on the above argument show that this kind of control is only possible for harmonics generated with the short trajectory. Indeed, the phase variation corresponding to the long trajectory is so large that the induced chirp (Fig. 2.7) determines in any case the observed spectral width. This is not true of the τ_1 contribution, characterized by a slower phase variation, for which chirp compensation by acting on the laser is feasible.

By locating the gas jet in a position where the short trajectory dominates (i.e. after the focus), one can analyze the HHG spectra as a function of the chirp of the fundamental. This can easily be changed by adjusting the voltages of the spatial light modulator used in the laser system (Sec. 2.1). Figure 2.11 shows a few harmonic peaks in argon as a function of the applied chirp. These are purely quadratic and vary from $+200 \text{ fs}^2$ to -200 fs^2 . Since the pulses become longer when they carry a residual chirp ($\sim 40 \text{ fs}$ vs. 35 fs for no additional chirp), the conversion efficiency in the harmonics comb and the cutoff extension are higher in the case of no chirp.

As expected, the harmonic peaks get broader when the generating pulse is nega-

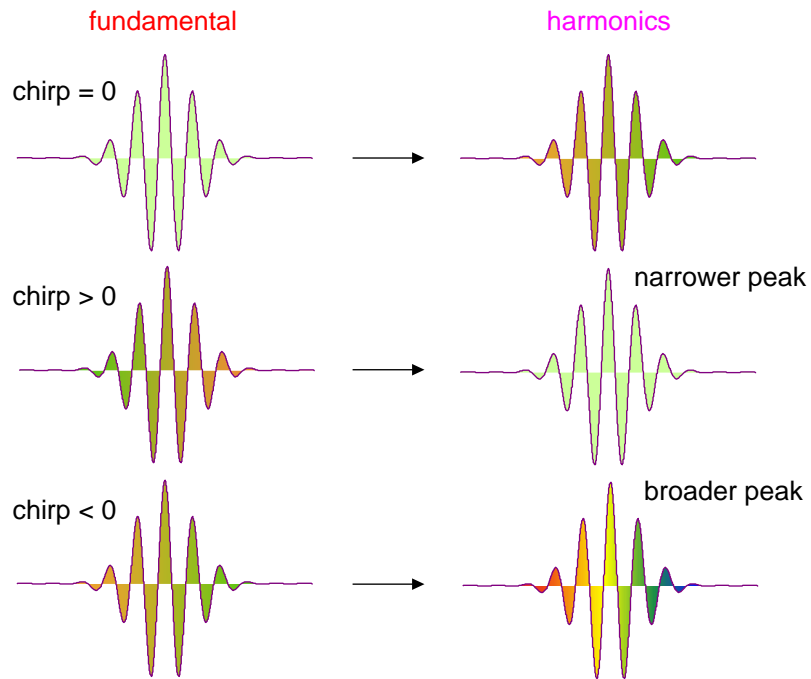


Figure 2.10: Principle of spectral reshaping by adjustment of the laser chirp.

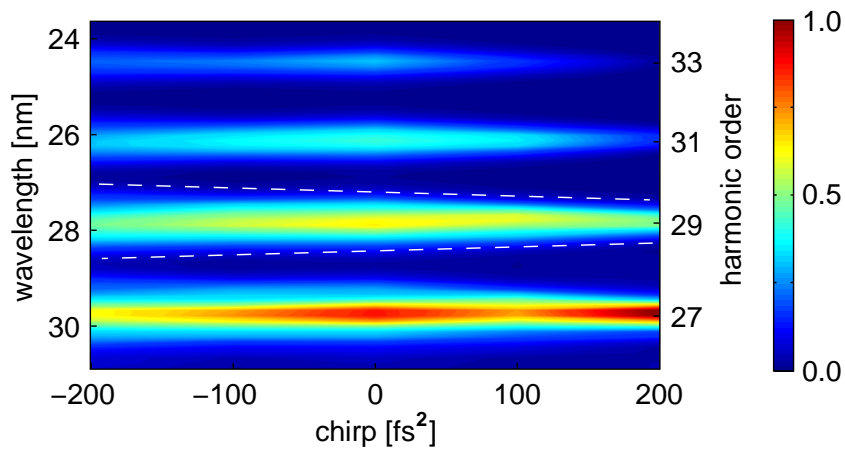


Figure 2.11: Measured HHG spectra (arb. units) in argon as a function of the chirp of the generating laser pulse. The spectral width increases for negative chirp, and decreases for positive chirp. The white dashed line is to guide the eye.

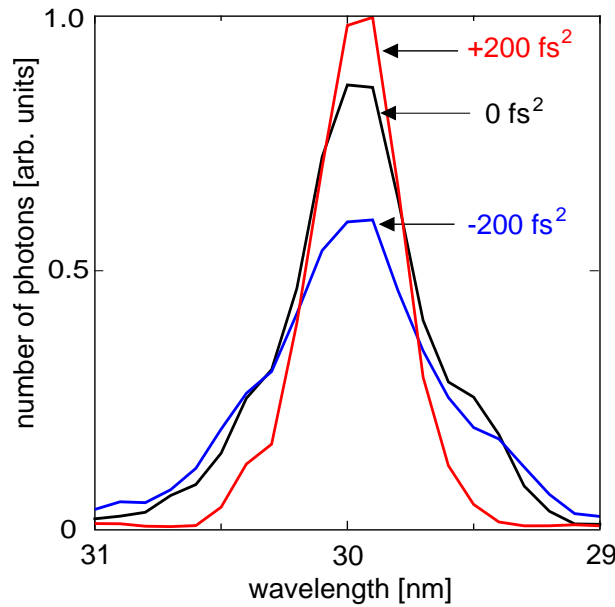


Figure 2.12: Spectrum of the 27th harmonic peak in argon for positive (red line), negative (blue line), and zero (black line) chirp of the laser pulse. The spectral width of the emitted harmonic radiation can be controlled by acting on the chirp of the laser.

tively chirped. This can be better seen in Fig. 2.12, showing the spectra of the 27th harmonic for positive (red, $+200 \text{ fs}^2$), negative (blue, -200 fs^2) and zero (black) chirp applied. Note that, when high degrees of ionization are reached, the HHG process takes place mainly in the leading edge of the pulse [cf. Fig. 1.4(b) on page 11]. Under these conditions, the use of a chirped pulse would result in relevant blue or red shifting of the harmonic peak. Since this is not observed, it is confirmed that ionization is not a major effect in these experimental conditions.

The narrow peak and the enhanced broadening observed for application of positive and negative chirp, respectively, confirm the agreement between the theoretical analysis and the experimental data. In particular, the macroscopic separation into the two quantum trajectories is here shown once more. Furthermore, this last result traces an extremely simple way of tailoring the shape of the spectrum on demand, a feature that might be essential for future applications of high harmonics.

Chapter 3

Determination of the absolute phase of few-cycle laser pulses

In recent years there has been increasing interest in the generation and application of ever shorter laser pulses. Pulse durations of less than 5 fs in the near-infrared (800 nm) are in fact routine since the introduction of the hollow-fiber pulse compression technique [Nisoli96, Nisoli97, Steinmeyer99]. For such laser pulses, the standard characterization techniques turn out to be not sufficient for an exhaustive description of the electric field. A new quantity, referred to as carrier-envelope phase (or *absolute phase*¹), had to be introduced. Though it is recognized that the absolute phase significantly affects the outcome of most experiments performed with ultrashort laser pulses, complete control of the phase had to date not yet been achieved.

In this chapter, experimental results of ATI performed with few-cycle laser pulses will be presented [Paulus03, Lindner04b]. These constitute the first determination of the value of the absolute phase without any ambiguity. After an introduction on the absolute phase, the experimental setup - including the laser system and the ATI spectrometer - will be presented. The measured ATI spectra will be then illustrated and compared with simulations relying on different theoretical models, showing the robustness of the phase determination against experimental uncertainties or theoretical approximations. The results presented here greatly attracted the attention of the scientific community, drawing also novel interest to the physical process of above-threshold ionization.

3.1 The absolute phase

For the shortest pulses generated to date, the amplitude of the electromagnetic wave changes almost as fast as the field oscillates. At a typical wavelength of 800 nm,

¹A very uninteresting discussion on whether this name is suitable surprisingly attracts the interest of many scientists.

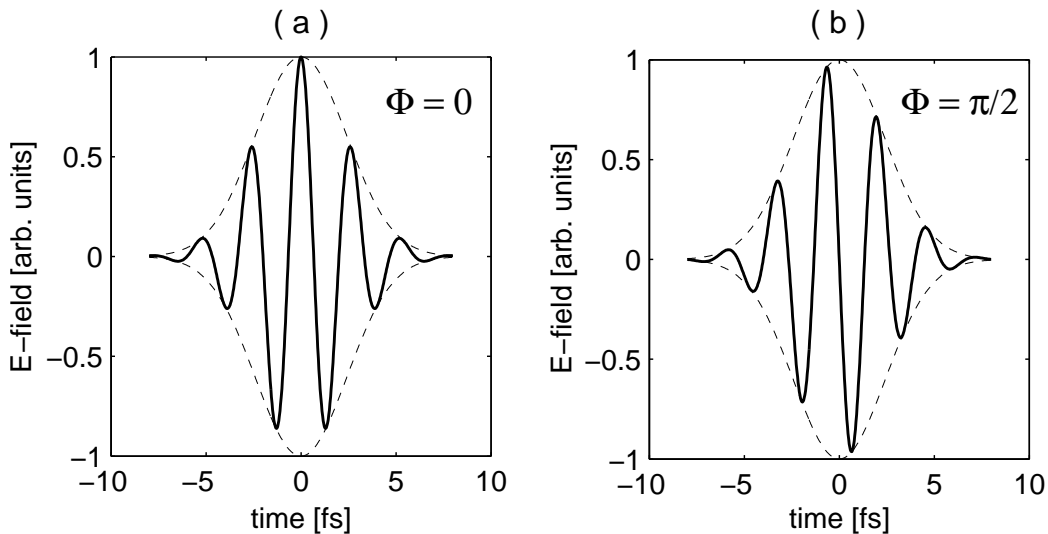


Figure 3.1: Electric field of a 4-fs pulse for absolute phase $\phi = 0$ (a) and $\phi = \pi/2$ (b). In (a) the maximum of the envelope coincides with a maximum of the electric field (cosine-like pulse); in (b) the maximum of the envelope coincides with a zero-crossing of the electric field (sine-like pulse).

the period of an optical cycle is 2.6 fs. Thus, laser pulses with durations below 10 fs merely consist of a few electromagnetic oscillations (few-cycle pulses). The temporal variation of the corresponding field therefore depends on whether the maximum of the pulse amplitude coincides with that of the wave or not, i.e. on the phase of the field with respect to the pulse envelope. The electric field of a linearly polarized laser pulse reads:

$$\vec{E}(t) = \vec{E}_0 a(t) \cos(\omega t + \phi) \quad (3.1)$$

where \vec{E}_0 defines the peak intensity and the laser polarization, $a(t)$ is the pulse envelope (normalized to 1) and defines the pulse shape and duration, ω is the carrier angular frequency and ϕ is the so-called *carrier-envelope* (CE) phase, or *absolute* phase. With respect to ϕ , the convention of choosing $t = 0$ at the maximum of the envelope is used. Then, $\phi = 0$ (π) corresponds to a *cosine-like* pulse with the absolute maximum of the electric field pointing to the positive (negative) direction. Accordingly, we speak of a *sine-like* pulse for $\phi = \pm\pi/2$ (Fig. 3.1). Evidently, it is possible to tailor the field of ultrashort pulses by controlling their absolute phase.

Due to the high sensitivity of the CE phase to small fluctuations in dispersion, which is affected by variations of pulse intensity, cavity length and temperature, laser chains normally deliver pulse trains with randomly changing and unknown phases. This results in a lack of control on nonlinear phenomena driven with few-cycle pulses. Indeed, all greatest challenges in ultrafast laser physics, for instance the reproducible generation of isolated attosecond x-ray pulses [Hentschel01, Kienberger04], rely on light pulses with *reproducible* and *known* absolute phase.

3.1.1 Absolute phase stabilization

A breakthrough in the field of few-cycle laser pulses control was the insight that an ideal femtosecond mode-locked oscillator delivers a pulse train characterized by a quantifiable CE phase slippage shot-to-shot [Reichert99]. In particular, two consecutive pulses present a phase difference given by:

$$\Delta\phi = 2\pi(f_{CEO}/f_{rep}) \quad (3.2)$$

where f_{rep} is the repetition rate of the oscillator (equal to the spacing of the modes oscillating in the cavity) and f_{CEO} (carrier-envelope offset) is the offset frequency obtained by extrapolating the modes comb to zero (Fig. 3.2).

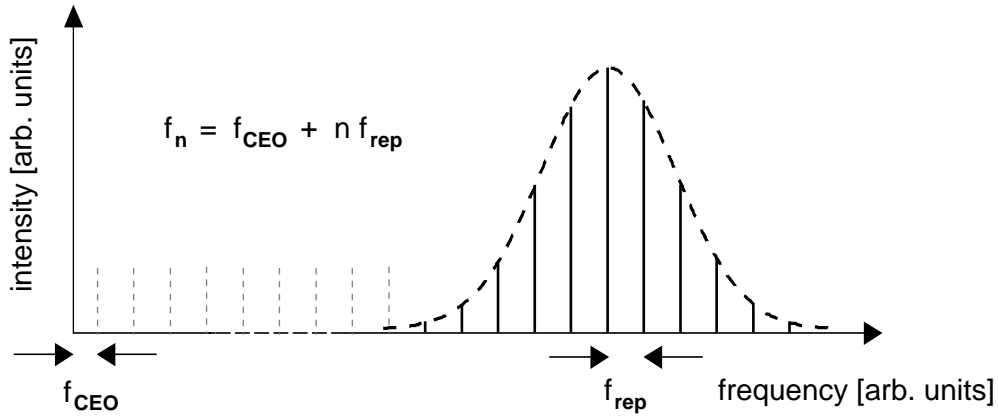


Figure 3.2: The modes of the frequency comb of a mode-locked laser are spaced by f_{rep} . The entire comb is offset from integer multiples of f_{rep} by an offset frequency f_{CEO} . Without active stabilization, f_{CEO} is a dynamic quantity, which is sensitive to perturbation of the laser.

Equation (3.2) is often derived by means of mathematical properties of Fourier transforms, connecting directly the frequency domain to the time domain. A more intuitive explanation can be achieved if one represents all modes oscillating in the cavity by rotating vectors in the complex plane (Fig. 3.3). The n -th mode is characterized by an angular velocity $\omega_n = 2\pi f_n = 2\pi(f_{CEO} + n f_{rep})$, and the pulse's electric field is given at each instant by the real part of the sum of all contributing modes. The pulse *envelope* shows a maximum when all vectors lie in the same direction. If at time $t = 0$ all vectors are aligned along the positive real axis, the resulting electric field acquires its maximum possible value in coincidence with the maximum of the pulse envelope. The corresponding absolute phase is thus $\phi = 0$. During the time interval occurring before the next pulse (given by $1/f_{rep}$), the n -th rotating vector will have completed n integer cycles, plus an additional fraction of cycle f_{CEO}/f_{rep} . Thus, all vectors lie in a direction characterized by the angle $2\pi(f_{CEO}/f_{rep})$. In this situation the value of the resulting electric field at the maximum of the pulse envelope is the previous one multiplied by the projection factor $\cos[2\pi(f_{CEO}/f_{rep})]$. It is then clear that the

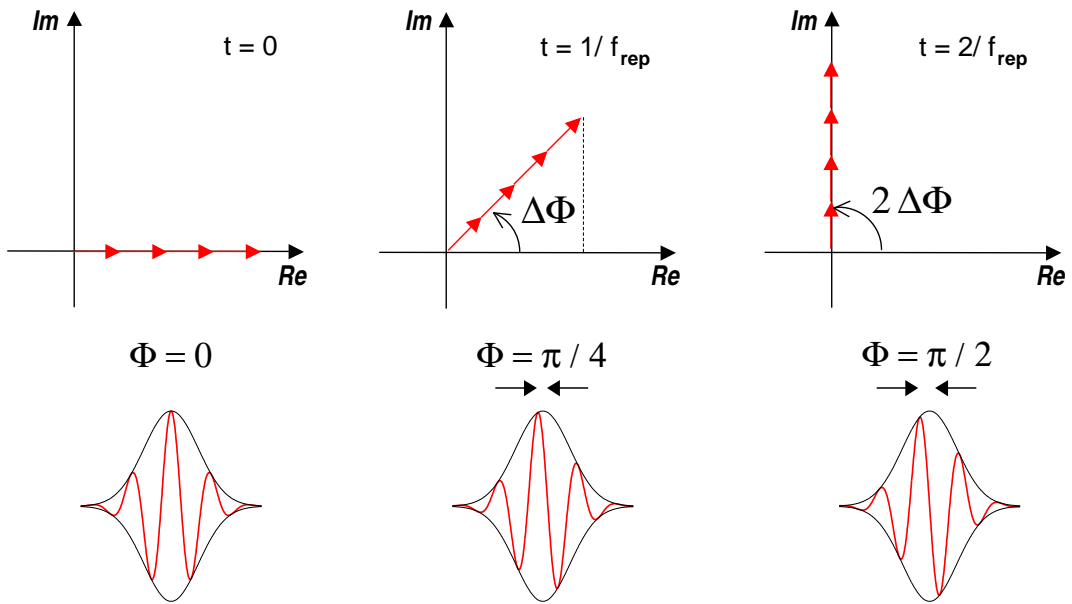


Figure 3.3: Schematic used to derive the relation between the offset f_{CEO} and the phase slippage shot-to-shot of a mode-locked laser. In this example, $f_{CEO} = f_{rep}/8$. For the sake of clarity, only four of the oscillating modes (here represented as rotating vectors) are shown.

absolute phase has changed its value by the amount $\Delta\phi$ given in Eq. (3.2).

The immediate consequence of Eq. (3.2) is that an oscillator delivers identical pulses if $f_{CEO} = 0$. If the offset is not zero, the pulse reproduces itself after $n = f_{rep}/f_{CEO}$ shots or, what is the same, pulses with identical phase have a repetition rate of f_{CEO} . This reproducibility of pulses with identical absolute phase, as already indicated, is endangered by the high sensitivity of the offset frequency to all kind of noise sources. As a consequence, without an active stabilization the pulse train is characterized by uncontrolled phase variations shot-to-shot.

A particular interferometric setup (the so-called f -to- $2f$ technique) allows measuring directly the offset frequency f_{CEO} [Reichert99]. Its value is typically in the radio frequencies range and can be conveniently stabilized² in a servo loop (Sec. 3.2). Using this technique, laser systems characterized by stable and reproducible absolute phases are today available [Jones00, Apolonski00, Baltuška03, Cundiff02]. While this approach is very reliable in locking the offset frequency f_{CEO} , the value of the phase is known only up to a constant offset extremely sensitive to experimental parameters. Thus, the f -to- $2f$ approach is only suitable for stabilizing to a constant, but still unknown, value of the phase.

²When both f_{CEO} and f_{rep} are stabilized, the comb of modes consist of a rigid ruler of exactly known frequencies. This represented a breakthrough in frequency metrology and spectroscopy [Reichert99, Jones00, Telle99].

3.1.2 Absolute phase and nonlinear phenomena

All nonlinear processes driven with high-field laser pulses depend on the constituting electromagnetic field. Overall properties of the pulse such as energy, duration and intensity are useful for deriving general scaling laws, but the details of the laser-atom interaction are intimately connected with the time dependence of the electric field of the pulse (see Chapter 1). For few-cycle pulses, it is therefore obvious that the outcome of most experiments should also depend on the absolute phase.

In the case of HHG, the effect of the absolute phase is illustrated in Fig. 3.4, showing the energy of the recolliding electron for absolute phase 0 (a) and $\pi/2$ (b). For cosine-like pulses the highest orders originate from a single optical half-cycle. Conversely, for sine-like pulses two optical half-cycles of similar strength contribute and interfere. As a consequence, the cutoff of a pulse with absolute phase 0 (or π) is expected to appear at higher energies and to merge into a continuum, while that of a pulse with phase $\pi/2$ (or $-\pi/2$) is characterized by a peak structure. Both these features have been observed in HHG experiments conducted with a phase-stabilized few-cycle laser system [Baltuška03]³. Those experiments also represent the key to reliable and reproducible generation of isolated attosecond pulses [Kienberger04].

In ATI the absolute phase is also expected to play an important role [Dietrich00, Cormier98]. Figure 3.5 shows the drift energy of the photoelectrons emitted in the two polarization directions (here indicated with positive and negative energies) for two different absolute phases. As for HHG, the cutoff position depends on the absolute phase. In fact, due to the rescattering process characterizing the high-energy electrons, this dependence is expected to be more pronounced than in HHG. Indeed, in order to produce high energy photoelectrons, the field amplitude needs to be as high as possible after the rescattering time t_1 . In addition, in order to detect a significant number of such electrons, the ionization probability at the start time t_0 also needs to be high. Since the start time t_0 and return time t_1 differ by almost one optical cycle, the two conditions, namely the highest possible field strength *at* t_0 and *after* t_1 are hard to meet and result in a strong dependence of the ATI plateau on the absolute phase. The number of cycles contributing to a given energy also depend on the phase, leading to phase-dependent peak structures. All these effects will be extensively discussed in the present and following chapters.

A very important difference between HHG and ATI is the insensitivity of the first to absolute phase shifts of π : Since HHG originates from electrons recombining with the ion core, no observable can reveal in which direction the electron has been previously driven by the electric field. Hence, the HHG spectrum produced by, e.g., laser pulses of phase 0 and π is identical. This is not the case for ATI, where symmetry is completely broken for few-cycle pulses⁴. Electrons recolliding and rescattering

³The dependence on the absolute phase has also been confirmed by single-shot HHG detection performed with a laser system without phase stabilization [Nisoli03].

⁴Indeed, no pulse shapes exist for which identical left-right emission is expected (cf. Fig. 3.10).

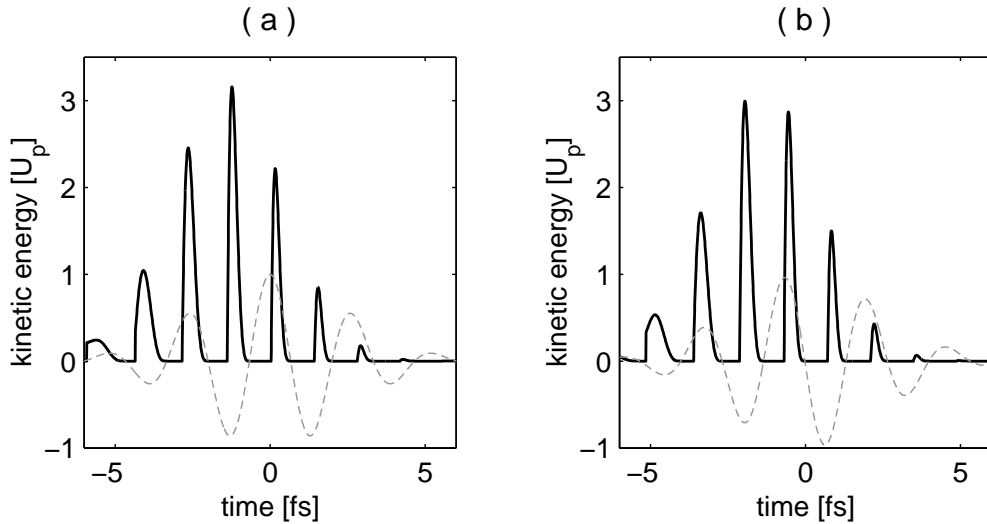


Figure 3.4: HHG: laser's electric field (dashed line) and kinetic energy of the electron returning to the ion core (solid line) as a function of the initial time t_0 for absolute phase 0 (a) and $\pi/2$ (b). The pulse duration is in both cases 4 fs FWHM.

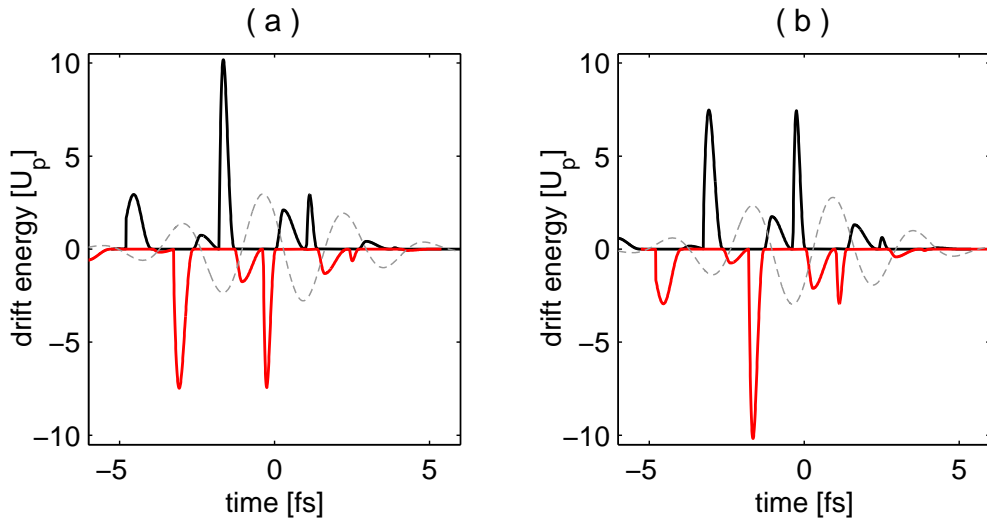


Figure 3.5: ATI: laser's electric field (dashed line) and drift energy of the electrons (solid lines) as a function of the initial time t_0 for absolute phase 0.9 rad (a) and 4 rad (b). This particular couple of phases gives rise to the strongest difference and is here chosen for the sake of clarity. The pulse duration is in both cases 4 fs FWHM. Note that the electron emission occurs in two opposite directions (here indicated with positive and negative energies). This makes ATI more powerful than HHG with respect to CE phase determination. For instance, the pulses in (a) and (b) lead to identical harmonics emission, but to strongly different electron emission.

off the ion acquire a drift energy in a direction determined by the sign of the electric field. Hence, detecting electrons emitted in the two opposite directions energy-resolved (Sec. 3.3) allows to retrieve *without sign ambiguity* the time variation of the electric field. Finally, compared to HHG, multiphoton ionization is less complex because it is a single-atom process (Chapter 1). This makes easier the use of ATI as a tool for determining the absolute phase of few-cycle pulses.

3.2 The laser system

The laser system used in the experiments described in the rest of this work is a CPA system delivering 5-fs, 0.5-mJ pulses at a repetition rate of 1 kHz [Baltuška03]. Sub-10 fs pulses from a Ti:Sa oscillator seed after appropriate stretching a commercial multi-pass amplifier (Femtopower Compact Pro, Femtolasers). Amplification and temporal recompression yield 20-fs, 1-mJ pulses, which are subsequently spectrally broadened in a hollow fiber filled with neon, and finally compressed on reflection off chirped multilayer mirrors.

Phase-stabilization of the femtosecond oscillator is achieved with the f -to- $2f$ technique. The reference frequency f_{CEO} (Sec. 3.1.1) is chosen to be a sub-multiple of the repetition rate of the oscillator. With this method and appropriate choice of the frequency ratio, the absolute phase recurrence of the oscillator is such that each *amplified* pulse exhibits the same electric-field waveform. The residual CE phase drift behind the amplifier is monitored by a second f -to- $2f$ interferometer and compensated in the same electronic loop controlling the oscillator. With this technique, high power, few-cycle pulses with identical absolute phase are produced, the value of the phase being still undetermined. Figure 3.6 shows a typical spectrum of the laser pulses and the corresponding electric field.

3.3 The stereo-ATI spectrometer

The idea behind the experimental setup is to take advantage of the anisotropic electron emission occurring with few-cycle pulses [Dietrich00, Cormier98]. With linearly (horizontally) polarized light, as discussed in Sec. 3.1.2, significant left-right asymmetry is expected. Two independent electron detectors placed in opposite directions with respect to the laser focus allow to investigate this asymmetry. This so-called *stereo-ATI* setup provided the first evidence of absolute phase phenomena in strong-field ionization [Paulus01b].

The experimental approach used in these experiments relies on time-of-flight spectroscopy (Fig. 3.7). Two opposing electrically and magnetically shielded drift tubes are mounted in an ultrahigh vacuum apparatus. Rare gases atoms effusing through a nozzle from the top are ionized in the focus of the laser beam. The laser polarization

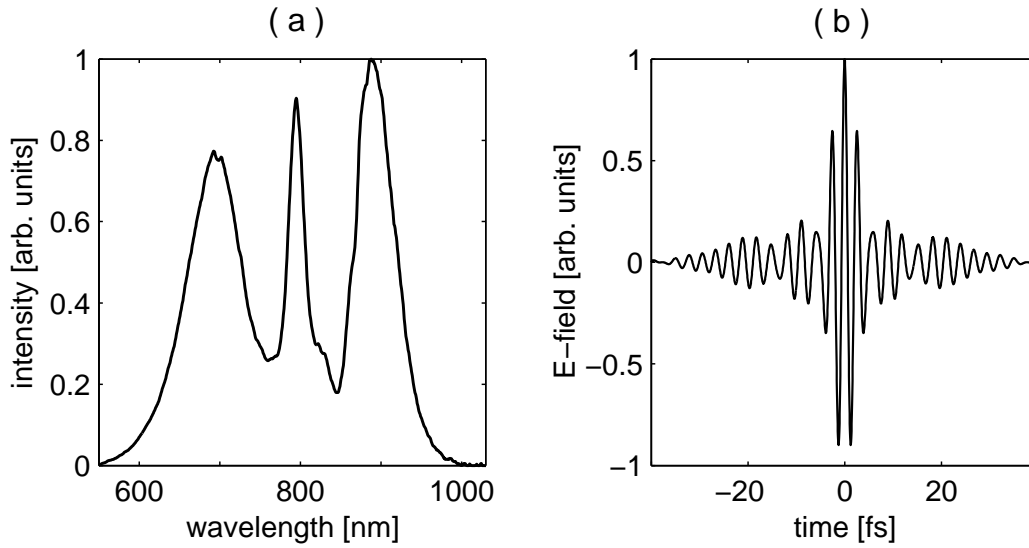


Figure 3.6: Typical spectrum of the amplified and spectrally broadened pulses (a) and corresponding electric field (b) by assuming ideal dispersion compensation. Note that small satellites are unavoidable due to the spectral shape. However, due to the high nonlinearity, all nonlinear processes take place just in the central part. The pulse shown in panel (b) corresponds to absolute phase $\phi = 0$.

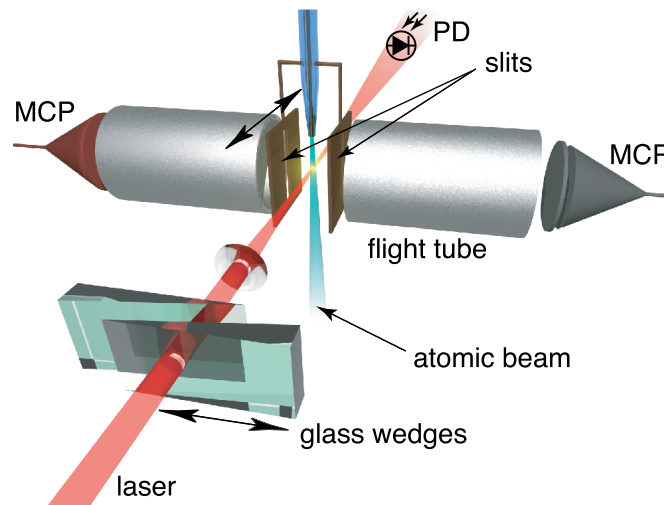


Figure 3.7: Scheme of the stereo-ATI spectrometer. PD = photodiode; MCP = microchannel plate. A pair of glass wedges is used to control the absolute phase of the pulses, as discussed in the next section. The focusing, here sketched with a lens, is actually achieved with a concave mirror.

is linear and parallel to the flight tubes. Slits with a width of $250\ \mu\text{m}$ are used to discriminate electrons created outside the laser focal region chosen. Electrons emitted to the left and to the right are independently detected by two 18-mm diameter microchannel plates (MCP, Burle BiPolar TOF Detector) located at a distance of 40 cm from the focus. The time-of-flight is measured by two computer-hosted multiscalers (FAST 7886, FAST ComTec, Oberhaching, Germany) with a time resolution of 0.5 ns. The start signal is generated by a fast photodiode, recording the arrival of the laser pulse (i.e. the birth time of all electrons), the stop signal by the MCPs, recording the arrival of each electron at the end of the drift tube. The electrons' time-of-flight is then used to calculate their kinetic energy.

3.3.1 Sensitivity of the spectrometer

An important feature of an electron spectrometer is its resolution, i.e. the ability of distinguishing electrons of very small kinetic energy differences. An analytic expression can be obtained with the following argument. If an electron of drift velocity v_1 needs a time t_1 to reach the detector, the closest distinguishable electron (characterized by the velocity v_2) will travel a time $t_2 = t_1 + \Delta t$, where Δt is the minimum time resolution of the detection system. Thus, one can write $v_1 = L/t_1$ and $v_2 = L/(t_1 + \Delta t)$, where L is the length of the drift tube and t_1 depends on the energy of the electron considered. With straightforward mathematics and suitable approximations one derives the minimum detectable energy difference $\Delta E = \frac{1}{2}m_e(v_2^2 - v_1^2)$:

$$\Delta E \sim \frac{2\sqrt{2}\Delta t}{m_e^{1/2}L}E^{3/2} \quad (3.3)$$

where m_e is the electron mass. Note the dependence on the kinetic energy E . Intuitively, the resolution improves with fast detection systems (small Δt) and with longer drift distances, justifying the choice of relatively long tubes. Figure 3.8 shows $\Delta E/E$ as a function of E for the stereo-ATI spectrometer ($L = 40\ \text{cm}$; $\Delta t = 0.5\ \text{ns}$).

Another important issue of the electron spectrometer is the number of electrons detectable per laser shot. An intrinsic limitation of the detection system used here is that, if two or more electrons characterized by exactly the same time-of-flight hit the detector, only one will be recorded⁵. This limitation is usually not critical due to the narrow time-of-flight window (0.5 ns). A more severe limit is given by the dead-time of the detection system. In this case, this is represented by the width of the pulses generated by the microchannel plate ($\sim 4\ \text{ns}$). In particular for the fast plateau electrons, this sets an upper limit to the number of detectable electrons per laser shot. For instance, not more than ~ 10 electrons can be recorded in the energy window [20 eV, 50 eV]. In most experimental situations, other limitations, such as

⁵This is due to the binary character of electron counting. At each time step, the detector can either deliver no signal or it can reveal the arrival of electrons (no matter how many).

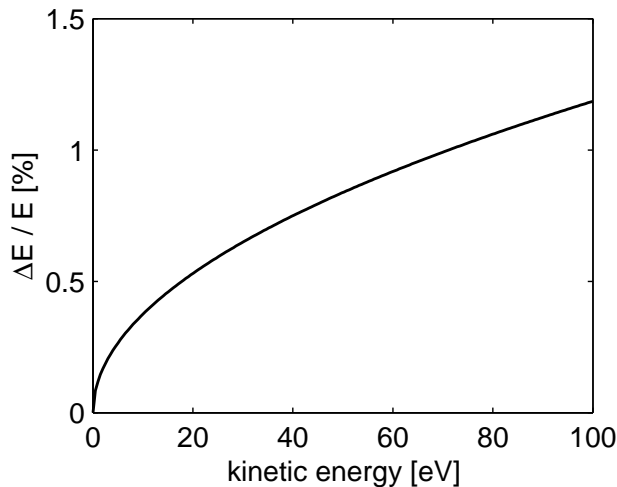


Figure 3.8: Resolution of the stereo-ATI spectrometer as a function of the detected electron energy. The resolution is expressed in percentage of the latter. The resolution gets worse for the fastest electrons, since the respective time-of-flight become less easily distinguishable. Nevertheless, it remains very good ($< 1\%$) in the interesting energy range (0-100 eV, see following sections).

space charge effects, suggest to keep the count rate to much lower values, where the limitations discussed here play no role.

3.4 Experimental results

The target gas used for these experiments was xenon, known to exhibit a strong plateau for few-cycle laser pulses [Grasbon03]. The pulse energy was considerably attenuated to $20 \mu\text{J}$ and the beam focused with a concave mirror of focal length 250 mm (f-number 30). The pair of slits can be moved along the beam propagation direction from outside the vacuum apparatus. This allows selecting the desired intensity, in this case below 10^{14} W/cm^2 . Higher intensities would result in possible detrimental saturation effects and, in particular, would smear out the characteristic plateau structure [Grasbon03] which is expected to show significant phase effects.

Figure 3.9 shows the measured ATI spectra with the phase-stabilization loop turned off. Here and in the following, red (black) -colored curves correspond to spectra measured on the left (right) of the propagating beam⁶ (see Fig. 3.7). Since the phase is not stabilized, pulses with random absolute phases contribute to the spectra. Hence, as expected, no difference in the two directions is detected. The measured spectra confirm the presence of a pronounced plateau in xenon. Its extent can be also used to gauge the laser intensity, since the most energetic electrons have a drift energy

⁶The similar use of colors in politics may help in remembering the color coding.

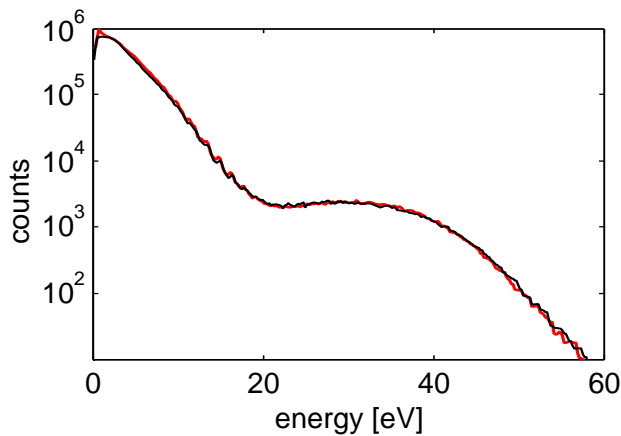


Figure 3.9: ATI spectra in xenon (semi-logarithmic scale) measured on the left (red line) and right (black line) detector without phase stabilization. Careful alignment of the slits ensures that both detectors *see* exactly the same focal region, yielding two identical spectra. The typical count rate is 50 electrons per laser pulse at each MCP.

of $10 U_p$ (cf. Sec. 1.5.1). This yields an estimated ponderomotive energy $U_p = 5 \text{ eV}$ (i.e. $I \sim 8 \times 10^{13} \text{ W/cm}^2$).

When the phase is stabilized, pulses with known phase differences $\Delta\phi$ can be realized by delaying the envelope with respect to the carrier. Since the envelope propagates with the group velocity and the carrier with the phase velocity of light, glass dispersion can be used to shift the absolute phase⁷. At a central wavelength of 760 nm [Fig. 3.6(a)] adding 52 μm of fused silica changes the phase by 2π without distinctly affecting the pulse duration. Thus, two glass wedges (apex angle 2.8°) which can be shifted with respect to each other (see Fig. 3.7) allow any phase to be adjusted.

Figure 3.10 shows ATI spectra measured in the two opposing directions for different absolute phases. The phase was changed in constant steps of $\pi/10$ by adding each time 2.6 μm of fused silica. The most striking phase effects can be observed, as expected, for rescattered electrons. Simply by inspecting the high-energy part of the spectra ($> 20 \text{ eV}$) one can verify that $\Delta\phi = \pi$ intuitively corresponds to a change from left to right, while when $\Delta\phi$ approaches 2π the spectra are faithfully reproduced. Note that the agreement with the expected periodicity is excellent, confirming that the absolute phase change can be indeed described simply by the difference of phase and group velocities.

⁷The carrier frequency is not well defined for the strongly modulated spectra characterizing few-cycle laser pulses (Fig. 3.6). Indeed, the absolute phase change can be estimated by calculating the difference of phase and group velocity only in a first approximation. However, simulations taking into account the actual spectral shape showed that the deviation is very small and can be neglected.

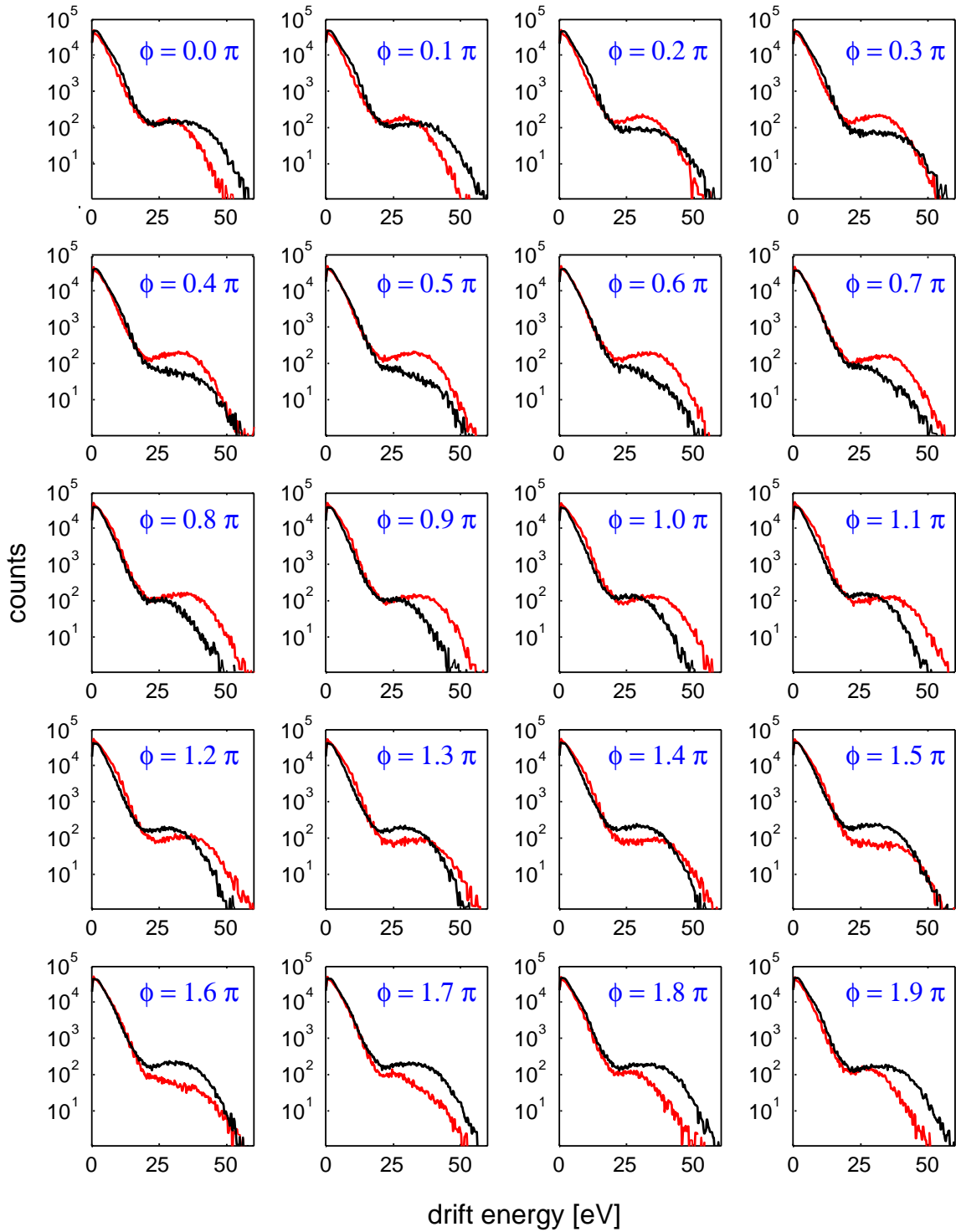


Figure 3.10: ATI spectra in xenon (semi-logarithmic scale) measured on the left (red lines) and right (black lines) detector with phase stabilization. The spectra were acquired by integrating 40s at each position and by changing the phase in constant steps of $\pi/10$. The blue labels indicate the absolute phases corresponding to each spectrum, as deduced from the phase assignment discussed in Sec. 3.5. Note that identical left-right emission is never observed if the phase is stabilized.

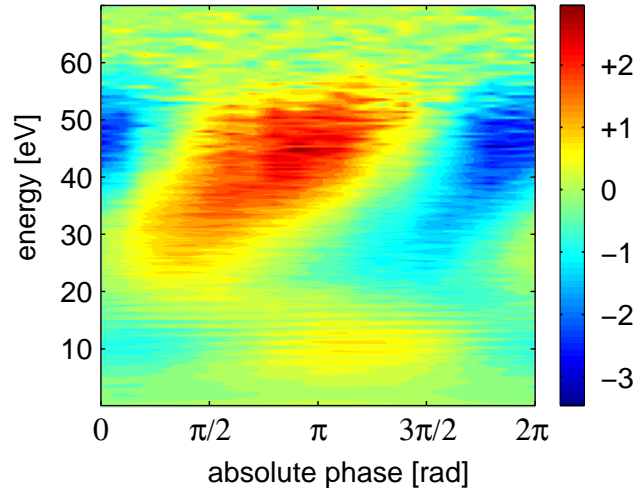


Figure 3.11: Left/right ratio (logarithmic scale) as a function of electron energy and absolute phase. Reddish colors correspond to dominant left emission, bluish colors to dominant right emission. From this representation it is obvious that the strongest asymmetry occurs in the ATI plateau (electron energy > 20 eV). The values of the phase (x-scale) correspond to the phase assignment discussed in Sec. 3.5.

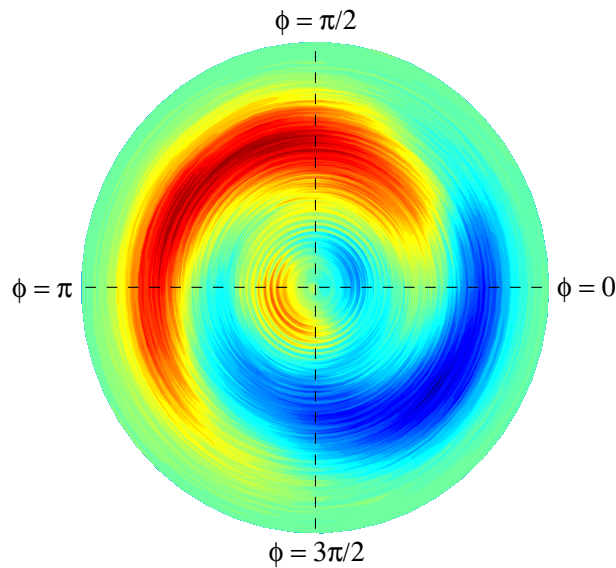


Figure 3.12: Polar representation of Fig. 3.11. Radial coordinate: electron energy. Polar coordinate: absolute phase. Reddish colors correspond to dominant left emission, bluish colors to dominant right emission.

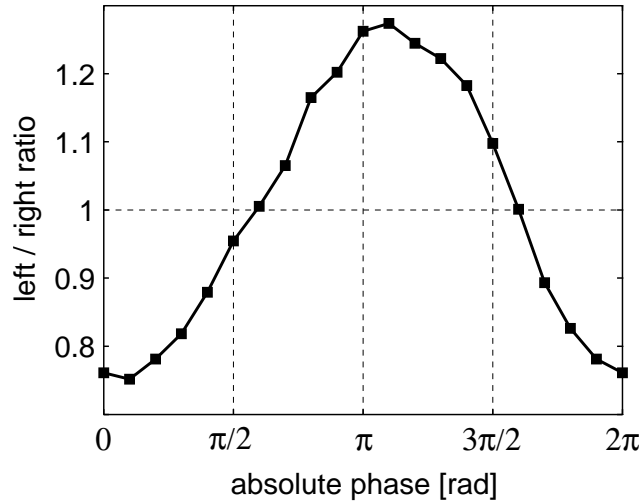


Figure 3.13: Left/right electron yield ratio (integrated over all energies) as a function of the absolute phase. The values of the phase (x-scale) correspond to the phase assignment discussed in Sec. 3.5.

All the information recorded is summarized in Fig. 3.11, showing the natural logarithm of the left/right ratio as a function of the electron energy and of the absolute phase. Positive values (reddish colors) correspond to dominant left emission, negative values (bluish colors) to dominant right emission. Clearly, the strongest asymmetry appears in the ATI plateau. Phase signatures are also visible in the low-energy part of the spectra and in the peak structure appearing for some phases. This will be extensively discussed in the following chapters.

The total yield (i.e. the integral over all energies) of each detector also depends on the absolute phase. Figure 3.13 shows the left/right electron yield ratio as a function of the phase. The contrast exceeds 25%, a very easily detectable quantity⁸. To retrieve the value of the phase, however, the best approach relies on the observation of the plateau.

3.5 Theoretical analysis

In this section, the experimental data are compared with theoretical simulations relying on different approaches. This leads for the first time to an unambiguous determination of the absolute phase without sign ambiguity and with an estimated error not exceeding $\pi/10$ ⁹. Note that this error is due to uncertainties in matching experiment and theory and not due to insufficient signal-to-noise in the measured data. This makes the stereo-

⁸This contrast strongly depends on the laser parameters (Chapter 5), in particular on the pulse duration.

⁹This error is smaller than the long-term phase stability delivered by the laser system itself.

ATI experiment an extremely powerful tool as a *phase meter* for applications requiring precise and long-term absolute phase control (Chapter 4).

3.5.1 Semiclassical model

The semiclassical treatment predicts phase dependence of the ATI emission, in particular in the high-energy part of the spectrum (Sec. 3.1.2). With the code developed along the lines given in Chapter 1, one can calculate the ATI spectra for the two emission directions for any CE phase. Figure 3.14 shows the results of the calculations taking into account only high-energy (rescattered) electrons. The pulse duration assumed is 4 fs FWHM, and the peak intensity 8×10^{13} W/cm². Note, however, that the characteristic pattern is qualitatively independent of the laser intensity, so that U_p as a scaled intensity is used.

In the theoretical as well as in the experimental data the ratio of emission to the left and to the right depends in a characteristic way on electron energy and CE phase. This leads to the inclined stripes in the false-color representation. Another common feature is that the asymmetry of left-right emission increases for increasing electron energy. It should be noted that, unlike the contrast of asymmetry, these characteristic features do *not* depend critically on pulse duration, shape, intensity and atomic species considered. The sharp edges visible in the calculation originate from classical energy conservation. This artifact is removed in quantum-mechanical models by energy-time uncertainty (Sec. 3.5.2). Matching the characteristic features of the theoretical (Fig. 3.14) and experimental (Fig. 3.11) data leads to the determination of the CE phase. Note that this phase assignment carries no $\pm\pi$ ambiguity, intrinsic, e.g., in HHG experiments [Baltuška03, Nisoli03, Yakovlev03].

The classical model also predicts a phase dependence of the integrated electron yield. Due to their much higher abundance, only direct electrons contribute significantly. Their drift velocity (and hence their emission direction) is given by the vector potential at the instant of ionization (Sec. 1.3). The immediate consequence, somewhat counterintuitive, is that a *cosine-like* pulse will ionize equally in both directions, whereas a *sine-like* pulse will yield the maximum asymmetry. The contrast of the left/right modulation is a nonlinear function of the pulse duration, and can be easily calculated by assuming suitable ionization rates (Sec. 1.2).

Figure 3.15(a) shows the calculated left/right electron yield (dashed line) as a function of the absolute phase. The pulse duration is 4 fs FWHM and the laser intensity is 8×10^{13} W/cm². For comparison, the experimental data are also plotted (solid line) as a function of the absolute phase deduced from the phase assignment based on the ATI plateau. The two curves do not fit neither in the amplitude of the oscillation nor in the phase. While the former could be explained by a difference in pulse duration, the latter must be due to the effect of the Coulomb potential of the ionized atom on the electron trajectories. Indeed, the classical model completely neglects its effect. The error corresponding to this approximation is expected to be particularly severe

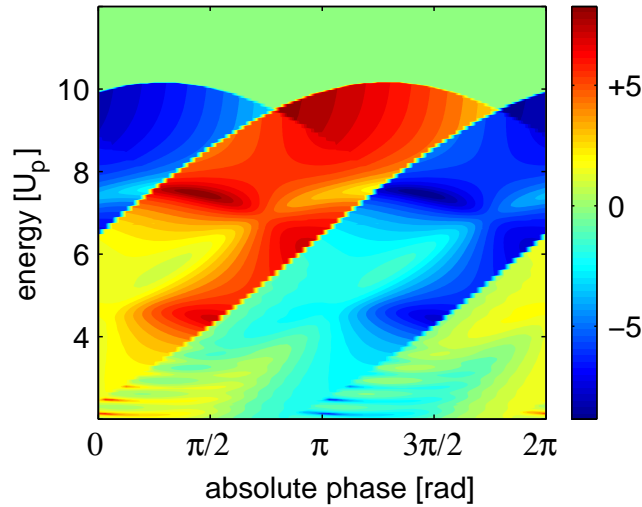


Figure 3.14: Calculated left/right ratio (logarithmic scale) as a function of electron energy and absolute phase. Only rescattered electrons are taken into account. The overall features in the high-energy part of the plateau are qualitatively independent on laser parameters and atomic species, and are therefore suitable for phase assignment. Comparison with the experimental data (Fig. 3.11) allows absolute phase determination. With the convention of Eq. (3.1), the electric field is uniquely characterized.

for those electron spending a significant time around the ion core. These are precisely the low-energy, direct electrons, mainly contributing to the overall yield. Thus, it is not surprising to observe a failure of the classical model with this respect, and for this reason the phase assignment must rely on the ATI plateau [Milošević03].

Figure 3.15(b) shows the total (integrated over both directions) ionization yield (dashed line) as a function of the absolute phase for the same pulse duration (4 fs). For comparison, the experimental values are also shown (solid line). Note the much smaller expected oscillation amplitude compared to Fig. 3.15(a). In the experimental data, no phase dependence is observed. This demonstrates the advantages of the *stereo* approach compared to schemes relying on integrated ionization yields. Due to the angular anisotropic emission, the contrast observable with two detectors is orders of magnitude higher. Furthermore, dividing the left and right electron yields automatically removes sources of common mode noise such as laser intensity fluctuations¹⁰. Finally, any phase determination relying on the integrated overall yield would inevitably introduce a $\pm\pi$ ambiguity, eliminated in the stereo approach.

¹⁰These fluctuations are amplified due to the highly nonlinear character of tunneling and multi-photon ionization [Fig. 3.15(b)].

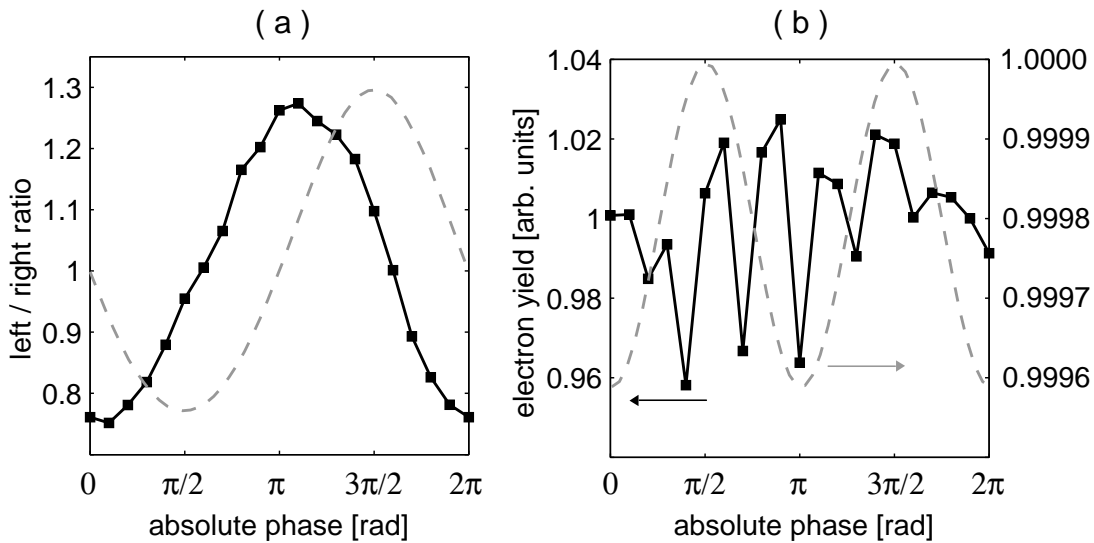


Figure 3.15: (a) Calculated left/right electron yield ratio (dashed line) as a function of the absolute phase. The pulse duration is 4 fs FWHM. The phase-shift with respect to the experimental contrast (solid line) is due to the Coulomb potential of the ion, not taken into account in the classical model. (b) Calculated total electron yield (dashed line) as a function of the absolute phase. The expected phase dependence is orders of magnitude smaller (note the different scales). The noise intrinsic in the experimental values (solid line) makes the modulation undetectable. Note that dividing left and right electron yields (stereo approach) removes the common mode noise.

3.5.2 Strong-field approximation

The dependence of ATI on the carrier-envelope phase of the generating laser pulse is also predicted by theoretical models relying on the strong-field approximation (SFA, Sec. 1.1). Figure 3.16 shows the calculated left/right asymmetry map as a function of electron energy and absolute phase. The formalism used in the calculation¹¹ includes rescattering effects (for details see [Becker02] and references therein), and is therefore particularly suitable for describing the high-energy part of the spectra.

The characteristic features of the asymmetry in the ATI plateau qualitatively reproduce both experimental (Fig. 3.11) and theoretical data obtained with the semiclassical model (Fig. 3.14). This additional comparison confirms and refines the phase assignment based on the classical model. Compared with the latter, the sharp edges visible there are smoothed out owing to quantum-mechanical uncertainties. Note that the SFA suffers from the same limitations of the semiclassical model, originating from the neglected Coulomb potential of the ion. Hence, the calculation is less reliable at low electron energy. Indeed, the asymmetric area observable around 10 eV in both experimental and theoretical data would lead to a different (wrong) phase assignment. For the same reason, the calculated asymmetry in the integrated left/right ionization

¹¹The quantum-mechanical calculations of this section are kindly provided by Dejan Milošević.

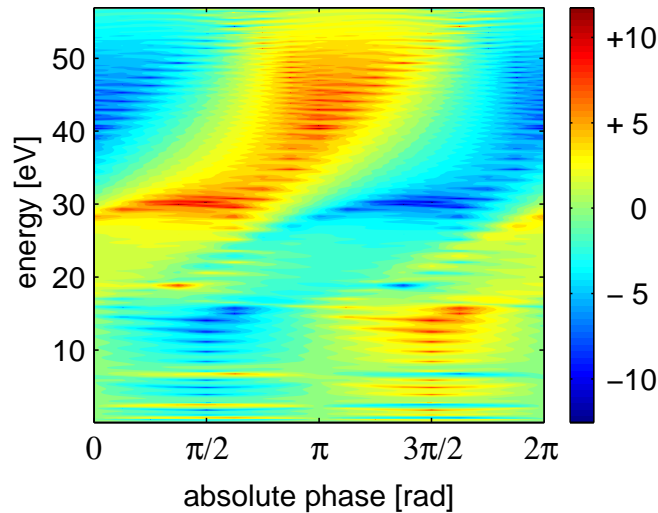


Figure 3.16: Left/right ratio (logarithmic scale) as a function of electron energy and absolute phase calculated with the strong-field approximation. The pulse duration is 4 fs FWHM, the peak intensity $8 \times 10^{13} \text{ W/cm}^2$. Comparison with the experimental data (Fig. 3.11) confirms the phase assignment based on the semiclassical model (Sec. 3.5.1).

yield cannot be used for phase determination.

Since high-energy electrons are the most appropriate to retrieve the value of the phase, another possible approach is to represent only the ATI plateau as a function of the absolute phase. Figure 3.17 displays that separately for the two detectors for both experimental data (a) and theoretical calculations performed with the SFA method (b) and using the semiclassical model (c). The clear phase dependence of the cutoff position shows once again the consistency of the phase assignment. Note that, although this approach still relies on the anisotropic angular emission, it is possible even with a single detector. The stereo approach is however more powerful, due to the eliminated common mode noise. In addition, the advantage is that the stereo approach allows phase determination from a single pair of ATI spectra, whereas a *mono* approach needs the acquisition of spectra at several phases before allowing conclusions on the phase value.

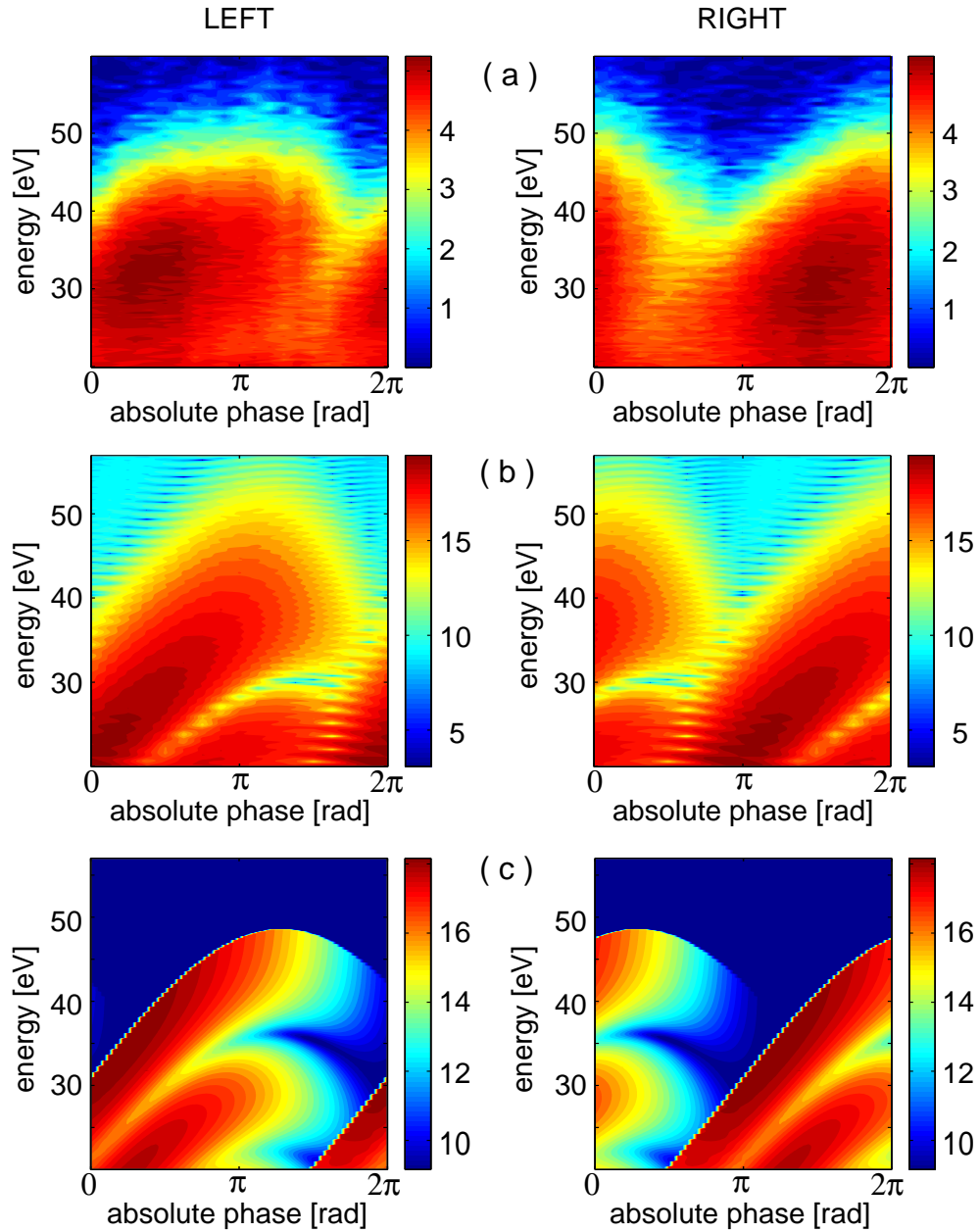


Figure 3.17: High-energy part of the ATI spectra (logarithmic scale) as a function of electron energy and absolute phase for the two detectors. The agreement between experimental (a) and theoretical data according to the SFA (b) and the classical model (c) confirms the phase assigned by using the asymmetry maps of Fig. 3.14 and 3.16. Note how the sharp edges in (c), originating from classically forbidden regions, are smoothed in (a) and (b). Despite the clearness of this method based on the cutoff position measured with a single detector, the most efficient phase assignment relies on the left/right ratio.

3.5.3 Numerical integration of the Schrödinger equation

The brute-force approach to study above-threshold ionization theoretically is solving the time-dependent Schrödinger equation (TDSE). The main advantage of this computational method is that, in principle, no severe physical approximations are made. In particular, the effect of the Coulomb potential is taken into account during the electron dynamics under the driving laser pulse.

Figure 3.18 shows the calculated left/right ratio of ionization yield (short dashed line) by numerically solving the three-dimensional TDSE¹². For comparison, the experimental data and the prediction of the classical model are also shown. Clearly, the TDSE calculation approaches better the experimental outcome in what concerns the phase of the oscillation, confirming that the failure of the classical model at low energies (and hence in predicting integrated ionization yields) is indeed due to the neglected Coulomb potential¹³.

The still not negligible difference from the experimental data is probably due to the shorter pulse duration (3.6 fs) assumed in the theoretical calculation. In addition, the maximum of the integrated left/right asymmetry is predicted to occur at a phase that depends on the intensity and on the pulse duration [Chelkowski02, Chelkowski04]. In many situations, this makes the integrated electron yield not suitable for phase determination, highlighting once more the importance of the ATI plateau in this respect.

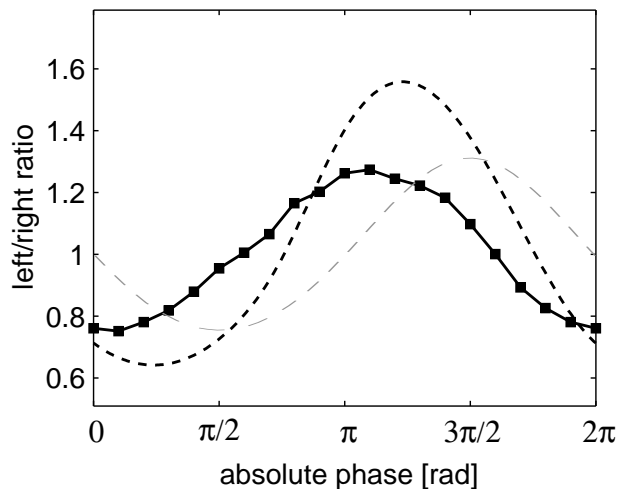


Figure 3.18: (a) Left/right electron yield ratio as a function of the absolute phase by numerical integration of the TDSE (short dashed line). The result approaches the experimental data (solid line) better than the classical model (long dashed line).

¹²The TDSE calculations of this section are kindly provided by Armin Scrinzi.

¹³Also very recent numerical results based on the TDSE [Chelkowski04] confirm these indications.

Chapter 4

A new stabilization scheme for the absolute phase

The possibility of measuring the absolute phase of laser pulses demonstrated in Chapter 3 represents a completely new pulse diagnostics. This is of obvious interest for any application of few-cycle pulses, since the absolute phase is known to play a major role. The availability of a *phase meter* immediately paves the way for new approaches both for monitoring and stabilizing the phase.

In this relatively short chapter, examples of these novel technical issues will be given. In particular, it will be shown how a combination of conventional phase-stabilization techniques and the use of the stereo-ATI experiment lead to unprecedented phase stability. The application of this technique makes it possible to perform experiments requiring long integration times, previously not possible due to seemingly unavoidable long-term phase drifts. Finally, an overview will be given on future developments of the stereo-ATI approach as an essential diagnostics tool for any few-cycle pulse laser system.

4.1 The stereo-ATI as a phase meter

The clear phase effects detected by the asymmetric left-right ATI emission allow testing the phase stability of the laser pulse train. While stabilization of femtosecond oscillators is a well established technique [Cundiff02], phase stabilization for amplified pulses is only a very recent achievement [Baltuška03]. Thus, measuring its steadiness, especially in the long-term, is particularly meaningful.

The reasons for the presence of phase drifts have to be found in the imperfections of the current stabilization scheme. Two of them seem to be particularly noteworthy: First, the feedback for the phase stabilization is taken after the femtosecond laser amplifier but before the pulses are spectrally broadened in the hollow fiber and

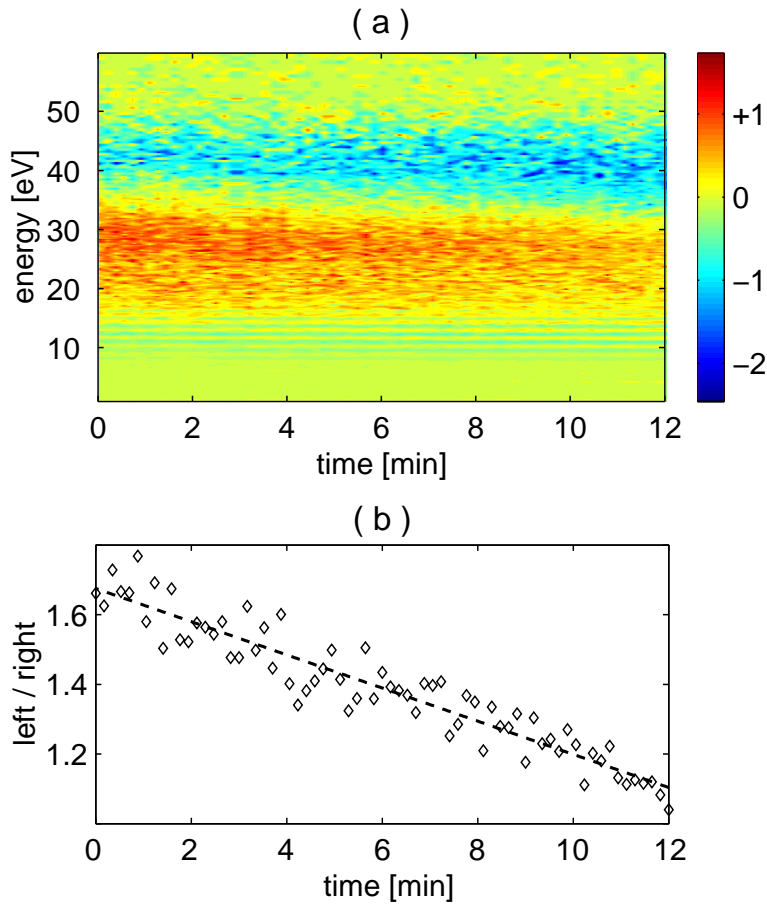


Figure 4.1: (a) Measured left/right asymmetry (logarithmic scale) as a function of electron energy and time. Reddish colors represent dominant left emission, bluish colors dominant right emission. (b) Respective left/right asymmetry in the ATI plateau (integration range from 20 eV to 60 eV). Each experimental point (diamonds) corresponds to an integration time of 10 s. A clear linear phase drift (dashed line) of 50 mrad/min can be measured.

recompressed to few-cycle pulses [Baltuška03]. Any drifts in the latter part, originating from beam pointing instabilities and amplitude-phase coupling, are therefore not compensated. Second, the stabilization scheme relies on comparison of frequencies in the red and blue wings of the spectrum (f -to- $2f$ scheme). Since dispersion at these wavelengths is different from the center wavelength decisive for the absolute phase, the present stabilization will introduce small phase errors as soon as it starts to compensate any drifts in the amplifier [Dombi04b, Dombi04a]. The ATI phase meter offers a possible solution to these problems.

A first approach to monitor the phase stability is to record ATI spectra in the left and right direction for a certain time, without changing anything in the beam path [i.e. without shifting the glass wedges (cf. Fig. 3.7 on page 46)]. During this *static* measurement the detected left/right asymmetry should ideally remain constant. Figure 4.1(a) shows the spectrally resolved asymmetry as a function of time. The

asymmetry pattern makes a slow transition, particularly visible in the ATI plateau. This can be better appreciated in Fig. 4.1(b), showing the left/right asymmetry in the yield of electrons in the energy range [20 eV, 60 eV]. A general clear trend can be identified, pointing to a constant phase drift during the measurement. Careful analysis indicates that the drift is of the order of 50 mrad/min. One should note that, although remarkably small, the drift is nevertheless large enough to endanger the possibility of performing phase-dependent experiments requiring acquisition times of more than 10-15 minutes.

A second approach to detect phase drifts is the following. First, ATI spectra in the left and right directions are recorded by successively *adding* glass in the beam path. This corresponds to increasing values of the absolute phase, being changed by shifting the glass wedges. Then, at the end of the scan, the procedure is reverted by *removing* glass from the beam path, until the initial position of the wedges is reached. Ideally, the asymmetries corresponding to identical glass thicknesses should overlap, any detected difference being related to a phase change occurred during the time interval between the two acquisitions. Figure 4.2 shows the left/right total electron yield asymmetry measured by moving the wedges forth (right-oriented triangles) and back (left-oriented triangles). Clearly, the two curves do not overlap. The time difference between the first and the last acquisition was 14 minutes, yielding once again a phase drift estimation of approximately 50 mrad/min¹.

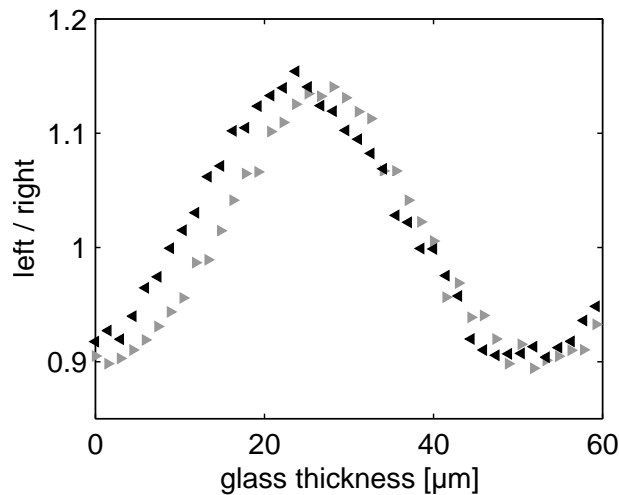


Figure 4.2: Detected left/right electron yield asymmetry as a function of the glass thickness introduced. The measurement was performed by increasing the amount of glass from 0 to 60 μm (right-oriented triangles) and immediately after by decreasing it from 60 μm to 0 (left-oriented triangles). The integration time for each experimental point is 10 s. The measured drift is clearly larger than the experimental uncertainty.

¹These two measurements (Figs. 4.1 and 4.2) were performed consecutively. It is thus no surprise that the resulting phase drift is similar. In general, this value depends on the laser's *mood*.

4.2 Phase stabilization

Since the ATI left/right asymmetry can clearly identify small phase drifts, it obviously has the potential to be used in a feedback loop. With respect to this, the main advantages of the stereo-ATI approach can be summarized as follows:

- ATI gives access to the actual value of the phase, whereas the standard phase stabilization scheme based on the f -to- $2f$ technique gives access only to the phase up to some unknown offset;
- the acquisition of two ATI spectra in opposite directions immediately gives the value of the phase, without requiring comparisons with other spectra corresponding to different phases. This is in contrast to phase detection based on a single detector (Fig. 3.17);
- while the precision of the phase measurement is presently limited by the theoretical understanding [$\Delta\phi \sim \pi/10$ (Sec. 3.5)], the sensitivity to phase deviations (critical for phase stabilization issues) is much higher.

4.2.1 Basic idea

To implement any active stabilization scheme, two elements are necessary: an error signal and a parameter that influences the quantity to be stabilized. Clearly, the first is given by the left/right electron asymmetry. Note that the error signal must be symmetric with respect to left/right reversal. A possible definition is $(L - R)/(L + R)$, where L and R are respectively the left and right electron yields in the energy window considered². This is represented in Fig. 4.3 for different energy intervals.

For choosing an appropriate energy range, both contrast and count rate have to be considered. For instance, choosing the cutoff region (red line) yields very pronounced left-right differences, however with considerable noise due to the low count rate. The opposite situation (low noise, but also low contrast) occurs for the total electron yield (blue line). A good compromise is obtained by considering the plateau range (green line). The choice of the integration time to acquire the error signal is also very important. Short integration times produce significant phase noise, whereas long integration times result in slow feedbacks, thus limiting the servo bandwidth. Since the stereo-ATI is supposed to correct long-term phase drifts, relatively long integration times can typically be used. Note that, regardless of the energy range and integration times chosen, better results are expected for shorter laser pulses, due to the higher contrast (see Sec. 5.3).

The second element needed is a parameter that influences the phase. So far, two methods have been demonstrated in femtosecond oscillators: swiveling the end mirror

²Equivalently, one can take the logarithm of the ratio left/right.

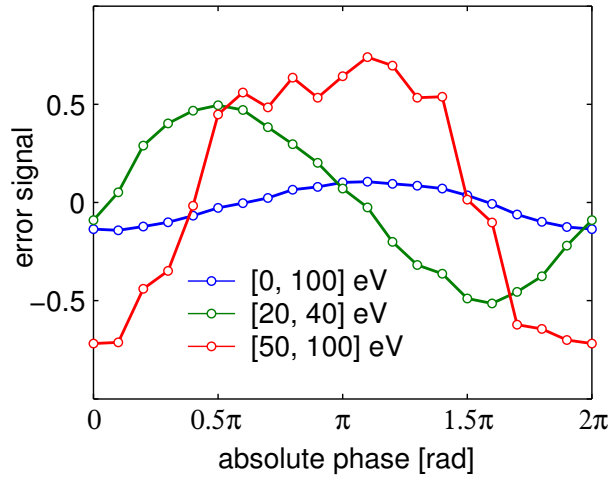


Figure 4.3: Measured error signal as a function of the absolute phase for three different energy windows. These data correspond to the measurements of Fig. 3.10. The integration time is 40 s for each point.

of the cavity [Udem99] and adjusting the laser pump power [Poppe01]. However, the easiest approach here is to use the error signal to control the position of the pair of glass wedges (Fig. 3.7). Removing and adding the amount of glass in the beam path should guarantee a stable phase in the experimental environment. Note that this approach is valid only as long as the introduced (or removed) glass does not affect the pulse shape and duration. This is not a limitation, since the expected residual phase errors to be corrected are very small. Future developments will integrate the ATI feedback in the electronic servo loop to provide the low-frequency component of the error signal.

Figure 4.4 shows the idea of phase stabilization. If a positive error signal is recorded, a proportional³ amount of glass is introduced (i.e. the absolute phase is increased). Vice versa, if a negative error signal is recorded, a proportional amount of glass is removed (i.e. the absolute phase is decreased). With this procedure, there are two equilibrium positions, A and B. However, only position B is characterized by *stable* equilibrium. Therefore, the phase will be stabilized to the corresponding value, in this case slightly higher than π . Stabilizing to different phase values is still possible by using a suitable offset for evaluating the error signal (for instance, the dashed line defines two new equilibrium positions, of which only D is stable). Better results are however expected where the slope of the error signal is larger, i.e. around zero. In addition, if one tried to stabilize to a value coincident or close to the maximum or the minimum of the error signal, the procedure would not converge. A more robust approach for stabilizing to an arbitrary value of the phase relies on simultaneous evaluation of error signals corresponding to different energy windows (Fig. 4.3).

³The constant of proportionality determines the speed and precision of convergence of the feedback loop. In particular, large constants result in fast convergence but considerable oscillations around the stable value, due to overestimation of noise. More sophisticated approaches, including adaptive

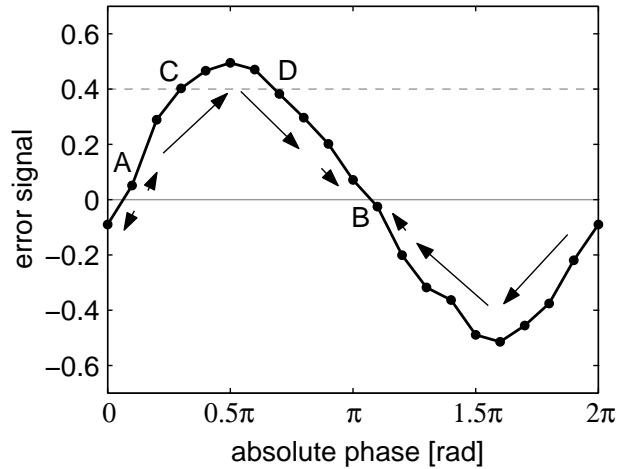


Figure 4.4: Phase stabilization idea. Glass is added (removed) for positive (negative) error signals. The arrows indicate the movement of the wedges. Thus, position A is unstable, whereas position B is stable.

4.2.2 Experimental results

In order to test the capability of the stereo-ATI of correcting low-frequency phase drifts, the following simple experiment can be performed. A slow, constant and known absolute phase drift is applied by changing the amount of glass in the beam path by means of one pair of wedges. The recorded ATI spectra in the left and right directions are then used to drive a second pair of wedges, along the lines given in the last section. If material and geometry of the two pairs of wedges are identical, ideally the movement of the first should be exactly compensated by the second.

Figure 4.5(a) shows the corresponding measurement. The first pair of wedges (red line) was moved at different (known) speeds in both directions. The amount of glass introduced can be directly translated in a phase value⁴. The movement of the second pair of wedges (blue line), controlled by the ATI signal, compensates in real time the *active* phase drift introduced by the first. The resulting phase (green line) is constant within an error not exceeding 0.5 rad, in the presence of a phase drift covering considerably more than one full period.

The phase stability can be verified also by displaying the left/right asymmetry as a function of time [Fig. 4.5(b)]. Note that the stabilization scheme consists of three sequential steps: (i) the first pair of wedges is moved; (ii) ATI spectra are acquired; (iii) the second pair of wedges is moved. Since the ATI spectra are measured *after* the first pair of wedges is moved and *before* the second corrects the movement, visible changes in the asymmetry pattern are expected in particular when the wedge movement is fast. This is observed between position B and C. However, as soon as the

control of the proportionality constant, yield better results.

⁴A glass thickness of 52 μm changes the phase by 2π (Chapter 3).

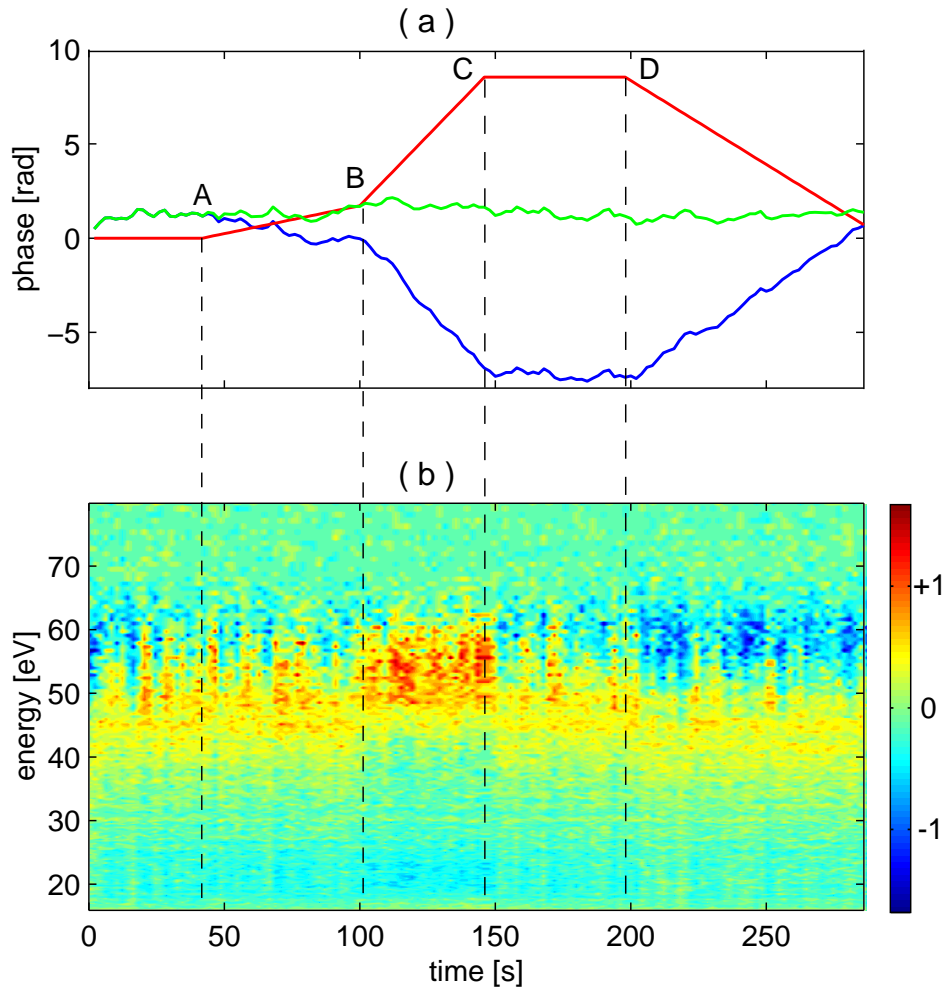


Figure 4.5: (a) Phase variation actively introduced by the first pair of wedges (red line) as a function of time. The ATI-driven second pair of wedges (blue line) compensates in real time the induced phase drift, leading to a resulting total glass thickness (green line, converted in phase) approximately constant. The induced phase drift was of $+1.8$ rad/min (A-B), $+9.0$ rad/min (B-C), 0 rad/min (C-D) and -5.4 rad/min (D-end). (b) Measured left/right asymmetry (logarithmic scale) as a function of electron energy and time. Reddish colors represent dominant left emission, bluish colors dominant right emission. The overall features are preserved during the whole measurement. This proves the capacity of the stereo-ATI experiment of correcting phase drifts of more than 2π rad/min.

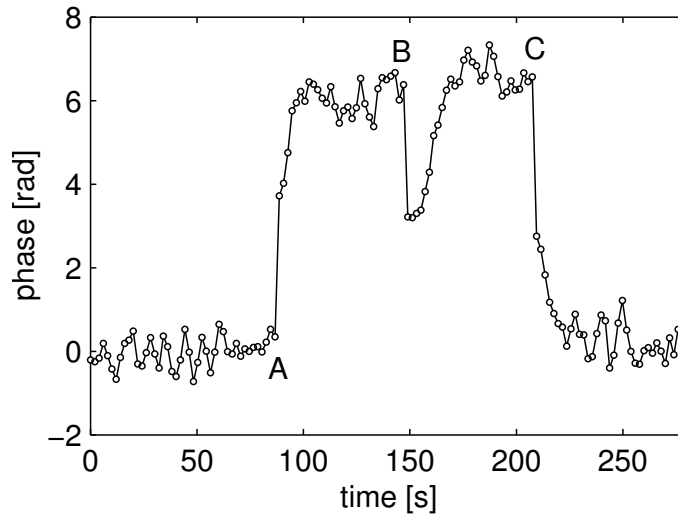


Figure 4.6: Position of the ATI-driven glass wedge (translated in phase value) as a function of time. At positions A, B and C, large phase jumps were applied, and the phase is subsequently automatically recovered within an acceptable error. Note that, depending on where the closest stable position is, the automatic procedure either increases (after transitions A and B) or decreases (after transition C) the glass thickness. Note also the short-term stability just after transition B, originating from the unstable equilibrium position shifted by π with respect to the stable one (Fig. 4.4).

first pair of wedges stops, the initial conditions are quickly restored (e.g. from C to D). Besides some intrinsic instability and noise⁵, the dominant spectral characteristics of the asymmetry are preserved during the whole measurement, indicating the success of this novel long-term phase stabilization technique.

Combining standard stabilization techniques and the stereo-ATI approach allows obtaining long-term and reliable absolute phase stability. In principle, this makes possible performing experiments requiring very long (several hours) integration times. Unfortunately, different factors, such as thermal fluctuations or environmental noise, typically limit the continuous operation of the laser system, requiring slight realignment and optimization. Any tuning operation performed in any part of the laser chain (oscillator, amplifier, compressor, hollow fiber, ...) results in a complete loss of the phase coherence. Once the phase is re-locked, standard stabilization techniques can neither retrieve nor determine the phase relation with the previous value. As a frustrating consequence, any on-going experiment would have to restart from the beginning.

The stereo-ATI phase meter offers a solution also to this problem. When the phase value is unknown, typically after laser readjustment, it is sufficient to run the phase

⁵It is worth noting that for this experiment the laser pulse duration was significantly longer than, e.g., for that of Fig. 4.3. This results in less pronounced left/right asymmetries and, as a consequence, in less precise phase stabilization.

stabilization procedure described in Sec. 4.2.1 in order to control the position of the glass wedge. This automatically stabilizes the phase exactly to the previous value. This is illustrated in Fig. 4.6, showing the absolute phase, as deduced from the position of the ATI-driven pair of wedges, as a function of time. At positions A, B and C, the phase was intentionally changed by a large amount by changing the wedge position. This is analogous in all respects to re-locking the phase to a different value after laser readjustment. Subsequently, the automatic phase retrieval takes place⁶ and, as soon as the phase reaches its asymptotic value, any previously on-going measurement can simply continue.

4.2.3 A first application: ATI and NSDI in parallel

The two demonstrated techniques of long-term phase stabilization (Fig. 4.5) and of phase retrieval (Fig. 4.6) opened the way to new exciting experiments. One of the most intriguing in the field of laser-atom interaction is certainly the study of multi-electron correlated phenomena like non-sequential double ionization (NSDI, Sec. 1.6). Similar to the ATI plateau, NSDI is intimately connected with rescattering of electrons driven back to the ion core by the light field. Hence, measuring the absolute phase dependence of this process should improve the understanding of the rescattering mechanism.

The method used to study NSDI is ion and electron momentum spectroscopy. A description of the experimental setup, based on the COLTRIMS (Cold Target Recoil Ion Momentum Spectroscopy) technique, can be found in [Moshhammer00, Moshhammer01]. The ion momenta can be measured with high resolution (~ 0.1 atomic units). However, in order to avoid any influence of space charge effects, the count rate in the experiments must be kept very low (less than one ionization event per laser shot). Under these conditions, the only possibility for performing systematic measurements with reasonable double ionization events statistics is to make use of long integration times⁷. To guarantee stable and reproducible phases during the acquisition, the use of the stereo-ATI was imperative.

Figure 4.7 shows the experimental arrangement used in order to run the two experiments simultaneously. The laser is divided with a beam splitter in order to steer one beam to the stereo-ATI and the second one to the COLTRIMS apparatus. Very conveniently, only 5% of the pulse energy is sufficient for ATI, leaving essentially the full power available for the other experiment. Careful dispersion compensation is achieved by separately tuning the amount of glass in the beam paths, ensuring short pulse durations in both spectrometers.

In order to control the absolute phase, one pair of glass wedges (W1) in the common beam path is driven by the stereo-ATI in order to compensate long-term phase drifts

⁶During this test the laser pulse duration was relatively long, resulting in relatively slow convergence and considerable oscillations around the stable value.

⁷For these kind of studies, the most efficient way is actually to use a high repetition rate laser system [Lindner02, Eremina03, Eremina04].

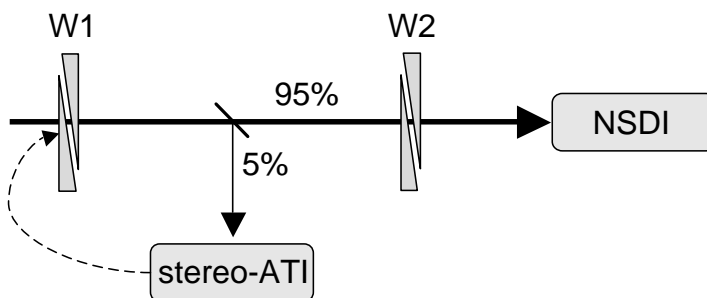


Figure 4.7: Experimental setup for studying non-sequential double ionization (NSDI) by using the stereo-ATI as a tool for stabilizing the absolute phase.

and retrieve the phase after laser readjustments, as described in the last section. Hence, during the whole measurement the absolute phase *in the ATI experiment* was kept to a unique, constant value. A second pair of glass wedges (W2) allows changing the phase *in the NSDI experiment* by known amounts, so that the ion momenta distribution could be investigated at all phases [Liu04]. Note that the phase difference between the two experiments, originating from the completely different beam paths, is unknown. However, what matters here is that it be precisely tunable (by means of the wedges W2).

The whole set of measurements lasted approximately 10 hours. During this time, the laser had to be optimized and slightly realigned several times. In addition, significant phase drifts were detected and compensated. All this did not affect at all the outcome of the experiments. As soon as laser readjustments became necessary, the NSDI acquisition was stopped. Then, the stereo-ATI retrieved the previous value of the phase (Fig. 4.6), and the NSDI acquisition could afterwards continue, phase stability being subsequently ensured by the permanently running ATI experiment. This not only permitted to gain unprecedented insight into the mechanisms of NSDI [Liu04], but at the same time constitutes a milestone for using ATI as a new diagnostic tool for few-cycle pulse lasers.

4.3 Future developments

The use of ATI as a phase stabilization tool has some distinctive technical advantages. Pulse energies of less than $20 \mu\text{J}$ are sufficient⁸; this is indeed negligible in a laser system delivering about $500 \mu\text{J}$ (Sec. 3.2). Hence, essentially the full power can be dedicated to other experiments (Fig. 4.7). Small technical improvements should further decrease the needed energy, allowing also higher repetition rate lasers (Sec. 2.1) to operate simultaneous experiments. Clearly, the increased repetition rate will result in much shorter measuring times even for experiments with intrinsically limited count rate.

⁸This value should not be considered a lower limit. Indeed, no attempts were made to reduce this value further.

Another advantage is that the target gas pressure is so low ($< 10^{-4}$ mbar) that the ATI experiment does not affect the laser beam. Thus, the stereo-ATI can be placed anywhere in a beam-line. In principle, if a long focus were available, it would be even possible to place the stereo-ATI and a second experiment (for instance, HHG) in a single vacuum chamber, allowing real-time calibration and stabilization of the absolute phase.

The current disadvantage is the small bandwidth of the stabilization scheme, which makes it suitable for correcting only long-term phase drifts. The reason for this is the reduced count rate in the ATI plateau, which is most efficient for deriving the error signal (Fig. 4.3). Increasing the count rate is easily possible by applying higher voltages to the microchannel plates or by rising the gas pressure. However, the huge number of slow (direct) electrons would rapidly saturate the MCP cartridges, introducing artifacts in the spectra and reducing the detectors' lifetime.

This problem was circumvented by mounting additional metal grids in front of the microchannel plates [Fig. 4.8(a)]. While the first (G1) is grounded to preserve the necessary field-free zone inside the time-of-flight tubes, the second (G2) is kept at some adjustable negative voltage. As a consequence, only high energetic electrons can overcome the created electric potential barrier, whereas low energetic electrons are repelled. This allows increasing significantly the count rate in the ATI plateau, without saturating the detectors with low-energy electrons. Note that the distance between the two grids is kept small in order to avoid influence on the electrons' time-of-flight and subsequent artifacts in the ATI spectra. Figure 4.8(b) shows ATI spectra obtained by applying a voltage of -20 V to the grid G2.

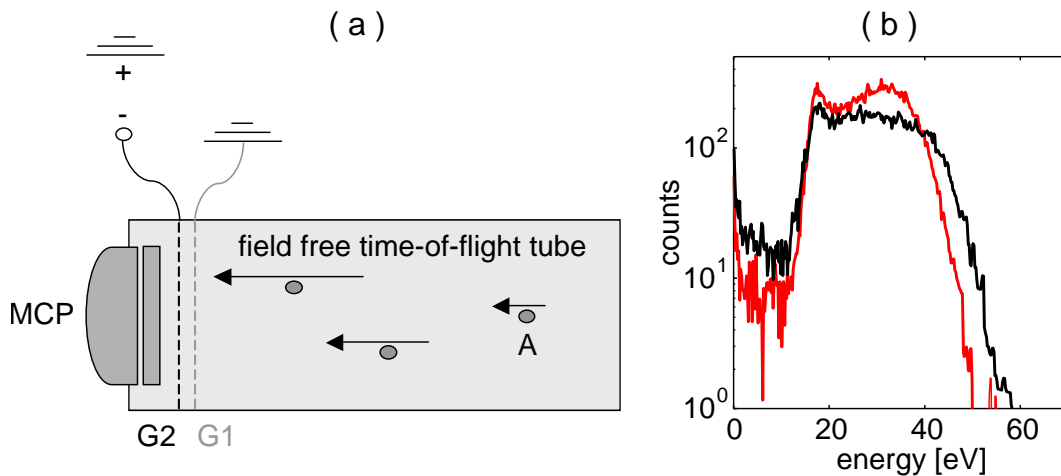


Figure 4.8: (a) A metal grid kept at a negative potential (G2) repels the slowest electrons (A). This allows significant increase of the count rate in the ATI plateau. A grounded grid (G1) is necessary to electrically shield the time-of-flight tube. (b) ATI spectra in the left (red line) and right (black line) direction obtained by applying a voltage of -20 V to the grid G2. Note the high count rate considering the short acquisition time (10 s). The spectral features in the plateau are not influenced by the electrostatic barrier of 20 eV.

The use of the repelling grid successfully allows increasing the count rate in the ATI plateau, making thus possible faster absolute phase corrections. However, an intrinsic limit is set by the detection system, relying on counting the number of electrons hitting the microchannel plate. As discussed in Sec. 3.3.1, the average width of the pulses generated by the MCPs (pulse-pair resolution ~ 4 ns) limits the number of electrons detectable per laser shot, in particular in the ATI plateau. As a consequence, the bandwidth of the phase stabilization seems to be currently limited to the 1-Hz regime⁹. In order to increase the bandwidth further, two solutions can be envisaged. On the one hand, slowing down all electrons by a careful ion optics design should allow very high count rates in the ATI plateau, due to the longer time-of-flight interval. On the other hand, the same effect could be obtained by a detection system measuring the electron current produced at the anode of the MCP. With such a method, the electrons could pile up to produce a high current, allowing simultaneous detection of an ideally unlimited number of electrons. In future laser systems, both systems could allow improving, integrating and possibly even replacing the standard phase stabilization servo loops based on the f -to- $2f$ technique.

⁹This is true at a laser repetition rate of 1 kHz. Obviously, increasing the repetition rate results in faster feedbacks.

Chapter 5

Full spatiotemporal characterization of the absolute phase

The potential of the stereo-ATI setup as a phase meter opened the way to a number of experimental studies hitherto not possible. As a consequence, also the theoretical study of the dependence of ionization processes on the absolute phase received considerable novel attention [Chelkowski02, Milošević03, Paulus04, Milošević04, Chelkowski04]. Experimental evidence of the predicted effects is not only of academic interest, but becomes of critical importance for all applications of ultrashort laser pulses with controlled and known absolute phase. So far, the most appealing seems to be isolated attosecond pulse generation [Hentschel01, Kienberger04], but it is not difficult to foresee a growth of the fields of application in the next years.

In this chapter, the absolute phase effects will be characterized with respect to all parameters which are typically changing in any laser-matter interaction experiment. The novelty of these results is intrinsic in the previously not possible phase control demonstrated in Chapter 3. First, the dependence of the absolute phase on the spatial position in the laser focus will be discussed [Lindner04a]. This is strictly connected with the well-known Gouy¹ phase anomaly and a simple theoretical analysis to explain it will be proposed. Then, the dependence of phase effects on laser parameters like intensity and pulse duration will be discussed, together with comparisons based on the semiclassical model.

¹After A. Siegman introduced the wrong spelling *Guoy* [Siegman86], the name of Louis-Georges Gouy is often misspelled.

5.1 Spatial dependence: the Gouy effect

An important issue of nonlinear processes driven with ultrashort light pulses is that they usually take place in a laser focus. It is known that an electromagnetic beam propagating through a focus experiences an additional π phase shift with respect to a plane wave. This phase anomaly was discovered by Gouy in 1890 [Gouy90] and has since then been referred to as the Gouy phase shift. This phase change is, in fact, a general property of any focused wave, and is also expected for sound waves [Holme03]. Intuitive explanations of the observed anomaly have been proposed [Boyd80, Feng01] and still attract the interest of the scientific community. The experimental evidence of the Gouy phase shift relied for years on interferometric measurements [Gouy90, Carpenter58]. More recently, direct observations of the polarity change of single-cycle terahertz pulses have been reported [Ruffin99, Kužel99, McGowan00].

The Gouy phase shift has important consequences in the optical range of the electromagnetic spectrum. In laser cavities, the determination of the resonant frequencies depends on the Gouy phase [Siegman86]. Phase matching in high-order harmonic generation (Sec. 1.4.2) is governed by the atomic response and the Gouy phase shift of the fundamental radiation [Lindner03]. More importantly, the Gouy phase strongly affects the spatial variation of the CE phase of ultrashort pulses in a laser focus. Thus, knowledge of the details of the phase variation is of critical importance for any application of phase-stabilized few-cycle laser pulses.

5.1.1 Physical picture

In principle, the Gouy phase shift of a TEM₀₀ cw-wave can be described by a simple formula depending on the focusing geometry and the wavelength [Svelto98],

$$\phi = -\arctan \left[\frac{z}{z_R(\lambda)} \right] \quad (5.1)$$

where the beam is traveling in the $+z$ direction and z_R is the Rayleigh distance (dependent on the wavelength λ). As few-cycle pulses consist of broad spectra with wavelengths spanning about one octave (cf. Fig. 3.6 on page 46), the different spectral components will experience the Gouy phase shift with different spatial scales. In particular, *blue* colors undergo a steeper phase change than *red* colors². This is illustrated in Fig. 5.1.

One first consequence is that the spectral components constituting the femtosecond pulse do not preserve their initial phase-locking during propagation in the focal area.

²This is readily understood by noting that each color is focused to a spot given by $w_0(\lambda) = \lambda f / \pi D$, where f is the focal length of the focusing optics and D is the diameter of the laser beam on the lens. Hence, the corresponding Rayleigh distance is $z_R(\lambda) = \pi w_0^2(\lambda) / \lambda = \lambda f^2 / \pi D^2$, i.e. it increases for increasing wavelengths. This argument also implies that any focused ultrashort laser pulse is spectrally reshaped in the focus. This *focusing-induced spatial chirp* is however usually negligible.

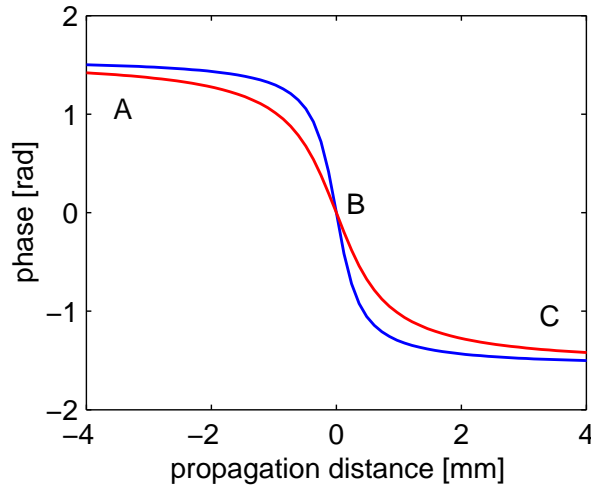


Figure 5.1: Geometrical phases of a beam focused with $f/20$ geometry. For the sake of clarity, two extreme wavelengths are considered here (500 nm, blue line, and 1100 nm, red line).

Thus, the pulse might be transform limited before the focus (A), in the center of the focus (B), and after the focus (C) where all phases have the same value, but not in an arbitrary position of the focus. The result is that the pulse duration depends on the z -position considered. This *focusing-induced dispersion* is however a very small effect that can be safely neglected even for extremely broad spectra.

The phase modulation $\phi(\omega, z)$ shown in Fig. 5.1 has much more interesting consequences on the pulse propagation properties. The phase velocity is defined by [Born89]

$$v_{ph}(\omega, z) = \frac{\omega}{|\partial\phi/\partial z|} \quad (5.2)$$

whereas the group velocity is

$$v_{gr}(z) = \frac{1}{\left| \nabla \frac{\partial\phi}{\partial\omega} \Big|_{\omega_0} \right|} \quad (5.3)$$

ω_0 being the central frequency of the spectrum. Figure 5.2(a) shows the calculated phase velocity of the carrier wave (ω_0) and the group velocity of the pulse as a function of the propagation distance in the focus. Note that the pulse is characterized by both *subluminal* and *superluminal* propagation, depending on the longitudinal position. The ratio v_{gr}/c does not depend on the spectral width of the pulse, but only on the focusing geometry, and can significantly differ from 1 for very tight focusing geometries.

From the difference of the two velocities it is straightforward to calculate the resulting carrier-envelope phase slippage in the neighborhood of the focus [Fig. 5.2 (b)]. Since the phase velocity is everywhere larger than the group velocity, the envelope is

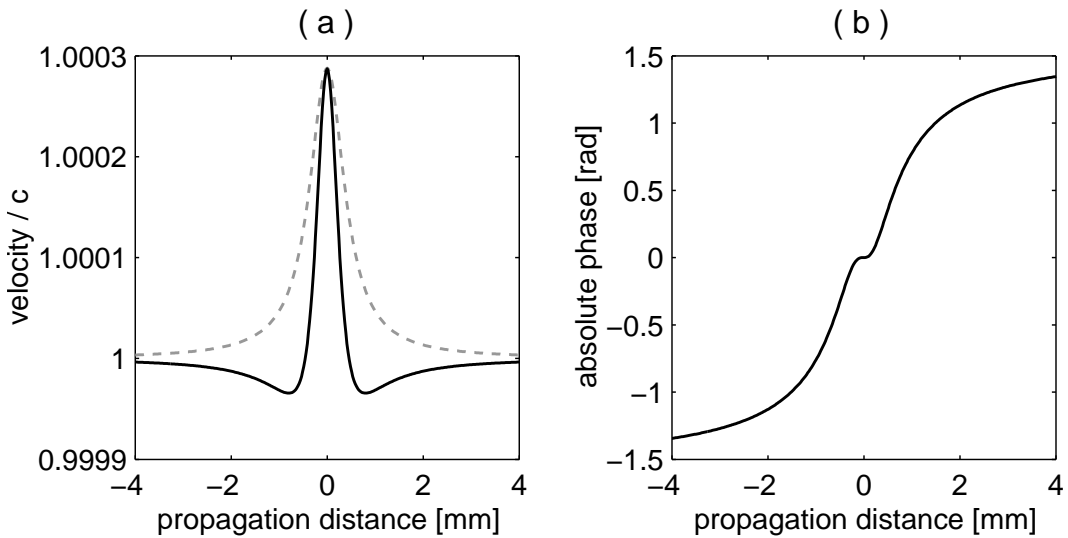


Figure 5.2: (a) Phase (dashed line) and group (solid line) velocities as a function of the propagation distance for a beam focused with $f/20$ geometry. The pulse exhibits both subluminal and superluminal behaviors. (b) Induced absolute phase shift as a function of the propagation distance. A π shift is expected from positions well before to well after the focus.

continuously delayed with respect to the carrier. In general the absolute phase variation cannot be described by a simple formula like Eq. (5.1). Indeed, the details of the phase change in the focus depend on the spatial profile of the laser beam (typically not Gaussian) and on the real focusing geometry (with unavoidable aberrations). In all cases, however, an overall π phase shift is expected between symmetric positions well distant from a spherical focus. Since the phase changes by π in the propagation through the focus, virtually all possible E-field shapes are available for the experiments. Thus, precise control of the spatial variation of the absolute phase in the whole focal region is crucial to any application of phase-stabilized few-cycle laser pulses.

5.1.2 Gouy phase measurement

The experimental setup and parameters are identical to those of the results shown in Chapter 3. Since measuring the Gouy phase shift implies scanning the whole focal region, a preliminary evaluation of the beam profile in the focus is very meaningful. Figure 5.3 shows the beam diameter in the horizontal and vertical direction as a function of the propagation distance. The angle of incidence on the focusing spherical mirror ($f = 25$ cm) is minimized to 7° , but the beam clearly shows astigmatism. In any case, the measured intensity profile suggests that the electric field should undergo the π phase shift within a range of a few millimeters.

To reveal the influence of the Gouy phase, one has to detect selectively the electrons generated at a well-defined position of the focus. This is guaranteed by the pair of moveable slits perpendicular to the beam axis and to the polarization axis (cf. Fig. 3.7

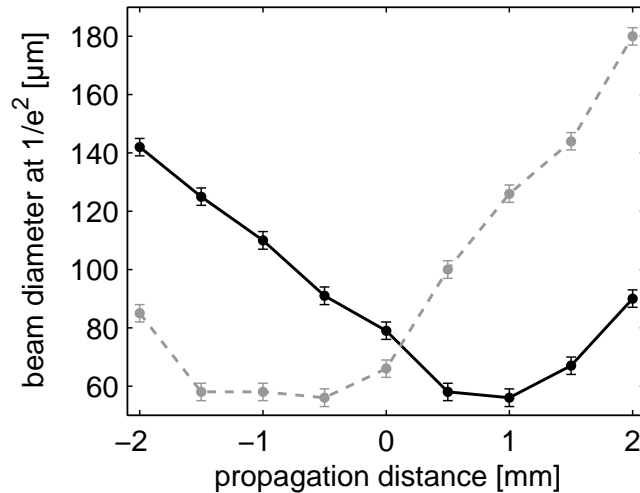


Figure 5.3: Measured diameter (intensity at $1/e^2$) of the focused beam in the horizontal (solid line) and vertical (dashed line) directions. The laser beam is traveling in the $+z$ -direction. The astigmatism is due to the off-axis spherical mirror used for focusing.

on page 46). The slit width is $250 \mu\text{m}$, well below the Rayleigh range ($\sim 1 \text{ mm}$), and, to achieve optimum spatial resolution in the z -direction, they are placed at a distance of only 1 mm from the beam. With this setup, the angular distribution of the emitted photoelectrons does not affect the phase resolution, which can be estimated to be $\sim 0.1 \text{ rad}$.

The anisotropic photoelectron emission occurring with phase-stabilized few-cycle laser pulses can be used to determine the Gouy absolute phase shift. One possibility to observe the change of sign of the electric field in passing through the focus is to compare the electron yield in the two directions before and after the focus. For instance, if one detects dominant left emission before the focus, the opposite is expected after the focus. This can be verified with all possible absolute phases simply by introducing a variable glass thickness in the beam path, as described in Sec. 3.4. Figure 5.4 shows the electron count rate asymmetry (left/right ratio) as a function of the glass thickness introduced. The measurement was made by moving the pair of slits to a distance of $\sim 2 \text{ mm}$ before (dashed line) and after (solid line) the focus. The clear phase shift of π between the two curves represents a direct measurement of the Gouy phase shift in the focus.

The electric field polarity reversal observed from before to after the focus does not describe the details of the phase slippage in the focus. Since many experiments take place over an extended area of the focus, e.g. high-order harmonic generation and attosecond pulse generation, it is essential to characterize the phase variation precisely and, in particular, to recognize possible anomalies in the behavior of the phase evolution. Indeed, the possible presence of a significant area of the focus with anomalous phase change has been suggested as an explanation of the observed enhancement of the HHG efficiency by using truncated Bessel beams [Nisoli02].

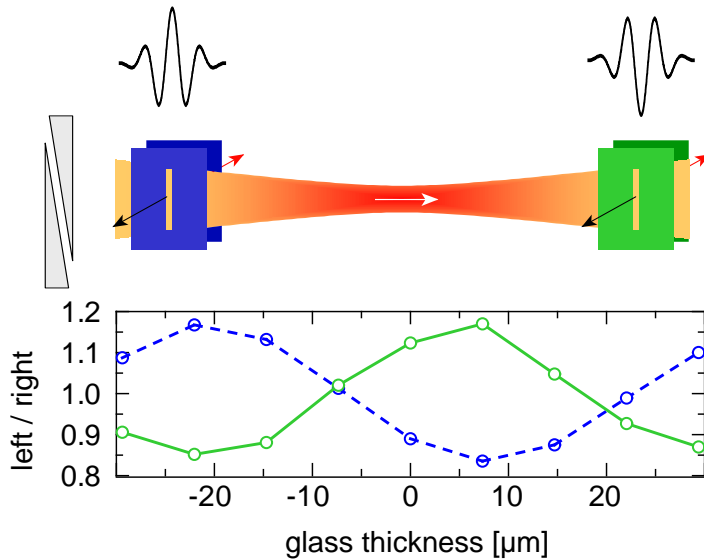


Figure 5.4: Varying the glass thickness in the beam path changes the absolute phase of the pulses. The left/right ratio of the electron yield exhibits clear oscillations with a periodicity consistent with glass dispersion at the wavelength of the laser. The measurement was performed before (dashed line) and after (solid line) the focus. The π phase shift is due to the Gouy phase shift in passing through the focus.

In order to analyze in detail the phase variation within the focal range, electron spectra at several positions were acquired by moving the pair of slits. Figure 5.5 shows the detected left/right asymmetry as a function of the electron energy and of the glass thickness introduced for a few z -positions. Different approaches are possible to retrieve the phase variation. The integrated electron yield provides a clear phase indication, and can be used to show the overall phase shift in the focus (Fig. 5.4). However, scanning the focal range implies measuring at constantly changing intensities. Since it is predicted that the maximum of the integrated left/right asymmetry should occur at a phase that depends on the intensity [Chelkowski02, Chelkowski04], it is not easy to decouple the Gouy phase shift from the possible intensity-dependent phase shift. A better approach relies therefore on the evident spectral information of Fig. 5.5. Dark reddish and bluish colors correspond to spectral regions of strong asymmetry: Since these are easily distinguishable, they can be used to follow the phase evolution. Note that the measurements were made by approaching the focus from the outer part and by moving alternatively the slits before and after the focus. With this procedure, measurements of symmetric positions around the focus are consecutive, thus reducing detrimental effects from possible long-term phase drifts.

The panels relative to $z < -1.5$ mm and $z > 1.5$ mm correspond to the outer part of the focal range. The strong asymmetry in the high-energy part of the spectra (ATI plateau) changes sign while passing through the focus, confirming the π phase shift already discussed (Fig. 5.4). More interestingly, in the panels corresponding to posi-

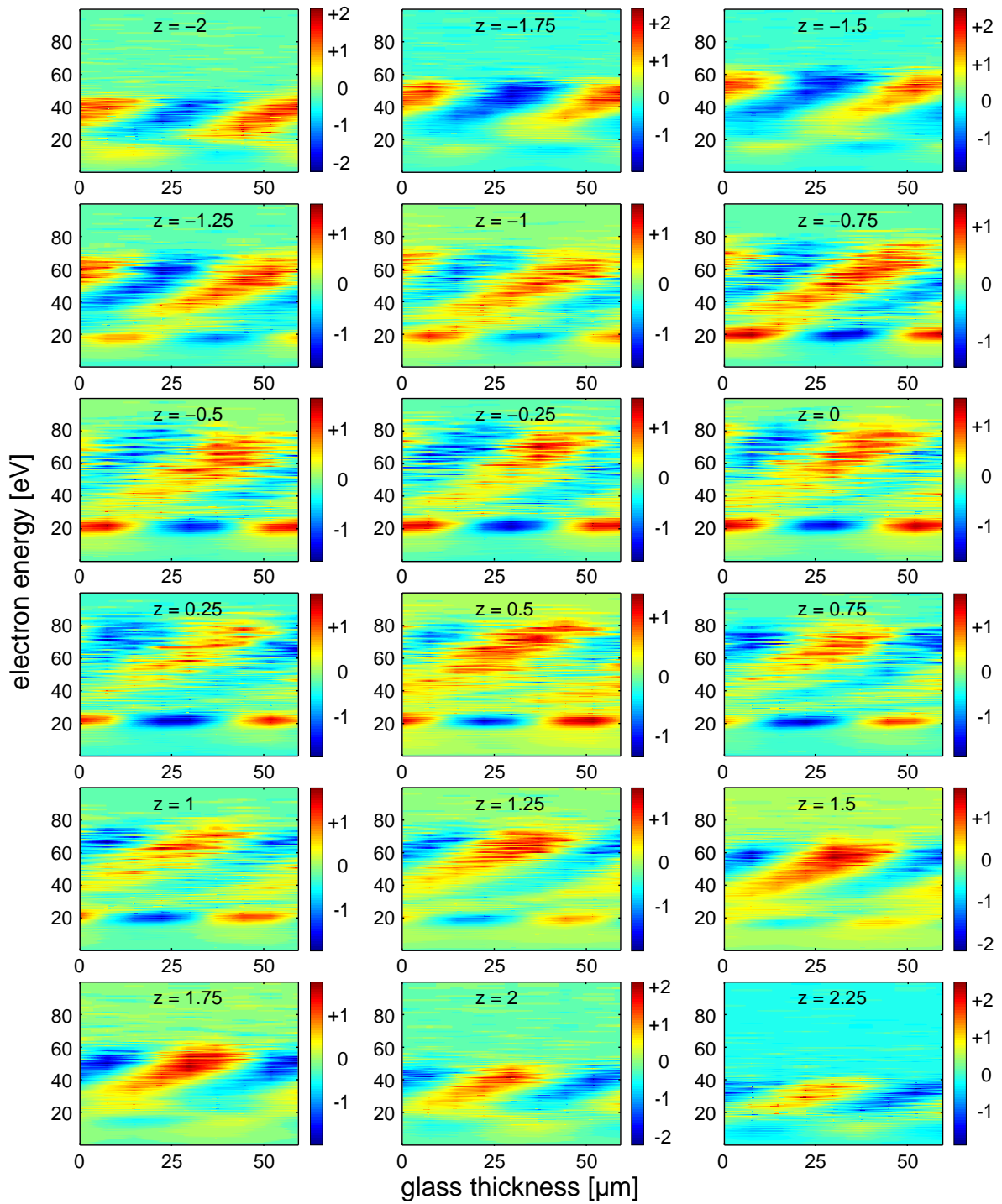


Figure 5.5: Left/right asymmetry maps (logarithmic scale) for different longitudinal positions as a function of electron energy and glass thickness introduced. Reddish colors indicate dominant left emission, bluish colors dominant right emission. The corresponding positions (mm) are indicated in each panel (positive values represent positions after the focus). The phase difference is determined by evaluating the shift of the characteristic structures of the asymmetry pattern.

tions in the central part of the focus, the asymmetry in the plateau is partly smeared out, but another clear asymmetric area appears in the low-energy part of the spectra (20 – 25 eV), just before the ATI plateau. Its origin will be explained in Sec. 5.2.2. Being definitely a phase effect, it can here be exploited to retrieve the phase variation in the focus. By moving in the direction of the beam propagation, i.e. from before to after the focus (from $z = -2$ mm to $z = +2.25$ mm), the characteristic pattern moves toward the left side of the graphs, i.e. toward decreasing glass thickness introduced. This is in full agreement with the intuitive physical origin of the Gouy absolute phase shift. Indeed, in a dispersive medium like glass the phase velocity exceeds the group velocity. The same situation occurs in the propagation of the ultrashort pulse in the laser focus (Fig. 5.2). Thus, it is not surprising that, to observe similar features, less glass is needed after the focus with respect to a symmetric position before the focus. The Gouy phase shift determination can be performed simply by numerically evaluating the shift of the asymmetry pattern; converting the glass thickness shift obtained (μm) into phase difference (rad) is then straightforward.

A more compact representation is given in Fig. 5.6, showing the detected left/right asymmetry as a function of energy and of propagation distance for a fixed laser pulse shape (i.e. for a fixed glass thickness introduced by the wedges). In (a) the absolute phase shifts from $\phi = 0$ to $\phi = \pi$, while in (b) it shifts from $\phi = \pi$ to $\phi = 2\pi$. The color transition observed indicates the change of electron asymmetry during propagation, and is a direct visualization of the Gouy effect.

Figure 5.7 shows the retrieved absolute phase shift as a function of the propagation distance. For comparison, the Gouy phase of a Gaussian beam [Eq. (5.1)] with a f/30 focusing geometry is also shown (solid line). It is worth emphasizing once again that the absolute phase shift is *not* expected to follow the Gouy phase, the latter being a property of cw lasers. The beam in these experiments is a few-cycle pulse truncated Bessel beam, and the focusing geometry inevitably introduces astigmatism (Fig. 5.3).

The pulses undergo the π phase shift within a few Rayleigh distances. Due to the rapid decrease of electron yield at lower intensities, the measurements were stopped at a distance of ~ 2 mm before and after the focus. This prevented observation of the expected area of constant phase in the outer part of the focus. Note, however, that the region of interest for all experiments is entirely covered, and the estimated error for the experimental data is relatively low (~ 0.1 rad). The phase changes smoothly with a constant slope and, what is particularly important for experiments, does not exhibit any wiggles or irregularities.

In conclusion, the absolute phase shift of laser pulses evolving through a focus induced by the geometrical Gouy phase was directly measured [Lindner04a]. This constitutes the first full characterization of phase-stabilized few-cycle optical pulses in space and time, an essential step for any application of such laser systems. Furthermore, these results provide access not only to the overall polarity reversal for pulses evolving through a focus [Ruffin99, Kužel99, McGowan00], but also, for the first time, to the details of the phase variation *in* the focus. This detailed knowledge permits the

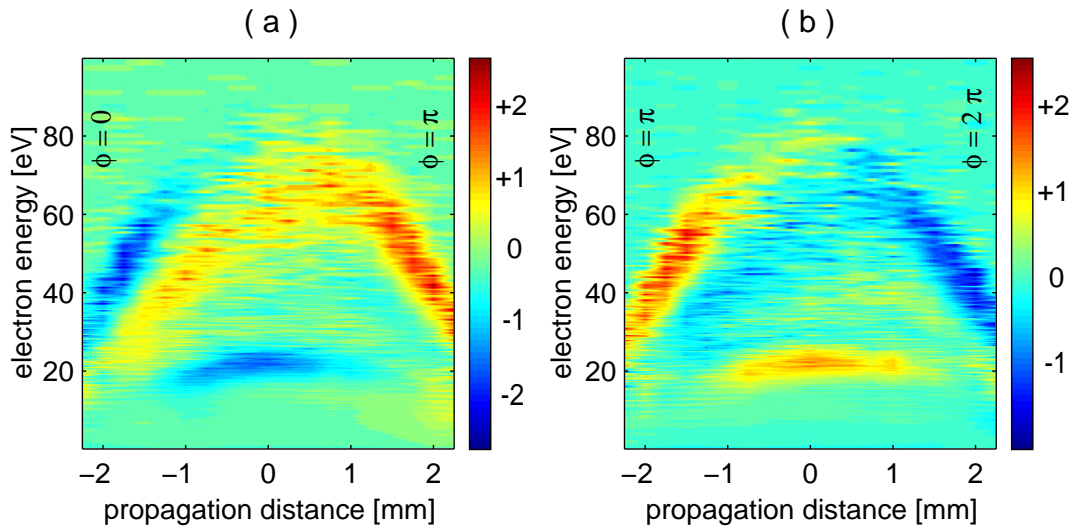


Figure 5.6: Left/right asymmetry maps (logarithmic scale) as a function of electron energy and propagation distance. Reddish colors indicate dominant left emission, bluish colors dominant right emission. The absolute phase before focusing ($z = -2$ mm) is here $\phi = 0$ (a) and $\phi = \pi$ (b).

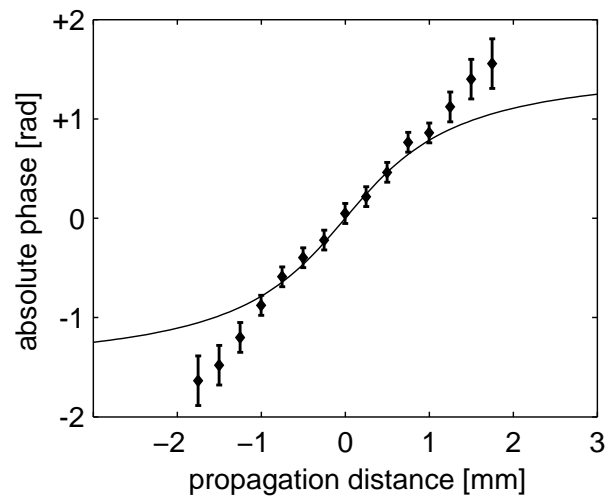


Figure 5.7: Retrieved Gouy phase shift as a function of the propagation distance in the focus. The solid line is the Gouy phase of a cw Gaussian beam, shown for comparison. Note that the electron count rate rapidly decreases in the outer part of the focus, making detection of additional experimental points difficult.

precise measurement of the difference of phase and group velocities and constitutes thus striking experimental evidence of anomalous (subluminal and superluminal) light propagation (see Fig. 5.2). Note that these are very general properties of laser beams. For few-cycle pulses, they are particularly meaningful, owing to the possibility of defining (and measuring) an *absolute* value of the phase.

5.2 Intensity dependence

5.2.1 Ionization yield

The integrated ionization yield depends nonlinearly on the laser intensity. This is intrinsic in any analytical formulas used to describe ionization both in the tunneling and in the multiphoton regime (Sec. 1.2.1), as well as in numerical models solving directly the time-dependent Schrödinger equation (TDSE). For few-cycle pulses, it is therefore expected that also the directional photoelectron asymmetries depend on the intensity in a characteristic way.

A first approach for varying the laser intensity generating the ATI emission is to move the gas source (a 30- μm thin glass capillary) along the beam propagation direction in the focal region. This allows measuring at smoothly changing intensities up to the peak intensity, reached in the center of the focus. The selection of electrons generated at a well-defined position in the focus is once again ensured by the two pair of slits used in the stereo-ATI setup (Fig. 3.7 on page 46).

To quantify the detected left-right asymmetry, a suitable parameter is defined as $(L - R)/(L + R)$, where L and R are the ionization yields respectively in the left and right direction. This quantity oscillates around zero, and the contrast of the measured oscillation can be expressed by its amplitude (peak-to-valley). Figure 5.8(a) shows the measured contrast of the oscillations as a function of the propagation distance in the focus. At each position, it is also indicated the laser intensity estimated from the position of the cutoff in the ATI spectra, occurring at an energy of $10 U_p$. Note the area of relatively constant intensity in the central part of the focus, not surprising due to the astigmatism of the beam (Fig. 5.3). The highest contrast is observed in the outer part of the focus, where the intensity is lowest. By moving toward the central part of the focus, the contrast decreases, reaches a minimum and increases again, acquiring relatively constant values in the center of the focus. By sorting the data, one can plot the contrast as a function of the intensity [Fig. 5.8(b)].

It is worth noting that, due to the strong dependence of the contrast of asymmetry also on the pulse duration (Sec. 5.3), Fig. 5.8(b) can *not* be used to calibrate the laser intensity in the experiments by measuring the asymmetry parameter. The best gauge in this respect remains the position of the cutoff in the ATI plateau. However, for a *fixed* pulse duration (as it is the case in Fig. 5.8), the contrast reveals to be an extremely sensitive indicator of intensity fluctuations. Indeed, the seemingly erratic behavior of

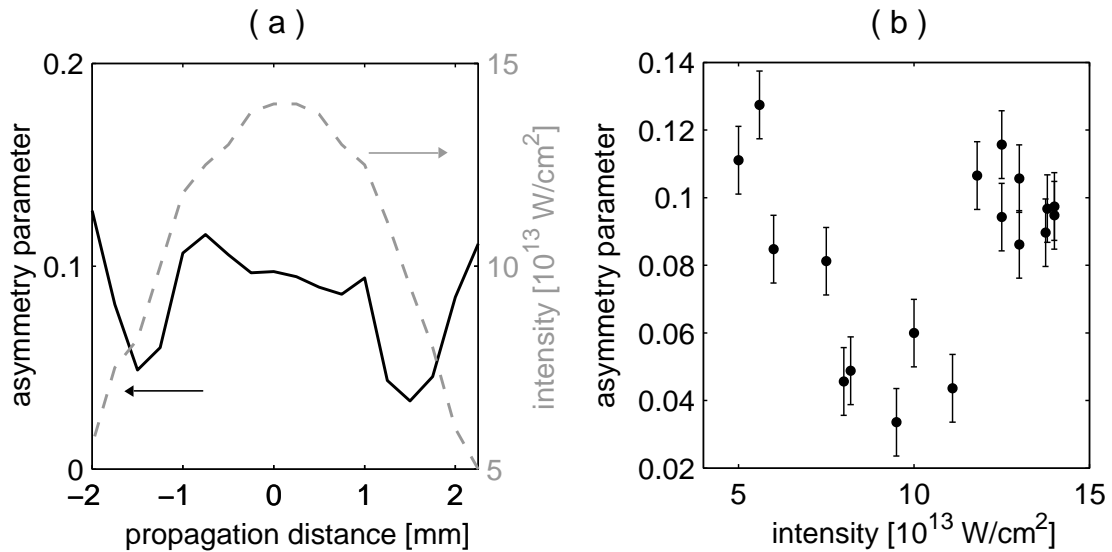


Figure 5.8: (a) Contrast of the left-right asymmetry (solid line) and estimated laser intensity (dashed line) as a function of the position in the focal range. (b) Asymmetry parameter as a function of intensity, as deduced from (a). The large error bars are due to uncertainties in estimating the intensity, not to poor signal-to-noise ratio. The contrast shows a minimum at intensities around 10^{14} W/cm². Note that the value of the parameter also strongly depends on the pulse duration.

the contrast in the central part of the focus [Fig. 5.8(a)] is actually a signature of small intensity variations, hard to recognize in the ATI plateau, but compatible with the aberrations of the focused beam.

To remove this source of intensity instability in the measurement, somewhat not under control, a second approach for studying the dependence of the contrast on the intensity is to change the pulse energy, while keeping fixed the position of the gas jet and of the slits. This can be done by attenuating the laser beam by means of thin pellicles positioned at tunable angles of incidence. The thickness of the pellicles ($4\ \mu\text{m}$) ensures that the pulse duration is not affected significantly, so that any observed difference in contrast can be attributed only to the different intensity. With this procedure the difference of intensity is known with high precision simply by measuring the pulse energy with a power meter.

Figure 5.9(a) shows the asymmetry parameter $(L - R)/(L + R)$ as a function of the absolute phase (as usually, varied by means of the glass wedges) for different intensities³. The value of the phase was independently determined for each intensity on the basis of the high-energy electrons, as described in Sec. 3.5. The intensity was estimated by means of the position of the ATI cutoff for the spectra taken at to 7.5×10^{13} W/cm² [violet curve in Fig. 5.9(a)], and subsequently scaled for the others

³For technical reasons, the very low energy electrons ($< 4\text{ eV}$) were discarded in these measurements. This weakly affects the value of the asymmetry, but not its intensity dependence, under investigation here.

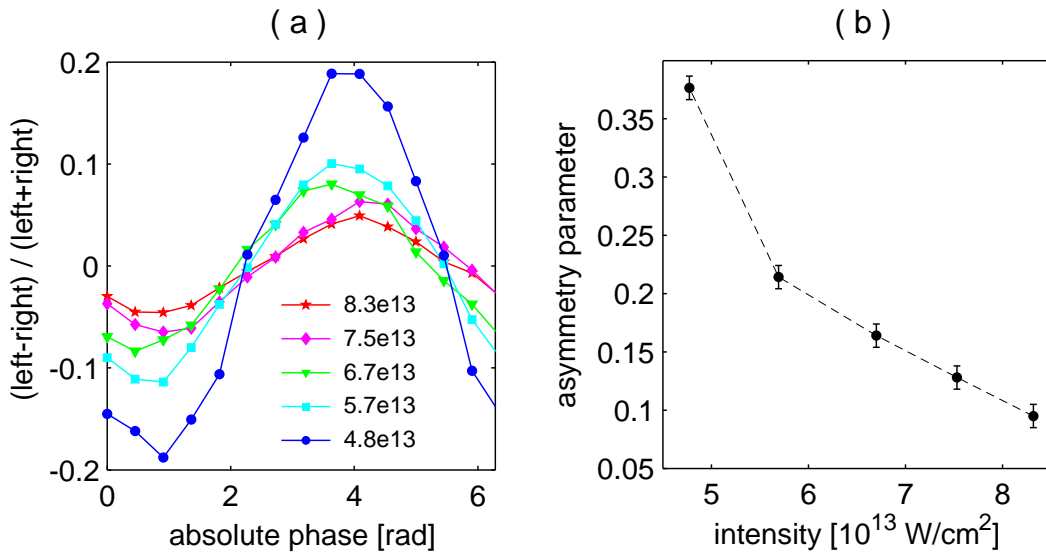


Figure 5.9: (a) Left-right asymmetry as a function of the absolute phase measured for different laser intensities, indicated on the plot. No intensity-dependent phase shift can be detected. (b) Contrast of the asymmetry as a function of the intensity, as deduced from (a). The increase at low intensities observed in Fig. 5.8(b) is here confirmed.

according to the measured pulse energy. Note that no intensity-dependent phase shift can be observed in this intensity range, i.e. the maximum contrast always occurs for approximately the same pulse shape, namely at a phase slightly higher than π ⁴. Figure 5.9(b) shows the measured contrast as a function of the intensity.

The main features observed in these experiments are currently object of theoretical investigations based on numerical solutions of the time-dependent Schrödinger equation [Chelkowski02]. The semiclassical model, on the other hand, is generally unsuitable for describing ionization asymmetries, obviously due to the influence of the Coulomb potential. However, it is still useful since it provides qualitative explanations of the physical processes. Figure 5.10 shows the calculated contrast of left-right asymmetry as a function of the laser intensity. The asymmetry parameter increases at low intensities, in qualitative agreement with the experimental data [Fig. 5.9(b)]. This is due to the dependence of the ionization rate [Eq. (1.9) on page 8] on the field strength, predicting higher nonlinearities at low intensities. The second remarkable characteristic of the contrast, namely the minimum appearing at intensities around 10^{14} W/cm² [Fig. 5.8(b)], can also be qualitatively explained by tunneling theory. Indeed, at intensities between 10^{14} and 2×10^{14} W/cm² the ionization probability of a xenon atom significantly grows and reaches saturation. Thus, ionization takes place mainly in the leading edge of the pulse (cf. Fig. 1.4 on page 11), resulting in an *effective* shorter pulse and increased contrast.

⁴This is in excellent agreement with very recent theoretical simulations [Chelkowski04].

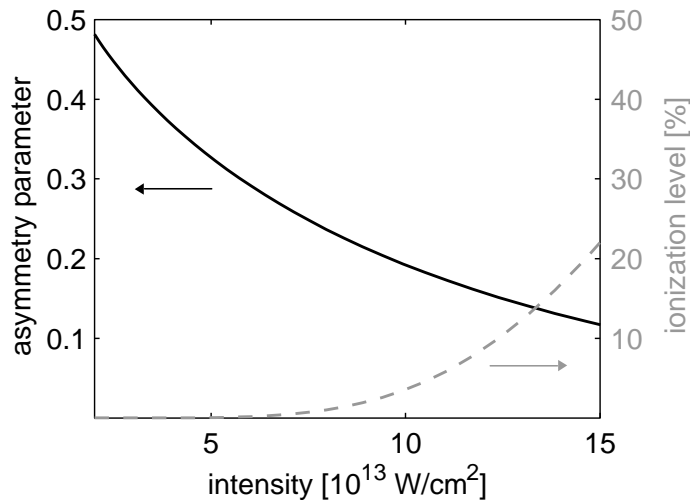


Figure 5.10: Asymmetry parameter (solid line) and ionization level of the atom (dashed line) as a function of the laser intensity. The calculation assumes xenon atoms ($I_p = 12.13$ eV) and a pulse duration of 5 fs FWHM. At high intensities, saturation starts playing a significant role, confining the ionization mainly in the leading edge of the pulse.

5.2.2 ATI spectra

The high-energy part of the ATI spectrum is known to be very sensitive to intensity variations. This has been investigated experimentally [Grasbon03]. The main feature is that the plateau appears only at intensities higher than a certain threshold. As the intensity increases, the spatial profile of the laser beam plays an important role (volume effect). The higher ionization yield occurring on the beam axis (high intensity) is compensated by the bigger volume of iso-intensity shells outside the center (low intensity). As a consequence, at high peak intensities plateaus of completely different extents are averaged, resulting in decreasingly pronounced variations of the slope of the ATI spectrum. On the other hand, at low peak intensity there are few contributions to the plateau signal, resulting in very prominent and distinguishable spectral characteristics.

Figure 5.11 shows ATI spectra in the two emission directions for different laser intensities. In all cases, the absolute phase is approximately zero (i.e. cosine-like pulses). Particularly interesting are the spectra corresponding to intensities below 5×10^{13} W/cm² [panel (a)]. In the left (red) direction there is essentially no plateau, whereas in the right (black) direction it is very pronounced. This confirms that the appearance of the plateau indeed occurs at a given threshold of the electric field strength, corresponding to a sudden increase of the rescattering electron cross-section. Note also that at low intensities a clear minimum in the ATI spectra is recognizable [label A in panel (b)]. This phenomenon is known as *ballistic interference* [Becker02] and is due to interference of electrons characterized by ionization times which differ by much less than an optical period (short and long trajectories, cf. Fig. 1.11 on page 22). Owing

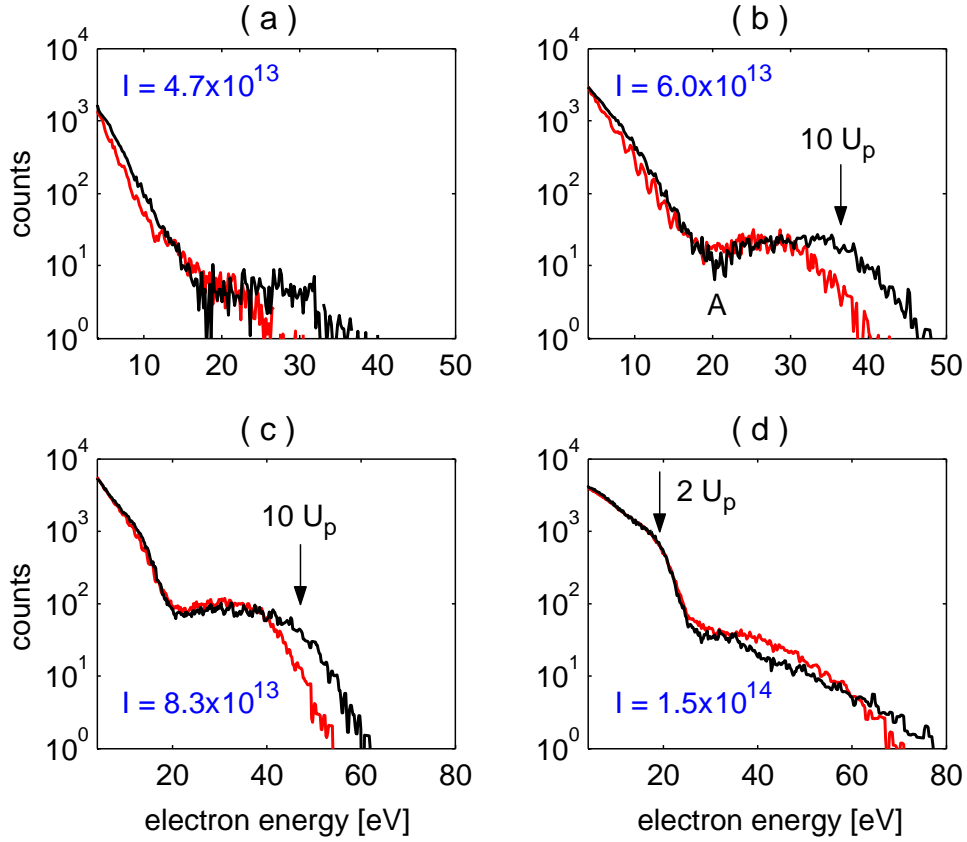


Figure 5.11: ATI spectra (semi-logarithmic scale) measured in the left (red lines) and right (black lines) direction for different laser intensities. Note the different energy scale in each panel. The pulse duration is approximately 5 fs FWHM, the absolute phase is $\phi = 0$ in all cases. The laser intensity is indicated in each panel (in W/cm²).

to the strong dependence of the positions of these minima on the laser intensity, the effect disappears at higher intensities, where averaging due to volume effects occurs. For the same reason, as already mentioned, the sharp cutoffs visible at intensities up to $9 \times 10^{13} \text{ W/cm}^2$ [panels (b) and (c)] disappear at higher intensities [panel (d)].

The end of the plateau is calculated to lie around $10 U_p$ (Sec. 1.5). If a sharp cutoff is visible [panels (b) and (c)], this gives a very reliable handle to calibrate the intensity. Estimations by conventional means give compatible results, but with considerably bigger uncertainties. At higher intensities, the degraded plateau structure makes individuation of the cutoff difficult. In this case, advantage can be taken from the low-energy part of the spectra, developing an increasingly clear kink at electron energies around $2 U_p$. This corresponds to the classical limit for electrons leaving the atom without rescattering (direct electrons, Sec. 1.5). The agreement of this cutoff is the better the higher the intensity [panel (d)]. This is not surprising because the oscillation amplitude of the electron is $q_e E_0 / m_e \omega^2$ (q_e is the electron's charge, E_0 the electric field peak strength, m_e the electron's mass, ω the laser's angular frequency), i.e. it gets bigger and thus more classical at high intensities⁵. Experiments in the microwave regime (small ω) confirmed this argument [Gallagher89].

The direct electrons' cutoff at $2 U_p$ is extremely useful also for absolute phase determination at high intensities. For few-cycle pulses, this low-energy cutoff depends on the phase and, in particular, should be asymmetric in the two emission directions. To connect the direct electrons' cutoff with a phase value, one has to remember that, without rescattering, the electrons conserve their canonical momentum (Sec. 1.3). As a consequence, the measured drift momentum is given by $-e \vec{A}(t_0)$, where e is the (positive) elementary charge and $\vec{A}(t_0)$ is the vector potential at the ionization time t_0 . Thus, asymmetric (symmetric) cutoffs will be observed for *cosine-like* (*sine-like*) vector potentials, i.e. for *sine-like* (*cosine-like*) electric fields⁶. This is the origin of the striking asymmetric area in the contour maps of Fig. 5.5. Figure 5.12 shows ATI spectra at high intensity and the corresponding phase deduced from the direct electrons' cutoff. The agreement with the usual phase assignment based on the rescattered electrons' cutoff (Chapter 3) is excellent.

⁵A more formal justification involves the evaluation of the Keldysh parameter γ (Sec. 1.2.1). At high intensities $\gamma < 1$ (Fig. 1.3 on page 10), and the tunneling model is thus applicable.

⁶The maximum drift energy of the direct electrons in, e.g., the *positive* (right) direction is expected for the most *negative* value of $\vec{A}(t_0)$, occurring for a vector potential of the form $\propto -a(t) \cos(\omega t)$, $a(t)$ being the temporal envelope. Since the electric field is given by $\vec{E}(t) = -\partial \vec{A}(t) / \partial t$, this corresponds to an electric-field waveform $\propto -a(t) \sin(\omega t)$, i.e. to an absolute phase $\phi = \pi/2$.

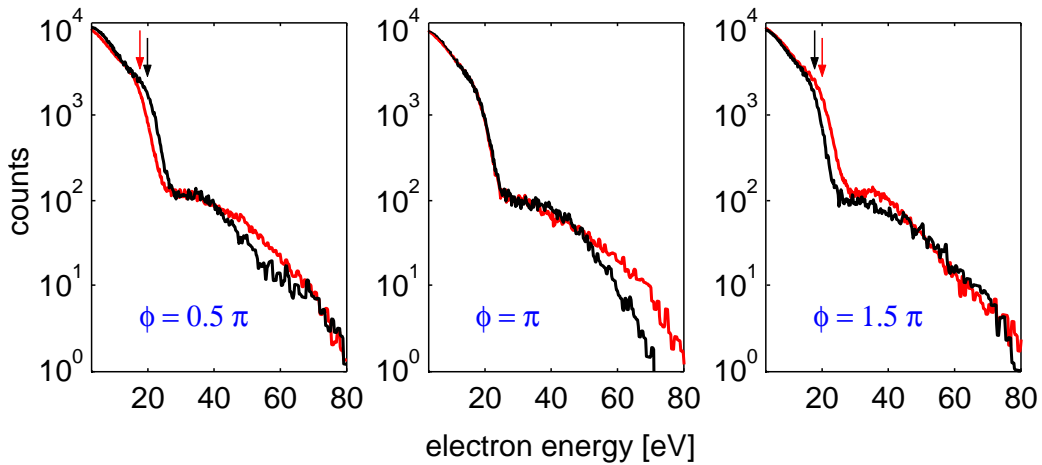


Figure 5.12: ATI spectra (semi-logarithmic scale) measured in the left (red lines) and right (black lines) direction at relatively high intensity ($1.5 \times 10^{14} \text{ W/cm}^2$). The clear cutoff difference of the direct electrons allows absolute phase determination. Note that, due to the relation between electric field and vector potential, pulses with absolute phases $\phi = 0$ and $\phi = \pi$ cannot be distinguished only by the direct electron cutoff. This ambiguity is easily removed just by observing also the high-energy part of the spectrum.

5.3 Pulse duration dependence

5.3.1 Ionization yield

Since all absolute phase effects originate from the fast variation of the envelope during the optical cycle, it is obvious that these effects should vanish quickly as the pulse duration increases. In order to investigate the dependence on the pulse duration of the left-right asymmetry, the simplest approach is to record several ATI spectra by adding a given amount of glass at each acquisition by means of the pair of wedges. In this way the amount of dispersion is precisely known and allows retrieving the pulse duration. A drawback of this procedure is that, since the peak intensity is inversely proportional to the pulse duration, it intrinsically couples the pulse duration dependence with the intensity dependence of photoionization.

While the amount of dispersion introduced is known without approximation, this is not the case for the duration of the *unchirped* pulse (i.e. before adding any glass). Standard autocorrelation techniques give only very approximate estimations for pulses well below 10 fs. Moreover, any usual pulse diagnostic takes place outside the experimental environment, resulting in additional uncertainty. Hence, also the *initial* pulse duration has to be estimated from the experiment.

Figure 5.13 shows the integrated (left+right) count rate in xenon as a function of the glass thickness introduced. The latter was changed in constant steps of $\sim 7 \mu\text{m}$. It is known that, below saturation, the ionization yield is proportional to I^N , where I is the laser intensity and N is the order of the process, i.e. the minimum number

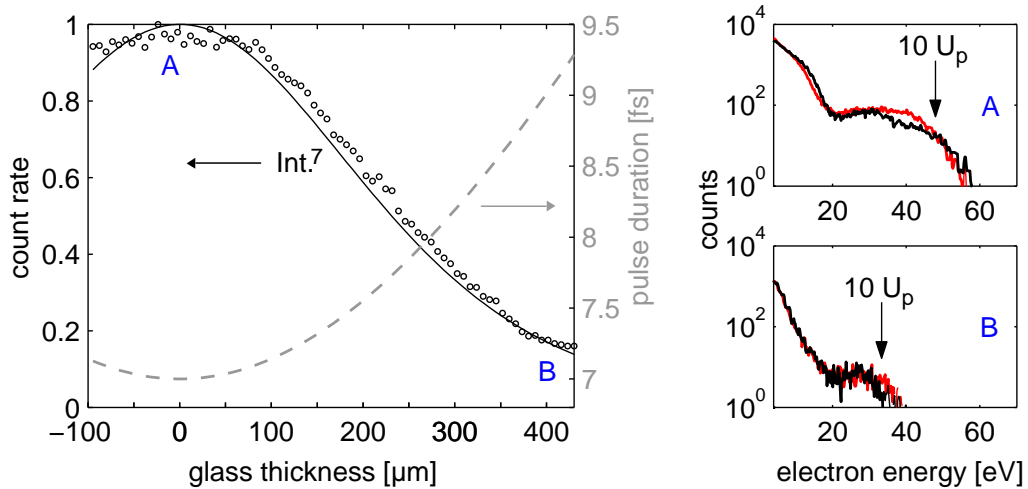


Figure 5.13: Integrated count rate (circles) as a function of the glass thickness introduced. Negative values mean that glass was removed from the configuration of optimum dispersion compensation. The 7th power of the intensity (solid line) well reproduces the experimental count rate if an unchirped pulse duration of 7 fs is assumed (dashed line). The two lateral panels show the ATI spectra measured for the shortest (A) and the longest (B) pulses.

of photons necessary to subdue the ionization potential (in this experiment, $N = 7$)⁷. The solid line represents the 7th power of the intensity, if an unchirped pulse duration of 7 fs is assumed. Therefore, the pulse duration ranges in very fine steps between 7 and more than 9 fs (dashed line). This pulse duration estimation can be cross-checked by inspecting the plateau of the ATI spectra corresponding to the shortest (A) and the longest (B) pulses. The intensity difference estimated by the cutoff position is in good agreement with the difference of pulse durations.

Figure 5.14 shows the asymmetry parameter defined in Sec. 5.2 as a function of the amount of glass introduced⁸. The clear maxima and minima are due to the continuously changing absolute phase. The period of the oscillations is constant and equal to $52 \mu\text{m}$, as already discussed in Chapter 3. The fact that no change of periodicity can be observed implies that, at least in the range of pulse durations investigated here, the maximum left-right asymmetry always occurs for the same absolute phase of the pulse. The amplitude of the oscillations, on the other hand, rapidly decreases as the pulses get longer. At a pulse duration of 9 fs, the residual modulation is below 1% and can not be distinguished from the experimental noise of the measurement. Note however that, by increasing the count rate and the integration time, smaller modulations should become clearly visible, possibly pushing the limit of detection of phase effects towards 10 fs.

⁷For xenon ($I_p = 12.13 \text{ eV}$) this corresponds to wavelengths below 710 nm, well covered by the very broad spectrum characterizing the pulse (Fig. 3.6).

⁸For technical reasons, the very low energy electrons ($< 3 \text{ eV}$) were discarded in these measurements. This weakly affects the value of the asymmetry, but not its pulse duration dependence, under investigation here.

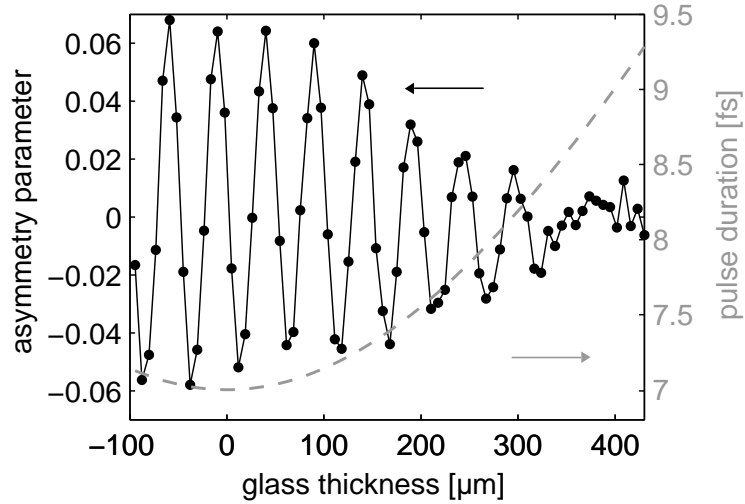


Figure 5.14: Asymmetry parameter $(L - R)/(L + R)$ (solid line) as a function of the glass thickness introduced. The integration time is 10 s per position (black circles), and the count rate is optimized for the shortest pulse. The pulse duration is also shown (dashed line). Beyond 9 fs FWHM, no phase effects can be detected.

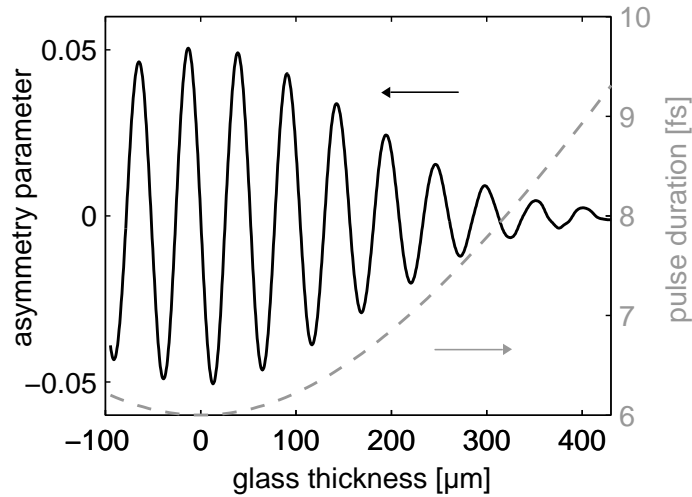


Figure 5.15: Calculated asymmetry parameter $(L - R)/(L + R)$ (solid line) as a function of the glass thickness ideally introduced. The short pulse (corresponding to 0 μm of glass) has a duration of 6 fs FWHM and an intensity of $7 \times 10^{13} \text{ W/cm}^2$, consistent with the observed ATI spectra (cf. Fig. 5.13). The calculation takes into account also the intrinsic change of intensity due to the different pulse durations (dashed line).

Finally, the semiclassical model can be used to verify the qualitative agreement of the observed trend. Figure 5.15 shows the calculated asymmetry parameter as a function of the amount of glass introduced. The unchirped pulse duration is here used as a fitting parameter to match experimental and theoretical data. This leads to a slightly different pulse duration estimate, namely of 6 fs FWHM. The theoretical calculation shows, in agreement with the experimental data, that the modulation amplitude for pulse durations > 9 fs is well below 1%. This comparison should not be taken too literally, since the classical model only gives rough estimates with respect to total ionization yields.

The dependence of the left-right ionization asymmetry on the pulse duration is currently subject of theoretical investigations based on numerical solutions of the time-dependent Schrödinger equation [Chelkowski02, Chelkowski04]. As in Sec. 5.2, the results presented here constitute the first and - up to now - only experimental evidence of the general behaviors predicted by the models⁹.

5.3.2 ATI spectra

Even more information is provided by analyzing the ATI spectra, in particular the high-energy part. Figure 5.16 shows the left/right asymmetry map as a function of electron energy and glass thickness introduced, for the same measurement of Figs. 5.13 and 5.14. As usually, reddish (bluish) colors indicate dominant left (right) emission. In agreement with Fig. 5.14, also in the ATI plateau the strongest contrast (here indicated by darker colors) is observed for the shortest pulses. Similarly, the extension of the plateau indicates the decreasing intensity as the pulse gets longer (cf. Fig. 5.13).

The most interesting feature is however the inclination of the characteristic stripes in the asymmetry map. Clearly, the slope decreases as the pulse duration increases (i.e. moving from the left to the right of the picture). This can be intuitively understood as follows. The periodicity of one absolute phase period is constant and equal to $52 \mu\text{m}$. On the other hand, the cutoff difference (in eV) in the two emission directions rapidly decreases if the pulses become longer, and eventually approaches zero for very long pulses. Hence, it is not surprising that the slope (expressed in $\text{eV}/\mu\text{m}$) of the characteristic stripes covering approximately one phase period is steeper in the case of short pulses. This is in full agreement with the predictions of the semiclassical model (Fig. 5.17). Note that, after suitable intensity calibration, this comparison should allow determination of the laser pulse duration much more precisely than conventional methods.

⁹In fact, it is worth noting that the remarkable acceleration of the experiments led to the rather uncommon situation of being far ahead of theory, although the latter has all the necessary tools at hand.

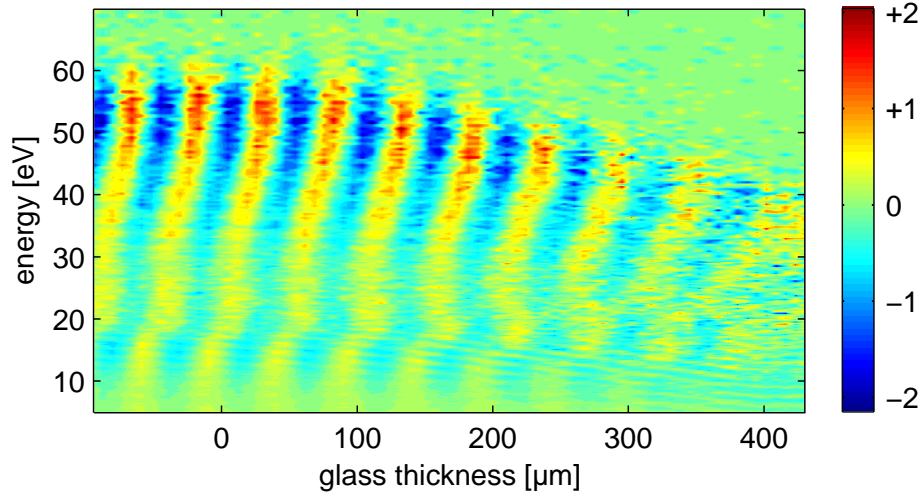


Figure 5.16: Left/right asymmetry (logarithmic scale) as a function of electron energy and amount of glass introduced in the beam path. Reddish (bluish) colors indicate dominant left (right) emission. Note the characteristic bending of the blue and red stripes as the pulse duration increases.

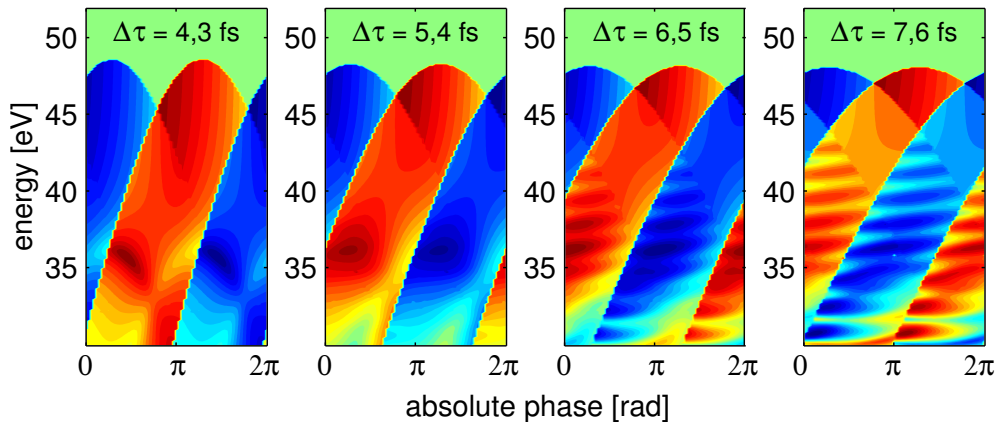


Figure 5.17: Calculated left/right asymmetry (logarithmic scale) as a function of electron energy and absolute phase for different pulse durations (indicated in each panel). Reddish (bluish) colors indicate dominant left (right) emission. Note the decreasing slope of the characteristic sharp edges as the pulses get longer. The peak structure appearing at some phases and pulse durations will be extensively discussed in the next chapter.

Chapter 6

Quantum mechanics in ATI with few-cycle pulses

While a semiclassical description can intuitively explain the principal features of above-threshold ionization, the physical origin of the observed spectra remains purely quantum-mechanical. Indeed, a deep understanding of the electron spectra often involves an interplay of classical arguments, quantum mechanics and atomic physics [Paulus94a, Salières01, Paulus98, Paulus00, Paulus01a]. However, due to the lack of phase control, so far experimental investigations were limited to the dependence on average properties of the light field. The complete control of the absolute phase allows studying electron interference patterns in much greater detail. This chapter will discuss extensively subtle characteristics of ATI spectra and connect them to the electric field's temporal shape. These features represent remarkably simple experimental evidence of fundamental quantum-mechanical principles, namely electron interference and Heisenberg's uncertainty principle.

After a brief introduction of electron interference in above-threshold ionization, experiments exhibiting prominent phase-dependent peak structures will be presented. The contrast of the ATI interference pattern can be enhanced and reduced by changing the absolute phase: This constitutes a striking time-domain analog of the Young's double-slit experiment with electrons [Lindner04c]. Most of the observed spectral features can be explained within the semiclassical description. This allows on the one hand to confirm the absolute phase assignment of Chapter 3, on the other hand to reconstruct the ionization process with unprecedented attosecond time resolution. Nonetheless, some spectral characteristics *cannot* be explained by classical arguments, providing evidence for classically forbidden electronic trajectories. With respect to this, it will also be shown how the extension of the ATI plateau can be in principle connected with the temporal structure of the electron wave-packet.

6.1 Electron interference in ATI

Electron diffraction has played a major role in the development of quantum mechanics, both for theory (De Broglie, 1923¹) and for experiments (Davisson, Germer and Thomson, 1927²). Evidence for the electron wave-particle duality is traditionally illustrated in the spatial domain, typically by observing the characteristic regular peaks obtained by scattering electrons on crystals. Completely analogous behavior, however, is to be expected both in spatial and in temporal domain. The greater importance of the former compared to the latter is only due to the fact that in the 1920s the spatial interference could be carried out more easily.

Above-threshold ionization constitutes the time-domain analog of the electron diffraction experiment of Davisson and Germer. This analogy is evident by considering the electron as a particle-wave characterized by the De Broglie's wavelength. The semiclassical model of ATI (Sec. 1.5) is in fact based on this duality. Following the analogy, the number of crystal planes producing interference corresponds to the number of laser cycles contributing to the ATI signal. Thus, it is obvious that the use of few-cycle pulses represents the equivalent of the double-slit experiment.

It is perhaps worth emphasizing the elegance and impact of the Young's double-slit experiment with electrons in physics³. After the pioneering works of Davisson, Germer and Thomson in 1927, it was clear what the outcome of the double-slit experiment *should* be. However, it remained a *Gedankenexperiment*. In 1961 Feynman stated in his lectures [Feynman91]: "We should say right away that you should not try to set up this experiment. This experiment has never been done in just this way. The trouble is that the apparatus would have to be made on an impossibly small scale to show the effects we are interested in. We are doing a *thought experiment*". Only years later electron interference from double-slit structures was reported [Jönsson61, Jönsson74, Merli76, Tonomura89]. So far, no analog experiment in time domain has been performed. By means of phase-stabilized few-cycle laser pulses, this is now possible.

In the limit of a long laser pulse, electrons of equal energy can be emitted at several instants separated by the laser period (Fig. 1.11 on page 22). When the pulse consists of merely a few optical cycles, the number of electron *sources* is dramatically reduced (Fig. 3.5 on page 44). If the pulse duration is well below 10 fs, depending on the shape of the electric field (and hence on the absolute phase) there may be one or at most two significant contributions. Therefore, adjusting the absolute phase is equivalent to *opening* and *closing* the slits. Furthermore, this manipulation on the sub-fs scale can be done separately for the two emission directions. In other words, one can open one

¹Pierre Louis-Victor Pierre Raymond de Broglie (1892-1987) was awarded with the Nobel Prize in physics in 1929 "for his discovery of the wave nature of electrons".

²Clinton Joseph Davisson (1881-1958) and George Paget Thomson (1892-1975) shared the Nobel Prize in physics in 1937 "for their experimental discovery of the diffraction of electrons by crystals".

³In September 2002 the readers of Physics World selected it as "the most beautiful experiment in physics".

slit to the left while closing another to the right and vice versa. In order to observe pronounced interference patterns, the amplitudes for the two contributions should be of the same order of magnitude. While this is straightforward in space-domain electron interference experiments, it represents an intriguing resource of control in the time domain. All these ideas will be further developed in Sec. 6.2.2.

Finally, this experiment is not only an elegant and pedagogical demonstration of probably the most fundamental principle of quantum mechanics. It also provides a new method of probing atomic processes on an unprecedented short time-scale, exactly in the same way as electrons are used to resolve spatial structures on sub-nm scales (e.g. electron microscopy). Table 6.1 and Fig. 6.1 summarize the analogy between electron interference in space and time domain.

	electron diffraction	above-threshold ionization
systematic periodicity	crystal planes' distance	laser period
measured quantity	directional distribution	time-of-flight distribution
wave-function dependence	$ \Psi(x)\rangle$	$ \Psi(t)\rangle$
number of contributions	double-slit	few-cycle pulse
resolution	sub-nm	sub-fs
uncertainty principle	$\Delta p \cdot \Delta x \sim \hbar$	$\Delta E \cdot \Delta t \sim \hbar$

Table 6.1: Analogy between electron diffraction and ATI.

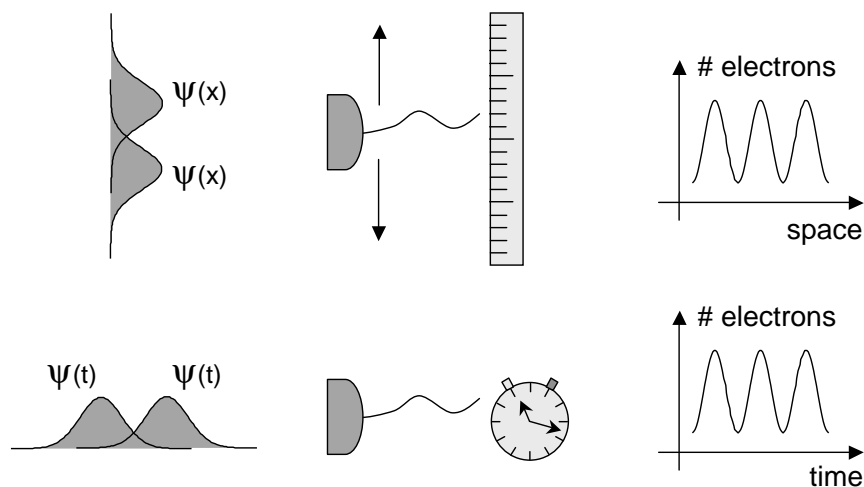


Figure 6.1: Electron interference from a double-slit is analog to above-threshold ionization with few-cycle laser pulses.

6.2 The double-slit experiment

6.2.1 Experimental evidence

Experimentally, virtually no ATI peaks are detected with few-cycle pulses without phase-stabilization [Grasbon03]. One might be tempted to attribute this to the shortness of the pulse, in the sense that photoemission from a single cycle dominates. This, however, is not true for all phases. Rather, it is the spatiotemporal intensity distribution of a laser focus (volume effect, Sec. 1.5.2) which tends to smear out ATI peak structures. In addition, a phenomenon similar to that observed for HHG, namely phase-dependent redshift and blueshift of peaks [Baltuška03, Nisoli03], might occur also in ATI. Thus, averaging of the electron spectra when the absolute phase has randomly changing values would considerably reduce the contrast of interference patterns.

When the absolute phase is stabilized, the situation is markedly different. Figure 6.2 shows the left/right asymmetry (logarithmic scale) as a function of electron energy and absolute phase. The intensity is approximately 10^{14} W/cm² and the atomic gas is argon. The spectral range between 10 and 25 eV is clearly characterized by phase-dependent peak structure. This can also be appreciated in Fig. 6.3, showing ATI spectra measured in the two emission directions for different absolute phases. Note how identical spectral features are observed in the two detectors by shifting the phase by π .

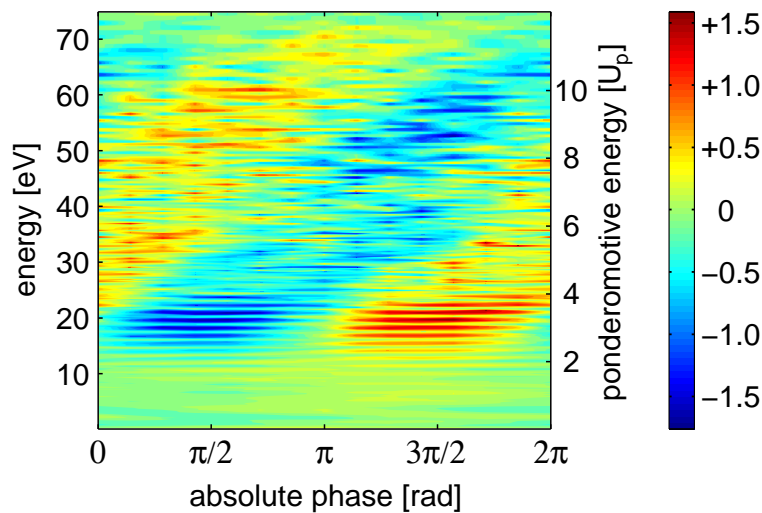


Figure 6.2: Left/right ratio (logarithmic scale) as a function of electron energy and absolute phase. Reddish (bluish) colors correspond to dominant left (right) emission. The phase can be easily calibrated by observing the characteristic asymmetric area after $2U_p$ (Sec. 5.2.2). The atomic gas is argon and the laser intensity approximately 10^{14} W/cm².

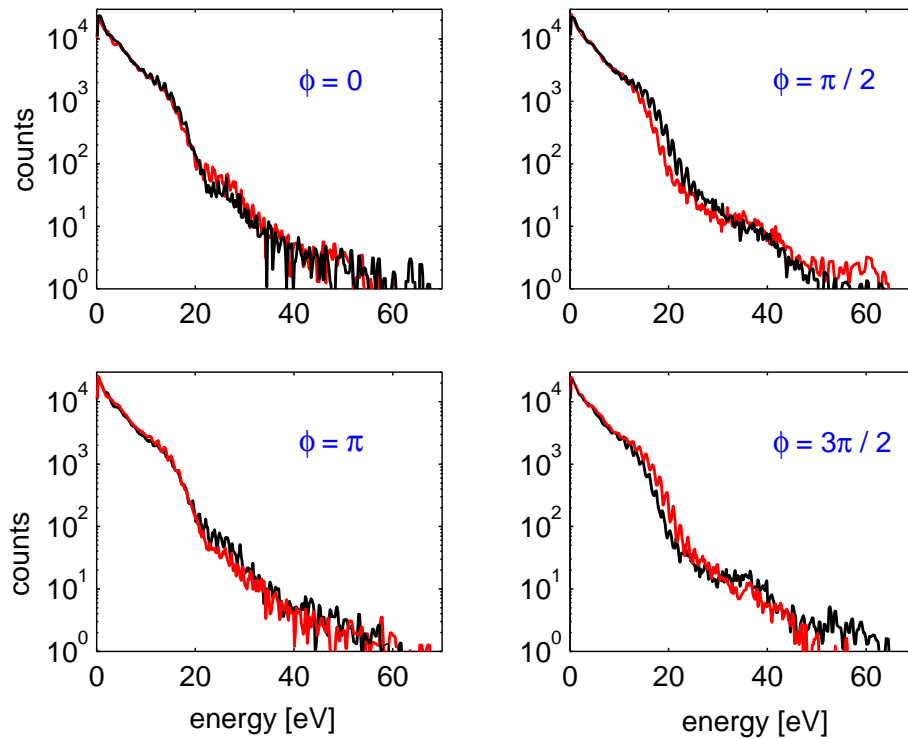


Figure 6.3: ATI spectra (semi-logarithmic scale) as a function of electron energy measured in the left (red line) and right (black line) direction for 4 different absolute phases. In the energy range between 10 and 25 eV, clear phase-dependent peak structure appears. The atomic gas is argon and the laser intensity approximately 10^{14} W/cm².

It is important to notice that the count rate in these experiments did not exceed 50 electrons per laser shot. Thus, the probability of emitting two electrons of identical energy in a single laser pulse is extremely low. Therefore, what is observed is not interference between *two* electrons. Rather, it is *one* electron that has two indistinguishable options of how to reach a given final state. This deep quantum-mechanical hypothesis will be always assumed in the following, even when referring to two ionization events or *contributions* in the laser pulse.

In order to quantify the characteristics of the interference patterns, three different properties of the peaks should be analyzed: spacing, contrast and absolute position. All these can be highlighted with a suitable normalization procedure⁴ consisting in

⁴Technically, the procedure works as follows: (i) acquisition of an ATI spectrum corresponding to randomly varying phases (this can be done either by switching off the stabilization servo loop or by averaging over spectra corresponding to equally spaced phases covering 2π . In particular when the laser system is running stable, the second option is often preferred by lasers' operators); (ii) fit of the obtained *random-phase* ATI spectrum with a suitable function (typically a combination of exponentials); (iii) division of all *phase-stabilized* ATI spectra by the *random-phase* fit function. An essential point is that the fit function be strictly monotonic. If this were not the case, the normalization would artificially produce irregularities and peaks. To improve the numerical stability of the fit function, the procedure is applied only in the spectral range where ATI peaks are observed.

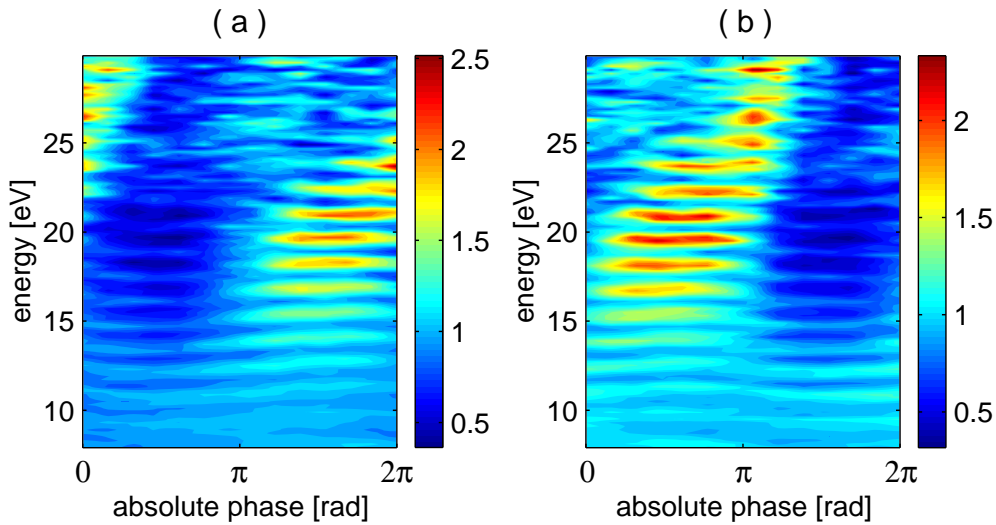


Figure 6.4: Electron count rate in the left (a) and right (b) direction as a function of energy and absolute phase after normalization, as described in footnote 4. The energy range chosen is from 8 to 30 eV, where most peaks appear. In both detectors the characteristic stripes are curved, indicating phase-dependent peak shifting. The atomic gas is argon and the laser intensity approximately 10^{14} W/cm².

removing the characteristic exponential decay of the ATI spectra, so that the visibility⁵ of the fringes is greatly enhanced. Figures 6.4 and 6.5 show the ATI spectra as a function of electron energy and phase obtained from Fig. 6.2 after normalization. Note that this method treats the spectra measured in the left and right direction in a completely independent way. Indeed, besides an obvious phase shift of π , the two detectors should give identical results. This redundancy of information is extremely useful since it offers an immediate cross-check against any experimental uncertainty.

Different features can be observed. Not surprisingly, the peak spacing is approximately 1.5 eV, equal to the photon energy at the carrier wavelength (Sec. 1.5.1). At increasing electron energies, the pattern is considerably more irregular. Though this could be explained simply by the lower count rate and the corresponding poor signal-to-noise ratio, real effects causing a peak splitting may also play a role (Sec. 6.3). The peak contrast clearly depends on the phase: The fringe visibility reaches remarkable values of approximately 50% at electron energies around 15-20 eV. In addition, also the peak position depends on the phase. This is clear from Fig. 6.5, where for sine-like pulses ($\phi = \pi/2$ and $\phi = 3\pi/2$) the maxima in one detector coincide with the minima in the other. This phase-dependent peak shifting immediately explains why no peaks are observed while averaging over randomly changing phases.

⁵The visibility of a fringe pattern is defined as $V = (I_{max} - I_{min}) / (I_{max} + I_{min})$.

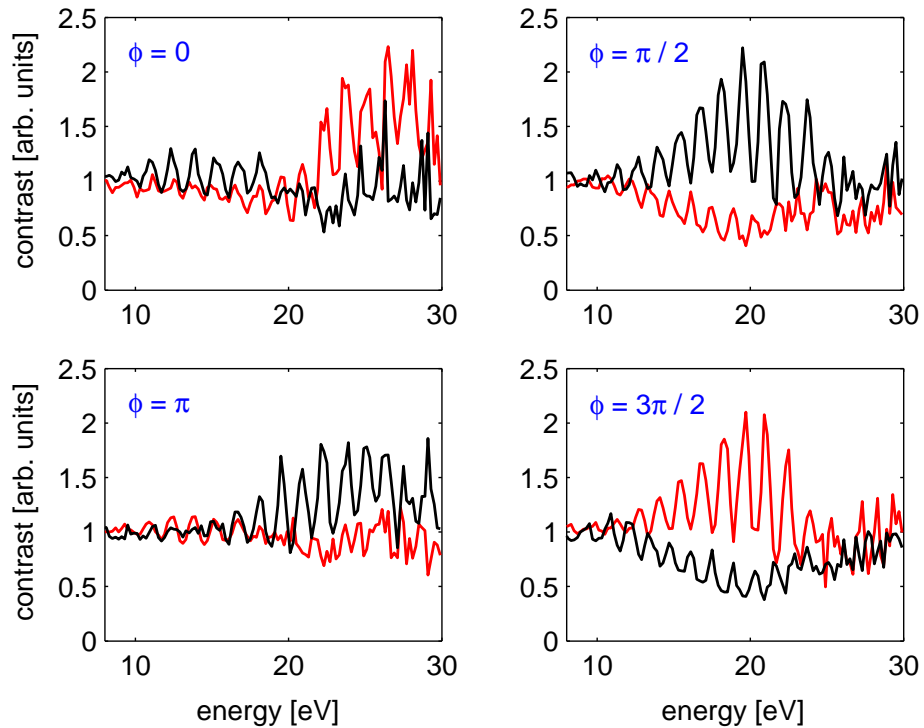


Figure 6.5: ATI spectra (linear scale) as a function of electron energy measured in the left (red line) and right (black line) direction for 4 different absolute phases after normalization. The fringe visibility reaches 50% at electron energies around 20 eV. Note also the phase-dependent shift of peaks, particularly evident for sine-like pulses. The atomic gas is argon and the laser intensity approximately 10^{14} W/cm².

6.2.2 Semiclassical description

The first remarkable feature observed in the experimental results of last section is that the most prominent peaks appear in a well-defined spectral range, namely between 10 and 30 eV. In units of the ponderomotive potential (here $U_p \sim 6$ eV) this corresponds to energies above the classical limit ($2U_p$) of direct electrons (Sec. 1.5). Thus, the observed interference pattern must be explained in terms of rescattered electrons.

Peaks in the spectra should be expected if electrons of a given energy can be created at two or more instants in the laser pulse. The complete lack of ATI peaks below 10 eV may thus seem counterintuitive, as very low energetic electrons can originate also from low field strengths, and hence from several optical cycles. However, for the same reason the effect of intensity averaging is particularly severe, since annular regions far from the beam axis can contribute. Thus, the broadening of the peaks induced by the ponderomotive shift (Sec. 1.5.2) is large enough to wash out any modulation in the initial part of the spectrum⁶. The opposite argument applies for the area of the spectrum close to the ATI cutoff. The broadening of the peaks there is negligible, since high-energy electrons can be generated only in the vicinity of the beam axis. However, for few-cycle pulses only the strongest optical cycle can lead to emission of very high energetic photoelectrons. Therefore, no interference is semiclassically expected in the vicinity of the cutoff. It is thus not surprising that ATI peaks are observed in the intermediate energy range, where a compromise between number of contributions and intensity averaging occurs.

The trajectories of rescattered electrons can be calculated with the semiclassical model developed in Chapter 1. The *number* of contributions at a given energy E_0 is given by the number of solutions of the equation $E_{drift} = E_0$, whereas the *amplitude* of each contribution is given by the ionization probability at the corresponding initial time t_0 . Due to the high nonlinearity of the tunneling probability, the two conditions of equal drift energy and equal amplitude are very hard to meet in few-cycle pulses. Finally, the *phase* of each contribution is given by the integral of the action along the electron trajectory [Eq. (1.17) on page 21].

Figure 6.6(a) shows the calculated drift energy of rescattered electrons as a function of time for absolute phase $\phi = 0.8$ rad and a pulse duration of 6 fs. The number of contributions at the energy E_0 can be easily visualized graphically. For instance, at $E_0 = 3U_p$ (dashed lines) there are 3 laser cycles contributing for each emission direction⁷. However, due to the corresponding ionization probability (indicated by the green shaded area), only some of these contribute significantly. In particular, two electron wave-packets of comparable amplitude are emitted in the positive (right)

⁶In addition, direct electrons are more strongly affected by the Coulomb potential of the ion. As a consequence, the relative phases of the different contributions may be also influenced in a non-systematic way.

⁷Note that each contribution actually consists of two contributions, characterized by different traveling times (Sec. 1.5). Typically, one of these strongly dominates due to the difference in tunneling probability.

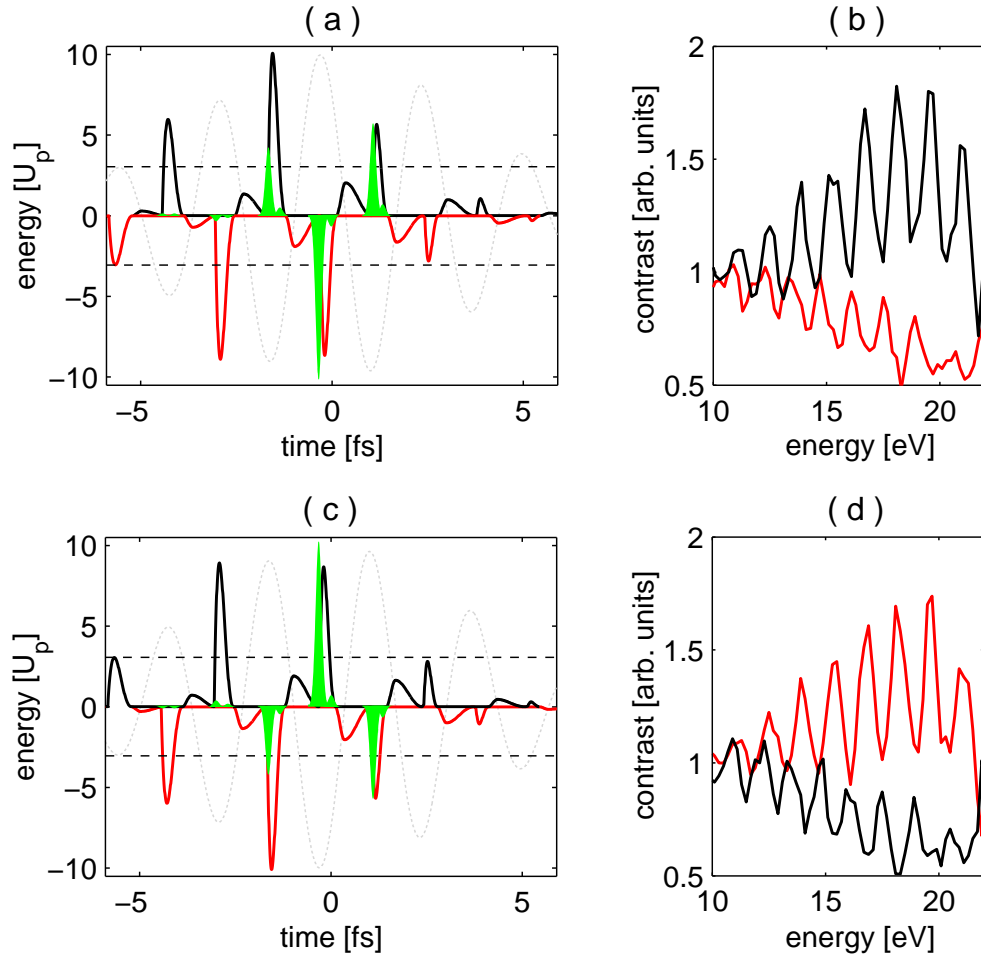


Figure 6.6: Double-slit experiment with electrons in the time domain. (a) Depending on the shape of the electric field (gray dotted line), there may be different possibilities of generating electrons with a given (dashed line) drift energy in the left (red line) and right (black line) emission direction. When two wave-packets (green shaded areas) of comparable amplitude interfere, a strong modulation in the energy spectrum (b) is observed. The time separation between each contribution determines the periodicity of the modulation observed in the spectra. By changing the absolute phase by π , one *slit* previously *opened* in the right direction is *closed*, whereas a second *slit* in the left direction is *opened*. Hence, the situation is exactly reversed for left and right [(c-d)].

direction, whereas only one is emitted in the negative (left) direction. Correspondingly, the observed peak contrast at $\phi = 0.8$ rad is considerably larger in the right direction compared to that in the left direction [Fig. 6.6(b)]. The situation is completely reversed by changing the absolute phase by π [Fig. 6.6(c-d)].

The agreement of these lines of arguments with the experimental data confirms the absolute phase assignment made by inspecting the ATI asymmetries in the two opposite emission direction (Chapter 3). Much more intriguingly, these experiments constitute the first double-slit experiment with electrons in the time domain. The ability of changing the absolute phase is equivalent to a manipulation of the *slits-structure* with unprecedented sub-fs precision. By proper choice of the absolute phase, the electron's quantum paths can be at will enhanced or suppressed, and this is immediately visible in the measured quantum interference: When only one channel is available, essentially no interference is observed.

Figures 6.6(a,c) can also explain the origin of the shift of the ATI peaks. Indeed, the electron wave-packets are emitted at field strengths significantly different, due to the rapid variation of the pulse envelope. Hence, they experience a different ponderomotive shift of the ionization potential. For instance, in Fig. 6.6(a), where the peak intensity is $U_p = 6$ eV, the contribution in the left direction is emitted at an instantaneous intensity corresponding to $U_p = 5.9$ eV, whereas the two contributions in the right direction at instantaneous intensities corresponding to $U_p = 4.8$ eV and $U_p = 5.3$ eV respectively. These differences are comparable to the peak spacing (1.55 eV at a wavelength of 800 nm) and explain the observed shift of the fringe pattern⁸. This is therefore a phenomenon strictly connected with the rapid variation of the pulse envelope, and hence limited to few-cycle pulses.

Finally, a complete description in the frame of the semiclassical model is given in Fig. 6.7, showing the calculated ATI spectra in the left (a) and right (b) direction as a function of electron energy and absolute phase. The spectra are restricted to the energy range where the peaks of highest visibility are observed (Fig. 6.4), namely between 18 and 30 eV. The phase dependence of the ATI peaks appears very clearly: on the left detector peaks are expected for absolute phases between π and 2π , while on the right detector they are expected for phases between 0 and π ⁹. This is in very good agreement with the experimental results of Fig. 6.4, confirming once more the validity of the semiclassical description of ATI.

In general, however, the comparison between Fig. 6.7 and the experimental results should not be taken too literally. Indeed, the details of the peak structure depend on

⁸More formally, the position of a maximum of the spectrum depends on the relative phases of the two contributing electronic trajectories. Since the phase is given by the integral of the action, and the latter clearly depends on the electric field's shape, it is not surprising that the position of the ATI peaks changes with the absolute phase.

⁹The local maximum occurring at energies between 18 eV and 26 eV for phases between 0 and π (π and 2π) on the left (right) detector is due to ballistic interference between short and long electron trajectories (Chapter 1). As this effect is very sensitive on intensity averaging and volume effects, it can be observed only under particular circumstances (Sec. 5.2.2).

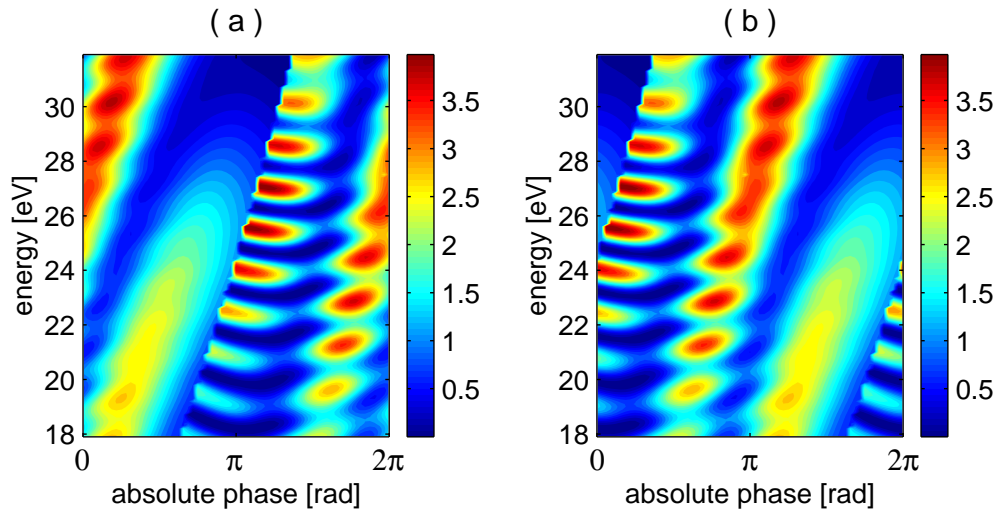


Figure 6.7: Calculated ATI spectra as a function of electron energy and absolute phase for the left (a) and right (b) detector. The general phase dependence of the ATI peaks is in very good agreement with the experimental results (Fig. 6.4).

the pulse duration and peak intensity assumed. In addition, intensity averaging effects intrinsic in the experimental results are here not taken into account. Nevertheless, the qualitative agreement supports the physical description given so far. The next section will show some features which *cannot* be explained within the semiclassical model. These issues are currently under experimental and theoretical investigation and might lead to a deeper comprehension of ionization processes in the near future.

6.3 Beyond the classical model: classically forbidden trajectories

In order to analyze the spectral contents of the observed electron interference in detail, a Fourier analysis can be performed on the ATI spectra obtained after the normalization procedure described in footnote 4. Fig. 6.8 shows the Fourier components (already translated in ATI peak spacing) of the spectra in Fig. 6.4 as a function of the absolute phase for the left (a) and right (b) detector. Not surprisingly, the main peak occurs at the photon energy (~ 1.5 eV) at phases between 0 and π (π and 2π) on the right (left) detector, consistent with classical expectations (Fig. 6.7). On the other hand, non-negligible components at the same frequency also appear (dashed lines) at phases where only a single classical trajectory contributes. The corresponding modulation is also clearly visible directly in the spectra [Fig. 6.6(b), red line; Fig. 6.6(d), black line]. In principle, this unexpected electron interference could be an indication that the laser pulse actually consists of more optical cycles than those represented in Fig. 6.6 (6 fs). However, the pronounced left-right asymmetry (Figs. 6.2 and 6.3) points to a relatively

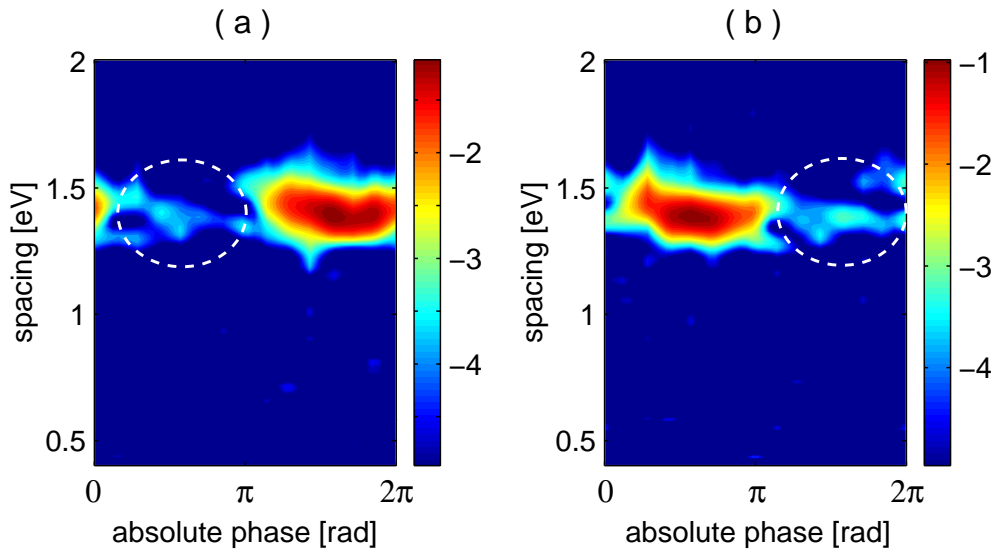


Figure 6.8: Fourier components (logarithmic scale) of the ATI spectra in argon of Fig. 6.4 for the left (a) and right (b) detector. The main component corresponds to the photon energy at the carrier wavelength (~ 1.5 eV). The dashed white lines indicate the presence of semiclassically unexpected electron interference.

short pulse length estimation. Apparently, electron interference is therefore due to the appearance of *classically forbidden* electron trajectories characterized by a time delay corresponding to a laser cycle.

More striking evidence of purely quantum effects appears in the measurements already presented in Fig. 3.10 on page 50. The atomic gas is xenon and the laser intensity ($\sim 8 \times 10^{13}$ W/cm²) slightly lower with respect to that used in the measurements in argon of Fig. 6.4. As usual, the peak structure can be highlighted by normalization in order to remove the exponential decay. The corresponding spectra are shown in Figs. 6.9 and 6.10. Note that, as in Fig. 6.4, the peak structure appears at energies above the classical limit ($2U_p$) of direct electrons.

Figure 6.11 shows the Fourier components of the spectra in Fig. 6.9 as a function of the absolute phase for the two emission directions. The main peaks occur at the same position as on Fig. 6.8, confirming that the semiclassical arguments apply also here. The peaks are, however, considerably broader in the frequency domain. This is an indication of shorter pulse duration¹⁰, for which the photon energy and, in particular, the time delay between the contributing electron wave-packets is less precisely defined. More interestingly, a clear phase dependent Fourier component (dashed white lines) appears at a spacing of 0.7 eV. This is by no means expected from the semiclassical model. By observing the spectra in Fig. 6.10, the origin of this high-frequency component can be found in an intrinsic mechanism of ATI peak-splitting, which for some

¹⁰The shorter pulse duration of this measurement is confirmed by the very pronounced left-right asymmetry observed both in the plateau and in the total electron yield (Sec. 3.4).

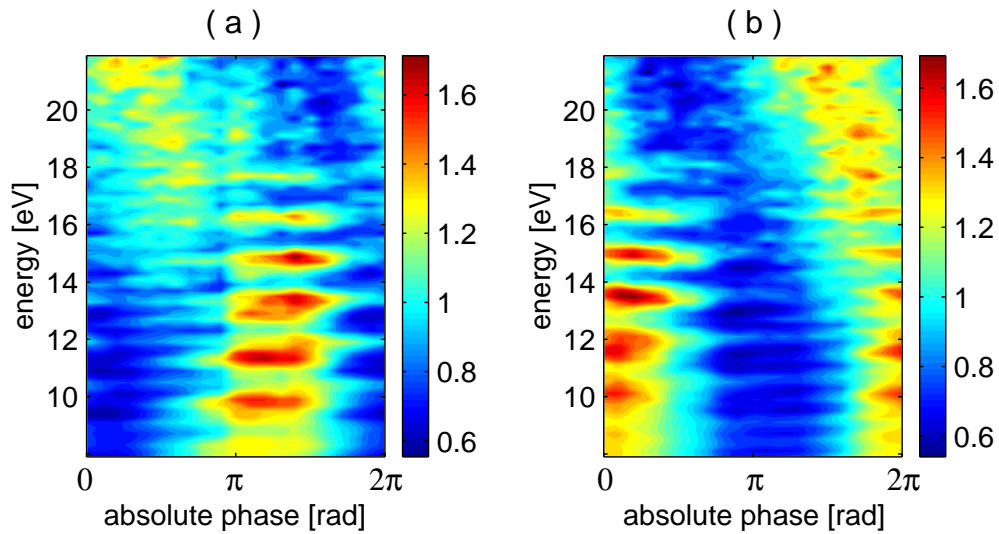


Figure 6.9: Contour maps of the ATI spectra of Fig. 3.10 after normalization as a function of electron energy and absolute phase for the left (a) and right (b) detector. The energy range chosen is from 8 to 22 eV, where most peaks appear. The atomic gas is xenon and the laser intensity approximately $8 \times 10^{13} \text{ W/cm}^2$.

phases leads to spectra strongly modulated at half the photon energy (e.g. $\phi = 0.4\pi$ in the left direction). Note that the characteristic behavior is well reproduced in both detectors. This completely new phenomenon is currently under investigation.

Quantum-mechanically, electron interferences are also expected in the ATI plateau, i.e. at very high energies. This is illustrated in Fig. 6.12, showing the calculated ATI spectra¹¹ for a pulse duration of 5 fs and a peak intensity of $6 \times 10^{13} \text{ W/cm}^2$. These interferences strongly depend on the absolute phase and appear even at energies exceeding the classical cutoff of $10 U_p$ of rescattered electrons. Clearly, this effect is completely beyond the classical model.

Experimental observations of peaks in the very high-energy part of the ATI spectra is however extremely difficult for two main reasons. First, the count rate, and hence the signal-to-noise ratio, is typically low in that range. Second, the energy resolution decreases significantly (Fig. 3.8 on page 48), and detection of modulations at high frequencies becomes more and more difficult. In order to emphasize the possible presence of peaks in the cutoff, a normalization procedure similar to that described in footnote 4 on page 95 must be followed. Here, each ATI spectrum is divided by its exponential fit¹². By using this method in the exponentially decreasing part (cutoff) of the spectra of Fig. 3.10, one obtains a seemingly erratic pattern for both detectors [Fig. 6.13(a,b)]. While at first sight no evident modulation appears, a Fourier analy-

¹¹These calculations, performed in the frame of the strong-field approximation, are kindly provided by Dejan Milošević.

¹²The difference with respect to the procedure of footnote 4 is therefore that each spectrum is here divided by a *different* fitting function. This accentuates any modulation occurring in the spectra.

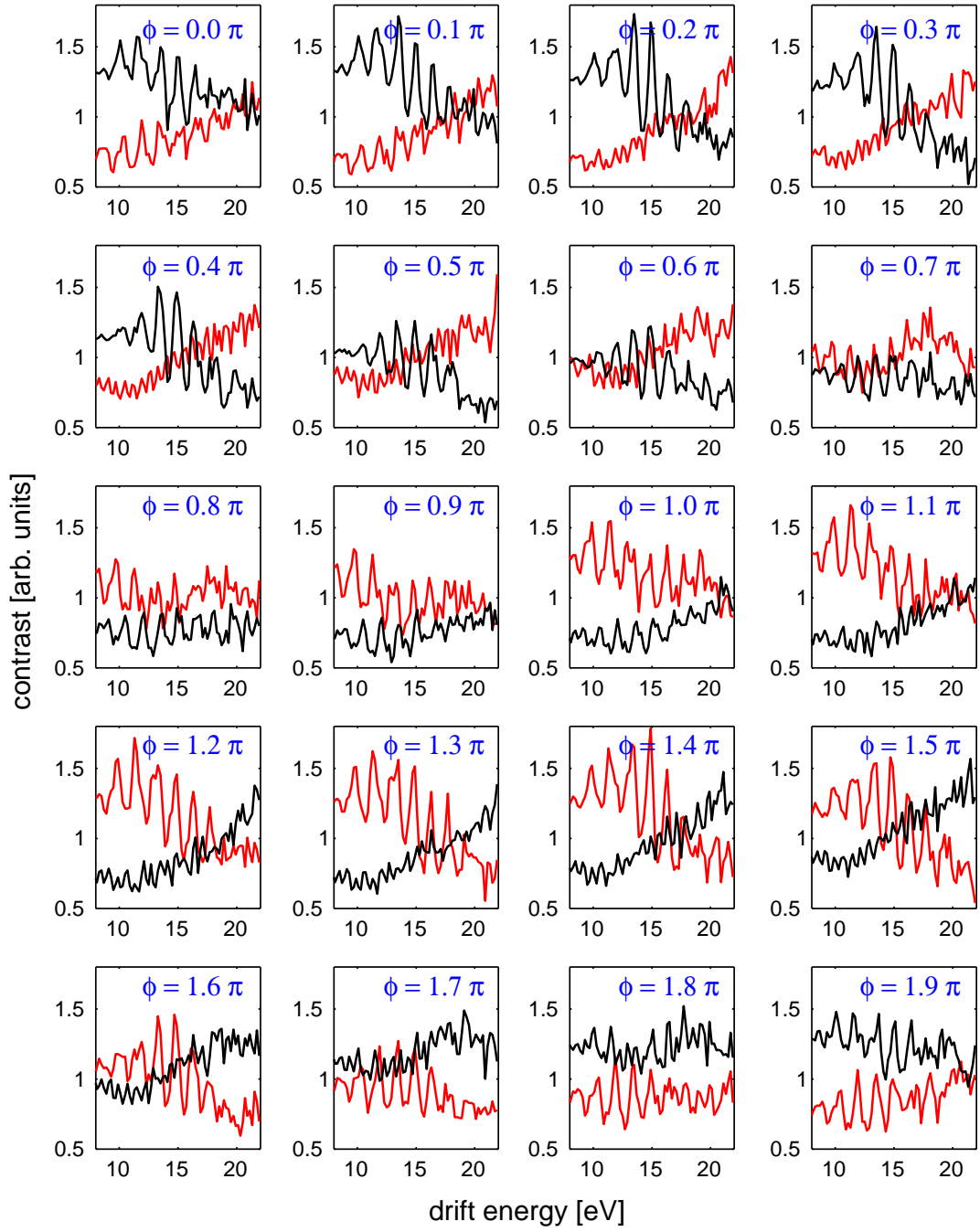


Figure 6.10: ATI spectra (linear scale) measured in the left (red line) and right (black line) direction after normalization for several absolute phases (blue labels). The atomic gas is xenon and the laser intensity approximately $8 \times 10^{13} \text{ W/cm}^2$.

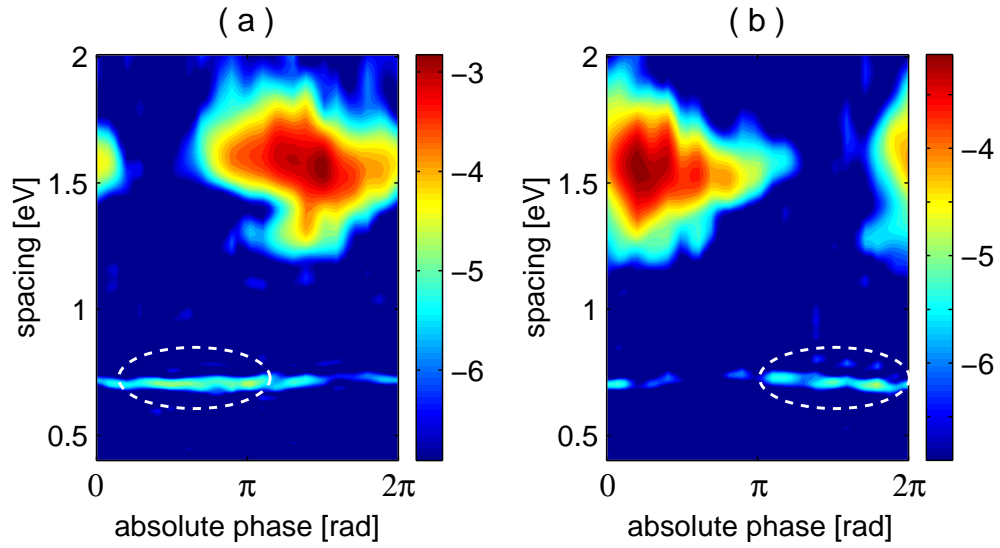


Figure 6.11: Fourier components (logarithmic scale) of the ATI spectra in xenon of Fig. 6.9 for the left (a) and right (b) detector. As in Fig. 6.8, the main component corresponds to the photon energy at the carrier wavelength (~ 1.5 eV). The dashed white lines indicate the presence of semiclassically unexpected electron interference.

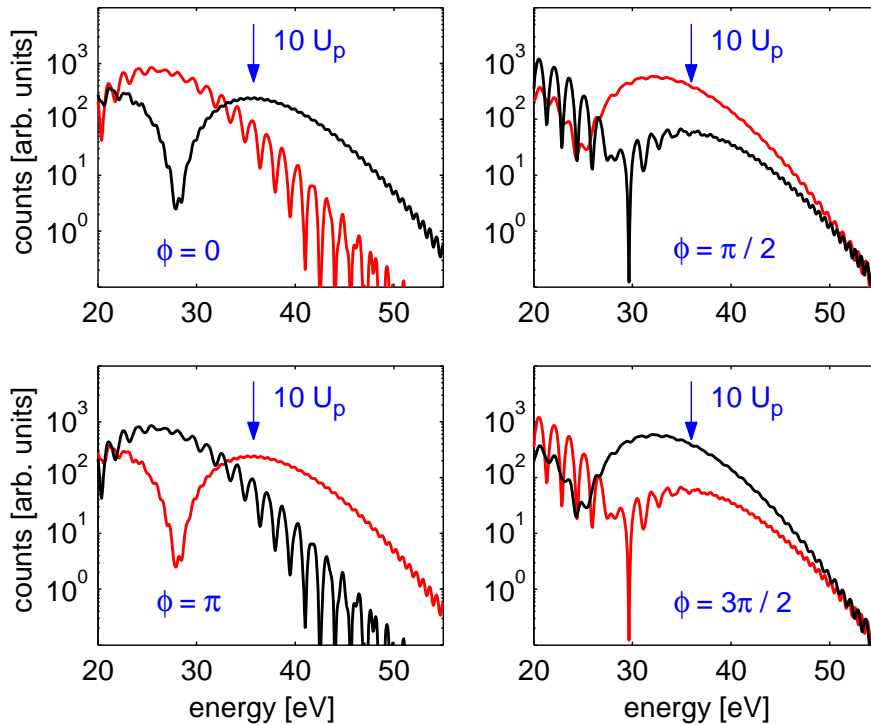


Figure 6.12: Calculated ATI spectra (semi-logarithmic scale) as a function of electron energy in the left (red line) and right (black line) direction for 4 different absolute phases. Note the phase-dependent peak structure appearing after the classical cutoff at $10 U_p$.

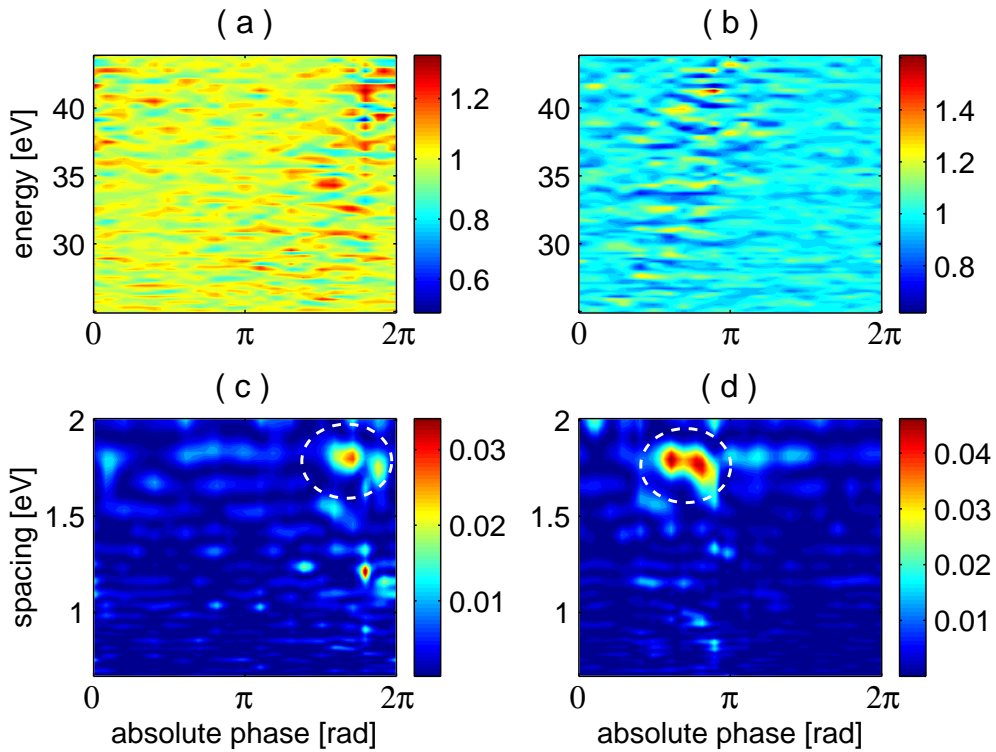


Figure 6.13: (a,b) ATI spectra in the left (a) and right (b) direction after normalization as a function of electron energy and absolute phase. The energy range is limited to the high-energy part of the spectra. The atomic gas is xenon and the laser intensity approximately $8 \times 10^{13} \text{ W/cm}^2$. (c,d) Corresponding Fourier components (linear scale) for the left (c) and right (d) direction. The dashed white lines indicate the presence of semiclassically unexpected electron interference.

sis [Fig. 6.13(c,d)] individuates components at a spacing corresponding to the photon energy (dashed lines). Despite the presence of some Fourier components originating from noise, the meaningful modulation is well above them and, what is particularly convincing, appears shifted by π on the two detectors. Furthermore, they occur in proximity of the phases where peaks are indeed theoretically expected (Fig. 6.12). Future experiments with increased count rate and higher resolution will investigate these promising features in detail.

6.4 Heisenberg's uncertainty principle

The whole semiclassical approach is based on the assumption that the electron is generated at a well-defined instant t_0 with a well-defined velocity $v_0 = 0$. Clearly, this assumption violates Heisenberg's principle, according to which the uncertainty in energy and time of a particle are connected by $\Delta E \cdot \Delta t \sim \hbar$. Thus, the energy of a particle at a given instant cannot be known with arbitrary precision.

Both v_0 and t_0 are classically connected with the drift velocity of the electron v_{drift} :

$$v_{drift} = v_0 + F(v_0, t_0) \quad (6.1)$$

where $F(v_0, t_0)$ includes the integral of the electric field from the time t_0 towards infinity and may incorporate rescattering of the electron on the ion core at a time $t_1(v_0, t_0)$. Equation (6.1) shows that any uncertainty in v_0 and t_0 will result in a corresponding uncertainty in v_{drift} . Furthermore, the classical relation (6.1) can be rewritten with appropriate quantum-mechanical operators in order to establish an analytical relation between ΔE_{drift} , ΔE_0 and Δt_0 , the last two being connected by Heisenberg's principle. Thus, measuring the uncertainty ΔE_{drift} should allow reconstructing the initial time structure of the electron wave-packet.

In general, it is not possible to measure ΔE_{drift} , since at intermediate energies the ATI spectrum is the result of different contributions, each characterized by its specific indetermination in initial time and energy. In the cutoff region, on the other hand, it is reasonable to assume that the signal mainly originates from the *only* contribution classically allowed. The latter can be (classically) localized in time with arbitrary precision, and the corresponding measured ΔE_{drift} quantifies the temporal spreading of the initial wave-packet (or, what is the same, the initial spreading in energy)¹³.

Figure 6.14(a) shows ATI spectra measured in the two opposite directions for absolute phase $\phi = 0$. For both directions, the corresponding classical limit is indicated by an arrow, and all electrons appearing at classically forbidden energies represent a direct measure of the uncertainty ΔE_{drift} of the single classical trajectory yielding the highest energy¹⁴. Since the ionization time t_0 corresponding to the cutoff is classically known [Fig. 6.14(b)], the measured slope of the cutoff (ΔE_{drift}) allows, in principle, retrieving information about the time uncertainty Δt_0 on a sub-fs scale¹⁵.

¹³Note that this argument only applies for few-cycle laser pulses, where the cutoff corresponds to a *single* classical trajectory.

¹⁴This requires the assumption that electron trajectories *classically* yielding energies smaller than the cutoff do not contribute beyond it.

¹⁵At high intensity the cutoff gets flatter and eventually degrades (cf. Fig. 5.11 on page 84). This may be explained not only by intensity averaging and volume effects (Sec. 5.2.2), but also by an intrinsic, physically acceptable dependence of the temporal width of the initial wave-packet on the intensity.

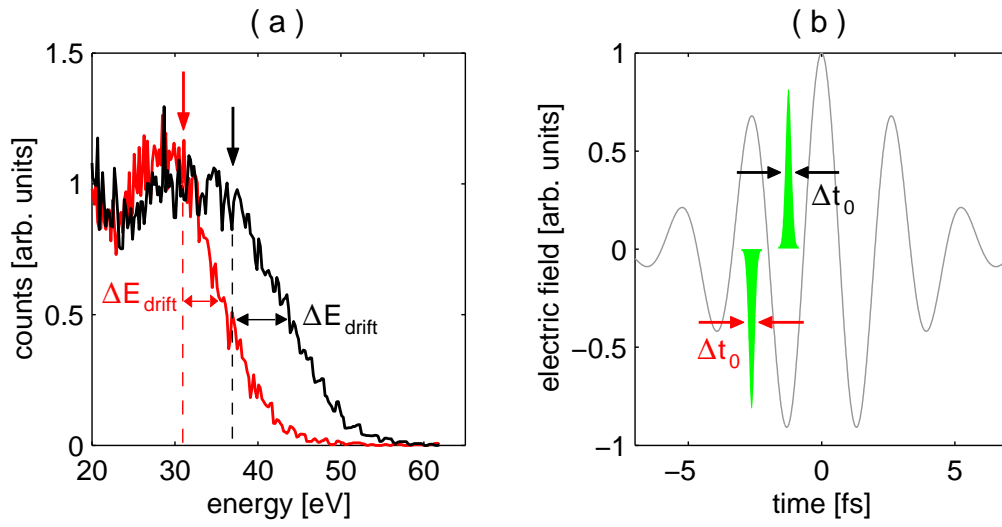


Figure 6.14: (a) High-energy part of the ATI spectra (linear scale) in the left (red line) and right (black line) direction for absolute phase $\phi = 0$. Note the typical exponential decay after the classical cutoffs (arrows). (b) Classically, the electron wave-packet corresponding to the cutoff is born at a well-defined instant t_0 . Measuring ΔE_{drift} allows, in principle, retrieving information about the time uncertainty Δt_0 .

Conclusion

The major part of this work was dedicated to the investigation of absolute phase effects occurring in nonlinear photoionization driven by few-cycle laser pulses. The significant progress of laser technology in the last two years made possible generation of laser pulse trains with identical absolute phases. The essential problem of determining the common electric-field waveform was here ultimately solved [Paulus03, Lindner04b] by means of the detected asymmetry of photoelectron emission in two opposing directions (stereo-ATI scheme). This remarkable result opened the way to a number of experimental studies characterized by phase control, formerly not possible. One of the most elegant applications is certainly the full spatial determination of the Gouy phase anomaly in the laser focus [Lindner04a]. Although this effect has been known for more than 100 years, no direct (i.e. non-interferometric) observation has ever been reported in the optical domain. This has been achieved in this work for the case of few-cycle laser pulses, which makes the Gouy effect even more intriguing due to its deep implications with superluminal light propagation phenomena.

The availability of the stereo-ATI phase meter also allowed significant technical improvements in what concerns phase-stabilization issues. Monitoring in real time the phase value made possible implementation of a new feedback loop which guaranteed essentially unlimited long-term phase stability. On the one hand, this permitted performing experiments hitherto not feasible [Liu04]; on the other hand, this result represents a milestone for the use of ATI as an essential laser diagnostic tool. Indeed, slightly modified stereo-ATI setups should soon allow extremely fast (in principle, single-shot) absolute phase measurements, of crucial importance, e.g., for generating and using attosecond light pulses.

The interest of above-threshold ionization with phase-stabilized few-cycle laser pulses is however certainly not limited to absolute phase measurements. Indeed, the complete control of the electric field constituting the laser pulse allows studying the laser-matter interaction with much higher precision than possible in earlier times. The most beautiful example is probably represented by the realization of the double-slit experiment with electrons in time domain [Lindner04c], where the possibility of manipulating the interference patterns in the ATI spectra provided exciting evidence of the electron's wave-particle duality in a simple, pedagogically clear context. These last experiments should also be regarded as a benchmark for the upcoming field of attosecond physics. By controlling the electric field waveform it is possible to deform

molecular potentials in a virtually arbitrary way. This could help to induce or analyze exotic chemical reactions. Furthermore, the electrons driven back to the ion core by the laser pulse might be used for performing electron-ion scattering experiments and for probing with unprecedented temporal and spatial resolution atomic and molecular potentials.

List of publications

- F. Lindner, M. G. Schätzel, H. Walther, A. Baltuška, E. Goulielmakis, M. Lezius, F. Krausz, D. B. Milošević, W. Becker and G. G. Paulus, *Double-slit experiment in time domain and attosecond interferometry*, in preparation.
- M. G. Schätzel, F. Lindner, G. G. Paulus, H. Walther, E. Goulielmakis, A. Baltuška, M. Lezius and F. Krausz, *Long-term stabilization of the carrier-envelope phase of few-cycle laser pulses*, *Applied Physics B* (submitted).
- X. Liu, H. Rottke, E. Eremina, W. Sandner, E. Goulielmakis, K. O’Keeffe, M. Lezius, F. Krausz, F. Lindner, M. G. Schätzel, G. G. Paulus and H. Walther, *Steering non-sequential double ionization at the few-optical-cycle limit*, *Physical Review Letters* (submitted).
- F. Lindner, G. G. Paulus, H. Walther, A. Baltuška, E. Goulielmakis, M. Lezius and F. Krausz, *Gouy phase-shift for few-cycle laser pulses*, *Physical Review Letters*, vol. 92, p. 113001 (2004). [selected for the April 2004 issue of the Virtual Journal of Ultrafast Science, <http://www.vjultrafast.org>]
- G. G. Paulus, F. Lindner, H. Walther, A. Baltuška, E. Goulielmakis, M. Lezius and F. Krausz, *Measurement of the phase of few-cycle laser pulses*, *Physical Review Letters*, vol. 91, p. 253004 (2003).
- E. Eremina, X. Liu, H. Rottke, W. Sandner, A. Dreischuh, F. Lindner, F. Grasbon, G. G. Paulus, H. Walther, R. Moshhammer, B. Feuerstein and J. Ullrich, *Laser-induced non-sequential double ionization investigated at and below the threshold for electron impact ionization*, *Journal of Physics B: Atomic, Molecular and Optical Physics*, vol. 36, p. 3269 (2003).
- F. Lindner, W. Stremme, M. G. Schätzel, F. Grasbon, G. G. Paulus, H. Walther, R. Hartmann and L. Strüder, *High-order harmonic generation at a repetition rate of 100 kHz*, *Physical Review A*, vol. 68, p. 013814 (2003). [selected for the August 2003 issue of the Virtual Journal of Ultrafast Science, <http://www.vjultrafast.org>]
- F. Lindner, G. G. Paulus, F. Grasbon, A. Dreischuh and H. Walther, *Dispersion control in a 100-kHz-repetition-rate 35-fs Ti:sapphire regenerative amplifier system*, *IEEE Journal of Quantum Electronics*, vol. 38, p. 1465 (2002).

- G. Paulus, F. Lindner, D. Milosevic and W. Becker, *Phase-controlled single-cycle strong-field photoionization*, in Proceedings of the XXIII International Conference on Photonic, Electronic and Atomic Collisions (ICPEAC), Stockholm, 2003 (in press).
- F. Lindner, G. G. Paulus, H. Walther, A. Baltuška, E. Goulielmakis, M. Lezius and F. Krausz, *Measurement of the absolute phase of few-cycle laser pulses*, in Ultrafast Optics IV: Selected Contributions to the 4th International Conference on Ultrafast Optics, Vienna, Austria, p. 211 (Springer-Verlag, New York, 2003).
- F. Lindner, M. G. Schätzel, F. Grasbon, G. G. Paulus, A. Dreischuh and H. Walther, *Dispersion control in a 100 kHz repetition rate 35-fs laser system*, in Proceedings of SPIE: 12th International School on Quantum Electronics, Laser Physics and Applications, Varna, Bulgaria, vol. 5226, p. 38 (2003).
- M. Zavelani-Rossi, F. Lindner, C. Le Blanc, G. Chériaux and J. P. Chambaret, *Control of thermal effects for high intensity Ti:sapphire laser chains*, Applied Physics B, vol. 70, p. S193 (2000).

Gouy Phase Shift for Few-Cycle Laser Pulses

F. Lindner,¹ G. G. Paulus,^{1,2,3} H. Walther,^{1,3} A. Baltuška,⁴ E. Goulielmakis,^{4,5} M. Lezius,^{4,5} and F. Krausz^{1,4}

¹Max-Planck-Institut für Quantenoptik, 85748 Garching, Germany

²Department of Physics, Texas A&M University, College Station, Texas 77843-4242, USA

³Ludwig-Maximilians-Universität München, 85748 Garching, Germany

⁴Institut für Photonik, Technische Universität Wien, Gusshausstrasse 27, A-1040 Wien, Austria

⁵Institut für Ionenphysik, Universität Innsbruck, Technikerstrasse 25, A-6020 Innsbruck, Austria

(Received 14 October 2003; published 17 March 2004)

We measured for the first time the influence of the Gouy effect on focused few-cycle laser pulses. The carrier-envelope phase is shown to undergo a smooth variation over a few Rayleigh distances. This result is of critical importance for any application of ultrashort laser pulses, including high-harmonic and attosecond pulse generation, as well as phase-dependent effects.

DOI: 10.1103/PhysRevLett.92.113001

PACS numbers: 32.80.Rm, 42.50.Hz, 42.65.Re

In recent years there has been increasing interest in the generation and application of short laser pulses. Pulse durations of less than 5 fs in the near-infrared (800 nm) are in fact routine since the introduction of the hollow-fiber pulse compression technique [1–3]. Since such laser pulses consist of merely a few field oscillations (few-cycle pulses), the actual time variation of the electric-field — and therefore all physical processes driven by the laser — depends on the phase of the carrier wave with respect to the envelope, the so-called carrier-envelope (CE) phase. Because of the high sensitivity of this quantity to small fluctuations in pulse intensity, cavity length, and temperature, ultrashort-pulse lasers normally deliver pulse trains with a randomly changing CE phase shot to shot. While phase stabilization of femtosecond oscillators is a well-established technique [4–7], the capability of stabilizing and controlling the phase of an amplified laser system was only recently demonstrated [8]. This allows precise electric-field shaping and offers exciting prospects including the reproducible generation and reliable measurement of isolated subfemtosecond pulses [9,10].

With the achievement of stabilization of the CE phase for amplified pulses, the question of determining the value of the phase had to be addressed. This problem was solved very recently [11]. However, an important issue of nonlinear processes driven with phase-stabilized few-cycle pulses is that they usually take place in a laser focus. It is known that an electromagnetic beam propagating through a focus experiences an additional π phase shift with respect to a plane wave. This phase anomaly was discovered by Gouy in 1890 [12] and has since been referred to as the Gouy phase shift. This phase change is, in fact, a general property of any focused wave and is also expected for sound waves [13]. Intuitive explanations of the observed anomaly have been proposed [14,15]. The experimental evidence of the Gouy phase shift relied for years on interferometric measurements [12,16]. More recently, direct observations of the polarity change of single-cycle terahertz pulses have been reported [17–19].

This phase shift has important consequences in the optical range of the electromagnetic spectrum. In laser cavities, the determination of the resonant frequencies depends on the Gouy phase [20]. Phase matching in high-order harmonic generation (HHG) is governed by the atomic response and the Gouy phase shift of the fundamental radiation [21–23]. More importantly, the Gouy phase strongly affects the spatial variation of the CE phase of ultrashort pulses in a laser focus, the subject of this Letter.

In principle, the Gouy phase shift of a TEM₀₀ wave can be described by a simple formula depending on the focusing geometry and the wavelength,

$$\phi = -\arctan\left(\frac{z}{z_R(\lambda)}\right), \quad (1)$$

where the beam is traveling in the $+z$ direction and z_R is the Rayleigh distance (dependent on the wavelength λ). As few-cycle pulses consist of broad spectra with the wavelengths spanning about one octave, the different spectral components will experience the Gouy phase shift with different spatial scales. In particular, *blue* colors undergo a steeper phase change than *red* colors. It has been shown theoretically [24,25] that this leads to a difference of phase and group velocities in the neighborhood of the focus and therefore to CE phase slippage. For this reason, in general the CE phase variation cannot be described by Eq. (1). Indeed, the details of the phase change in the focus depend on the spatial profile of the laser beam and on the focusing geometry. In all cases, an overall π phase shift is expected between symmetric positions well distant from a spherical focus. Since the phase changes by π in the propagation through the focus, virtually all possible *E*-field shapes are available for the experiments. Thus, precise control of the spatial variation of the CE phase in the whole focal region is crucial to any kind of phase-dependent experiment.

In this Letter we present the first experimental determination of the evolution of the CE phase in the focus of

few-cycle laser pulses. Together with the ability to determine the value of the CE phase with high accuracy [11], this result constitutes the first full and unambiguous characterization of the electric field of the laser pulses in space and time within the paraxial approximation (i.e., neglecting the very small longitudinal component of the electric field).

Because of the lack of inversion symmetry of few-cycle pulses, nonlinear photoionization of noble gases exhibits significant asymmetries in the spatial photoelectron distribution [26–29]. Thus, simultaneous photoelectron spectroscopy in the two opposite polarization directions is a possibility to retrieve the time variation of the electric field. This so-called stereo-ATI (above-threshold-ionization) scheme has proven to be the most efficient method of CE phase determination to date [11,30]. In our experiment we used a phase-stabilized laser amplifier system capable of producing few-cycle pulses [8]. The pulse energy was attenuated to $20 \mu\text{J}$ and the beam focused with a $f/30$ geometry into a low-density xenon gas jet. Electrons emitted to the left and to the right are independently detected by two microchannel plates (Burle BiPolar TOF Detector, diameter 18 mm) located at a distance of 40 cm from the focus. With our focusing geometry, the electric field is expected to undergo the π phase shift within a range of a few millimeters. To reveal the influence of the Gouy phase, one has to detect selectively the electrons generated at a well-defined position of the focus. A pair of moveable slits perpendicular to the beam axis (z direction) and to the polarization axis allows the entire focal region to be scanned. The slit width is $250 \mu\text{m}$, well below the Rayleigh range ($\approx 1 \text{ mm}$), and, to achieve optimum spatial resolution in the z direction, they are placed at a distance of only 1 mm from the beam (Fig. 1). With this setup, the angular distribution of the emitted photoelectrons does not affect the phase resolution, which can be estimated to be $\approx 0.1 \text{ rad}$.

The photoelectron emission in the two opposite polarization directions measured with phase-stabilized pulses significantly differs in many aspects. On the one hand, the total count rate detected in the two arms of the spectrometer shows clear asymmetries; on the other hand, the difference of the two electron spectra can be used directly to retrieve the phase [11]. Both these features can be used to determine the Gouy CE phase shift. One possibility to observe the change of sign of the electric field in passing through the focus is to compare the electron yield in the two directions before and after the focus. For instance, if one detects dominant left emission before the focus, the opposite is expected after the focus. This can be verified with all possible CE phases simply by introducing a variable glass thickness in the beam path. At 760 nm, adding $52 \mu\text{m}$ of glass changes the phase by 2π without appreciably affecting the pulse duration. Such precise control is easily achieved by shifting a pair of wedges with a stepper motor (see Fig. 1). Figure 2 shows the

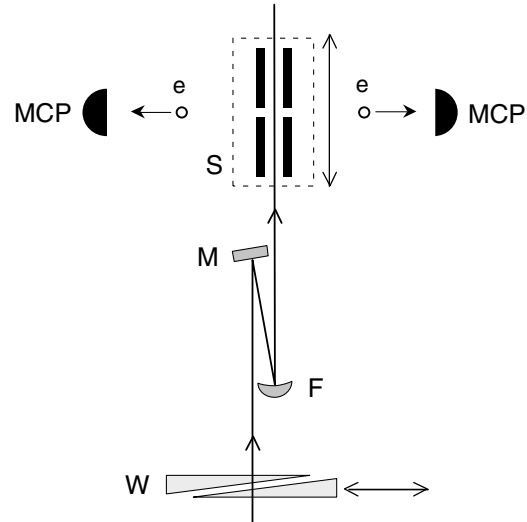


FIG. 1. Schematic of the experimental setup. W: pair of glass wedges to control the CE phase; M: flat mirror; F: focusing spherical mirror ($f = 250 \text{ mm}$); MCP: microchannel plates; S: moveable slits (width = $250 \mu\text{m}$). The angle of incidence on the focusing mirror is minimized to reduce astigmatism.

electron count rate asymmetry (left/right ratio) as a function of the glass thickness introduced. We made the measurement by moving the pair of slits to a distance of $\approx 2 \text{ mm}$ before (dashed line) and after (solid line) the focus. The clear phase shift of π between the two curves represents a direct measurement of the Gouy CE phase shift in the focus.

The electric-field polarity reversal observed from before to after the focus does not describe the details of the phase slippage in the focus. Since many experiments take place over an extended area of the focus, e.g., HHG, it is

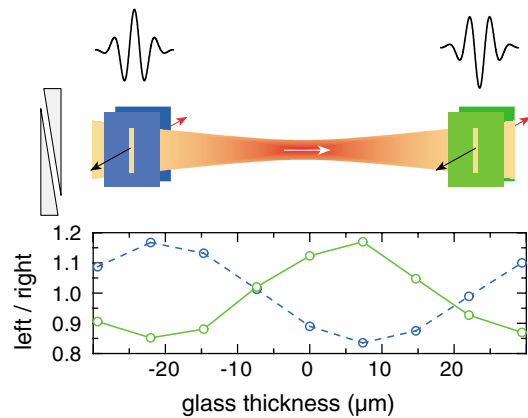


FIG. 2 (color). Varying the glass thickness in the beam path changes the CE phase of the pulses. The left/right ratio of the electron yield exhibits clear oscillations with a periodicity consistent with glass dispersion at the wavelength of the laser. The measurement was performed before (dashed line) and after (solid line) the focus. The π phase shift is due to the Gouy CE phase shift in passing through the focus.

essential to characterize the phase variation precisely and, in particular, to recognize possible anomalies in the behavior of the CE phase evolution. Indeed, the possible presence of a significant area of the focus with anomalous phase change has been suggested as an explanation of the observed enhancement of the HHG efficiency by using truncated Bessel beams [31].

In order to analyze in detail the phase variation within the focal range, we acquired electron spectra at several positions by moving the pair of slits. Figure 3 shows the detected left/right asymmetry as a function of the electron energy and of the CE phase for a few z positions. As in Fig. 2, the phase was changed by shifting the glass wedges. Different approaches are possible to retrieve the phase variation. The integrated electron yield provides a clear phase indication and can be used to show the overall phase shift in the focus (Fig. 2). However, scanning the focal range implies measuring at constantly changing

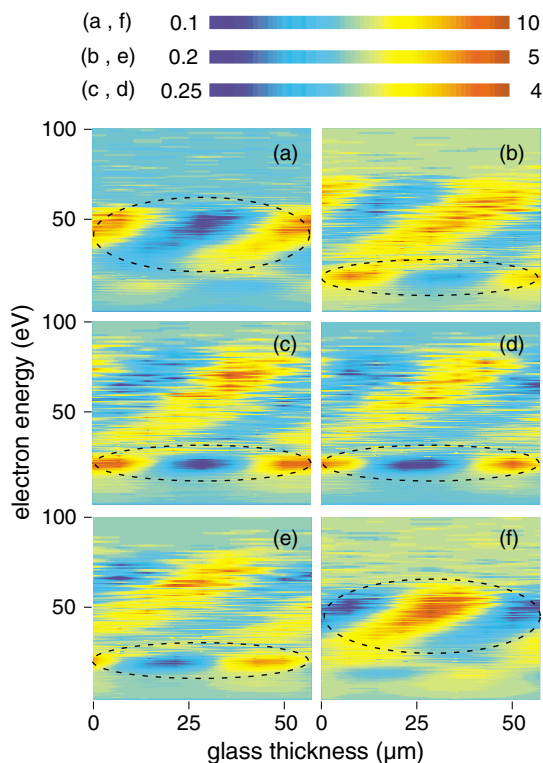


FIG. 3 (color). Left/right asymmetry maps (logarithmic scale) for different longitudinal positions as a function of the electron energy and glass thickness introduced. Reddish colors indicate dominant left emission; bluish colors dominant right emission. The maps (a)–(f) correspond, respectively, to the positions: $z = -1.75$ mm, $z = -1.0$ mm, $z = -0.25$ mm, $z = +0.25$ mm, $z = +1.0$ mm, $z = +1.75$ mm (positive values represent positions *after* the focus). The phase difference is determined by evaluating the shift of the characteristic structures (indicated by the dashed lines) of the asymmetry pattern. The extension of the electron yield to higher energies in the central part of the focus is due to the higher intensity.

intensities. Since it is predicted that the maximum of the integrated left/right asymmetry should occur at a phase that depends on the intensity [28], it is not easy to decouple the Gouy phase shift from the possible intensity-dependent phase shift. A better approach relies therefore on the evident spectral information of Fig. 3. Dark reddish and bluish colors correspond to spectral regions of strong asymmetry: Since these are easily distinguishable, they can be used to follow the phase evolution. Note that the measurements were made by approaching the focus from the outer part and by moving alternatively the slits before and after the focus. With this procedure, measurements of symmetric positions around the focus are consecutive, thus reducing detrimental effects from possible long-term phase drifts.

Figures 3(a) and 3(f) correspond to the outer part of the focal range. The strong asymmetry in the high-energy part of the spectra (ATI plateau, dashed area) changes sign while passing through the focus, confirming the π phase shift already discussed (see Fig. 2). More interestingly, Figs. 3(b)–3(e) correspond to positions in the central part of the focus. The asymmetry in the plateau is partly smeared out, but another clear asymmetric area appears in the low-energy part of the spectra (20–25 eV, dashed area), just before the ATI plateau. Its nature is not entirely understood, but, being definitely a CE phase effect, it can be exploited to retrieve the phase variation in the focus. By moving in the direction of the beam propagation, i.e., from before to after the focus [Figs. 3(a)–3(f)], the characteristic pattern moves toward the left side of the graphs, i.e., toward decreasing glass thickness introduced. This is in full agreement with the intuitive physical origin of the Gouy CE phase shift. Indeed, in a dispersive medium like glass the phase velocity exceeds the group velocity. The same situation occurs in the propagation of the ultrashort pulse in the laser focus [24,25]. Thus, it is not surprising that, to observe similar features, less glass is needed after the focus with respect to a symmetric position before the focus. The Gouy CE phase shift determination can be performed simply by numerically evaluating the shift of the asymmetry pattern; converting the glass thickness shift obtained (μm) into phase difference (rad) is then straightforward.

Figure 4 shows the retrieved CE phase shift for the positions of Fig. 3 and for several others not shown there. For comparison, the Gouy phase of a Gaussian beam [Eq. (1)] with a $f/30$ focusing geometry is also shown (solid line). Note that the CE phase shift is *not* expected to follow the Gouy phase, the latter being a property of cw lasers. The beam in our experiments is a few-cycle pulse truncated Bessel beam, and the focusing geometry in our setup (see Fig. 1) inevitably introduces a slight astigmatism.

The pulses undergo the π phase shift within a few Rayleigh distances. Because of the rapid decrease of

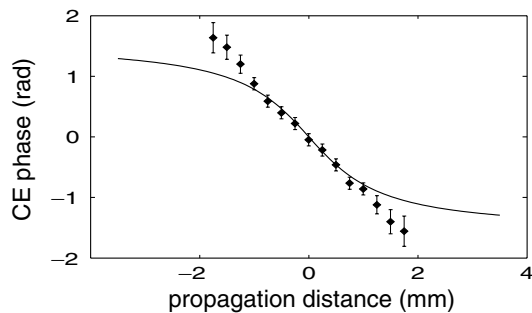


FIG. 4. Retrieved CE Gouy phase shift as a function of the propagation distance in the focus. The solid line is the Gouy phase of a cw Gaussian beam, shown for comparison. Note that, in the outer part of the focus, the electron count rate rapidly decreases, making detection of additional experimental points difficult.

electron yield at lower intensities, the measurements were stopped at a distance of ≈ 2 mm before and after the focus. This prevented observation of the expected area of the constant CE phase in the outer part of the focus. However, we point out that the region of interest for all experiments is entirely covered, and the estimated error for the experimental data is relatively low (≈ 0.1 rad). The phase changes smoothly with a constant slope and, what is particularly important for experiments, does not exhibit any wiggles or irregularities.

In conclusion, we have directly measured the CE phase shift of laser pulses evolving through a focus induced by the geometrical Gouy phase. This constitutes the first full characterization of phase-stabilized few-cycle optical pulses in space and time, an essential step for any application of such laser systems. Furthermore, these results provide access not only to the overall polarity reversal for pulses evolving through a focus [17–19], but also, for the first time to our knowledge, to the details of the phase variation *in* the focus.

This work has been supported by the Austrian Science Fund (Grants No. F016, No. Z63, and No. P15382) and by The Welch Foundation (Grant No. A-1562).

-
- [1] M. Nisoli, S. De Silvestri, and O. Svelto, *Appl. Phys. Lett.* **68**, 2793 (1996).
- [2] M. Nisoli, S. De Silvestri, O. Svelto, R. Szipöcs, K. Ferencz, Ch. Spielmann, S. Sartania, and F. Krausz, *Opt. Lett.* **22**, 522 (1997).
- [3] G. Steinmeyer, D. H. Sutter, L. Gallman, N. Matuschek, and U. Keller, *Science* **286**, 1507 (1999).
- [4] J. Reichert, R. Holzwarth, Th. Udem, and T.W. Hänsch, *Opt. Commun.* **172**, 59 (1999).
- [5] H. R. Telle, G. Steinmeyer, A. E. Dunlop, J. Stenger, D. H. Sutter, and U. Keller, *Appl. Phys. B* **69**, 327 (1999).
- [6] D. J. Jones, S. A. Diddams, J. K. Ranka, A. Stentz, R. S. Windeler, J. L. Hall, and S. T. Cundiff, *Science* **288**, 635 (2000).
- [7] A. Apolonski, A. Poppe, G. Tempea, Ch. Spielmann, Th. Udem, R. Holzwarth, T.W. Hänsch, and F. Krausz, *Phys. Rev. Lett.* **85**, 740 (2000).
- [8] A. Baltuška, Th. Udem, M. Uiberacker, M. Hentschel, E. Goulielmakis, Ch. Gohle, R. Holzwarth, V.S. Yakovlev, A. Scrinzi, T.W. Hänsch, and F. Krausz, *Nature (London)* **421**, 611 (2003).
- [9] M. Hentschel, R. Kienberger, Ch. Spielmann, G. A. Reider, N. Milosevic, T. Brabec, P. Corkum, U. Heinzmann, M. Drescher, and F. Krausz, *Nature (London)* **414**, 509 (2001).
- [10] R. Kienberger, E. Goulielmakis, M. Uiberacker, A. Baltuška, V. Yakovlev, F. Bammer, A. Scrinzi, Th. Westerwalbesloh, U. Kleineberg, U. Heinzmann, M. Drescher, and F. Krausz, *Nature (London)* **427**, 817 (2004).
- [11] G. G. Paulus, F. Lindner, H. Walther, A. Baltuška, E. Goulielmakis, M. Lezius, and F. Krausz, *Phys. Rev. Lett.* **91**, 253004 (2003).
- [12] L. G. Gouy, *C.R. Acad. Sci. Paris* **110**, 1251 (1890).
- [13] N. C. R. Holme, B. C. Daly, M. T. Myaing, and T. B. Norris, *Appl. Phys. Lett.* **83**, 392 (2003).
- [14] R. W. Boyd, *J. Opt. Soc. Am.* **70**, 877 (1980).
- [15] S. Feng and H. G. Winful, *Opt. Lett.* **26**, 485 (2001).
- [16] C. R. Carpenter, *Am. J. Phys.* **27**, 98 (1958).
- [17] A. B. Ruffin, J. V. Rudd, J. F. Whitaker, S. Feng, and H. G. Winful, *Phys. Rev. Lett.* **83**, 3410 (1999).
- [18] P. Kužel, M. A. Khazan, and J. Kroupa, *J. Opt. Soc. Am. B* **16**, 1795 (1999).
- [19] R. W. McGowan, R. A. Cheville, and D. Grischkowsky, *Appl. Phys. Lett.* **76**, 670 (2000).
- [20] A. E. Siegman, *Lasers* (University Science Books, Sausalito, 1986).
- [21] Ph. Balcou and A. L'Huillier, *Phys. Rev. A* **47**, 1447 (1993).
- [22] M. Lewenstein, P. Salières, and A. L'Huillier, *Phys. Rev. A* **52**, 4747 (1995).
- [23] F. Lindner, W. Stremme, M. G. Schätzel, F. Grasbon, G. G. Paulus, H. Walther, R. Hartmann, and L. Strüder, *Phys. Rev. A* **68**, 013814 (2003).
- [24] Z. L. Horváth, J. Vinkó, Zs. Bor, and D. von der Linde, *Appl. Phys. B* **63**, 481 (1996).
- [25] M. A. Porras, *Phys. Rev. E* **65**, 026606 (2002).
- [26] P. Dietrich, F. Krausz, and P. Corkum, *Opt. Lett.* **25**, 16 (2000).
- [27] I. P. Christov, *Appl. Phys. B* **70**, 459 (2000).
- [28] S. Chelkowski and A. Bandrauk, *Phys. Rev. A* **65**, 061802 (2002).
- [29] D. Milošević, G. G. Paulus, and W. Becker, *Opt. Express* **11**, 1418 (2003).
- [30] G. G. Paulus, F. Grasbon, H. Walther, P. Villorresi, M. Nisoli, S. Stagira, E. Priori, and S. De Silvestri, *Nature (London)* **414**, 182 (2001).
- [31] M. Nisoli, E. Priori, G. Sansone, S. Stagira, G. Cerullo, S. De Silvestri, C. Altucci, R. Bruzzese, C. de Lisio, P. Villorresi, L. Poletto, M. Pascolini, and G. Tondello, *Phys. Rev. Lett.* **88**, 033902 (2002).

Measurement of the Phase of Few-Cycle Laser Pulses

G. G. Paulus,^{1,2,3} F. Lindner,² H. Walther,^{2,3} A. Baltuška,⁴ E. Goulielmakis,⁴ M. Lezius,^{4,5} and F. Krausz^{2,4}

¹*Department of Physics, Texas A&M University, College Station, Texas 77843-4242, USA*

²*Max-Planck-Institut für Quantenoptik, 85748 Garching, Germany*

³*Ludwig-Maximilians-Universität München, 85748 Garching, Germany*

⁴*Institut für Photonik, Technische Universität Wien, Gusshausstrasse 27, A-1040 Wien, Austria*

⁵*Institut für Ionenphysik, Universität Innsbruck, Technikerstrasse 25, A-6020 Innsbruck, Austria*

(Received 17 June 2003; published 18 December 2003)

For the shortest pulses generated to date, the amplitude of the electromagnetic wave changes almost as rapidly as the field oscillates. The temporal variation of the field, which directly governs strong-field interactions, therefore depends on whether the maximum of the pulse amplitude coincides with that of the wave cycle or not, i.e., on the phase of the field with respect to the pulse envelope. It is demonstrated that the direction of electron emission from photoionized atoms can be controlled by varying the phase of the field, providing for the first time a tool for its accurate determination. Directing fast electron emission to the right or to the left with the light phase constitutes a new kind of coherent control.

DOI: 10.1103/PhysRevLett.91.253004

PACS numbers: 32.80.Rm, 42.50.Hz, 42.65.Re

Generation of laser pulses with a pulse energy around 500 μJ and duration of 5 fs (measured at full width at half maximum) has become routine in past few years [1,2]. One of the most intriguing features of such pulses is that their envelope varies almost as fast as the electromagnetic field itself. Considering a typical wavelength of 760 nm, an optical cycle has a duration of 2.5 fs; i.e., the pulses consist of very few optical cycles only (few-cycle pulses). One of the most momentous consequences is that the time variation of the laser field will depend on the phase of the carrier frequency with respect to the envelope, the so-called carrier-envelope (CE) phase. Although few-cycle pulses have hitherto mainly been used for generating coherent soft x rays [3,4] and attosecond pulses [5], there is a high potential for applications in many other fields, ranging from coherent control of molecular dynamics to particle acceleration. All the processes involved depend on the time variation of the field and thus on the CE phase. The ability to measure and precisely stabilize the CE phase is therefore a crucial point for all applications. So far, clear evidence of phase effects has been seen in photoionization without phase control for the few-cycle pulses [6], in soft x-ray generation with phase-stabilized pulses [7], and virtually at the same time as the present experiment in photoemission from surfaces with non-amplified few-cycle pulses [8]. Phase-dependent effects in semiconductors have been predicted [9]. Here we present experimental results of nonlinear photoionization with intense phase-stabilized few-cycle visible light pulses. The spatially asymmetric field of few-cycle laser pulses leads to different photoionization rates for opposite directions. By detecting this difference it was possible for the first time to measure the CE phase of powerful few-cycle laser pulses.

The electric part $\mathcal{E}(t)$ of the field of a laser pulse can be written as

$$\vec{\mathcal{E}}(t) = \vec{e}_x \mathcal{E}_0(t) \cos(\omega t + \varphi), \quad (1)$$

where \vec{e}_x denotes the axis of polarization, $\mathcal{E}_0(t)$ denotes the envelope of the pulse, $\omega/2\pi$ denotes the carrier frequency of the laser, and φ denotes the phase. The latter describes a general property of the pulse and is therefore also commonly referred to as the “absolute” phase. For a few-cycle pulse, the width of $\mathcal{E}_0(t)$ (measured at half the maximum) is about 2 times the optical period $2\pi/\omega$. With respect to φ , the convention of choosing $t = 0$ at the maximum of the envelope is used. Then, $\varphi = 0$ corresponds to a “cosine-like” pulse with the absolute maximum of the electric field pointing to the right. Accordingly, we speak of a sine-like pulse for $\varphi = -\pi/2$ (see Fig. 1). Evidently, it is possible to tailor the field of ultrashort pulses by controlling their absolute (CE) phase.

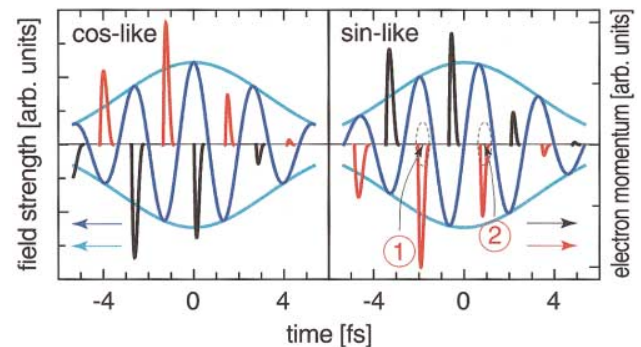


FIG. 1 (color). Electric field (blue) and envelope (light blue) of a 5 fs laser pulse for CE phase 0 (left panel) and $-\pi/2$ (right panel). The drift momentum of high-energy photoelectrons as a function of the ionization time t_0 is shown in black (emission to the right) and red (emission to the left). It was calculated with a classical model. Note that highest momentum does not necessarily coincide with highest electron yield: In the right panel the ionization probability at times labeled with 1 is considerably lower than those labeled with 2 because of lower field strength at t_0 .

Conventional femtosecond lasers, however, generate pulses with more or less randomly changing phase. Its stabilization is routinely performed for femtosecond laser oscillators and has led to a breakthrough in frequency metrology [10–12]; for a recent review, see [13]. In contrast, phase stabilization for amplified pulses is a very recent achievement [7]. Considering the asymmetry of the field of few-cycle pulses [14], it appears that an obvious approach is to look for the signatures of the CE phase in nonlinear photoionization. Particular emphasis is given to noninversion symmetric emission of the photoelectrons, i.e., a different count rate for electrons emitted to the right and to the left. A number of theoretical investigations have been devoted to the problem in the past years [15–20]. Most of them concentrate on total yields of photoelectrons.

In our experiments xenon atoms were ionized with 5 fs long laser pulse of peak intensities of nearly 10^{14} W/cm². Absorption of eight photons is necessary in order to subdue the ionization threshold. As a matter of fact, processes of much higher order, i.e., absorption of photons in excess of those necessary for ionization, can be observed, and thus correspondingly high photoelectron energies. This phenomenon is known as above-threshold ionization (ATI) [21]. Our experimental approach to analyzing this phenomenon relies on time-of-flight spectroscopy; see Fig. 2.

Figure 3(a) shows a series of ATI spectra corresponding to different CE phases. Pulses with known phase differences $\Delta\varphi$ can be realized by delaying the envelope with respect to the carrier. Since the envelope propagates with the group velocity and the carrier with the phase velocity of light, glass dispersion can be used to shift the CE phase. At a central wavelength of 760 nm adding 52 μm of fused silica will change φ by 2π without distinctly affecting the pulse duration. Thus, two glass wedges which can be shifted with respect to each other allow any phase to be adjusted (see Fig. 2). Simply by inspecting the high-energy part (> 20 eV) of the spectra one can verify that $\Delta\varphi = \pi$ corresponds to a change from left to right, while $\Delta\varphi = 2\pi$ faithfully reproduces the spectra. For high electron energies, the ratio of left/right electron yield approaches 1 order of magnitude and can be controlled by adjusting the CE phase. This constitutes a new kind of *coherent control* and, to our knowledge, is the highest contrast observed so far.

Figure 3(b) displays the ratio of photoemission to the left and to the right for different spectral regions. The ratio of high- and low-energy electrons oscillates with a periodicity of $\Delta\varphi$ in excellent agreement with the periodicity expected from glass dispersion. Besides the much higher contrast for high-energy electrons, a phase shift of both sets of data is also apparent. To determine the CE phase we have to establish the connection between the phase of the field and the ATI signal. This is done by using the high-energy (> 20 eV) electrons. One reason certainly is their higher sensitivity to the CE

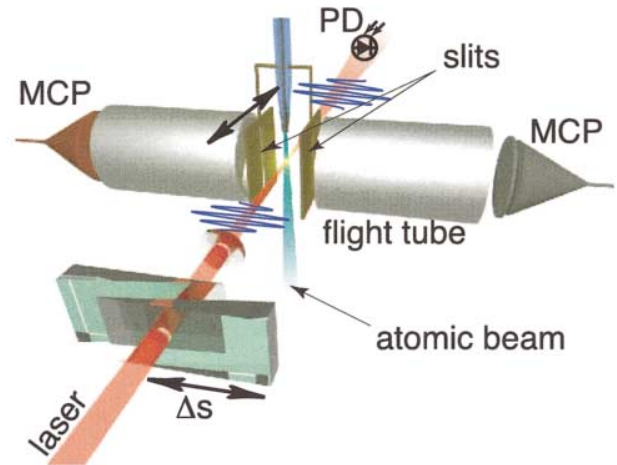


FIG. 2 (color). "Stereo-ATI" spectrometer. Two opposing electrically and magnetically shielded time-of-flight spectrometers are mounted in an ultrahigh vacuum apparatus. Xenon atoms fed in through a nozzle from the top are ionized in the focus of a few-cycle laser beam. The focal length is 250 mm (the lens shown in the sketch is in reality a concave mirror), and the pulse energy was attenuated to 20 μJ . The laser polarization is linear and parallel to the flight tubes. Note that the laser field changes sign while propagating through the focus. Slits with a width of 250 μm are used to discriminate electrons created outside the laser focus region chosen. The slits can be moved from outside the vacuum system. A photodiode (PD) and microchannel plates (MCP) detect the laser pulses and photoelectrons, respectively. Throughout this Letter, spectra corresponding to electrons detected with the left red-colored (right black-colored) detector are colored in red (black). The laser repetition rate is 1 kHz and 50 electrons per pulse are recorded at each MCP. A pair of glass wedges (apex angle 2.8°) is used to optimize dispersion and adjust the CE phase. Therefore, movement of one wedge by Δs introduces $\Delta x = \Delta s \tan(2.8^\circ)$ glass.

phase. More importantly, the dominant overall features in this spectral region are known not to depend on specific properties of the atomic species or on intensity. Figure 4 shows a comparison between measurements and results from classical calculations, the latter taking into account only high-energy electrons. The concept of the calculation will be explained below. In the experimental as well as in the theoretical data the ratio of emission to the left and right depends in a characteristic way on electron energy and the CE phase. This leads to the inclined stripes in the false-color representations. Another common feature is that the asymmetry of left-right emission increases for increasing electron energy. It should be noted that, unlike the contrast of asymmetry, these characteristic features do *not* depend critically on pulse shape or pulse duration. The sharp edges visible in the calculation originate from classical energy conservation. This artifact is removed by energy-time uncertainty in quantum mechanics. Matching the characteristic features of the theoretical and experimental data leads

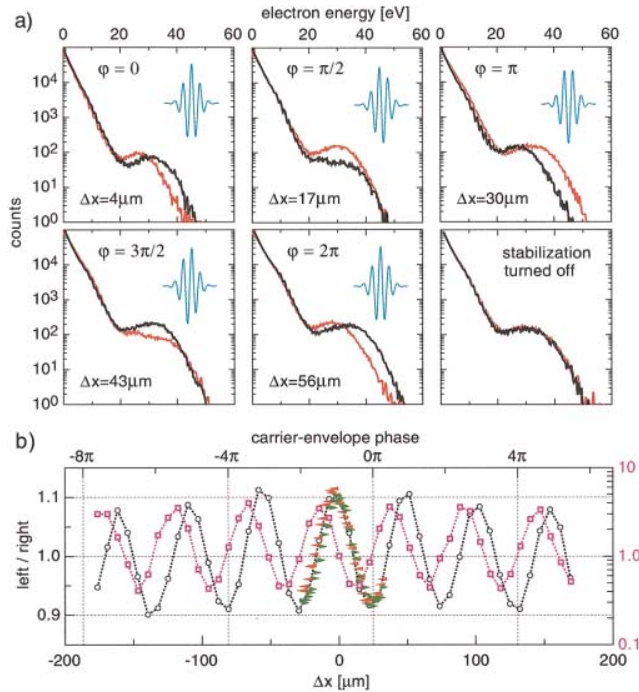


FIG. 3 (color). (a) Photoelectron spectra for different CE phases controlled by fine movement of one of the wedges. Δx indicates the glass added hereby. The black curves correspond to emission to the right (positive direction), the red ones to the opposite direction. The insets show the corresponding real time variation of the electric field, as deduced from the phase assignment shown in Fig. 4. Only without phase stabilization were identical spectra measured left and right as expected. (b) Left-right ratio of the total electron yield (circles) and high-energy electrons (squares) as a function of glass thickness Δx added or subtracted by moving one of the wedges. $\Delta x = 0$ corresponds to optimal dispersion compensation, i.e., the shortest pulses. Maximal left/right ratio for the total yield does not coincide with that for high-energy electrons. Note the different scales for low- and high-energy electrons. The upper x scale indicates the carrier-envelope phase of the pulse, as deduced from the comparison with theory shown in Fig. 4. The measurement of the CE phase drift was performed by a scan forth (triangles pointing to the right) and back (triangles pointing to the left) with finer variation of the glass thickness. The mismatch at the start and the end point indicates a phase drift of ≈ 50 mrad/min.

to an unambiguous determination of the CE phase with an estimated error of $\pi/10$.

The calculation used to determine the CE phase is based on the insight that, at high intensities, ATI can be understood in terms of quasistatic field ionization at some time t_0 and subsequent classical evolution of the electron in the laser field [22,23]. For a recent review, see [24]. A considerable fraction of the photoelectrons generated when atoms or molecules are exposed to intense laser pulses do not escape directly. Rather they return to the ion core within times of typically less than an optical cycle and in precise synchronization with the electric field of the laser pulse. The characteristics of returning

electrons can be observed in the kinetic energy spectra of photoelectrons. The underlying mechanism is elastic scattering of the electrons when they return to the ion core at time $t = t_1$ and are subsequently accelerated by the laser field. As a consequence, photoelectrons with high kinetic energy can be observed. In the photoelectron spectra, they manifest themselves in the high-energy plateau-like annex to the exponentially decreasing count rate at low electron energies [25,26].

The kinetic energy spectrum of the plateau electrons is sensitive to the CE phase for several reasons. First of all, high-energy electrons returning to the ion core can be created only in subfemtosecond time intervals close to peaks of the electric field of the laser pulse (see Fig. 1). However, the probability that they tunnel through the atomic potential at t_0 depends exponentially on the field strength $\mathcal{E}(t_0)$ and as few-cycle pulses are involved it is likely only for those very few optical half-cycles close to the pulse maximum. Generally, the highest kinetic energies are reached for electrons returning to the core when the electric field becomes nearly zero [$\mathcal{E}(t_1) = 0$]. For few-cycle pulses in addition, the field amplitude \mathcal{E}_0 needs to be as high as possible for $t > t_1$ in order to allow efficient acceleration after rescattering. Since the start time t_0 and return time t_1 differ by almost one optical cycle, both conditions, namely, the highest possible field strength at t_0 and highest possible amplitude after t_1 are hard to meet and result in a strong dependence of photoionization on the CE phase. Number, strength, and timing of the wave packets lead to distinctive structures in the ATI spectra. Their analysis therefore provides detailed information about the key processes of attosecond science. Quantum mechanical calculations are in very good qualitative agreement with this classical treatment [20].

Having established that ATI can be used for precise determination of the CE phase, an example of the sensitivity of the instrument should be given. In Fig. 3(b) also a measurement with small steps $\Delta\varphi$ is shown. This measurement reveals small phase drifts, which have to be attributed to the laser system and its stabilization scheme. The phase drifts are of the order of 50 mrad/min, measured over more than 10 min. As the stereo-ATI phase meter not only can measure the CE phase and also detect small phase drifts, it clearly has the potential to be used in a feedback loop. In this respect it should be emphasized that the target gas pressure is so low ($< 10^{-4}$ mbar) that the ATI experiment does not affect the laser beam; i.e., a stereo-ATI phase meter can be placed anywhere in a laser beam line.

In summary, we have shown that strong-field photoionization provides a very efficient means of measuring the CE phase of few-cycle femtosecond laser pulses with $no \pm \pi$ phase ambiguity inherent in many other schemes. Conversely, the emission direction of photoelectrons can be steered by choosing the CE phase, establishing a new kind of coherent control scheme. Control of the CE phase allows one to tailor the field of a few-cycle pulse. A

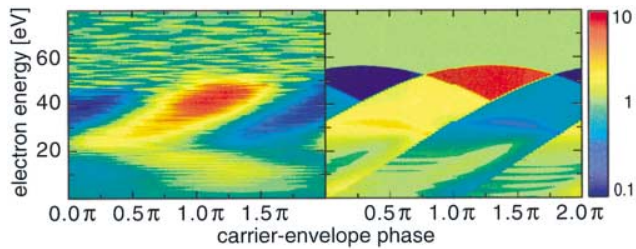


FIG. 4 (color). Determination of the CE phase. False-color representation (logarithmic scale) of the left-right ratio of photoelectrons as a function of the electron energy and the CE phase. Positive values (red) indicate dominant left emission, negative values (blue) dominant right emission. For the theoretical part (right panel), only rescattered electrons were taken into account. The parameters used are the same as in the experiment. This comparison allows precise carrier-envelope phase determination. With the convention of Eq. (1), the electric field is now uniquely characterized.

tailored field variation would deform molecular potentials in a virtually arbitrary way. This could help to induce or analyze exotic chemical reactions. In fact, it is possible to choose conditions such that the field vanishes upon the return of the wave packet. The very high current densities corresponding to the returning wave packets should facilitate electron-ion scattering experiments, hitherto hardly possible. Furthermore, investigation of interference patterns in ATI spectra will allow ionization to be studied in real time.

This work has been supported by the Austrian Science Fund (Grants No. F016, No. Z63, and No. P15382) and by The Welch Foundation (Grant No. A-1562).

[1] M. Nisoli, S. De Silvestri, O. Svelto, R. Szipöcs, K. Ferencz, Ch. Spielmann, S. Sartania, and F. Krausz, *Opt. Lett.* **22**, 522 (1997).
 [2] G. Steinmeyer, D. Sutter, L. Gallmann, N. Matuschek, and U. Keller, *Science* **286**, 1507 (1999).
 [3] Ch. Spielmann, N. H. Burnett, S. Sartania, R. Koppitsch, M. Schnürer, C. Kan, M. Lenzner, P. Wobrauschek, and F. Krausz, *Science* **278**, 661 (1997).
 [4] P. Villorresi, P. Ceccherini, L. Poletto, G. Tondello, C. Altucci, R. Bruzzese, C. de Lisio, M. Nisoli, S. Stagira, G. Cerullo, S. De Silvestri, and O. Svelto, *Phys. Rev. Lett.* **85**, 2494 (2000).
 [5] M. Hentschel, R. Kienberger, Ch. Spielmann, G. A. Reider, N. Milosevic, T. Brabec, P. Corkum, U. Heinzmann, M. Drescher, and F. Krausz, *Nature (London)* **414**, 509 (2001).

[6] G. G. Paulus, F. Grasbon, H. Walther, P. Villorresi, M. Nisoli, S. Stagira, E. Priori, and S. De Silvestri, *Nature (London)* **414**, 182 (2001).
 [7] A. Baltuška, Th. Udem, M. Uiberacker, M. Hentschel, E. Goulielmakis, Ch. Gohle, R. Holzwarth, V. S. Yakovlev, A. Scrinzi, T. W. Hänsch, and F. Krausz, *Nature (London)* **421**, 611 (2003).
 [8] A. Apolonski, P. Dombi, G. G. Paulus, M. Kakehata, R. Holzwarth, Th. Udem, Ch. Lemell, J. Burgdörfer, T. W. Hänsch, and F. Krausz, *Phys. Rev. Lett.* (to be published).
 [9] O. D. Mücke, T. Tritschler, M. Wegener, U. Morgner, and F. X. Kärtner, *Phys. Rev. Lett.* **89**, 127401 (2002).
 [10] J. Reichert, R. Holzwarth, Th. Udem, and T. W. Hänsch, *Opt. Commun.* **172**, 59 (1999).
 [11] D. J. Jones, S. A. Diddams, J. K. Ranka, A. Stentz, R. S. Windeler, J. L. Hall, and S. T. Cundiff, *Science* **288**, 635 (2000).
 [12] H. R. Telle, G. Steinmeyer, A. E. Dunlop, J. Stenger, D. H. Sutter, and U. Keller, *Appl. Phys. B* **69**, 327 (1999).
 [13] S. T. Cundiff and Jun Ye, *Rev. Mod. Phys.* **75**, 325 (2003).
 [14] A relationship of few-cycle pulses with bichromatic fields with commensurate frequencies is obvious: A. N. Chudinov, Yu. E. Kapitzky, A. A. Shulginov, and B. Ya. Zel'dovich, *Opt. Quantum Electron.* **23**, 1055 (1991); D. W. Schumacher, F. Weihe, H. G. Müller, and P. H. Bucksbaum, *Phys. Rev. Lett.* **73**, 1344 (1994).
 [15] E. Cormier and P. Lambropoulos, *Eur. Phys. J. D* **2**, 15 (1998).
 [16] P. Dietrich, F. Krausz, and P. B. Corkum, *Opt. Lett.* **25**, 16 (2000).
 [17] I. P. Christov, *Appl. Phys. B* **70**, 459 (2000).
 [18] R. M. Potvliege, N. J. Kylstra, and C. J. Joachain, *J. Phys. B* **33**, L743 (2000).
 [19] S. Chelkowski and A. D. Bandrauk, *Phys. Rev. A* **65**, 061802(R) (2002).
 [20] D. B. Milošević, G. G. Paulus, and W. Becker, *Opt. Express* **11**, 1418 (2003).
 [21] P. Agostini, F. Fabre, G. Mainfray, G. Petite, and N. K. Rahman, *Phys. Rev. Lett.* **42**, 1127 (1979).
 [22] P. B. Corkum, *Phys. Rev. Lett.* **71**, 1994 (1993).
 [23] K. C. Kulander, K. J. Schafer, and K. L. Krause, in *Super-Intense Laser-Atom Physics*, edited by B. Piraux, A. LHuillier, and K. Rzazweski, NATO Advanced Study Institutes, Ser. B, Vol. 316 (Plenum, New York, 1993), p. 95.
 [24] W. Becker, F. Grasbon, R. Kopold, D. B. Milošević, G. G. Paulus, and H. Walther, *Adv. At. Mol. Opt. Phys.* **48**, 35 (2002).
 [25] G. G. Paulus, W. Nicklich, H. Xu, P. Lambropoulos, and H. Walther, *Phys. Rev. Lett.* **72**, 2851 (1994).
 [26] G. G. Paulus, W. Becker, W. Nicklich, and H. Walther, *J. Phys. B* **27**, L703 (1994).

Long-term Stabilization of the Carrier-Envelope Phase of Few-cycle Laser Pulses

M. G. Schätzel¹, F. Lindner¹, G. G. Paulus^{1,2,3}, H. Walther^{1,2}, E. Goulielmakis⁴, A. Baltuška⁴, M. Lezius^{4,5}, F. Krausz^{1,2,4}

¹ Max-Planck-Institut für Quantenoptik, Hans-Kopfermann-Str. 1, D-85748 Garching, Germany

² Ludwig-Maximilians-Universität München, Am Coulombwall 1, D-85748 Garching, Germany

³ Department of Physics, Texas A&M University, College Station, TX 77843-4242, USA

⁴ Institut für Photonik, Technische Universität Wien, Gusshausstr. 27, A-1040 Wien, Austria

⁵ Institut für Ionenphysik, Universität Innsbruck, Technikerstr. 25, A-6020 Innsbruck, Austria

Received: date / Revised version: date

Abstract The temporal variation of the electromagnetic field of a few-cycle laser pulse depends on whether the maximum of the pulse amplitude coincides with that of the wave cycle or not, i. e. it depends on the phase of the field with respect to the pulse envelope. Fixation of this “carrier-envelope” phase has only very recently become possible for amplified laser pulses. This paved the way for a completely new class of experiments and for coherent control down to the attosecond time scale because it is the field and not the pulse envelope which governs laser-matter interactions. However, this novel technique still affords much potential for optimization. In this paper we demonstrate a novel stabilization scheme for the carrier-envelope phase that not only guarantees a stable phase for arbitrarily long measurements, but also makes it possible to restore any given phase for an application after a pause of any kind. This is achieved by combining a *stereo-ATI* phase meter with a feedback loop to correct phase drifts inside and outside the laser system.

PACS 07.05.Dz; 32.80.Rm; 42.50.Hz

Key words carrier-envelope phase – stabilization scheme – stereo ATI

1 Introduction

Femtosecond laser technology has greatly promoted fundamental investigations of strong-field physics. An essential achievement was the realization of extremely short laser pulses comprising only few optical cycles at near-infrared wavelengths [1, 2]. To a good approximation, the electric field $\mathcal{E}(t)$ of such a short laser pulse can be described as $\mathcal{E}(t) = \mathcal{E}_0(t) \cos(\omega_L t + \phi)$. Besides the carrier

frequency ω_L and pulse envelope $\mathcal{E}_0(t)$, the phase difference ϕ between the pulse envelope and its carrier wave, conventionally termed carrier-envelope (C-E) or “absolute” phase, also plays a decisive role in the temporal evolution of the electric field. Although this has been known for years (see, for example, [3]), the first C-E phase effect was only recently detected, with the C-E phase randomly fluctuating [4].

While phase stabilization of femtosecond oscillators can now be routinely achieved [5–8], a phase-stabilized laser system with a power amplifier was only recently realized [9]. Using amplified phase-stable few-cycle laser pulses, phase effects were measured in high-order harmonic generation (HHG) [9], above threshold ionization (ATI) [10], and nonsequential double ionization (NSDI) [11]. A growing number of publications also examines these effects theoretically [12–19]. Phase stabilization of the amplified laser system works very well on moderate time scales, but certain experiments need phase stability over an extended period of several hours, which so far cannot be guaranteed. A new stabilization scheme for this purpose is demonstrated here.

2 Principles

The basic idea for stabilizing the carrier-envelope phase of a laser system is to use the f -to- $2f$ technique [5, 6]. It allows the carrier-envelope offset frequency f_{CEO} to be directly measured and conveniently stabilized in a servo loop. This servo loop either controls an acousto-optic modulator (AOM) to modify the pump power of the laser oscillator [20] or controls a piezo to swivel a mirror inside the cavity [21]. Both methods change the relative value of v_{group} and v_{phase} , thereby shifting f_{CEO} . A phase-stable offset frequency f_{CEO} is equivalent to a stable (and known) drift of the C-E phase ϕ ; for $n = f_{\text{rep}}/f_{\text{CEO}}$ every n^{th} pulse has an identical phase.

Correspondence to: Fax: +49 (0)89 32905-200, e-mail: Michael.Schaetzel@mpq.mpg.de

To generate stabilized high-power pulses, n is chosen as an integer and the ratio of the repetition rates of the oscillator and multipass amplifier is tuned so that only pulses of identical ϕ are amplified. The residual C-E phase drift after amplification is monitored by a second f -to- $2f$ interferometer and compensated in the same electronic loop controlling the oscillator [9]. Few-cycle pulses are then generated by spectral broadening of the amplified pulses in a hollow fiber [1] filled with neon and subsequent compression by reflections off chirped multilayer dielectric mirrors [22].

While this approach is very reliable in locking the phase ϕ , its value is not known and it is extremely sensitive to experimental parameters. Consequently, if the phase lock is lost it is not possible to lock to the same value as before, since the system has to be realigned. In addition, long-term stability cannot be guaranteed over extended periods of time (see Fig. 1), even if re-locking does not become necessary. The reason for this are small phase drifts which are not always compensated by the f -to- $2f$ technique. Two particularly noteworthy imperfections in the stabilization scheme are responsible for this: First, the f -to- $2f$ stabilization scheme relies on comparison of frequencies in the red and blue wings of the spectrum. Since dispersion at these wavelengths is different from the center wavelength decisive for the carrier-envelope phase, the present stabilization will introduce small phase errors as soon as it starts to compensate any drifts in the amplifier [23]. Second, the feedback for the phase stabilization is taken after the femtosecond laser amplifier but before the pulses are spectrally broadened in the hollow fiber and recompressed to few-cycle pulses. Any drifts in the latter part, possibly originating from beam-pointing instabilities and amplitude-phase coupling, are therefore not compensated. The first problem mentioned depicts an inherent shortcoming of the f -to- $2f$ scheme, namely the inability to correctly detect phase drifts induced outside the cavity of the mode-locked oscillator, while the second one merely is a technical problem.

Combining the stereo-ATI phase meter with an external stabilization loop as presented in this paper offers a powerful solution to these problems. The experimental setup is described in Sec. 3. The underlying physics of the stereo-ATI experiment has already been described elsewhere [4, 10] and is only briefly reviewed.

Above-threshold ionization is a prominent effect in photoionization at high intensity [24]. More photons than necessary for ionization can be absorbed and, accordingly, photoelectrons with a kinetic energy of many times the photon energy can then be observed. In the strong-field limit [25], a simple semi-classical model (for a review see [26]) explains this as follows: At some time t_0 , an electron enters the continuum due to tunnel ionization. The laser's electric field then accelerates the electron away from the atom. When the field changes direction, it may drive the electron back to its parent

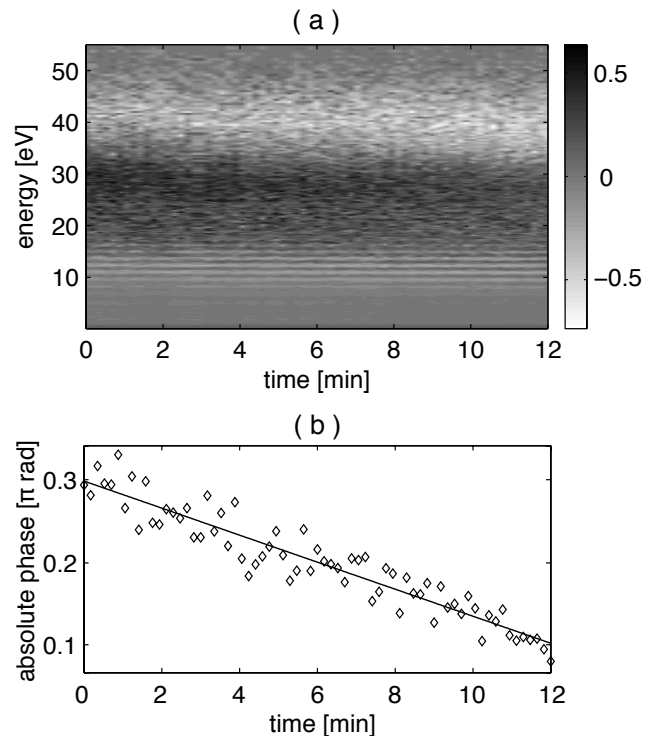


Fig. 1 (a) Measured left/right asymmetry $[(L-R)/(L+R)]$, where L (R) denotes the number of electrons seen on the left (right) detector] of the electron spectra in the *stereo-ATI* experiment, as a function of electron energy and time. Dark colors represent dominant left emission, bright colors dominant right emission. (b) Respective phase retrieved from panel (a) and the underlying raw data. Note that due to limited theoretical understanding the absolute value of the phase has an uncertainty of $\pi/10$, but the relative phase values are far more precise. Each experimental point corresponds to an integration time of 10 s. Note that the visible phase jitter is partly due to the short integration time chosen (corresponding to low count rates) and does not represent the shot-to-shot phase jitter of the laser. A clear linear phase drift (solid line) of ~ 50 mrad/min can be detected, which represents a typical value. The actual stability of the laser system varies with time, as does the value of the phase drift.

ion, where it may scatter either elastically or inelastically. The electron is then further accelerated by the electric field. In the electron spectra, the rescattering mechanism creates a plateau-shaped annex at the high-energy (> 25 eV) side of the nearly exponentially decreasing low-energy ‘direct’ electrons that did not undergo rescattering [27]. A simple classical calculation yields a maximum kinetic energy of $2U_p$ for direct electrons and $10U_p$ for elastically ‘rescattered’ electrons (the so-called ‘cut-off’). U_p denotes the ponderomotive energy $U_p = \mathcal{E}^2/4\omega_L^2$ (atomic units). Quantum mechanics considerably softens these sharp energy limits.

Due to the nonlinear nature of ATI, the carrier-envelope phase of the laser pulse is expected to play an important role [15, 18]. Not only does the position of the cut-off depend on the phase ϕ , but also the number of

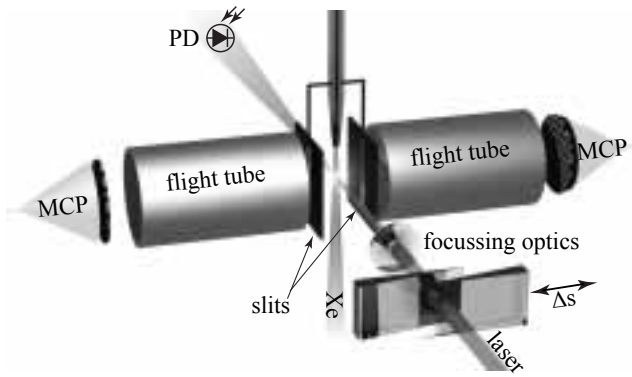


Fig. 2 “Stereo-ATI” spectrometer. PD: photodiode, MCP: microchannel plate. A pair of glass wedges (apex angle 2.8°) is used to adjust the carrier-envelope phase. The lens shown in the sketch is in reality a concave mirror. For more details see text of Sect. 3.

cycles contributing to a given energy, leading to phase-dependent peak structures. The idea of phase detection is to exploit this anisotropic electron emission. With linearly and circularly polarized light a significant left-right asymmetry is expected.

3 Experimental setup

The experimental setup consists of two parts: (i) the stereo-ATI phase meter (Fig. 2) combined with an appropriate software algorithm to determine the carrier-envelope phase ϕ of the laser pulses and (ii) a feedback loop controlling a device to keep (or set) ϕ at a given value. To use the combined machinery of laser and stabilization for an independent experiment applying phase-stable few-cycle pulses, the beam has to be split as shown in Fig. 3.

The acquisition of the photo-electron spectra relies on time-of-flight spectroscopy. Two opposing electrically and magnetically shielded drift tubes 50 cm in length are mounted in an ultrahigh-vacuum ($p < 10^{-7}$ mbar) apparatus. Rare-gas atoms fed in through a nozzle from the top are ionized by the few-cycle laser beam, which is focused with a concave mirror of focal length 250 mm (f-number 30). The laser polarization is linear and parallel to the flight tubes. Slits with a width of 250 μm are used to discriminate electrons created outside the laser focal region chosen. Electrons emitted to the left and to the right are independently detected by two 18-mm diameter microchannel plates (MCP, Burle BiPolar TOF Detector). The time-of-flight is measured by two computer-hosted multiscalers (FAST 7886, FAST ComTec, Oberhaching, Germany) with a time resolution of 0.5 ns. The start signal is generated by a fast photodiode (PD), recording the arrival of the laser pulse; the stop signal by the MCPs, recording the arrival of each electron at the end of the drift tube. The electrons’ time-of-flight is then used to calculate their kinetic energy. For

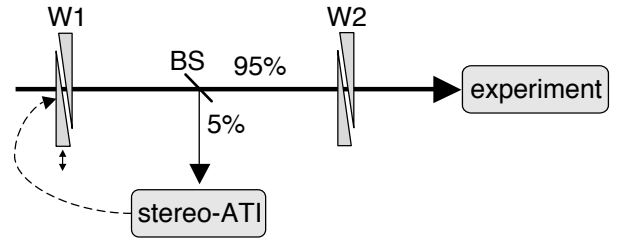


Fig. 3 Experimental arrangement used in order to run an independent experiment while guaranteeing a stable carrier-envelope phase for an extended length of time. The laser is divided with a beam splitter (BS) to steer a small part of the beam to the stereo-ATI setup. Less than 5% of the pulse energy ($\approx 20 \mu\text{J}$ for a pulse of 5 fs FWHM) is sufficient for ATI, leaving essentially the full power available. Careful dispersion compensation is achieved by separately tuning the amount of glass in the beam paths, ensuring short pulse durations in both the stereo-ATI and the other experiment of interest. W1 is the glass wedge controlled by the feedback loop to keep ϕ constant in the whole beam path afterwards. W2 can be used to conveniently change ϕ in the experiment without affecting any other parameter. Basically, everything up to W2 can be viewed as part of an ultra-stable laser system for any user not interested in the origin of the laser pulses needed to perform the experiment.

each laser shot about 50 electrons are recorded at each MCP. The characteristic appearance of the apparatus eventually resulted in the term *stereo-ATI* spectrometer.

The gas used for these experiments is xenon, known to exhibit a strong ATI plateau for few-cycle laser pulses [28]. Absorption of eight photons is necessary in order to subdue the ionization threshold, but processes of much higher order can be observed. The pulse energy is attenuated to 20 μJ . The pair of slits can be moved along the beam propagation direction from outside the vacuum apparatus. This allows the desired intensity to be selected, in our case $\approx 8 \cdot 10^{13} \text{ W/cm}^2$. Considerably higher intensities would result in detrimental saturation effects and, in particular, would smear out the characteristic plateau structure, which shows the most dramatic phase effects.

Careful analysis of the acquired ATI spectra yields the absolute value of the phase ϕ in the interaction region to within an accuracy of $\pi/10$ rad [10]. The acquisition of two ATI spectra in opposite directions immediately gives the value of the phase, without requiring comparison with other spectra corresponding to different phases. So far the characterization is not fully automated, since the photo-electron spectra depend not only on the phase but also on the atom species [28] and the intensity (dependent on both pulse length and power) in the interaction zone. However, for stabilization the actual value of ϕ need not be known and the sensitivity to phase deviations is much higher than the accuracy stated.

An immediate way of generating a phase-dependent error signal is to examine the measured spectra for asymmetries in the emission to the left and right. As shown

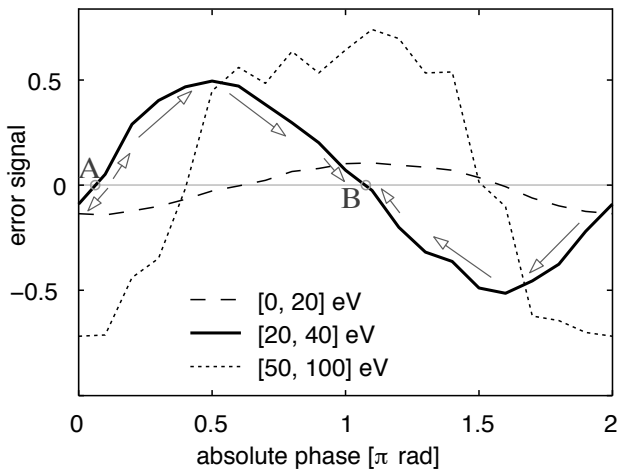


Fig. 4 Measured error signal as a function of the carrier-envelope phase for three different energy windows. The integration time is fixed to 40 s for each experimental point. The signal is calculated from the measured spectra as $(L - R)/(L + R)$, considering only the given energy window. The phase stabilization idea is as follows, denoted by the gray arrows: A proportional amount of glass is added (removed) for positive (negative) error signals. Thus, position A is unstable, whereas position B is stable.

in Fig. 4, the contrast of this method strongly depends on the energy region of the electrons considered. This is not surprising, since high-energy electrons are much more affected by the shape of the electric field due to the time delay introduced by the rescattering mechanism. The disadvantage of high-energy electrons is their considerably lower abundance as compared with low-energy electrons, which show a comparatively weak phase dependence. For an optimum choice of electrons both contrast and count rate have to be considered. A good compromise is obtained by considering the plateau range (here typically 20 – 40 eV). A proper integration time to acquire the error signal is also very important. Short integration times produce significant phase noise, whereas long integration times result in slow feedback, thus limiting the servo bandwidth. Since the stereo-ATI apparatus is supposed to correct long-term phase drifts, relatively long integration times can be used. Note that, regardless of the energy range and integration times chosen, better results are expected for shorter laser pulses, due to the stronger phase effects.

After detection of a phase drift, a means of correcting it is needed. Besides the standard methods of pump-power modulation or swiveling of a cavity mirror in the laser oscillator, another possible method is to introduce a known amount of glass into the beam path. Changing ϕ corresponds to delaying the envelope with respect to the carrier. This is equivalent to reducing the group velocity v_{group} with respect to the phase velocity v_{phase} of light, which can be achieved with normal dispersion of glass. At a central wavelength of 760 nm adding 52 μm of fused silica changes the phase by 2π without significantly af-

fecting the pulse duration. A pair of glass wedges (apex angle 2.8°), one of which is driven by a stepper motor ($\Delta x = \Delta s \tan(2.8^\circ)$) glass is introduced by a horizontal movement of Δs , is used here. The stabilization can thus be operated completely independently of the laser system as such.

Figure 4 also shows the idea of phase stabilization. If a positive error signal is recorded, a proportional amount of glass is introduced (i. e. the carrier-envelope phase is increased). Vice versa, if a negative error signal is recorded, a proportional amount of glass is removed (i. e. the carrier-envelope phase is decreased). With this procedure, there are two equilibrium positions, A and B, where the error signal is zero. Only position B is characterized by a *stable* equilibrium. The phase will therefore be stabilized to the corresponding value, in this case slightly higher than π . Stabilizing to different phase values is still possible by using a suitable offset for evaluating the error signal. Best results are expected however, where the slope of the error signal is largest, i. e. around zero. Furthermore, if one were to try to stabilize to a value coincident or close to an extremum of the error signal, the procedure would not converge. A more robust approach for stabilizing to an arbitrary value of the phase relies on simultaneous evaluation of error signals corresponding to different energy windows, because the relative positions of the respective extrema are different.

4 Results

In order to test the capability of the stereo-ATI apparatus for correcting low-frequency phase drifts, two basic experiments were performed. First, a slow, constant, and known carrier-envelope phase drift is applied by changing the amount of glass in the beam path by means of an additional pair of wedges. The stereo-ATI servo loop then drives the ‘corrective’ pair of wedges, as explained above. If the material and geometry of the two pairs of wedges are equal, their movement is expected to be identical but in opposite directions.

Figure 5 (a) shows the corresponding measurement. The first pair of wedges (dotted line) was moved at different speeds in both directions. The amount of glass introduced can be directly translated to a phase value. The movement of the second pair of wedges (lower gray line), controlled by the ATI signal, compensates in real time the phase drift deliberately introduced by the first. The resulting phase (black line) is constant within an error not exceeding 0.5 rad, while the phase drift covered considerably more than 6 rad. Panel (b) of the same figure shows the measured left/right asymmetry over the full electron spectra. The overall features are preserved during the measurement. This proves the capability of the stereo-ATI experiment of fully correcting phase drifts of more than π rad/min. Thorough examination reveals a slight shift in the spectra when the applied phase drift

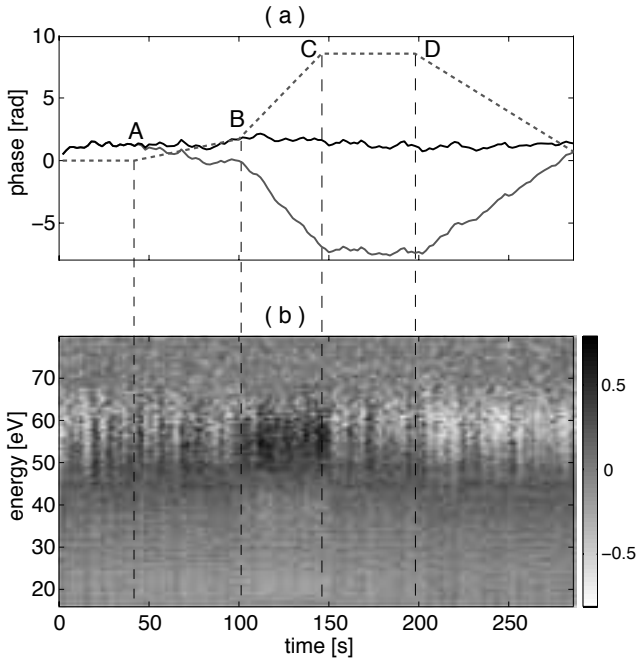


Fig. 5 (a) Phase variation deliberately introduced by a pair of glass wedges (dotted line) as a function of time. The pair of wedges driven by the stereo-ATI servo-loop (lower gray line) compensates in real time the induced phase drift, leading to a resulting total glass thickness (black line, converted to phase values) approximately constant. The induced phase drift was $+1.8$ rad/min (A-B), $+9.0$ rad/min (B-C), 0 rad/min (C-D), -5.4 rad/min (D-end). (b) Measured left/right asymmetry (same color coding as in Fig. 1) as a function of electron energy and time. From this the necessary movement of the ‘corrective’ wedge was derived.

is fast (between B and C). This is to be expected, since the temporal sequence of subsequent steps in this setup was (i) change the ‘error’ wedges, then (ii) measure the phase, and finally (iii) correct it by moving the ‘corrective’ wedges. It should also be borne in mind that typical phase drifts of the laser system without this additional servo loop are of the order of 50 mrad/min, more than two orders of magnitude less than in this example. Even here, as soon as the artificial phase drift stops, the initial spectral properties and thus the phase are quickly restored (see interval from C to D).

The second test aims at restoring the phase ϕ after it has been completely lost due to an external disturbance (e.g. laser readjustment). The stereo-ATI phase meter also offers a solution to this problem. Running the stabilization procedure in order to control the position of the ‘corrective’ glass wedge automatically stabilizes the phase exactly to the previous value. This is illustrated in Fig. 6, showing the carrier-envelope phase (deduced from the position of the ‘corrective’ pair of wedges) as a function of time. At the instants A, B, and C, the phase was intentionally changed by a large amount by externally changing the wedge position. This is analogous in all respects to relocking the phase to a different value

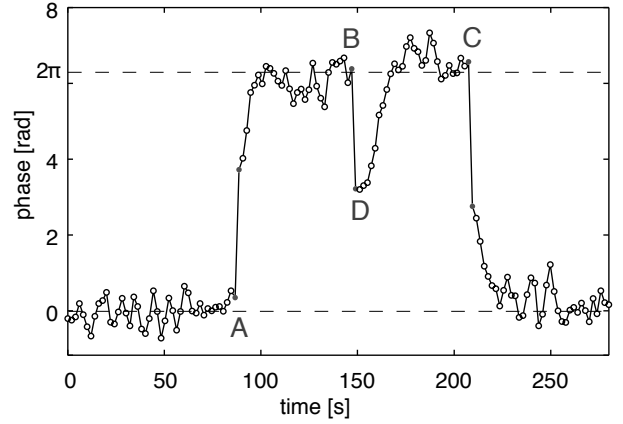


Fig. 6 Position of the ‘corrective’ glass wedge (translated in phase value) as a function of time. At the instants A, B, and C, large phase jumps were applied, and the phase is subsequently automatically recovered within an acceptable error. Note that, depending on where the closest stable position is, the automatic procedure either increases (after transitions A and B) or decreases (after transition C) the glass thickness. Note also the short-term stability D just after transition B, originating from the unstable equilibrium position shifted by π with respect to the stable one (see Fig. 4).

after laser readjustment. Subsequently, the servo loop takes action and ϕ soon reaches its initial value (modulo 2π). In some cases the stabilization can be slowed down in a locally stable phase region (Fig. 6 D and Fig. 4 A), but an appropriate algorithm or the concurrent use of error signals from different energy windows (Fig. 4) is able to avoid this.

The rather high noise in these two examples is due to pulse durations being not fully optimized. Accordingly, the contrast of the left/right signal was rather low. Longer integration times for each phase measurement can always minimize the noise.

5 Conclusion

A novel scheme to stabilize the carrier-envelope phase ϕ for an in principle unlimited time has been demonstrated. Even after a complete loss of stabilization the described stereo-ATI stabilization loop can restore the phase initially chosen. This was demonstrated in a recent experiment with a momentum spectrometer [11]. Such experiments have hitherto not been possible, since a measurement time of several hours for each carrier-envelope phase chosen was required.

Another appealing aspect of the ATI phase meter is the small amount of power (< 20 μ J) needed. Basically all the laser power is thus available for other experiments. Future technical improvements should further decrease the energy required, allowing also higher-repetition-rate lasers to operate simultaneous experiments. Another benefit is that the target gas pressure is so low ($p < 10^{-4}$ mbar) that the ATI experiment does

not affect the laser beam. The stereo-ATI apparatus can thus be placed anywhere in a beam line. In principle, if a long focus were available, it would even be possible to place the stereo-ATI and a second experiment in a single vacuum chamber, allowing real-time calibration and stabilization of the carrier-envelope phase.

The current disadvantage is the small bandwidth of the stabilization scheme, which limits its suitability to correcting only long-term phase drifts. Modifications to the acquisition of the electron spectra are being investigated with the ultimate aim of completely replacing the currently used second f -to- $2f$ servo loop, with the setup described here.

Acknowledgements This work was supported by the German Research Foundation (Grant No. PA730/2), the Welch Foundation (Grant No. A-1562), and the Austrian Science Fund (Grants No. F016, No. Z63, and No. P15382).

References

1. M. Nisoli, S. De Silvestri, and O. Svelto, *Appl. Phys. Lett.* **68**, (1996) 2793.
2. M. Nisoli, S. De Silvestri, O. Svelto, R. Szipöcs, K. Ferencz, Ch. Spielmann, S. Sartania, and F. Krausz, *Opt. Lett.* **22**, (1997) 522.
3. L. Xu, Ch. Spielmann, A. Poppe, T. Brabec, F. Krausz, and T. W. Hänsch, *Opt. Lett.* **21**, (1996) 2008.
4. G. G. Paulus, F. Grasbon, H. Walther, P. Villoresi, M. Nisoli, S. Stagira, E. Priori, and S. De Silvestri, *Nature* **414**, (2001) 182.
5. J. Reichert, R. Holzwarth, Th. Udem, and T. W. Hänsch, *Opt. Comm.* **172**, (1999) 59.
6. H. R. Telle, G. Steinmeyer, A. E. Dunlop, J. Stenger, D. H. Sutter, and U. Keller, *Appl. Phys. B* **69**, (1999) 327.
7. D. J. Jones, S. A. Diddams, J. K. Ranka, A. Stentz, R. S. Windeler, J. L. Hall, and S. T. Cundiff, *Science* **288**, (2000) 635.
8. A. Apolonski, A. Poppe, G. Tempea, Ch. Spielmann, Th. Udem, R. Holzwarth, T. W. Hänsch, and F. Krausz, *Phys. Rev. Lett.* **85**, (2000) 740.
9. A. Baltuška, Th. Udem, M. Uiberacker, M. Hentschel, E. Goulielmakis, Ch. Gohle, R. Holzwarth, V. S. Yakovlev, A. Scrinzi, T. W. Hänsch, and F. Krausz, *Nature* **421**, (2003) 611.
10. G. G. Paulus, F. Lindner, H. Walther, A. Baltuška, E. Goulielakis, M. Lezius, and F. Krausz, *Phys. Rev. Lett.* **91**, (2003) 253004.
11. X. Liu, H. Rottke, E. Eremina, W. Sandner, E. Goulielmakis, K. O. Keeffe, M. Lezius, F. Krausz, F. Lindner, M. G. Schätzel, G. G. Paulus, and H. Walther, *to be published*.
12. A. de Bohan, P. Antoine, D. B. Milošević, and B. Piraux, *Phys. Rev. Lett.* **81**, (1998) 1837.
13. G. Sansone, C. Vozzi, S. Stagira, M. Pascolini, L. Poletto, P. Villoresi, G. Tondello, S. De Silvestri, and M. Nisoli, *Phys. Rev. Lett.* **92**, (2004) 113904.
14. E. Cormier and P. Lambropoulos, *Eur. Phys. J. D* **2**, (1998) 15.
15. P. Dietrich, F. Krausz, and P. B. Corkum, *Opt. Lett.* **25**, (2000) 16.
16. D. B. Milošević, G. G. Paulus, and W. Becker, *Phys. Rev. Lett.* **89**, (2002) 153001.
17. S. Chelkowski and A. D. Bandrauk, *Phys. Rev. A* **65**, (2002) 061802.
18. D. B. Milošević, G. G. Paulus, and W. Becker, *Opt. Ex.* **11**, (2003) 1418.
19. X. Liu and F. de Morisson Faria, *Phys. Rev. Lett.* **92**, (2004) 133006.
20. A. Poppe, R. Holzwarth, A. Apolonski, G. Tempea, Ch. Spielmann, T. W. Hänsch, and F. Krausz, *Appl. Phys. B* **72**, (2001) 373.
21. Th. Udem, J. Reichert, R. Holzwarth, and T. W. Hänsch, *Phys. Rev. Lett.* **82**, (1999) 3568.
22. R. Szipöcs, K. Ferencz, Ch. Spielmann, and F. Krausz, *Opt. Lett.* **19**, (1994) 201.
23. P. Dombi, A. Apolonski, Ch. Lemell, G. G. Paulus, M. Kakehata, R. Holzwarth, Th. Udem, K. Torizuka, J. Burgdörfer, T. W. Hänsch, and F. Krausz, *New J. Phys.* **6**, (2004) 39.
24. P. Agostini, F. Fabre, G. Mainfray, G. Petite, and N. K. Rahman, *Phys. Rev. Lett.* **42**, (1979) 1127.
25. P. B. Corkum, *Phys. Rev. Lett.* **71**, (1993) 1994.
26. W. Becker, F. Grasbon, R. Kopold, D. B. Milošević, G. G. Paulus, and H. Walther, *Adv. At. Mol. Opt. Phys.* **48**, (2002) 35.
27. G. G. Paulus, W. Nicklich, H. Xu, P. Lambropoulos, and H. Walther, *Phys. Rev. Lett.* **72**, (1994) 2851.
28. F. Grasbon, G. G. Paulus, H. Walther, P. Villoresi, G. Sansone, S. Stagira, M. Nisoli, and S. De Silvestri, *Phys. Rev. Lett.* **91**, (2003) 173003.

Phase-controlled single-cycle strong-field photoionization

G. G. Paulus^{1,2,3}, F. Lindner³, D. B. Milošević⁴, W. Becker⁵

¹*Department of Physics, Texas A&M University, College Station, TX 77843-4242*

²*Sektion Physik, Ludwig-Maximilians-Universität München, 85748 Garching, Germany*

³*Max-Planck-Institut für Quantenoptik, 85748 Garching, Germany*

⁴*Faculty of Science, University of Sarajevo, Zmaja od Bosne 35, 71000 Sarajevo, Bosnia and Herzegovina and*

⁵*Max-Born-Institut, Max-Born-Strasse 2a, 12489 Berlin, Germany*

The evolution of the electric field of laser pulses consisting of a few optical cycles depends on the so-called absolute phase. Strong-field photoionization not only provides means to measure the absolute phase. Rather phase-controlled few-cycle pulses allow investigating photoionization on the attosecond time scale as the sub-cycle ionization dynamics becomes manifest in the photoelectron spectra. Few-cycle pulses thus can serve as a time-domain microscope for investigation of electronic transitions.

INTRODUCTION

The typical wavelength of Ti:Sapphire femtosecond lasers is ≈ 800 nm and corresponds to an optical period T of ≈ 2.5 fs. One of the most remarkable breakthroughs in femtosecond laser technology has been the generation of powerful pulses with a duration (FWHM) around 5 fs, i.e. pulses consisting of just 2 optical cycles (few-cycle pulses) [1]. This leads to the new situation that the pulse envelope \mathcal{E}_0 varies on the same time-scale as the electric field \mathcal{E} . More importantly, the temporal variation of the electric field depends on the phase φ of the carrier wave with respect to the envelope. This can be seen by expressing the field as a product of envelope and carrier:

$$\mathcal{E}(t) = \mathcal{E}_0(t) \cdot \cos(\omega t + \varphi). \quad (1)$$

Choosing the convention that $t = 0$ at the maximum of the envelope leads to “cosine-like” pulses for $\varphi = 0$ and “sine-like” pulses for $\varphi = -\pi/2$. As φ characterizes a global property of a few-cycle pulse, it is commonly referred to as the “absolute” phase.

The significance of the absolute phase comes from the fact that it determines by definition the field at and around the pulse maximum. Therefore, any application taking advantage of few-cycle pulses will depend on the absolute phase. So far, generation of soft-X-ray radiation and isolated attosecond pulses have taken advantage of control of the absolute phase [2]. It is foreseeable that coherent control of atomic and molecular behavior will be one of the next fields in this respect: absolute-phase-control together with control of spectral phase, amplitude and eventually polarization will allow generating tailored variations of strong electric fields. These will deform molecular potential surfaces in a virtually arbitrary way and should make possible to steer chemical reactions with unprecedented precision. An even nearer application could be electron-ion collisions: Atoms or ions ex-

posed to intense laser pulses are photoionized. During the ionization process, an appreciable fraction of the electron wave packet can return to the vicinity of the core with considerable kinetic energy. The returning electron wave packet corresponds to enormously high current densities otherwise only available in the most advanced accelerators. Using few-cycle pulses and controlling the absolute phase, it is possible to adjust conditions such that the electrons return at a zero crossing of the field and thus probe the ion core.

It is likely that the list of single or sub-cycle applications can be almost endlessly continued thus touching biophotonics, solid-state, nuclear, and plasma physics.

The absolute phase (or, to be precise, the rate with which it changes) has attracted attention in a field of physics hardly brought into connection with strong-field physics so far: Controlling the absolute phase [3–5] allows using femtosecond lasers as optical clock-works [6, 7]. In fact, the technical realization of phase-stabilization revolutionized optical frequency metrology in the past years and at the same time launched the field of phase-dependent strong-field physics outlined above [8]. Meanwhile it is possible to generate powerful few-cycle pulses with stabilized absolute phase [2]. However, measurement of the absolute phase has been achieved only very recently by photoionization [9] and by photoemission experiments [10].

PHOTOIONIZATION BY FEW-CYCLE PULSES

The purpose of this paper is to review basic aspects of photoionization with few-cycle pulses and its phase dependence. At near-infrared wavelengths ionization is a multiphoton process. This holds in particular for rare gas atoms as considered here. Multiphoton ionization at high field strength can cause atoms to absorb more photons than necessary for ionization leading to photo-

electron energies considerably higher than the photon energy (above-threshold ionization, ATI) [11]. In addition, the photoelectron can undergo a scattering process during ionization and thus acquire much higher kinetic energy [12]. The latter process is highly non-perturbative and leads to photoelectron spectra (ATI spectra) characteristic for intense-field photoionization: The ionization probability as a function of kinetic photoelectron energy decreases steeply for low energies, stays almost constant for energies beyond 20 to 30 eV, and rolls off after this so-called plateau-region (cutoff), see Figure 1. This general behavior is well understood and in fact can be explained with simple classical arguments [13]. For a recent review see [14].

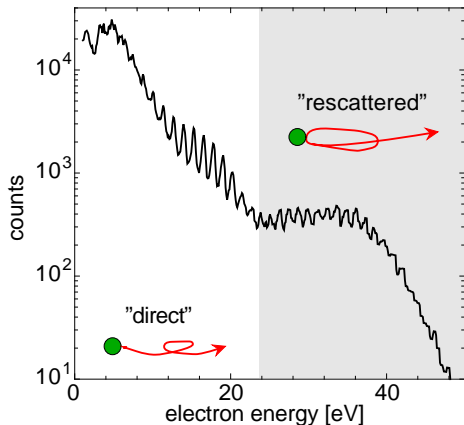


FIG. 1: Photoelectron spectrum of Xenon irradiated with 50 fs laser pulses of a peak intensity of $0.7 \cdot 10^{14} \text{ W/cm}^2$. Much more photons than necessary for ionization are absorbed by some atoms leading to photoelectron energies much higher than the photon energy (1.55 eV corresponding to a laser wavelength of 800 nm). A markedly non-perturbative behavior is observed for electron energies above $\approx 25 \text{ eV}$ (shaded part) as the ionization yield stays constant for an extended energy region thus leading to a plateau-like annex to the spectrum.

Coming back to few-cycle pulses, it is quite natural to predict a non-inversion symmetric electron yield from the asymmetric and phase-dependent shape of the field [15]. Therefore, an approach to detect and eventually measure the absolute phase is to record electrons emitted in opposite directions. The first work investigating this problem theoretically was published by Cormier and Lambropoulos [16]. They considered alkali atoms ionized with cosine-like pulses of moderate intensity, i.e. in the perturbative regime. The phase-effects predicted under these conditions were discouragingly small. Later work by Dietrich et al. [17], Christov [18], and Chelkowski and Bandrauk [19] used higher intensities and also higher ionization thresholds. However, only the total electron yield was considered. The asymmetries predicted for electron emission in opposite directions are in the 10% region for 5 fs-pulses and thus in principle readily observable. Only

recently, Milošević *et al.* [20] calculated electron spectra for strong-field ionization and obtained orders of magnitude stronger phase-effects for high-energy photoelectrons.

On the experimental side, the first report of an absolute-phase effect was observed in 2001 [21], although the absolute phase was randomly varying from pulse to pulse in that experiment. The key idea had been that the asymmetry in electron emission translates into an anti-correlation of electrons emitted in opposite direction if investigated shot by shot. Very recently, ATI has been studied using phase-stabilized few-cycle pulses which, as indicated above, yielded the first measurement of the absolute phase. Phase stabilization made possible to record photoelectron spectra (and not just total rates) as a function of the absolute phase. The experiment agreed with the theoretical finding that the phase-dependence of high-energy (i.e. plateau) electrons exceeds that of low-energy electrons (which determine also the total rate) by almost two orders of magnitude. It is therefore interesting to discuss the origin of this eye-catching difference in phase sensitivity.

LOW-ENERGY (“DIRECT”) PHOTOELECTRONS

Atomic behavior in intense laser field can – at least in a qualitative way – be well described within the strong-field approximation (SFA). Its classical version [22–24] assumes that an electron is lifted into the continuum at some time t_0 . Assuming the initial conditions $x(t_0) = 0$ and $\dot{x}(t_0) = 0$ [25, 26] the electron trajectory $x(t)$ can be calculated by solving the equation of motion

$$m\ddot{x} = F = -e \cdot \mathcal{E}(t), \quad (2)$$

where m is the electron mass and e the elementary charge. Apparently, the atomic potential V is neglected hereby. V enters only by determining the ionization rate R together with the field strength $\mathcal{E}(t_0)$. Obviously, a highly non-linear function of both V and \mathcal{E} has to be assumed. This situation is shown in Figure 2 for a sine- and cosine-like pulse with linear polarization being assumed. It is obvious that the asymmetry of R exceeds that of the field by far due to the nonlinearity of ionization.

Now it is most important to realize that an electron lifted into the continuum at $t = t_0$ will *not* necessarily fly in the (negative) direction of the electric field $\mathcal{E}(t = t_0)$ at that time t_0 of ionization. Rather from conservation of the canonical momentum

$$p_{\text{can}} = m\dot{x}(t) - \frac{e}{c}A(t) \quad (3)$$

together with the initial condition $\dot{x}(t_0) = 0$ it follows that a photoelectron created at $t = t_0$ will have a drift momentum proportional to the vector potential

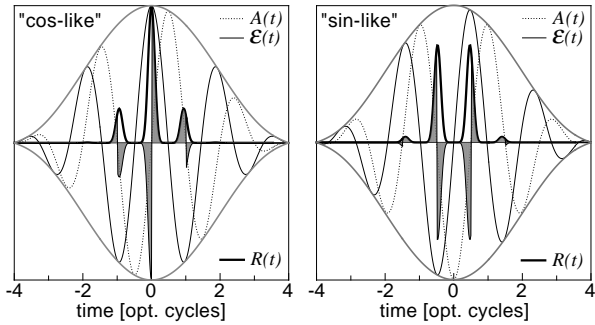


FIG. 2: Explanation for the weak phase dependence of low-energy (“direct”) electrons. The thin solid curve represents the electric field $\mathcal{E}(t)$ of a few-cycle pulse for absolute phase $\varphi = 0$ (cosine-like, left) and $\varphi = -\pi/2$ (sine-like, right). The instantaneous ionization rate $R(t)$ (bold curve) depends in a highly non-linear way on the magnitude of the electric field \mathcal{E} and thus amplifies the asymmetry. The electrons however eventually drift in the direction which the vector potential had at the time t_0 when the electron entered the continuum. Therefore, the number of electrons flying in positive direction is given by the integral of R over all times where A is positive and vice versa. One immediately sees that the phase effect is strongly reduced due to the deflection of the electrons by the oscillating field.

$A(t = t_0)$. The vector potential however has just the opposite parity than the field. A cosine-like field for example has a sine-like vector potential. Therefore, the ionization probability in positive direction is given by the integral of the ionization rate $R(t)$ over those times t for which $A(t)$ is positive and vice versa. This is also depicted in Figure 2. Two features following from this discussion are noteworthy.

First, the most asymmetric field variation (i.e. the \pm cosine-like pulse) leads to equal electron yield in opposite directions, while the most symmetric field leads to the most asymmetric electron emission. This surprising consequence of the strong-field approximation, however, should not be over-emphasized as the atomic potential neglected in the framework of the SFA might influence the electron trajectories due to the low kinetic energy of the majority of the photoelectrons [27].

The other consequence is less susceptible to details of the ionization process: The asymmetry in photoionization, which one might have expected to be very pronounced because of the non-linear dependence of ionization on field strength, in fact is extensively canceled by the deflection of the photoelectrons in the oscillating laser field.

For circular polarization the situation is different. There the electric field of a few-cycle pulse can be visualized as a screw the radius of which increases and eventually decreases within a few rotations. The absolute phase can be identified with the direction to which the field at the maximum of the pulse points. Changing the absolute phase therefore just changes the direction to which the field points at the maximum of the pulse.

Analogous to linear polarization, the momenta of the photoelectrons will be determined by the vector potential and the Coulomb potential. In contrast to linear polarization, however, electrons are emitted in all directions perpendicular to the laser beam and the spatial asymmetry in ionization, which is of course due to the spatial asymmetry of the field, is not cancelled by subsequent deflection of the photoelectrons in the field [17]. Circular polarization thus seems to offer advantages for phase measurement as compared to linear polarization. However, detailed calculations [28] unveil that the improvement is hardly bigger than a factor of 2. Under most circumstances this will not outweigh the disadvantages of circular polarization: Femtosecond lasers by construction produce linear polarization. Conversion to circular polarization is not trivial considering the tremendous bandwidth associated with few-cycle pulses [29]. More importantly, the processes underlying present approaches to attosecond physics [30–32] require linear polarization.

HIGH-ENERGY (“PLATEAU”) PHOTOELECTRONS

So far, only low-energy electrons were considered. From a technical point of view these (as compared to plateau electrons) appear to be much more interesting for a measurement of the absolute phase because of their higher abundance. However, recalling the mechanism of generation of plateau electrons leads to the conjecture that plateau electrons are much more sensitive to the absolute phase. This has in fact been proven valid in a recent experiment [9].

The plateau electrons originate from electron trajectories which return to the vicinity of the parent atom typically within less than one optical cycle. Such trajectories are only possible for linear polarization to which we come back now. If a returning electron is elastically back-scattered upon its revisit to the core at time $t = t_1$, it will be accelerated by the laser field due to the change in sign of the electron velocity at $t = t_1$. The maximum drift energy the electrons may acquire via this process is $10U_P$, where U_P denotes the ponderomotive potential [33]. Rescattering certainly is not the only option the returning electron has. Rather, scattering might also be inelastic. In the case of recombination this leads to the production of soft X-rays [34, 35] and attosecond pulses [31, 32], while non-sequential (i.e. correlated) multiple ionization is observed in the case of impact ionization [24, 36, 37]. Thus, all prominent effects of atoms in strong fields find a simple and intuitive explanation. However, one should not fail to mention highly visible effects which seem to be beyond this simple classical model as well as its quantum version [38–40].

In order to explain the origin of plateau electrons more explicitly, we first consider long pulses, i.e. the time-

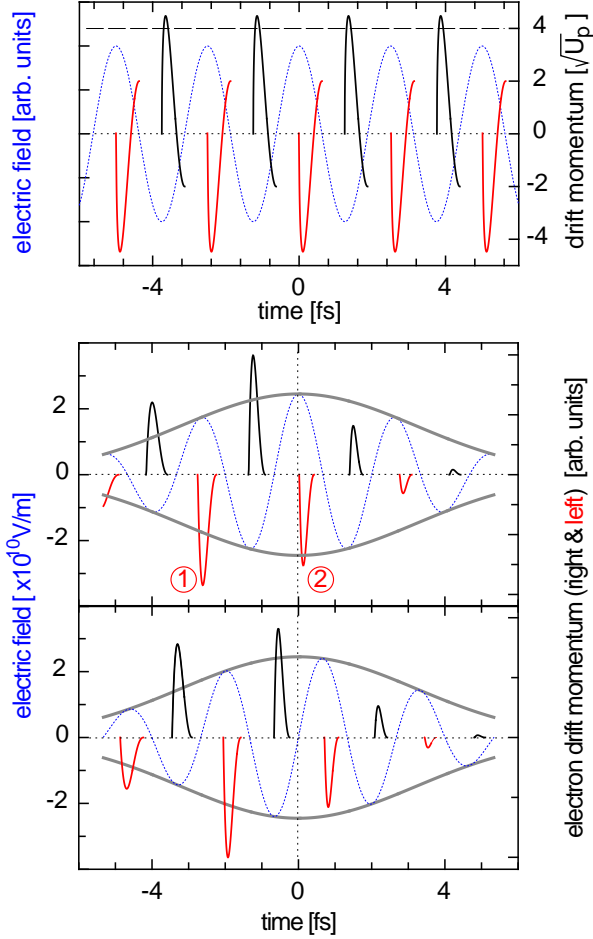


FIG. 3: Classical drift momentum of plateau electrons for long (upper panel) and few-cycle (lower pair of panels) laser pulses. The laser field is represented by the oscillating electric field (dotted curve). The other curves represent the drift momentum an electron will acquire if it rescatters elastically during the ionization process. This drift momentum is shown as a function of t_0 . Ionization in subsequent half cycles leads to electron emission in alternating directions (black and grey curves). The ionization probability for a certain electron energy and emission direction can be calculated by identifying all trajectories having the respective momentum. For $E = 8U_P$ ($p = 4\sqrt{U_P}$) and positive direction these are given by the intersections with the dashed line. Coherent summation yields the ionization probability, see Figure 4. For few-cycles pulses the pattern gets phase-dependent as expected. At first glance there does not seem to be much of a difference between emission in positive and negative direction. The maximum energy of the photoelectrons is similar. A high electron energy, however, does not necessarily mean that the yield of electrons is also high. Rather, the yield is determined by the field strength $\mathcal{E}(t_0)$. For example: Ionization at times labeled with (1) leads to electrons with higher energies than ionization near (2). Nevertheless, ionization will be much stronger for (2) because of the higher field strength, see also Figure 4.

dependence of the amplitude \mathcal{E}_0 is neglected. Always implying the well-established initial condition $\dot{x}(t_0) = 0$, returning trajectories are only possible if the initial ionization takes place between an extremum and the following zero crossing of the electric field, see Figure 3. Electrons injected into the field at a time t_0 where the field assumes an extreme value will return to the core exactly one optical cycle later, i.e. $t_1 = t_0 + T$. Obviously, the velocity of the electron then is zero again, $\dot{x}(t_1) = 0$. The other limiting case is injection of the electron at the zero crossing. This is a trivial case as $t_1 = t_0$ and consequently again $\dot{x}(t_1) = 0$. As the travel time $\tau := t_1 - t_0$ changes from T to 0 between these limiting cases, the velocity upon return $\dot{x}(t_1)$ cannot vanish for all t_0 . Therefore, there must be a maximum for $|\dot{x}(t_1)|$ and thus also for the return energy E_1 . Rescattering leads to a change in sign for $\dot{x}(t_1)$. This is the prerequisite for further acceleration of the electron in the field after $t = t_1$. It turns out that the maximum electron energy is reached for ionization times t_0 close to (but not at) extremal values of the field. The field strength at t_0 is very important because the probability for ionization at is a strongly non-linear function of $\mathcal{E}(t_0)$.

Usually, it is not explicitly mentioned that, besides a high field strength $\mathcal{E}(t_0)$, the amplitude after rescattering at $t = t_1$ should be as high as possible, too. This after all is self-evident for long pulses. However, it is exactly at this point where there is a qualitative difference between “ultrashort” (meaning femtosecond) pulses and few-cycle. In order to get an appreciable yield of high-energy electrons, $\mathcal{E}(t_0)$ and $\mathcal{E}(t > t_1)$ should be as high as possible. For a few-cycle pulse these two conditions are hard to meet at the same time because $t_1 - t_0$ is in the order of the optical period within which the amplitude of the field necessarily changes appreciably. Changing the absolute phase affects the interplay between these competing requirements for production of plateau electrons. This is the main (although not the only) reason for the high sensitivity of plateau electrons on the absolute phase.

TIME-DOMAIN INFORMATION OF ELECTRONIC TRANSITIONS

At this point, it might be instructive to realize another difference between low- and high-energy electrons. For the former, one can find an absolute phase for which both spectra corresponding to emission in opposite directions (parallel to the polarization) are the same. The simplest approach to explain this feature is to assume that ionization is an instantaneous process in the sense as outlined above: Electron yield and momentum are entirely determined by the field and the vector potential at $t = t_0$. Disregarding small effects from the non-vanishing derivative of the envelope, one can find an ab-

solute phase ($\varphi = 0$ when neglecting the Coulomb potential, see above) for which the ionization rate $R(t)$ is inversion symmetric with respect to time. This together with instantaneous ionization leads immediately to symmetric electron emission.

The high-energetic plateau electrons, in contrast, are created through a more complex mechanism that involves two times, namely the time t_0 at which the electron enters the continuum and the time t_1 at which it returns to the ion core and scatters. Under these circumstances, a pulse for which ionization in opposite directions would be the same is difficult to envision. Inversion symmetry as in the case of instantaneous ionization is not possible: An electron injected into the field before the maximum of the pulse envelope can acquire a much higher drift momentum as an electron injected in the inversion-symmetric instant, which is after the pulse maximum (see Figure 3). The built-in delay in the ionization process for plateau electrons breaks the symmetry discussed above.

This basic feature of photoionization as a function of the absolute phase is in beautiful agreement with the prevailing model of strong-field laser atom interaction. However, the experimental evidence also sticks a question mark on this model since symmetric ionization occurs at the “wrong” absolute phase. It is likely that this has to do with the Coulomb potential neglected in the strong-field approximation. Nevertheless, fundamental properties of phase-dependent photoionization spectra impose stringent conditions on possible alternatives and provide access to time-domain information on electronic transitions elapsing on the attosecond time scale.

Even more detailed temporal information can be gained by considering interference effects. We start by explaining how to calculate the ATI plateau in the framework of the classical model and include quantum aspects thereafter. From Figure 3 one can extract that, in general, electrons with a given drift momentum can be generated at several times t_0 within the pulse. In order to get the intensity of these electrons, the ionization probabilities at these times t_0 have to be added. A more complete model would also take into account the scattering cross section as a function of the impact energy.

Evidently, the “electrons” created at several instants t_0 within the laser pulse in reality are wave packets which may and, not surprisingly, which do interfere. For long pulses, in every optical cycle identical wave packets are created. This immediately leads to alternating constructive and destructive interference with a periodicity given by the photon energy. The interference pattern is nothing than the well-known ATI structure. For completeness we mention that two times within one optical (half-)cycle lead to electrons with the same momentum. Closer inspection shows that these two times correspond to a short and a long trajectory. Due to the smaller temporal distance, the resulting interference pattern has a longer periodicity in energy space. The interference of short and

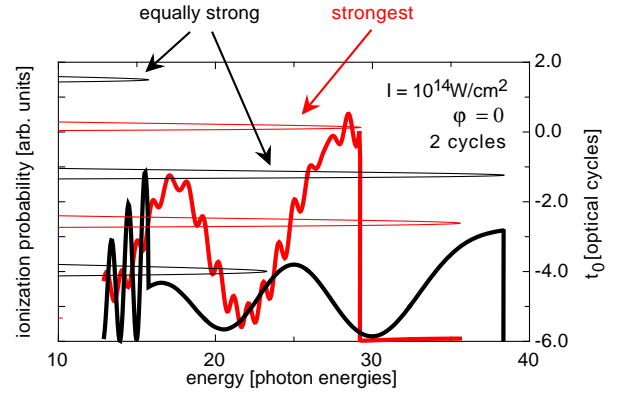


FIG. 4: Calculated ATI spectra (rescattered electrons only) for a cosine-like 2-cycle pulse. Like in Figure 3 black corresponds to emission in positive and grey to emission in negative direction. The strength of the electron signal and the contrast of the ATI peak structure is nicely explained by the analysis shown in Figure 3. To this end, the respective curves of that figure were converted to energy and rotated by 90° , i.e. the right ordinate is a time axis. The cutoff energies exhibited by the spectra are faithfully reproduced. The strength of the spectra is determined by the electric field corresponding to the horizontal spikes. Note that the pulse maximum has been chosen to be at $t = 0$. Therefore, strongest emission at high energy is observed in negative direction. Interference with high contrast is only possible, if two of the horizontal spikes contribute *and* if the corresponding field strength is similar for both. This is the case below $\approx 15\hbar\omega$ for emission in positive direction. The sharp cutoffs are an artefact of the classical model and would be smoothed in a quantum mechanical description [20].

long trajectories thus leads to a modulation of the envelope of ATI spectra.

In order to quantify such interference effects, the phases of the electron wave packets need to be calculated. This again is quite simple as the phase is given by S/\hbar , where S is the classical action of the electron trajectories considered throughout this article. An example for such a calculation is shown in Figure 4. ATI peak structure of high contrast needs at least two optical cycles which yield ionization of comparable strength. As it can be seen in Figures 3 and 4, for most electron energies and absolute phases there are at least two optical cycles. Nevertheless, ATI peak structure is weak or absent in most cases, in particular for moderate and high electron energies, see Figure 4. The reason is that the electric field amplitude in these different optical cycles is comparable only for a very small range of absolute phases. Appreciable contrast of interference structure excludes a high degree of “Welcher-Weg” information and thus knowledge which optical cycle and thus which trajectory contributed strongest to the signal at the detector. Phase-dependent interference effects as discussed here were already observed [9]. The future will show how much this eventually will contribute to the understanding of electronic transitions.

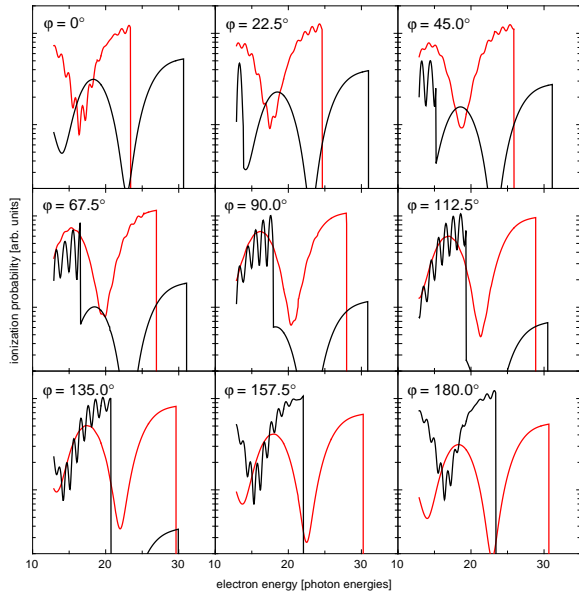


FIG. 5: Calculated ATI spectra (rescattered electrons only) for various absolute phases. Again, black (grey) curves correspond to spectra recorded in positive (negative) direction. The spectra are in good agreement with results from quantum calculations [20]. The intensity is $0.8 \cdot 10^{14} \text{ W/cm}^2$ and a logarithmic scale is used.

CONCLUSION

Fundamental aspects of laser of phase-dependent strong-field photoionization have been discussed. The different sensitivity of low- and high-energy electrons to the absolute phase has been explained employing simple classical arguments. Quantum mechanical extensions to the model allow explaining interference phenomena. All three phase effects discussed are suitable for measuring the absolute phase. Less profane, phase phenomena provide a new gateway to unsolved problems in strong-field laser matter interaction, in particular to the role of the atomic or ionic potential. A particular exciting aspect is direct access to time-domain information for electronic transitions, photoionization being their prototype. Clearly, the vision to drive atomic and molecular behavior and reactions by single optical cycles and to steer them by controlling the absolute phase has come close to reality. The single-cycle aspect together with attosecond timing precision bears the character of time-domain microscopy of such reactions.

GGP and DBM gratefully acknowledge support by the Welch-Foundation and the Volkswagen-Stiftung, respectively.

- [1] M. Nisoli *et al.*, *Appl. Phys. Lett.* **68**, 2793 (1996).
M. Nisoli *et al.*, *Opt. Lett.* **22**, 522 (1997).
- [2] A. Baltuska *et al.*, *Nature* **421**, 611 (2003).
[3] J. Reichert *et al.*, *Opt. Comm.* **172**, 59 (1999).
[4] D. J. Jones *et al.*, *Science* **288**, 635 (2000).
[5] A. Apolonski *et al.*, *Phys. Rev. Lett.* **85**, 740 (2000).
[6] J. N. Eckstein, Thesis, Stanford Univ. (1978).
[7] H. R. Telle *et al.*, *Appl. Phys. B* **69**, 327 (1999).
[8] S. T. Cundiff, *J. Phys. D* **35**, R43 (2002).
[9] G. G. Paulus *et al.*, submitted to *Phys. Rev. Lett.* .
[10] A. Apolonski *et al.*, (submitted).
[11] P. Agostini *et al.*, *Phys. Rev. Lett.* **42**, 1127 (1979).
[12] G. G. Paulus *et al.*, *Phys. Rev. Lett.* **72**, 2851 (1994).
[13] G. G. Paulus *et al.*, *J. Phys. B* **27**, L703 (1994).
[14] W. Becker *et al.*, *Adv. At. Mol. Opt. Phys.* **48**, 35 (2002).
[15] A relationship of few-cycle pulses with bichromatic fields with commensurate frequencies is obvious:
A. N. Chudinov *et al.*, *Opt. Quan. Elect.* **23**, 1055 (1991)
D. W. Schumacher *et al.*, *Phys. Rev. Lett.* **73**, 1344 (1994)
[16] E. Cormier and P. Lambropoulos, *Eur. Phys. J. D* **2**, 15 (1998).
[17] P. Dietrich *et al.*, *Opt. Lett.* **25**, 16 (2000).
[18] I. P. Christov, *Appl. Phys. B* **70**, 459 (2000).
[19] S. Chelkowski and A. D. Bandrauk, *Phys. Rev. A* **65**, 061802(R) (2002).
[20] D. B. Milošević *et al.*, *Opt. Expr.* **11**, 1418 (2003)
[21] G. G. Paulus *et al.*, *Nature* **414**, 182 (2001).
[22] H. B. v. Linden v.d. Heuvel and H. G. Muller, in *Multiphoton Processes, Studies in Modern Optics* No. 8, 25, Cambridge (1988).
[23] K. C. Kulander *et al.*, in *Proceedings of the SILAP III Workshop*, Plenum Press, New York (1993).
[24] P. B. Corkum, *Phys. Rev. Lett.* **71**, 1994 (1993).
[25] T. F. Gallagher, *Phys. Rev. Lett.* **61**, 2304 (1988).
[26] S. J. McNaught *et al.*, *Phys. Rev. Lett.* , 626 (1997).
[27] V. R. Bhardwaj, *Phys. Rev. Lett.* **86**, 3522 (2001).
[28] D. B. Milošević, private communication.
F. Lindner, private communication.
[29] S. Stagira *et al.*, *Phys. Rev. A* **66**, 033810 (2002).
[30] H. Niikura *et al.*, *Nature* **417**, 917 (2002).
[31] P. M. Paul *et al.*, *Science* **292**, 1689 (2001).
[32] M. Hentschel *et al.*, *Nature* **414**, 509 (2001).
[33] The ponderomotive potential is defined as the quiver energy of a free electron in an oscillating electric field. A useful formula is $U_P = 0.09337 \cdot I[\text{W/cm}^2] \cdot \lambda^2[\text{m}]$. For a wavelength of $\lambda = 800 \text{ nm}$ and an intensity of $I = 10^{14} \text{ W/cm}^2$ the ponderomotive energy will be $U_P = 6 \text{ eV}$ which is almost four times the photon energy.
[34] M. Ferray *et al.*, *J. Phys. B* **21**, L31 (1988).
[35] J. J. Macklin *et al.*, *Phys. Rev. Lett.* **70**, 766 (1993).
[36] A. l'Huillier *et al.*, *Phys. Rev. A* **27**, 2503 (1983).
[37] Th. Weber *et al.*, *Nature* **405**, 658 (2000).
[38] M. B. Gaarde *et al.*, *Phys. Rev. Lett.* **84**, 2822 (2000).
[39] E. Eremina *et al.*, *J. Phys. B* **36**, 3269 (2003).
[40] F. Grasbon *et al.*, submitted.

[1] M. Nisoli *et al.*, *Appl. Phys. Lett.* **68**, 2793 (1996).
M. Nisoli *et al.*, *Opt. Lett.* **22**, 522 (1997).

High-order harmonic generation at a repetition rate of 100 kHzF. Lindner,^{1,*} W. Stremme,¹ M. G. Schätzel,¹ F. Grasbon,¹ G. G. Paulus,^{1,2} H. Walther,^{1,2} R. Hartmann,³ and L. Strüder³¹*Max Planck Institut für Quantenoptik, Hans-Kopfermann-Strasse 1, 85748 Garching, Germany*²*Ludwig-Maximilians-Universität München, Am Coulombwall 1, 85748 Garching, Germany*³*Max Planck Institut für extraterrestrische Physik, Halbleiterlabor, Otto-Hahn-Ring 6, 81739 München, Germany*

(Received 25 February 2003; published 18 July 2003)

We report high-order harmonic generation (HHG) in rare gases using a femtosecond laser system with a very high repetition rate (100 kHz) and low pulse energy ($7 \mu\text{J}$). To our knowledge, this is the highest repetition rate reported to date for HHG. The tight focusing geometry required to reach sufficiently high intensities implies low efficiency of the process. Harmonics up to the 45th order are nevertheless generated and detected. We show evidence of clear separation and selection of quantum trajectories by moving the gas jet with respect to the focus, in agreement with the theoretical predictions of the semiclassical model of HHG.

DOI: 10.1103/PhysRevA.68.013814

PACS number(s): 42.65.Ky

I. INTRODUCTION

When a short, intense laser pulse interacts with an atomic gas, the atoms respond in a nonlinear way and emit efficiently coherent radiation at frequencies that are odd multiples of the laser frequency [1,2]. In recent years this phenomenon of high-order harmonic generation (HHG) has become one of the major topics in multiphoton physics, since it provides a unique source of high-brightness coherent radiation extending to the vacuum ultraviolet (VUV) and soft x-ray spectral ranges. Applications of such light sources are naturally in the fields of spectroscopy and holography. Furthermore, harmonics extending into the “water window” (4.4–2.3 nm) have been generated by means of tabletop laser systems [3,4], opening the way to applications in photobiology. A high repetition rate is especially desirable in the field of metrology, for coincidence experiments, and also in situations where space charge effects play a critical role.

A full understanding of the physical process can increase the flexibility of these sources in terms of spectral characteristics and tunability [5], and is therefore essential for future applications in many fields of physics. Furthermore, the effort towards increased conversion efficiencies has recently become one of the main issues in HHG [6–11]. In this respect, a thorough comprehension of the physics involved is a necessary step in the search for new solutions. For a recent review of HHG see Ref. [12].

This paper presents experimental results of HHG obtained by means of a femtosecond laser system with very high repetition rate (100 kHz). This is orders of magnitude higher than what has been reported to date for HHG. It should be pointed out that the conditions of our experiment are indeed different from those normally reported for HHG, where energies in the μJ range can be reached in the harmonics comb itself [10], whereas we use $7 \mu\text{J}$ pulses to generate the harmonics. In fact, to our knowledge, this is the first experimental study of HHG at this relatively low pulse energy. Nevertheless, the conventional theoretical treatment of HHG is

highly applicable and provides a simple tool for interpreting experimental results.

The paper is organized as follows. In Sec. II we recall the basic semiclassical theory of HHG and show how this model can be used to take into account single-atom response as well as phase-matching effects. In Sec. III we introduce the experimental setup, including the laser system and the extreme ultraviolet (XUV) spectrometer. In Sec. IV phase-matching effects are shown to dominate the macroscopic response of the medium, in agreement with theoretical predictions. In particular, it is shown that the position of the gas jet with respect to the laser focus can select a single “quantum trajectory” followed by the electron [13].

II. QUASICLASSICAL TREATMENT

A breakthrough in the theoretical framework is represented by the so-called three-step model [14,15]. According to it, the physical process of HHG can be regarded as consisting of three sequential steps. First, ionization occurs by tunneling of the electron through the potential barrier created by the atomic potential perturbed by the intense laser field. Then (second step) the dynamics of the free electron is classically governed by the oscillating laser field. The electron, therefore, follows a trajectory that strongly depends on the intensity and phase of the laser at the moment of tunneling. For linear polarization the electron may revisit the ion core, and recombination can take place (third step), giving rise to a photon with an energy equal to the instantaneous kinetic energy of the “returning” electron plus the ionization potential of the atom.

This description clearly indicates the role of the laser field amplitude and phase in determining the evolutions of the electron trajectory and subsequent photon emission. Since the approach is classical, the solution simply consists in solving the equation of motion of a free electron in an oscillating electric field. In the following, we consider a linearly polarized periodic field:

$$E = E_0 \sin(\omega t), \quad (1)$$

where ω is the laser’s angular frequency. The electron is assumed to be shifted into the continuum with zero velocity

*Electronic address: fal@mpq.mpg.de-

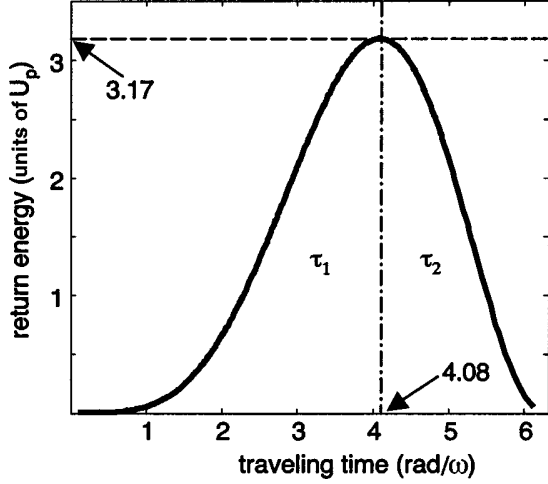


FIG. 1. Calculated kinetic energy of the electron revisiting the ion core as a function of the traveling time τ . U_p = ponderomotive energy of the laser, ω = angular frequency of the laser, τ_1 = “short” trajectories, τ_2 = “long” trajectories.

at some phase ωt_0 of the external laser field. The evolution of the electron can easily be determined from Eq. (1). Particularly, interesting for HHG is the time t_1 when the electron revisits the ion. An elegant graphical solution for determining it has been proposed [16]. Introducing the so-called “traveling time” $\tau = t_1 - t_0$, i.e., the time interval spent by the electron in the continuum, also provides an analytical solution:

$$t_0 = \frac{1}{\omega} \arctan\left(\frac{-\omega\tau + \sin\omega\tau}{1 - \cos\omega\tau}\right), \quad (2)$$

from which all parameters of interest (return time t_1 and corresponding kinetic energy) can be found.

The main results of this approach are summarized in Fig. 1, showing the instantaneous kinetic energy of the returning electron (in units of the ponderomotive energy U_p of the laser, i.e., the mean kinetic energy acquired by the electron during a cycle of the field, $U_p \propto E^2$) as a function of the traveling time (in units of phase of the laser field). The calculation predicts a maximum of $3.17U_p$ for the kinetic energy of the returning electron. This happens if tunneling occurs at a field phase of 1.88 rad, with a correspondent traveling time of 4.08 rad/ ω . The subsequent maximum photon energy is given by $3.17U_p + I_p$, where I_p is the ionization potential of the atom. A sharp cutoff in the harmonic spectrum has been predicted [17] and observed [18], validating this simple physical model.

For energies lower than the cutoff, two different solutions exist. Since they differ in the traveling time, they are referred to as short (τ_1) and long (τ_2) trajectories. In particular, trajectories that started earlier (laser field phase at tunneling < 1.88 rad) will return later. The picture suggests similarities to a classical projectile motion, the launch angle to the vertical being replaced by the phase of the electric field.

The fact that the harmonic emission shows peaks at odd multiples of the fundamental frequency is due to parity con-

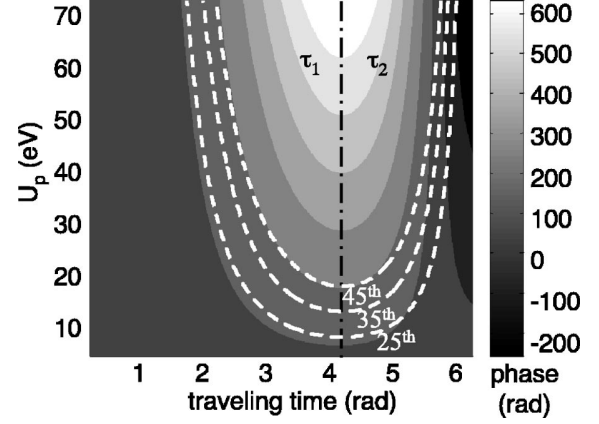


FIG. 2. Contour plot of the phase of the emitted harmonic field in argon as a function of the traveling time τ and laser ponderomotive energy U_p . The dashed lines represent the 25th, 35th and 45th harmonics.

servation in centrosymmetric media (typically rare gases). Similarly, the periodicity of the electric field shows that even orders, as well as arbitrarily generated frequencies, do not add in phase from cycle to cycle. They are thus rapidly washed out, whereas odd orders grow up from cycle to cycle and give a nonzero net contribution.

A fully quantum mechanical model [19] confirms the validity of the results listed above, indicating that only a few relevant quantum trajectories actually contribute to the harmonic emission. In addition, this model emphasizes the role of the phase of the emitted harmonic electric field. Indeed, since a large number of atoms are involved, the macroscopic response of the medium critically depends on the relative phases of the elementary electric fields.

According to the quantum model [20] and in the spirit of Feynman’s path integral method, the radiation is emitted with a phase with respect to the fundamental proportional to the so-called quasiclassical action acquired by the electron along the trajectory followed:

$$S(p, t_0, t_1) = \int_{t_0}^{t_1} dt \left(\frac{p^2(t)}{2m_e} + I_p \right), \quad (3)$$

where t_0 is the tunneling time, t_1 the recombination time, p the electron’s classical momentum, m_e the electron mass, and I_p the ionization potential of the atom. Since recombinations take place at different times t_1 , all phases must be referred to a common time axis. The phase of the emitted elementary harmonic field then reads

$$\theta = -\frac{S(p, t_0, t_1)}{\hbar} + q\omega t_1, \quad (4)$$

where q stands for the harmonic order and ω stands for the laser’s angular frequency.

By solving the equation of motion it is possible to calculate the above integral for all possible times t_0 . Since the focusing of the laser beam in the experiments causes strong spatial variation of the intensity, it is particularly interesting to investigate the dependence of the phase of the emitted harmonics on the intensity.

Figure 2 shows a contour plot of the phase θ as a function

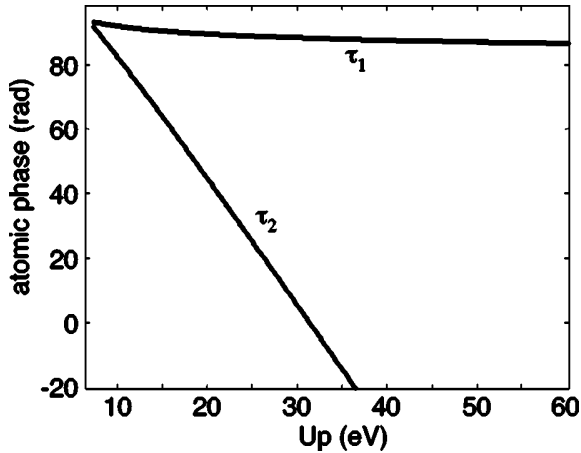


FIG. 3. Intensity dependence of the 25th harmonic in argon for the short (τ_1) and long (τ_2) trajectories.

of the laser ponderomotive energy U_p and the traveling time τ . The atomic gas is argon and the fundamental wavelength is 800 nm. The dashed line connects all points giving rise to a harmonic photon of equal energy (e.g., 39 eV in Fig. 2, corresponding to the 25th harmonic). Short trajectories (τ_1 , left-hand side of the plot) are characterized by small variation of the phase along the line, whereas long trajectories (τ_2 , right-hand side of the plot) undergo appreciable variation of the phase. The dependence is found to be almost linear:

$$\theta = -\eta U_p, \quad (5)$$

and the coefficient η depends strongly on the type of trajectory followed (τ_1 or τ_2) and only slightly on the harmonic order and ionization potential of the atoms. For instance, for the 25th harmonic of Fig. 2 we find phases of $\theta_2 = -3.9U_p$ rad/eV and $\theta_1 = -0.11U_p$ rad/eV for the long and short trajectories, respectively. In fact, the linear approximation is very good for the former, but a bit rough for the latter, as can be seen in Fig. 3. Moreover, these values also depend on the harmonic order. In particular, harmonics generated by long trajectories are characterized by a slope slightly decreasing with increasing harmonic order, while the opposite applies to short trajectories.

Besides this intrinsic intensity-dependent “atomic” phase, one has to take into account the phase induced by the fundamental laser beam, known as the “Gouy” phase [21]. This depends on the focusing geometry only, and produces a phase shift (on axis) of $q\pi$ while passing through the focus. Incidentally, this behavior could explain the observed [22] reduction of the plateau extent, as compared with the prediction of the single-atom response. This can be understood by observing that good phase matching requires that the phase variation induced by the atomic phase be compensated by the geometrical Gouy phase. Figure 4 shows the sum of these two phases (on axis) for the case of the short trajectory and for a low-order harmonic (11th), indicating that this compensation selects an area of “good” phase matching. Since only the geometrical phase scales with the harmonic order q , de-

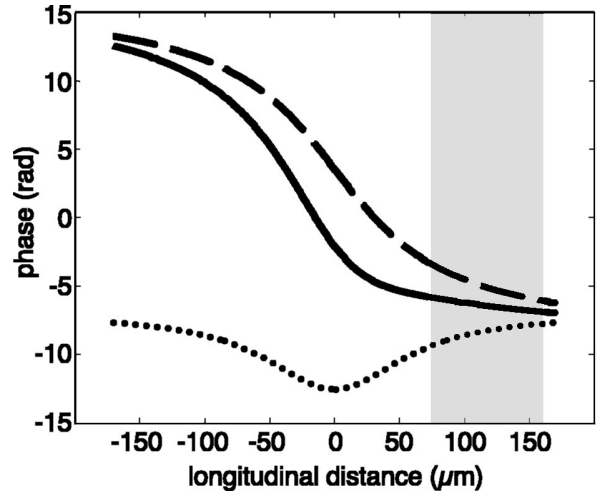


FIG. 4. Phase-matching plot on axis for the 11th harmonic (short trajectory) in argon. The laser parameters are as indicated in Sec. III. The dashed, dotted, and solid lines represent the geometrical, atomic, and resulting phases, respectively. The shading represents the area of “good” phase matching.

pending on the laser parameters phase matching will eventually degrade with increasing harmonic order, thus leading to a reduced plateau extent.

For the sake of completeness, one should also consider dispersion effects due to neutral atoms, ions, and, in particular, free electrons. However, since in our experiments we deal with low pressures (<10 mbar) and very tight focusing geometry (f -number 8), none of these effects play a crucial role. Even in the (nonrealistic) case of complete ionization of the atomic medium, the coherence length (i.e., the length over which the phase slippage is π) associated with the dispersion of the free electrons is of the order of the laser confocal parameter. In this range, the variation of the Gouy phase is much larger. Hence, all dispersion effects will be neglected.

One might argue that the atomic phase does not produce a large phase variation through the focus compared with the Gouy phase either, and that one could also neglect it. Note, however, that both the Gouy phase and free electron dispersion phase have odd symmetry around the focus, while the atomic phase has even symmetry, being proportional to the intensity. Neglecting it would thus qualitatively change the physical picture, while neglecting the free electron phase only results in a (good) numerical approximation. This observation is also supported by the experimental results (see Sec. IV) that clearly indicate the balancing of two-phase contributions of different symmetry.

Figure 5 shows contour plots of the phase of the 25th harmonic generated in argon. It results from the sum of the intrinsic atomic phase and the geometrical phase, including the Gouy phase and the curvature of the laser phase front. The laser parameters correspond to those used in our experiments (see Sec. III). The beam propagates from left to right, and the radial symmetry is guaranteed. Note that, according to the model, the diagrams have physical meaning only inside the solid line, where the intensity is high enough to

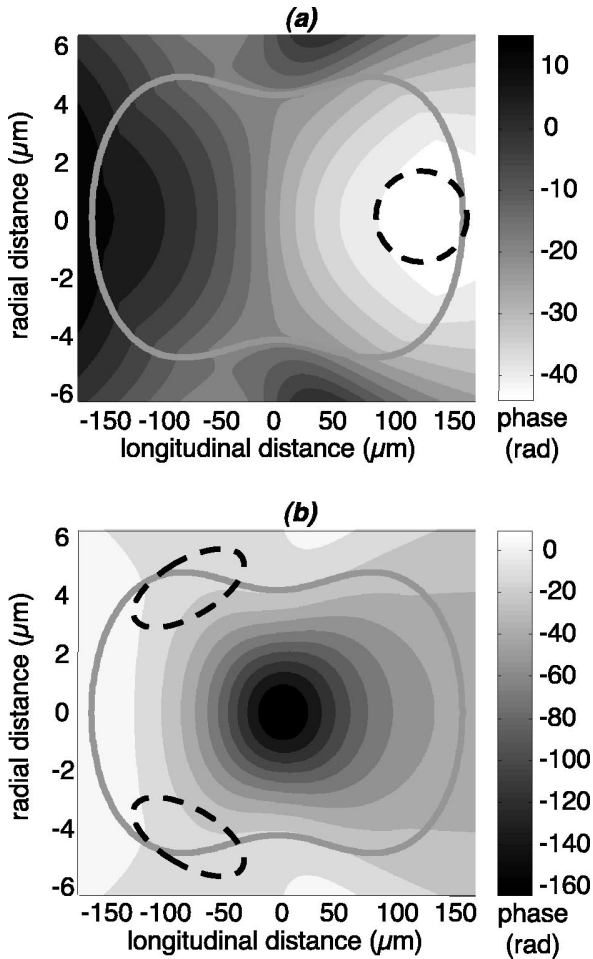


FIG. 5. Contour map of the phase of the 25th harmonic in argon for the short (a) and long (b) trajectories. The laser parameters are as indicated in Sec. III. The solid lines represent the cutoff intensity for the 25th harmonic; the dashed lines indicate areas of “good” phase matching.

create the harmonic considered. The harmonic field can efficiently develop only if phases during generation match over a significant area. For the sake of clarity, the phase accumulated by the propagation of a plane wave in the forward direction ($-qkz$) has already been subtracted. Constructive interference in the forward direction therefore occurs where the displayed phases have the same value, i.e., where the gradient approaches zero (dashed-line regions in Fig. 5).

A striking difference appears in phase-matching conditions for short [Fig. 5(a)] and long [Fig. 5(b)] trajectories. The latter gives rise to a rapidly varying phase, with only a small off-axis annular region of good phase matching before the focus [23]. On the other hand, short-trajectory-generated harmonics show a quite flat phase, with a large on-axis region of very good phase matching after the focus. This behavior has been pointed out in the previous works [24,25] and can be reproduced fairly well by means of the semiclassical model. These remarkable differences should be recognizable in the experimental results.

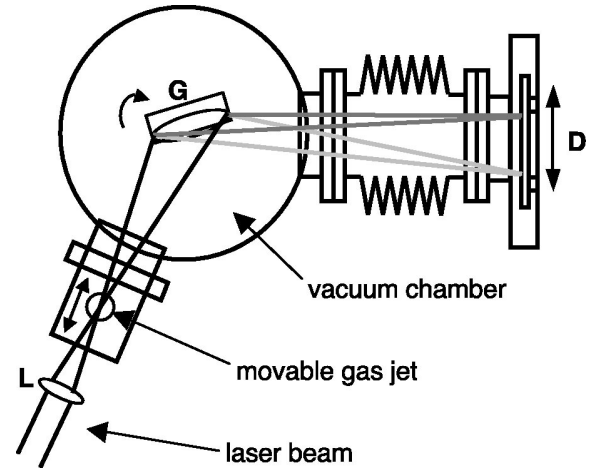


FIG. 6. The XUV spectrometer for high-order harmonic detection. L, achromatic lens ($f=80$ mm); G, flat-field toroidal grating; D, pn-CCD detector.

III. EXPERIMENTAL SETUP

The laser system [26] used in our experiments is an 800-nm Ti:sapphire regenerative amplifier system delivering pulses of $7 \mu\text{J}$ at a repetition rate of 100 kHz. It consists of a femtosecond oscillator, a regenerative amplifier, a prism compressor and a spatial light modulator in a $4f$ setup for fine dispersion compensation. The pulse duration is 35 fs full width at half maximum.

The relatively low pulse energy requires a tight focusing geometry in order to reach the high intensities necessary for driving the nonlinear process. The beam is expanded and focused (f -number 8) with an achromatic lens ($f=80$ mm, B. Halle Nachfl., Berlin) into a rare gas jet. Intensities of up to $3 \times 10^{14} \text{ W/cm}^2$ are reached in the focus ($U_p=18$ eV). However, since the interaction volume is extremely small (confocal parameter $\approx 100 \mu\text{m}$), the conversion efficiency into the harmonics comb is $< 10^{-9}$, i.e., lower than normally reported in HHG experiments. The detection of the light field has, therefore, to be optimized. Advantage can be taken of the very high repetition rate of the laser. However, also high efficiency of the XUV spectrometer is essential. This is schematically illustrated in Fig. 6.

The gas pressure before the effusive nozzle (diameter = $100 \mu\text{m}$) is usually kept between 100 and 300 mbar. The nozzle position can be finely adjusted in all directions. On the basis of gas flow measurements, we estimated a pressure in the interaction volume not exceeding 5–10 mbar. Note that at these low pressures the absorption length ($L_{abs} = 1/\sigma\rho$, where ρ is the gas density and σ is the ionization cross section [27]) for, for example, the 25th harmonic generated in argon is a few millimeters, i.e., much larger than the medium length. In this particular focusing geometry, reabsorption, therefore, does not play any role.

The generating gases used in our experiments are typically argon, krypton, and xenon. Due to the lower ionization potential, the latter is characterized by a higher yield and a less pronounced plateau extension. However, no qualitative differences have been observed with respect to quantum tra-

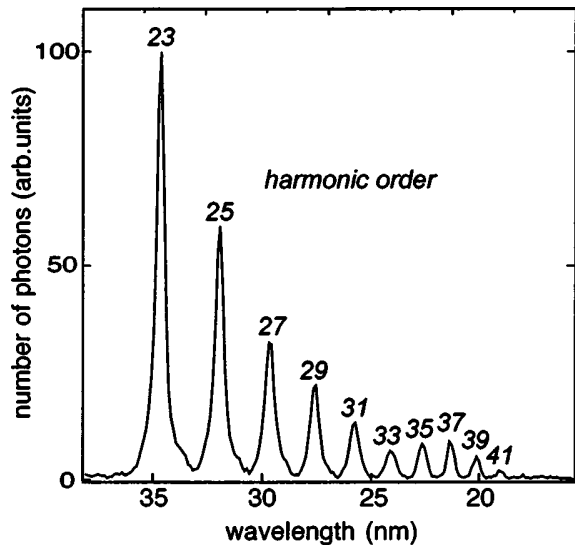


FIG. 7. Typical harmonic spectrum detected with the XUV spectrometer.

jectory separations. For this reason, most systematic studies were carried out with argon (see Sec. IV).

The high-order harmonics generated are incident on a flat-field toroidal grating (1800 grooves/mm, Jobin-Yvon Instruments, S.A.) that separates and focuses the harmonics. A thin (2000 Å) aluminum filter in front of the detector removes scattered light from the fundamental beam. The detector is placed in the focal plane at a distance of approximately 40 cm from the grating. It consists of a backside illuminated pn-charged coupled device (CCD) chip [28,29] of very high quantum efficiency (20–70 %) in the range 15–70 eV. The detector length is 30 mm (64×200 pixels), which yields a spectral resolution of approximately 1 Å/pixel. Figure 7 shows a typical harmonics spectrum.

IV. TRAJECTORY SEPARATION

In Sec. II the different behaviors of phase-matching conditions with respect to the electron trajectory were pointed out. In particular, the optimum occurs in a region located after the focus, and short trajectories τ_1 are favored. Figure 8 shows the measured conversion efficiency into the 25th harmonic as a function of the nozzle position with respect to the focus. The generating gas is argon. Although the gas jet size is comparable to the focus size in our experiments, testing of the position dependence of phase matching is still possible owing to the density profile of the gas.

The maximum conversion efficiency occurs approximately 100 μm after the focus, indicating, in agreement with the theoretical analysis, that the short trajectory dominates [see Fig. 5]. Note that other effects producing asymmetries, such as reabsorption in the atomic gas, would lead to a maximum on the opposite side of the focus. Hence, what is observed is clearly a phase-matching effect. The observed asymmetry also indicates, as already outlined in Sec. II, that phase terms of different symmetry (i.e., the Gouy and atomic phases) compensate each other.

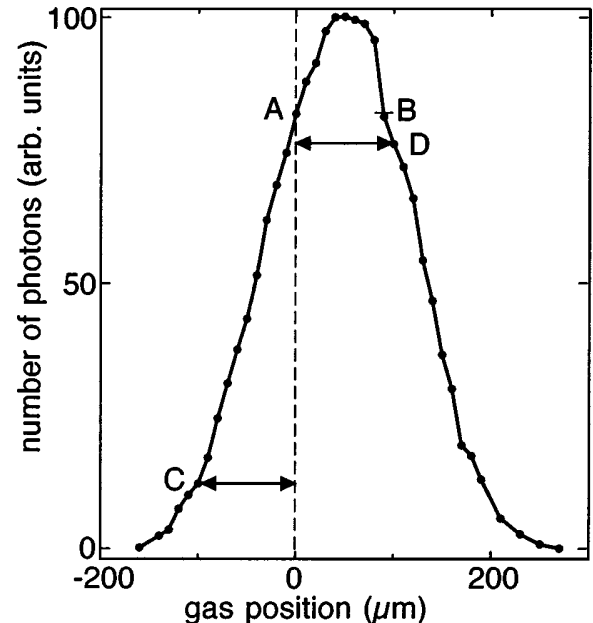


FIG. 8. Conversion efficiency (arb. units) for the 25th harmonic in argon as a function of the position of the gas jet. The laser parameters are as indicated in Sec. III.

The phase modulation induced by the atomic response discussed in Sec. II has interesting consequences on the spectral characteristics of the high-order harmonics generated [12]. Since we are dealing with short pulses and high peak intensities, the rapid time variation of the intensity results in modulation of the instantaneous harmonic frequency:

$$\delta\omega = -\frac{\partial\theta}{\partial t} = +\eta\frac{\partial I}{\partial t}, \quad (6)$$

and therefore in broadening of the spectrum. In particular, the leading edge of the harmonic pulse is blue shifted, and the trailing edge is red shifted. In other words, the generated harmonic carries a negative chirp that depends on the peak intensity, the pulse duration, and the slope (η) of the atomic phase. This phenomenon is similar to self-phase modulation of an intense laser pulse in a medium with negative Kerr index n_2 [30]. A measurement of this induced chirp on high harmonics was recently proposed [31].

The maximum broadening should be observed at the laser focus, where the temporal derivative of I is largest. Figure 9(a) shows the spectrum of the 25th harmonic for two different positions of the gas jet (A and B in Fig. 8). For both positions the conversion efficiency (represented by the integral of the harmonic peak) is the same, i.e., the number of photons generated is equal. As expected, when the gas jet is located exactly in the focus (case A), the larger phase modulation experienced results in a broader peak than in case B, where the peak intensity is lower.

More interestingly, we can compare the spectra corresponding to two symmetric positions of the nozzle with respect to the focus [Fig. 9(b), corresponding to positions C and D in Fig. 8]. The peak intensity of the fundamental is now the same in the two cases, and differences in the spectra

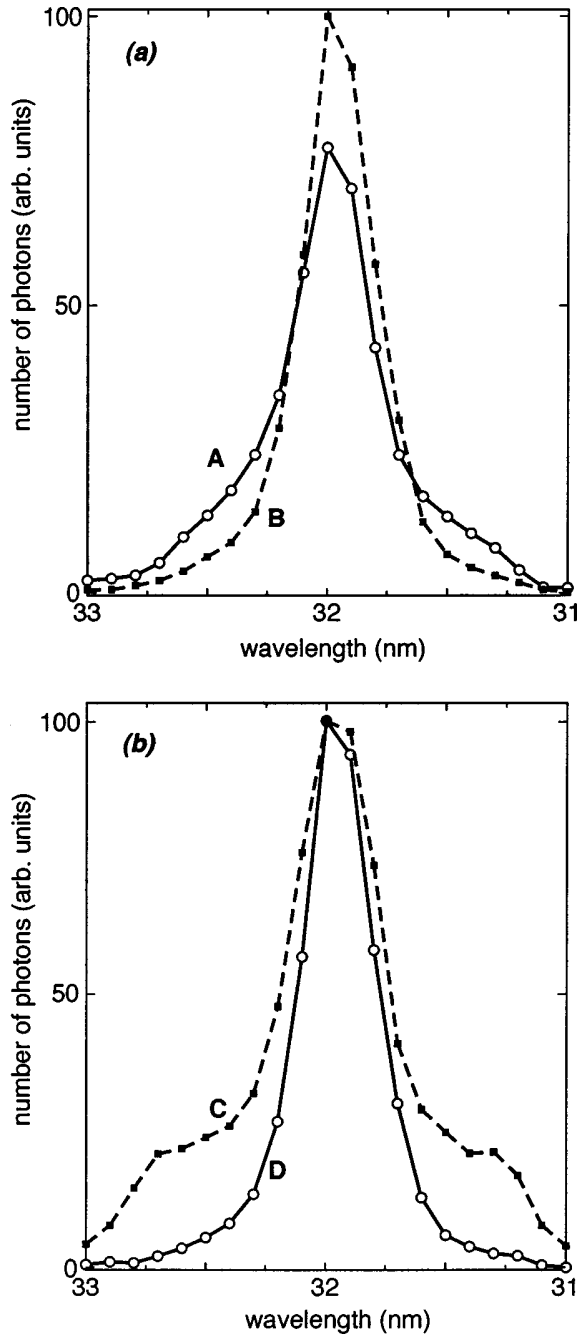


FIG. 9. Spectrum of the 25th harmonic peak for various positions of the gas jet (A, B, C, D of Fig. 8). (a) Influence of the peak intensity on the spectral broadening. The conversion efficiency (represented by the integral of the spectrum) in A and B is identical. (b) Influence of the electron trajectory on the spectral broadening. Since the conversion efficiency in C is lower than that in D, suitable normalization is necessary for the sake of clarity.

must be explained in terms of the coefficient η in Eq. (6). The peak observed in D is relatively narrow, while in C it is broader and suggests a double structure. Indeed, the position C corresponds [see Fig. 5] to a region where the harmonics can be efficiently generated off axis from the electrons that have followed the long (τ_2) trajectory. In fact, the spectrum

in C may actually consist of two superimposed contributions, one from the short trajectory (with phase matching almost degraded), giving rise to the central peak, and the other from the long trajectory (with increasingly good phase matching), leading to the observed wings in the spectrum. The harmonic pulse would thus be characterized by different generation processes, and therefore by regions of different spatial and temporal coherence [32,33].

The chirp of the harmonics induced by the rapid phase variation can, in principle, be controlled by an appropriate chirp on the fundamental laser pulse. If the fundamental beam carries a positive chirp, the “red” frequencies on the leading edge of the pulse will be blue shifted, and the “blue” frequencies on the trailing edge will be red shifted. The resulting spectrum will thus appear quite narrow and will be limited by the natural bandwidth of the harmonic pulse. On the other hand, for a negative chirp on the fundamental one should observe enhanced spectral broadening. This has been pointed out both theoretically [34] and experimentally [35,36]. However, these experiments were conducted under conditions where ionization plays a major role, resulting in strong blue shifting or red shifting of the harmonic radiation.

Numerical estimates similar to that presented in Ref. [33] show that, at least for orders where a clear separation between short and long trajectories is possible, i.e., not too close to the cutoff, this control is only possible for harmonics generated with the short trajectory. Indeed, the phase variation corresponding to the long trajectory is so large that the correspondent chirp determines in any case the observed spectral width. This is not true of the τ_1 contribution, characterized by a slower phase variation (see Fig. 3), for which chirp compensation is feasible.

By locating the gas jet in a position where the short trajectory dominates, we analyzed the spectra of the harmonic peaks as a function of the chirp of the fundamental. This can easily be changed by adjusting the voltages of the spatial light modulator used in the laser system [26]. Figure 10 shows the spectra of the 27th harmonic in argon for positive, negative, and zero chirp applied. These are purely quadratic and correspond approximately to $+200 \text{ fs}^2$, -200 fs^2 (corresponding to a pulse duration of 40 fs), and 0 fs^2 (35 fs). Since the pulses become longer when they carry a residual chirp, the conversion efficiency (represented by the integral of the harmonic spectrum) is higher in the case of no chirp. Note that no relevant blue or red shifting of the harmonic peak can be observed, indicating that ionization is not a major effect in our experiments.

The narrow peak and the enhanced broadening observed for application of positive and negative chirp, respectively, confirm the agreement between the theoretical analysis and the experimental data. In particular, the macroscopic separation into the two quantum trajectories is here once more corroborated. Furthermore, this last result traces an extremely simple way of tailoring the shape of the spectrum on demand, a feature that might be essential for future applications of high harmonics.

V. CONCLUSION

We have presented experimental results obtained under conditions different from those normally reported for HHG.

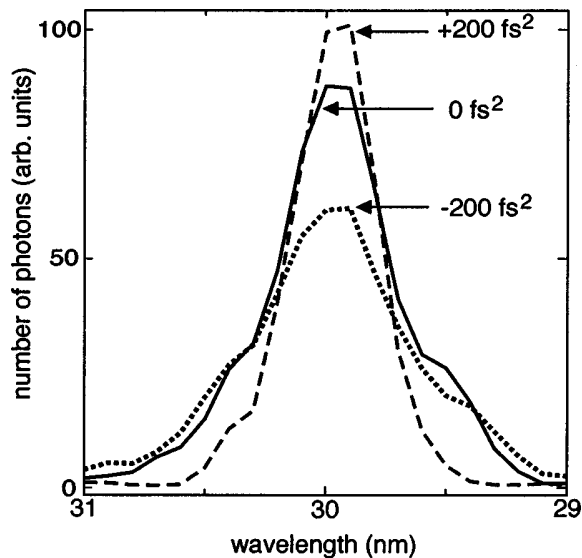


FIG. 10. Spectrum of the 27th harmonic peak for positive (dashed line), negative (dotted line), and zero (solid line) chirp of the fundamental beam.

To our knowledge, this is the first experimental study of high-order harmonics performed at very high repetition rate (100 kHz). The low pulse energy requires extremely tight focusing geometry, normally not used in HHG for the consequent low conversion efficiency. Under these conditions,

free electrons due to ionization do not play a crucial role and phase matching is entirely determined by the atomic and geometrical phases.

Despite these differences with normal HHG setups, we have shown that the semiclassical treatment of the physical process is essentially valid and represents a simple method of intuitively modeling the single-atom response and predicting the macroscopic response of the atomic media. We identified clear evidence of phase-matching effects and, in particular, of separation of quantum trajectories by adjusting the gas position. This effect, predicted [33] and observed [13], is here confirmed under qualitatively different experimental conditions.

It should be noted that not only is separation of the harmonic field into the two τ_1 and τ_2 components a significant result from the point of view of theoretically understanding the HHG process, it can also represent a way of providing xuv radiation with desired spatial and spectral characteristics. In this respect, adjusting the laser fundamental chirp seems to be an efficient way of shaping the spectrum of the harmonics and hence their coherence properties.

ACKNOWLEDGMENTS

We would like to thank R. Stötter and C. von Zanthier for technical support with the CCD detector, F. Zacher for the initial design of the experiment, and P. Salières for fruitful discussions of the physics.

- [1] M. Ferray, A. L'Huillier, X.F. Li, L.A. Lompré, G. Mainfray, and C. Manus, *J. Phys. B* **21**, L31 (1988).
- [2] A. McPherson, G. Gibson, H. Jara, U. Johann, T.S. Luk, I.A. McIntyre, K. Boyer, and C.K. Rhodes, *J. Opt. Soc. Am. B* **4**, 595 (1987).
- [3] C. Spielmann, N.H. Burnett, S. Sartania, R. Koppitsch, M. Schnürer, C. Kan, M. Lenzner, P. Wobrauschek, and F. Krausz, *Science* **278**, 661 (1997).
- [4] Z. Chang, A. Rundquist, H. Wang, M.M. Murnane, and H.C. Kapteyn, *Phys. Rev. Lett.* **79**, 2967 (1997).
- [5] C. Altucci, R. Bruzzese, C. de Lisio, M. Nisoli, S. Stagira, S. De Silvestri, O. Svelto, A. Boscolo, P. Ceccherini, L. Poletto, G. Tondello, and P. Villoresi, *Phys. Rev. A* **61**, R021801 (1999).
- [6] A. Rundquist, C.G. Durfee, III, Z. Chang, C. Herne, S. Backus, M.M. Murnane, and H.C. Kapteyn, *Science* **280**, 1412 (1998).
- [7] M. Schnürer, Z. Cheng, M. Hentschel, G. Tempea, P. Kálmán, T. Brabec, and F. Krausz, *Phys. Rev. Lett.* **83**, 722 (1999).
- [8] E. Constant, D. Garzella, P. Breger, E. Mével, Ch. Dorrer, C. Le Blanc, F. Salin, and P. Agostini, *Phys. Rev. Lett.* **82**, 1668 (1999).
- [9] Y. Tamaki, J. Itatani, Y. Nagata, M. Obara, and K. Midorikawa, *Phys. Rev. Lett.* **82**, 1422 (1999).
- [10] J.-F. Hergott, M. Kovacev, H. Merdji, C. Hubert, Y. Mairesse, E. Jean, P. Breger, P. Agostini, B. Carré, and P. Salières, *Phys. Rev. A* **66**, R021801 (2002).
- [11] A. Paul, R.A. Bartels, R. Tobey, H. Green, S. Weiman, I.P. Christov, M.M. Murnane, H.C. Kapteyn, and S. Backus, *Nature (London)* **421**, 51 (2003).
- [12] P. Salières, A. L'Huillier, P. Antoine, and M. Lewenstein, *Adv. At., Mol., Opt. Phys.* **41**, 83 (1999).
- [13] P. Salières, B. Carré, L. Le Déroff, F. Grasbon, G.G. Paulus, H. Walther, R. Kopold, W. Becker, D.B. Milošević, A. Sanpera, and M. Lewenstein, *Science* **292**, 902 (2001).
- [14] K.C. Kulander, K.J. Schafer, and J.L. Krause, in *Super-Intense Laser-Atom Physics*, Vol. 316 of *NATO Advanced Study Institute, Series B: Physics*, edited by B. Piraux, A. L'Huillier, and K. Rzazewski (Plenum, New York, 1993).
- [15] P.B. Corkum, *Phys. Rev. Lett.* **71**, 1994 (1993).
- [16] G.G. Paulus, W. Becker, and H. Walther, *Phys. Rev. A* **52**, 4043 (1995).
- [17] J.L. Krause, K.J. Schafer, and K.C. Kulander, *Phys. Rev. Lett.* **68**, 3535 (1992).
- [18] A. L'Huillier and Ph. Balcou, *Phys. Rev. Lett.* **70**, 774 (1993).
- [19] M. Lewenstein, Ph. Balcou, M.Yu. Ivanov, A. L'Huillier, and P.B. Corkum, *Phys. Rev. A* **49**, 2117 (1994).
- [20] M. Lewenstein, P. Salières, and A. L'Huillier, *Phys. Rev. A* **52**, 4747 (1995).
- [21] A.E. Siegman, *Lasers* (University Science Books, Mill Valley, CA, 1986).
- [22] A. L'Huillier, M. Lewenstein, P. Salières, Ph. Balcou, M.Yu. Ivanov, J. Larsson, and C.G. Wahlström, *Phys. Rev. A* **48**, R3433 (1993).

- [23] Note that slightly better phase-matching conditions could be expected by considering local propagation in arbitrary directions (i.e., subtracting tilted waves in Fig. 5), which would yield harmonics of bigger divergence. However, the position and size of the areas of good phase matching do not significantly change for small angles.
- [24] P. Salières, A. L'Huillier, and M. Lewenstein, *Phys. Rev. Lett.* **74**, 3776 (1995).
- [25] Ph. Balcou, P. Salières, A. L'Huillier, and M. Lewenstein, *Phys. Rev. A* **55**, 3204 (1997).
- [26] F. Lindner, G.G. Paulus, F. Grasbon, A. Dreischuh, and H. Walther, *IEEE J. Quantum Electron.* **38**, 1465 (2002).
- [27] W.F. Chan, G. Cooper, X. Guo, G.R. Burton, and C.E. Brion, *Phys. Rev. A* **46**, 149 (1992).
- [28] R. Hartmann, K.-H. Stephan, and L. Strüder, *Nucl. Instrum. Methods Phys. Res. A* **439**, 216 (2000).
- [29] L. Strüder, *Nucl. Instrum. Methods Phys. Res. A* **454**, 73 (2000).
- [30] A.E. Shen, *The Principles of Nonlinear Optics* (Wiley-Interscience, New York, 1984).
- [31] T. Sekikawa, T. Katsura, S. Miura, and S. Watanabe, *Phys. Rev. Lett.* **88**, 193902 (2002).
- [32] M. Bellini, C. Lyngå, A. Tozzi, M.B. Gaarde, T.W. Hänsch, A. L'Huillier, and C.G. Wahlström, *Phys. Rev. Lett.* **81**, 297 (1998).
- [33] M.B. Gaarde, F. Salin, E. Constant, Ph. Balcou, K.J. Schafer, K.C. Kulander, and A. L'Huillier, *Phys. Rev. A* **59**, 1367 (1999).
- [34] P. Salières, P. Antoine, A. de Bohan, and M. Lewenstein, *Phys. Rev. Lett.* **81**, 5544 (1998).
- [35] J. Zhou, J. Peatross, M.M. Murnane, H.C. Kapteyn, and I. Christov, *Phys. Rev. Lett.* **76**, 752 (1996).
- [36] Z. Chang, A. Rundquist, H. Wang, I. Christov, H.C. Kapteyn, and M.M. Murnane, *Phys. Rev. A* **58**, R30 (1998).

Dispersion Control in a 100-kHz-Repetition-Rate 35-fs Ti:Sapphire Regenerative Amplifier System

F. Lindner, G. G. Paulus, F. Grasbon, A. Dreischuh, and H. Walther

Abstract—This paper presents a 100-kHz femtosecond amplifier system delivering pulses with a duration of 35 fs and an energy of 7 μJ . The system does not include a stretcher, since the large amount of dispersion accumulated during the amplification process is sufficient to prevent self-focusing. Compensation in approximately all orders is achieved through a combination of a prism compressor, chirped mirrors, and a liquid-crystal modulator, allowing the amplified pulses to be shortened to nearly the bandwidth limit.

Index Terms—Dispersion control, femtosecond laser, high repetition rate, pulse shaping, regenerative amplifier, ultrafast optics.

I. INTRODUCTION

FEMTOSECOND technology based on Ti:sapphire crystals opened the way to generating intense optical fields using reliable tabletop laser systems. Lasers based on this technology are used to explore elementary processes in many fields of physics, chemistry, and photobiology [1]. The energies of the laser pulses generated directly from various types of Ti:sapphire oscillators are suitable for specific applications. Many others require, however, higher pulse energies. The problem of achieving the highest energies without damaging the crystal is usually solved by stretching the input pulse before amplification and recompressing it afterwards. This technique is referred to as chirped-pulse amplification (CPA) [2], [21].

There are two basic amplifier designs. In a multipass amplifier, the beam passes a few times through a gain medium pumped with a pulsed source. In a regenerative amplifier, on the other hand, the pulse is injected into a resonator (pumped either continuous wave (CW) or pulsed) and is ejected after many round trips, when amplification has saturated.

The multipass configuration has two main advantages [3]. First, the absence of a cavity reduces the buildup of amplified spontaneous emission (ASE). Second, due to the high gain (in the strongly pumped medium), fewer passes are needed and the total accumulated dispersion is much less than in the regenerative configuration. The repetition rate of the output pulses from multipass amplifiers is given by the pump laser (~ 10 Hz to

10 kHz). At 1 kHz, 15-fs pulses are obtained with a pulse energy of 1 mJ [4]. A multipass system with sub-30-fs pulse durations which delivers ~ 1.4 mJ at 5 kHz was recently reported [5].

In regenerative amplifiers, the pump-signal overlap does not change on successive passes through the gain medium. Therefore, this design is more suitable when a high number of passes in the crystal is required. At 5 kHz, 30-fs pulses are obtained in a single-stage regenerative amplifier system showing saturation after about 20 round trips [6]. Furthermore, the highest repetition rates (> 10 kHz) are only possible with CW pumping. In that case, a Q switch in the amplifier cavity is used to suppress ASE and achieve optimal amplification. The upper limit of the repetition rate is then imposed by the radiative lifetime of the Ti:sapphire (~ 3 μs) to ~ 250 kHz. At this repetition rate, pulse energies of ~ 3 μJ at a pulse duration of < 60 fs can be achieved with a commercially available system (RegA 9050, Coherent) based on the setup of [7]. However, the maximum energy storage occurs at a repetition rate of 100 kHz.

It should be noted that a combination of different amplifiers allows peak powers of terawatts [8] with femtosecond pulses at low repetition rates (up to 1 kHz). These multistage systems [9], [22], [23] are capable of producing peak intensities exceeding $\sim 10^{19}$ W/cm², i.e., an intensity regime where relativistic effects play a major role in the interaction of light with matter.

The tabletop system presented here can achieve an intensity of more than $5 \cdot 10^{14}$ W/cm² (f-number 8) at a repetition rate of 100 kHz. It proves to be a perfect tool for investigating above-threshold ionization and high-harmonic generation phenomena [10], [24], [25]. Conventional chirped-pulse-amplification is not used, i.e., the laser pulses are not stretched in a dedicated stage before amplification. Nevertheless, the pulses have to be compressed due to the large amount of dispersion accumulated during the amplification process. Compensation of dispersion in many orders is possible through an efficient combination of several optical techniques: a special prism compressor, chirped mirrors, and a liquid-crystal phase modulator. This allows the amplified pulses to be shortened down to 35 fs, with an energy exceeding 7 μJ .

II. DESCRIPTION OF THE LASER SYSTEM

The laser system consists of a Ti:sapphire oscillator, a spatial light modulator (SLM) in 4f configuration, a regenerative amplifier (RegA), and a prism compressor.

A. Ti:Sapphire Oscillator

A standard Kerr-lens mode-locked oscillator generates the pulses to be amplified. The mean output power is 200 mW at

Manuscript received November 7, 2001; revised June 5, 2002.

F. Lindner and G. G. Paulus are with the Max-Planck-Institut für Quantenoptik, 85748 Garching, Germany.

F. Grasbon was with the Max-Planck-Institut für Quantenoptik, 85748 Garching, Germany. He is now with the Patent Department, Siemens, D-91058 Erlangen, Germany.

A. Dreischuh is with the Max-Planck-Institut für Quantenoptik, 85748 Garching, Germany, and also with Sofia University, 1164 Sofia, Bulgaria.

H. Walther is with the Max-Planck-Institut für Quantenoptik, 85748 Garching, Germany, and also with Ludwig-Maximilians-Universität München, 85748 Garching, Germany.

Digital Object Identifier 10.1109/JQE.2002.804295.

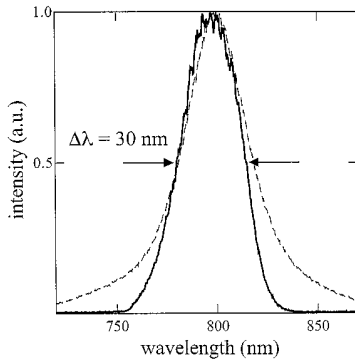


Fig. 1. Power spectra of the oscillator (dashed line) and regenerative amplifier (solid line) outputs.

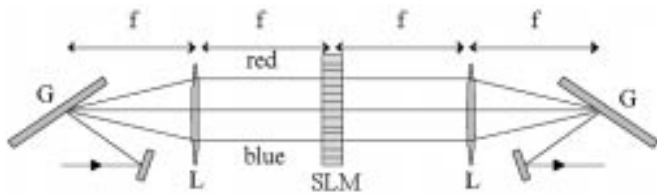


Fig. 2. 4f setup with achromatic spherical lenses (L) and spatial light modulator (SLM) in the Fourier plane. The diffraction gratings (G) are nearly at the Littrow angle.

a repetition rate of 78 MHz. Group velocity dispersion (GVD) control is achieved through a prism pair [11] and three chirped mirrors [12], [26]. This leads to a spectrum of 35 nm (Fig. 1) and a pulse duration of about 20 fs. Directly after the cavity, the direction of the oscillator beam is stabilized with a set of quadrant diodes and piezo-driven mirrors. This is very convenient, since it makes the whole system independent of any adjustment on the oscillator.

B. Phase Modulator in the 4f Setup

While the lion's share of dispersion is compensated after amplification, which will be discussed below, we precompensate the rest with a phase modulator in a 4f setup. It consists of two gratings (1200 lines/mm) and identical achromatic lenses ($f = 80$ mm, Halle, Berlin) in a symmetric zero-dispersion configuration. A liquid-crystal phase modulator (SLM 128-CRI) is placed in the Fourier plane (Fig. 2) [13], [27]. The modulator is controlled via a GPIB interface and programmed by an evolutionary algorithm with a scheme similar to that used in [14]. This is illustrated in Section III. The angle of incidence onto the first grating is as close as possible to the Littrow angle. The overall transmission of the system is 50%. Spherical lenses are used instead of cylindrical ones since the not-yet-amplified pulses cannot damage the liquid crystal. Nevertheless, we use a shutter to prevent accidental strong focusing of continuous-wave radiation on the SLM when the oscillator is not mode locked.

C. Regenerative Amplifier

After passing through the 4f setup, a proper choice of focusing mirrors matches the input beam to the mode of the amplifier cavity. The oscillator pulses are not stretched and seed a

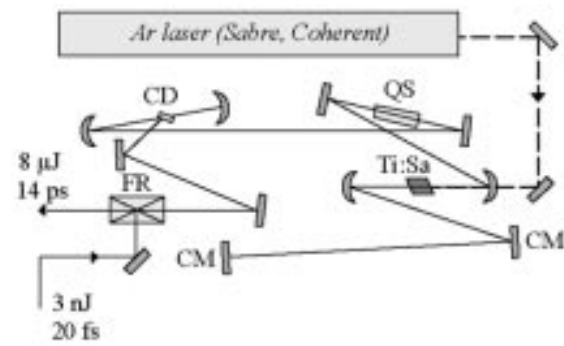


Fig. 3. Scheme of the regenerative amplifier. Ti:Sa—Ti:sapphire crystal. CM—TOD chirped mirrors. CD—cavity dumper. QS—Q switch. FR—Faraday isolator.

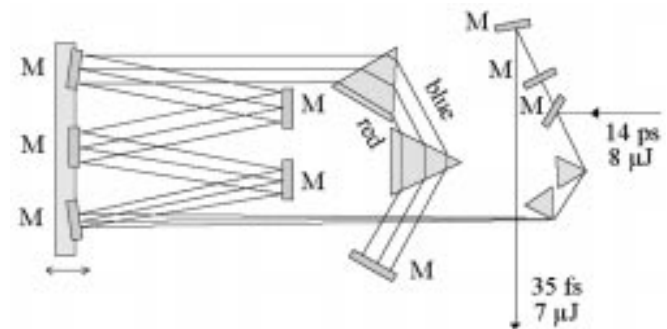


Fig. 4. Prism compressor of Proctor-Wise type. Prism material—S LAL 59 (OHARA). M—broadband dielectric mirrors, three of them mounted on a common translation stage.

commercial regenerative amplifier (RegA 9050, Coherent—see Fig. 3). The Q-switched cavity of the amplifier is CW pumped by 17 W of an Ar^+ ion laser (Sabre, Coherent). The design allows repetition rates of up to 250 kHz. However, due to the higher pulse energy, a repetition rate of 100 kHz is favored in our experiments. The resonator was modified by adding a variable number of reflections on specially designed chirped mirrors, which introduce additional third-order dispersion (TOD). The number of round trips is kept as low as possible in order to reduce the total accumulated dispersion. After 18 round trips, the amplified pulses are ejected with a pulse energy exceeding $8 \mu\text{J}$, and a spectral width of approximately 30 nm (Fig. 1).

D. Prism Compressor

The huge amount of dispersion accumulated in the amplifier stage has to be compensated in order to obtain short pulse durations. This is done through a prism compressor (Fig. 4). The most reasonable choice of design is a Proctor-Wise double prism pair configuration [15]. This reduces the length by a factor of ~ 4 in relation to a standard Fork compressor [11] with the same type of glass. The choice of the special glass (S LAL 59, OHARA) is discussed in detail in the following section. The prism separation, adjustable with a movable folding mirror set, is determined by compensating second-order dispersion (SOD). To reduce the prism distance, the compressor is passed twice. The resulting distance between the prism pairs is 2.25 m. The

TABLE I
SIGNS OF THE SOD, TOD, AND FOD DISPERSION FOR OPTICAL MATERIAL, A GRATING COMPRESSOR, AND A PRISM COMPRESSOR

	SOD	TOD	FOD
Material	+	+	+/-
Grating compressor	-	+	-
Prism compressor	-	-	-

total transmittance of the compressor is almost 90% with an output energy of 7 μ J.

The prism compressor, the TOD mirrors, and the phase modulation applied to the SLM allow precise dispersion control and generation of pulses with a duration of 35 fs.

III. DISPERSION COMPENSATION

Control of the dispersion in all orders is crucial for the pulse compression in the ultrashort time domain. In the following, first the material dispersion of our laser system is presented; then the design of the compressor and the choice of the prism material are discussed; finally, it is shown how the compensation of large amounts of higher order dispersion is achieved with chirped mirrors and a phase modulator. The dispersion control scheme extends that presented in [16], [28], since it allows, in principle, compensation in all orders.

Many CPA systems include a stretcher stage before amplification. Our laser, on the other hand, simply relies on the fact that sufficient broadening of the pulses naturally occurs due to the accumulated dispersion during the amplification process. The Q switch (42-mm SiO₂), the cavity dumper (3-mm SiO₂), and the Ti:sapphire crystal (20 mm) induce a dispersion approximately equivalent to 15 cm of fused silica per round trip. This large amount of dispersion is peculiar to our system, where the high repetition rate (100 kHz) prevents the use of a pulsed pump laser and, therefore, requires a Q switch to reach the desired inversion in the gain medium. After 18 round trips, a large amount of positive SOD (SOD = +100 000 fs²) is produced. The positive TOD (TOD = +76 000 fs³) also affects the temporal pulse shape, while fourth-order dispersion (FOD) is small (FOD = -28 000 fs⁴). The pulse duration already increases to 700 fs after the first round trip and to almost 14 ps before cavity dumping. Considering the pulse energies and the cavity design, the nonlinear phase—represented by the B integral—is well below its critical value [2], [21].

The absence of a dedicated stretcher stage, present in many femtosecond laser chains, is a great advantage with respect to the complexity of the system. However, clever alignment of the grating stretcher and compressor allows compensation of not only second order, but also higher order dispersion [3], since these systems provide the possibility to adjust the separation and the angle of incidence on the gratings [17], [29]. In this sense, using a prism compressor without stretcher reduces the number of parameters to adjust the dispersion. This is regarded as a disadvantage, since new methods of controlling higher order dispersion have to be found.

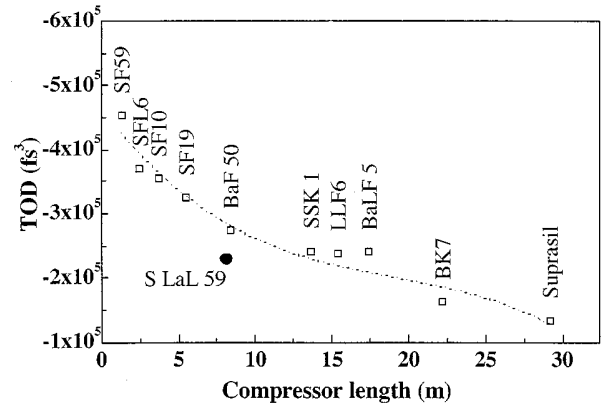


Fig. 5. Calculated TOD and compressor length needed to compensate for the SOD introduced by the amplifier, for different types of glasses.

Despite this and the large dimension required, the choice of a prism compressor can be motivated as follows. First, the efficiency (>80%) is higher than that of the widely used grating compressor (ca. 60%). Second, the TOD of the prism compressor is negative, while in conventional grating compressors it is positive. Table I summarizes the signs of the first orders of dispersion for an optical material, a grating compressor, and a prism compressor [3]: while the grating compressor increases the TOD of the amplifier, the prism compressor balances it. In other words, after compensating for the SOD, the prism compressor minimizes the TOD.

The residual TOD can be roughly corrected by inserting a suitable number of high-reflectivity TOD mirrors (Femtolasers, $R = 99\%$) in the amplifier cavity. Considering the losses they introduce, the number of reflections on these intracavity chirped mirrors should, however, be kept as low as possible. Moreover, these mirrors also introduce some residual SOD that has to be considered for balancing the dispersion.

Both the residual TOD and the length of the compressor are determined by the prism glass. In Fig. 5, we show for some glasses the length needed to compensate for the given SOD of the amplifier, and the corresponding negative TOD induced by the compressor. Note that all glasses overcompensate the positive TOD of the amplifier (+76 000 fs³).

In ultrashort laser physics, the standard material with the lowest dispersion is Suprasil. It would leave a relatively low residual TOD, but would require an inconvenient length of 29 m. On the other hand, highly dispersive glasses such as SF59 shorten the compressor to only 1.3 m, but the residual TOD would require too many reflections on the TOD mirrors in order to be compensated. A good compromise is afforded by using the special glass S LAL 59 (OHARA). The length of

TABLE II
DISPERSION BALANCE IN THE LASER SYSTEM, WITHOUT USING THE SLM:
SOD, TOD, AND FOD DISPERSION

Dispersion	SOD (fs ²)	TOD (fs ³)	FOD (fs ⁴)
RegA / RT	+5 560	+4 240	-1 550
Prism compressor / mm	-12.36	-28.36	-55.23
TOD mirror / reflection	+130	+1 800	+10 000 (?)
RegA (18 RT)	+100 000	+76 000	-28 000
Prism compressor (L=9.15 m)	-113 000	-259 000	-505 000
TOD mirrors (100 reflections)	+13 000	+180 000	+1 000 000 (?)
Residual dispersion	≈ 0	≈ -3 000	≈ +500 000 (?)

the compressor is 8 m (as short as for BaF50) and the residual TOD is $-230\,000\text{ fs}^3 + 76\,000\text{ fs}^3 = -154\,000\text{ fs}^3$ (as low as for LLF6). Since each passage on a TOD mirror introduces approximately $+1800\text{ fs}^3$, 85 reflections would be necessary to compensate for the TOD. Considering also the positive SOD of the chirped mirrors ($+130\text{ fs}^2$), a balance is provided by using three such mirrors in the amplifier (five reflections per round trip, giving 90 reflections) and some additional ones outside the cavity (ten reflections) for fine adjustment. The corresponding total length of the compressor is 9.15 m.

Table II shows the balance of the first three orders of dispersion in the laser system. It should be noted that these calculations should not be taken too literally. In fact, the indicated dispersion of the TOD mirrors is a theoretical estimate whose reliability is not very high, especially for the FOD. Moreover, these values are dependent on the angle of incidence, which can be chosen in our system since some TOD mirrors are used as folding mirrors. Nevertheless, it can be stated that the output pulses are characterized by a compensated SOD, a very low residual TOD, and a high residual FOD.

Fig. 6 shows the corresponding noncollinear autocorrelation. Taking the Fourier transform of the spectrum gives a bandwidth limit of 32 fs and indicates that the assumption of a Gaussian shape is very good. The pulse duration can then be estimated to $\sim 60\text{ fs}$, far above the bandwidth limit. Moreover, the presence of a huge pedestal indicates that the pulse energy is actually dispersed over a longer time, due to the uncompensated higher orders of dispersion.

The liquid-crystal phase modulator is used for fine precompensation of these higher orders. It consists of an array of $N = 128$ pixels which can independently influence the phase of the respective spectral component by means of an applied voltage. The width of each pixel is $97\text{ }\mu\text{m}$ and their mutual separation is $3\text{ }\mu\text{m}$. As already mentioned, the SLM is placed in the Fourier plane of the 4f setup (see Fig. 2), where optimum spatial separation of frequencies occurs. The overall accepted bandwidth of the modulator is 120 nm, well above that of the incident pulse, and the resolution is approximately 0.95 nm/pix . Careful alignment guarantees a symmetric setup, with the central wavelength passing in the center of the array.

According to the Nyquist theorem, the phase difference between two adjacent pixels should not exceed π [18]. For

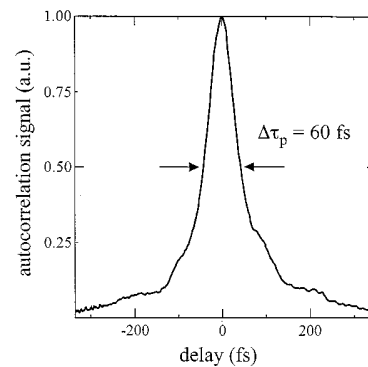


Fig. 6. Noncollinear autocorrelation of the amplified and compressed pulses without SLM in operation. A Gaussian shape is assumed for determination of the pulse duration.

a purely quadratic, cubic, or quartic phase distribution, this implies—in our case—a limitation of 5.10^3 fs^2 , 5.10^4 fs^3 , and 8.10^5 fs^4 , respectively, for the maximum SOD, TOD, and FOD applicable. The simultaneous presence of terms of different sign in the phase expansion may eventually lead to even increased acceptable values. Moreover, large phase gradients in the border of the array do not affect the phase modulation, since the actual spectrum is incident only on the central pixels of the SLM mask. For example, applying the Nyquist theorem only to the 64 central pixels, we estimated possible values of 10^4 fs^2 , 2.10^5 fs^3 , and 8.10^6 fs^4 for the SOD, TOD, and FOD, respectively. These limitations clearly indicate that the use of the SLM is appropriate to compensate for higher orders of dispersion, provided that the main compensation is realized elsewhere.

The phase distribution applied is chosen by adjusting the voltage values in a feedback loop. We focus the beam in a nonlinear crystal (BBO, $20\text{ }\mu\text{m}$) and record the resulting second harmonic (SH) as a feedback signal. Adjustment of the voltage of each pixel for maximum SH represents an optimization problem which is solved with an evolutionary algorithm [4], [14], [18]. Convergence of the procedure [Fig. 7(a)] is rather fast if advantage is taken of the *a-priori* physical knowledge such as the expected sign and extent of the dispersion that has to be applied.

Use of the SLM has also afforded the possibility of reducing the number of TOD mirrors used in the system. This is highly

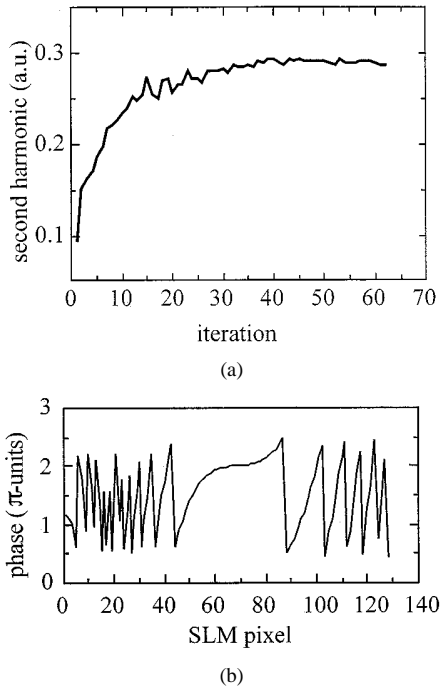


Fig. 7. (a) Convergence of the SH signal while running the evolutionary algorithm. (b) Typical phase distribution applied by the SLM for fine control of the higher order dispersion. The shape clearly indicates the presence of a positive TOD term.

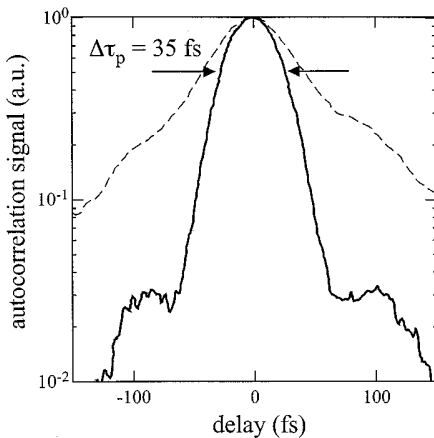


Fig. 8. Noncollinear autocorrelation (semilogarithmic scale) of the amplified and compressed pulses with SLM in operation (solid line). For comparison, the same autocorrelation of Fig. 6 (without SLM) is also shown (dashed line). A Gaussian shape is assumed for determination of the pulse duration.

desirable in view of the losses they introduce. In the final configuration, there are only two TOD mirrors in the amplifier (three reflections per round trip—see Fig. 3). The typical phase function retrieved by the algorithm is shown in Fig. 7(b). This distribution compensates for the higher orders and, as expected, is dominated by a positive TOD term.

Fig. 8 shows the noncollinear autocorrelation of the amplified and compressed pulses with the SLM in operation. The significant reduction of the pedestal confirms that higher order dispersion is almost completely removed by the liquid crystal phase modulator. The pulse duration is 35 fs, slightly above the band-

width limit, probably due to the discrete nature of the phase distribution of the SLM.

If a feedback directly related to the peak intensity is available from the experiment (e.g., integral rates in an ionization experiment), it is possible to make the pulse shortest in the experimental environment itself. This makes the system very flexible if optical elements (waveplates, polarizers, ...) are added. Furthermore, in principle it is possible to use differential rates as feedback, allowing the evolutionary algorithm to selectively optimize different physical processes as in [19] and [30]. Convergence of the procedure is fast (typically 2–3 min) and, in order to improve the long-term stability of the system, it can be conveniently repeated.

IV. CONCLUSION

We have reported a 100-kHz Ti:sapphire laser system delivering pulses with energies of $7 \mu\text{J}$ and durations of 35 fs. Due to the high repetition rate, CW pumping, and Q switching of the regenerative amplifier are needed, and a much larger amount of dispersion than in typical 1–10 kHz lasers is accumulated. The corresponding broadening of the pulse permits amplification without stretching. Pulse compression is achieved through a particular combination of a prism compressor, chirped mirrors, and a liquid-crystal phase modulator.

This procedure is precise and stable, allowing nearly transform-limited output pulses to be obtained routinely. The high peak intensities of the pulses and the high repetition rate make this system a valuable tool for investigating highly nonlinear phenomena, such as high-harmonic generation, above-threshold ionization [10], [24], [25], and, in particular, coincidence techniques requiring very low probability of an event per laser shot (e.g., COLTRIMS [20], [31]). With respect to these applications, the great advantage of using the SLM is, as outlined in Section III, the possibility of obtaining the shortest pulses in the interaction region. This allows the study of elementary atomic processes at the highest intensities available at this repetition rate.

REFERENCES

- [1] D. E. Spence, P. N. Kean, and W. Sibbett, "60-fsec pulse generation from a self-mode-locked Ti:sapphire laser," *Opt. Lett.*, vol. 16, pp. 42–44, 1991.
- [2] P. Maine, D. Strickland, P. Bado, M. Pessot, and G. Mourou, "Generation of ultrahigh peak power pulses by chirped pulse amplification," *IEEE J. Quantum Electron.*, vol. QE-24, pp. 398–403, 1988.
- [3] S. Backus, Ch. G. Durfee, III, M. M. Murnane, and H. C. Kapteyn, "High power ultrafast lasers," *Rev. Sci. Instrum.*, vol. 69, pp. 1207–1223, 1998.
- [4] E. Zeek, R. Bartels, M. M. Murnane, H. C. Kapteyn, S. Backus, and G. Vdovin, "Adaptive pulse compression for transform-limited 15-fs high-energy pulse generation," *Opt. Lett.*, vol. 25, pp. 587–589, 2000.
- [5] S. Backus, R. Bartels, S. Thompson, R. Dollinger, H. C. Kapteyn, and M. M. Murnane, "High-efficiency, single-stage 7-kHz high-average-power ultrafast laser system," *Opt. Lett.*, vol. 26, pp. 465–467, 2001.
- [6] K. Wynne, G. D. Reid, and R. M. Hochstrasser, "Regenerative amplification of 30-fs pulses in Ti:sapphire at 5 kHz," *Opt. Lett.*, vol. 19, pp. 895–897, 1994.
- [7] T. B. Norris, "Femtosecond pulse amplification at 250 kHz with a Ti:sapphire regenerative amplifier and application to continuum generation," *Opt. Lett.*, vol. 17, pp. 1009–1011, 1992.
- [8] J. Zhou, C.-P. Huang, C. Shi, M. M. Murnane, and H. C. Kapteyn, "Generation of 21-fs millijoule-energy pulses by use of Ti:sapphire," *Opt. Lett.*, vol. 19, pp. 126–128, 1994.

- [9] A. Antonetti, F. Blasco, J. P. Chambaret, G. Cheriaux, G. Darpentigny, C. Le Blanc, P. Rousseau, S. Ranc, G. Rey, and F. Salin, "A laser system producing 5.10^{19} W/cm² at 10 Hz," *Appl. Phys. B*, vol. 65, pp. 197–204, 1997.
- [10] G. G. Paulus, F. Grasbon, A. Dreischuh, H. Walther, R. Kopold, and W. Becker, "Above-threshold ionization by an elliptically polarized field: Interplay between electronic quantum trajectories," *Phys. Rev. Lett.*, vol. 84, pp. 3791–3794, 2000.
- [11] R. L. Fork, O. E. Martinez, and J. P. Gordon, "Negative dispersion using pairs of prisms," *Opt. Lett.*, vol. 9, pp. 150–152, 1984.
- [12] R. Szipocs, K. Ferencz, C. Spielmann, and F. Krausz, "Chirped multilayer coatings for broadband dispersion control in femtosecond lasers," *Opt. Lett.*, vol. 19, pp. 201–203, 1994.
- [13] A. M. Weiner, "Femtosecond optical pulse shaping and processing," *Prog. Quant. Electr.*, vol. 19, pp. 161–237, 1995.
- [14] T. Brixner, M. Strehle, and G. Gerber, "Feedback-controlled optimization of amplified femtosecond laser pulses," *Appl. Phys. B*, vol. 68, pp. 281–284, 1999.
- [15] B. Proctor and F. Wise, "Quartz prism sequence for reduction of cubic phase in a mode-locked Ti:sapphire laser," *Opt. Lett.*, vol. 17, pp. 1295–1297, 1992.
- [16] C. Spielmann, M. Lenzner, F. Krausz, and R. Szipocs, "Compact, high-throughput expansion–compression scheme for chirped pulse amplification in the 10 fs range," *Opt. Commun.*, vol. 120, pp. 321–324, 1995.
- [17] O. E. Martinez, J. P. Gordon, and R. L. Fork, "Negative group-velocity dispersion using refraction," *J. Opt. Soc. Amer. A*, vol. 1, pp. 1003–1006, 1984.
- [18] D. Zeidler, T. Hornung, D. Proch, and M. Motzkus, "Adaptive compression of tunable pulses from a noncollinear-type OPA to below 16 fs by feedback-controlled pulse shaping," *Appl. Phys. B*, vol. 70, pp. S125–S131, 2000.
- [19] R. Bartels, S. Backus, E. Zeek, L. Misoguti, G. Vdovin, I. P. Christov, M. M. Murnane, and H. C. Kapteyn, "Shaped-pulse optimization of coherent emission of high-harmonic soft X-rays," *Nature*, vol. 406, pp. 164–166, 2000.
- [20] R. Moshhammer, M. Unverzagt, W. Schmitt, J. Ulrich, and H. Schmidt-Böcking, "A 4π recoil-ion electron momentum analyzer: A high resolution 'microscope' for the investigation of the dynamics of atomic, molecular and nuclear reactions," *Nucl. Instrum. Methods Phys. Res. B*, vol. 108, pp. 425–445, 1996.
- [21] M. Pessot, J. Squier, P. Bado, G. Mourou, and D. Harter, "Chirped pulse amplification of 300 fs pulses in an alexandrite regenerative amplifier," *IEEE J. Quantum Electron.*, vol. 25, pp. 61–66, Jan. 1989.
- [22] C. Le Blanc, E. Baubeau, F. Salin, J. A. Squier, C. P. J. Barty, and C. Spielmann, "Toward a terawatt–kilohertz repetition-rate laser," *IEEE J. Select. Topics Quantum Electron.*, vol. 4, pp. 407–413, 1998.
- [23] Y. Nabekawa, Y. Kuramoto, T. Togashi, T. Sekikawa, and S. Watanabe, "Generation of 0.66-TW pulses at 1 kHz by a Ti:sapphire laser," *Opt. Lett.*, vol. 23, pp. 1384–1386, 1998.
- [24] G. G. Paulus, F. Grasbon, H. Walther, R. Kopold, and W. Becker, "Channel-closing-induced resonances in the above-threshold ionization plateau," *Phys. Rev. A*, vol. 64, no. 021 401, 2001.
- [25] P. Salieres, B. Carre, L. Le Deroff, G. G. Paulus, F. Grasbon, H. Walther, R. Kopold, W. Becker, D. B. Milosevic, A. Sanpera, and M. Lewenstein, "Feynman's path-integral approach for intense-laser–atom interactions," *Science*, vol. 292, pp. 902–905, 2001.
- [26] A. Stingl, C. Spielmann, F. Krausz, and R. Szipocs, "Generation of 11-fs pulses from a Ti:sapphire laser without the use of prisms," *Opt. Lett.*, vol. 19, pp. 204–206, 1994.
- [27] A. M. Weiner, "Femtosecond pulse shaping using spatial light modulators," *Rev. Sci. Instrum.*, vol. 71, pp. 1929–1960, 2000.
- [28] M. Lenzner, C. Spielmann, E. Wintner, F. Krausz, and A. J. Schmidt, "Sub-20-fs, kilohertz-repetition-rate Ti:sapphire amplifier," *Opt. Lett.*, vol. 20, pp. 1397–1399, 1995.
- [29] O. E. Martinez, "Design of high-power ultrashort pulse amplifiers by expansion and recompression," *IEEE J. Quantum Electron.*, vol. QE-23, pp. 1385–1387, 1987.
- [30] A. Assion, T. Baumert, M. Bergt, T. Brixner, B. Kiefer, V. Seyfried, M. Strehle, and G. Gerber, "Control of chemical reactions by feedback-optimized phase-shaped femtosecond laser pulses," *Science*, vol. 282, pp. 919–922, 1998.
- [31] R. Moshhammer, B. Feuerstein, W. Schmitt, A. Dorn, C. D. Schröter, J. Ullrich, H. Rotke, C. Trimp, M. Wittmann, G. Korn, K. Hoffmann, and W. Sandner, "Momentum distributions of Ne³⁺ ions created by an intense ultrashort laser pulse," *Phys. Rev. Lett.*, vol. 84, pp. 447–450, 2000.

F. Lindner was born in Milan, Italy, in 1974. He received the degree in nuclear engineering from the Politecnico di Milano, Milan, Italy, in 1999. He is currently working toward the Ph.D. degree in physics at the Max-Planck-Institute for Quantum Optics, Garching, Germany.

Between 1998 and 1999, he was with the Applied Optics Laboratory, Ecole Polytechnique—ENSTA, Paris, France.

G. G. Paulus was born in Neustadt (Aisch), Germany, in 1966. He received the diploma degree in physics and the Ph.D. degree in physics from the Ludwig-Maximilians-University, Munich, Germany, in 1992 and 1995, respectively.

He has since been with the Max-Planck-Institute for Quantum Optics, Garching, Germany.

F. Grasbon was born in Weilheim, Germany, in 1969. He received the diploma degree in physics from the University of Heidelberg, Heidelberg, Germany, in 1997, and the Ph.D. degree in physics from the Ludwig-Maximilians-University, Munich, Germany, in 2001.

He is currently with the Patent Department, Siemens, Erlangen, Germany.

A. Dreischuh was born in Sofia, Bulgaria, in 1961. He received the M.S. degree (in engineering physics-quantum electronics) and the Ph.D. and Dr. Sci. degrees from the Sofia University, Bulgaria, in 1987, 1991, and 2001, respectively.

During 1997–1999, he was with the Max-Planck-Institut für Quantenoptik, Garching, Germany. He is currently with the Department of Quantum Electronics, Sofia University, Sofia, Bulgaria.

Dr. Dreischuh is a member of the Bulgarian Physical Union, the SPIE, and the Humboldt-Club, Bulgaria.

H. Walther received the Ph.D. degree in physics from the University of Heidelberg, Heidelberg, Germany, in 1962.

He was previously with JILA, Boulder, CO, and was also a Professor in various locations throughout Germany. Since 1981, he has been a Director at the Max-Planck-Institute for Quantum Optics, Garching, Germany.

Bibliography

- [Agostini79] P. Agostini, F. Fabre, G. Mainfray, G. Petite and N. K. Rahman, *Free-free transitions following six-photon ionization of xenon atoms*, Phys. Rev. Lett., **42**, 1127 (1979).
- [Ammosov87] M. V. Ammosov, N. B. Delone and V. P. Krainov, Sov. Phys. JETP, **64**, 1191 (1987).
- [Apolonski00] A. Apolonski, A. Poppe, G. Tempea, C. Spielmann, T. Udem, R. Holzwarth, T. W. Hänsch and F. Krausz, *Controlling the phase evolution of few-cycle light pulses*, Phys. Rev. Lett., **85**, 740 (2000).
- [Balcou97] P. Balcou, P. Salières, A. L’Huillier and M. Lewenstein, *Generalized phase-matching conditions for high harmonics: The role of field-gradient forces*, Phys. Rev. A, **55**, 3204 (1997).
- [Baltuška03] A. Baltuška, T. Udem, M. Uiberacker, M. Hentschel, E. Goulielmakis, C. Gohle, R. Holzwarth, V. S. Yakovlev, A. Scrinzi, T. W. Hänsch and F. Krausz, *Attosecond control of electronic processes by intense light fields*, Nature, **421**, 611 (2003).
- [Bauer99] D. Bauer and P. Mulser, *Exact field ionization rates in the barrier-suppression regime from numerical time-dependent Schrödinger-equation calculations*, Phys. Rev. A, **59**, 569 (1999).
- [Becker02] W. Becker, F. Grasbon, R. Kopold, D. B. Milošević, G. G. Paulus and H. Walther, *Above-threshold ionization: from classical features to quantum effects*, Advances in atomic, molecular, and optical physics, **48**, 35 (2002).
- [Bellini98] M. Bellini, C. Lyngå, A. Tozzi, M. B. Gaarde, T. W. Hänsch, A. L’Huillier and C. G. Wahlström, *Temporal coherence of ultrashort high-order harmonic pulses*, Phys. Rev. Lett., **81**, 297 (1998).
- [Born89] M. Born and E. Wolf, *Principles of Optics* (Pergamon Press, Oxford, 1989).

-
- [Boyd80] R. W. Boyd, *Intuitive explanation of the phase anomaly of focused light beams*, J. Opt. Soc. Am., **70**, 877 (1980).
- [Carpenter58] C. R. Carpenter, *Gouy phase advance with microwaves*, Am. J. Phys., **27**, 98 (1958).
- [Chan92] W. F. Chan, G. Cooper, X. Guo, G. R. Burton and C. E. Brion, *Absolute optical oscillator strengths for the electronic excitation of atoms at high resolution. III. The photoabsorption of argon, krypton, and xenon*, Phys. Rev. A, **46**, 149 (1992).
- [Chelkowski02] S. Chelkowski and A. D. Bandrauk, *Sensitivity of spatial photoelectron distributions to the absolute phase of an ultrashort intense laser pulse*, Phys. Rev. A, **65**, 061802(R) (2002).
- [Chelkowski04] S. Chelkowski, A. D. Bandrauk and A. Apolonski, *Measurement of the carrier-envelope phase of few-cycle laser pulses using asymmetric photoionization* (2004), submitted.
- [Corkum89] P. B. Corkum, N. H. Burnett and F. Brunel, *Above-threshold ionization in the long-wavelength limit*, Phys. Rev. Lett., **62**, 1259 (1989).
- [Corkum93] P. Corkum, *Plasma perspective on strong-field multiphoton ionization*, Phys. Rev. Lett., **71**, 1994 (1993).
- [Cormier98] E. Cormier and P. Lambropoulos, *Effect of the initial phase of the field in ionization by ultrashort laser pulses*, Eur. Phys. J. D, **2**, 15 (1998).
- [Cundiff02] S. Cundiff, *Phase stabilization of ultrashort optical pulses*, J. Phys. D: Appl. Phys., **35**, R43 (2002).
- [Delone94] N. B. Delone and V. P. Krainov, *Multiphoton processes in atoms* (Springer-Verlag, Berlin, 1994).
- [Dietrich00] P. Dietrich, F. Krausz and P. B. Corkum, *Determining the absolute carrier phase of a few-cycle laser pulse*, Opt. Lett., **25**, 16 (2000).
- [Dombi04a] P. Dombi, A. Apolonski, C. Lemell, G. G. Paulus, M. Kakehata, R. Holzwarth, T. Udem, K. Torizuka, J. Burgdörfer, T. W. Hänsch and F. Krausz, *Direct measurement and analysis of the carrier-envelope phase in light pulses approaching the single-cycle regime*, New Journal of Physics, **6**, 39 (2004).
- [Dombi04b] P. Dombi, A. Apolonski, G. G. Paulus, M. Kakehata, K. Torizuka, R. Holzwarth, T. Udem, C. Lemell, J. Burgdörfer, T. W. Hänsch and F. Krausz, in F. Krausz, G. Korn, P. Corkum and I. A. Walmsley, editors, *Ultrafast Optics IV: Selected Contributions to the 4th International*

Conference on Ultrafast Optics, Vienna, Austria (Springer-Verlag, New York, 2004).

- [Eremina03] E. Eremina, X. Liu, H. Rottke, W. Sandner, A. Dreischuh, F. Lindner, F. Grasbon, G. G. Paulus, H. Walther, R. Moshhammer, B. Feuerstein and J. Ullrich, *Laser-induced non-sequential double ionization investigated at and below the threshold for electron impact ionization*, J. Phys. B: At. Mol. Opt. Phys., **36**, 3269 (2003).
- [Eremina04] E. Eremina, X. Liu, H. Rottke, W. Sandner, M. Schätzel, A. Dreischuh, G. G. Paulus, H. Walther, R. Moshhammer and J. Ullrich, *Influence of molecular structure on double ionization of N_2 and O_2 by high intensity ultra-short laser pulses*, Phys. Rev. Lett., in press (2004).
- [Feng01] S. Feng and H. G. Winful, *Physical origin of the Gouy phase shift*, Opt. Lett., **26**, 485 (2001).
- [Ferray88] M. Ferray, A. L'Huillier, X. F. Li, L. A. Lompré, G. Mainfray and C. Manus, *Multiple-harmonic conversion of 1064 nm radiation in rare gases*, J. Phys. B: At. Mol. Opt. Phys., **21**, L31 (1988).
- [Feynman65] R. P. Feynman and A. R. Hibbs, *Quantum mechanics and path integrals* (McGraw-Hill, New York, 1965).
- [Feynman91] R. P. Feynman, R. B. Leighton and M. L. Sands, *The Feynman lectures on physics* (Addison-Wesley, 1991).
- [Freeman87] R. R. Freeman, P. H. Bucksbaum, H. Milchberg, S. Darack, D. Schumacher and M. E. Geusic, *Above-threshold ionization with subpicosecond laser pulses*, Phys. Rev. Lett., **59**, 1092 (1987).
- [Gaarde99] M. B. Gaarde, F. Salin, E. Constant, P. Balcou, K. J. Schafer, K. C. Kulander and A. L'Huillier, *Spatiotemporal separation of high harmonic radiation into two quantum path components*, Phys. Rev. A, **59**, 1367 (1999).
- [Gallagher89] T. F. Gallagher and T. J. Scholz, *Above-threshold ionization at 8 GHz*, Phys. Rev. A, **40**, 2762 (1989).
- [Gouy90] L. G. Gouy, *Sur une propriété nouvelle des ondes lumineuses*, C. R. Acad. Sci. Paris, **110**, 1251 (1890).
- [Grasbon03] F. Grasbon, G. G. Paulus, H. Walther, P. Villorresi, G. Sansone, S. Stagira, M. Nisoli and S. D. Silvestri, *Above-threshold ionization at the few-cycle limit*, Phys. Rev. Lett., **91**, 173003 (2003).

- [Hentschel01] M. Hentschel, R. Kienberger, C. Spielmann, G. A. Reider, N. Milosevic, T. Brabec, P. Corkum, U. Heinzmann, M. Drescher and F. Krausz, *Attosecond metrology*, Nature, **414**, 509 (2001).
- [Hergott02] J.-F. Hergott, M. Kovacev, H. Merdji, C. Hubert, Y. Mairesse, E. Jean, P. Breger, P. Agostini, B. Carré and P. Salières, *Extreme-ultraviolet high-order harmonic pulses in the microjoule range*, Phys. Rev. A, **66**, 021801(R) (2002).
- [Holme03] N. C. R. Holme, B. C. Daly, M. T. Myaing and T. B. Norris, *Gouy phase shift of single-cycle picosecond acoustic pulses*, Appl. Phys. Lett., **83**, 392 (2003).
- [Jones00] D. J. Jones, S. A. Diddams, J. K. Ranka, A. Stentz, R. S. Windeler, J. L. Hall and S. T. Cundiff, *Carrier-envelope phase control of femtosecond mode-locked lasers and direct optical frequency synthesis*, Science, **288**, 635 (2000).
- [Jönsson61] C. Jönsson, *Elektroneninterferenzen an mehreren künstlich hergestellten Feinspalten*, Zeitschrift für Physik, **161**, 454 (1961).
- [Jönsson74] C. Jönsson, *Electron diffraction at multiple slits*, Am. J. Phys., **42**, 4 (1974).
- [Keldysh65] L. V. Keldysh, Sov. Phys. JETP, **20**, 1307 (1965).
- [Kienberger04] R. Kienberger, E. Goulielmakis, M. Uiberacker, A. Baltuška, V. Yakovlev, F. Bammer, A. Scrinzi, T. Westerwalbesloh, U. Kleineberg, U. Heinzmann, M. Drescher and F. Krausz, *Atomic transient recorder*, Nature, **427**, 817 (2004).
- [Krause92] J. L. Krause, K. J. Schafer and K. C. Kulander, *High-order harmonic generation from atoms and ions in the high intensity regime*, Phys. Rev. Lett., **68**, 3535 (1992).
- [Kulander93] K. C. Kulander, K. J. Schafer and K. L. Krause, *Super-Intense Laser-Atom Physics*, 95 (Plenum, New York, 1993).
- [Kužel99] P. Kužel, M. A. Khazan and J. Kroupa, *Spatiotemporal transformations of ultrashort terahertz pulses*, J. Opt. Soc. Am. B, **16**, 1795 (1999).
- [Landau65] L. D. Landau and E. M. Lifshitz, *Quantum mechanics* (Pergamon, New York, 1965).
- [Lewenstein94] M. Lewenstein, P. Balcou, M. Y. Ivanov, A. L'Huillier and P. B. Corkum, *Theory of high-harmonic generation by low-frequency laser fields*, Phys. Rev. A, **49**, 2117 (1994).

- [Lewenstein95] M. Lewenstein, P. Salières and A. L’Huillier, *Phase of the atomic polarization in high-order harmonic generation*, Phys. Rev. A, **52**, 4747 (1995).
- [L’Huillier83] A. L’Huillier, L. A. Lompre, G. Mainfray and C. Manus, *Multiply charged ions induced by multiphoton absorption in rare gases at 0.53 μm* , Phys. Rev. A, **27**, 2503 (1983).
- [L’Huillier93] A. L’Huillier and P. Balcou, *High-order harmonic generation in rare gases with a 1-ps 1053-nm laser*, Phys. Rev. Lett., **70**, 774 (1993).
- [Lindner02] F. Lindner, G. G. Paulus, F. Grasbon, A. Dreischuh and H. Walther, *Dispersion control in a 100-kHz-repetition-rate 35-fs Ti:sapphire regenerative amplifier system*, IEEE J. Quantum Electron., **38**, 1465 (2002).
- [Lindner03] F. Lindner, W. Stremme, M. G. Schätzel, F. Grasbon, G. G. Paulus, H. Walther, R. Hartmann and L. Strüder, *High-order harmonic generation at a repetition rate of 100 kHz*, Phys. Rev. A, **68**, 013814 (2003).
- [Lindner04a] F. Lindner, G. G. Paulus, H. Walther, A. Baltuška, E. Goulielmakis, M. Lezius and F. Krausz, *Gouy phase shift for few-cycle laser pulses*, Phys. Rev. Lett., **92**, 113001 (2004).
- [Lindner04b] F. Lindner, G. G. Paulus, H. Walther, A. Baltuška, E. Goulielmakis, M. Lezius and F. Krausz, in F. Krausz, G. Korn, P. Corkum and I. A. Walmsley, editors, *Ultrafast Optics IV: Selected Contributions to the 4th International Conference on Ultrafast Optics, Vienna, Austria* (Springer-Verlag, New York, 2004).
- [Lindner04c] F. Lindner, M. Schätzel, H. Walther, A. Baltuška, E. Goulielmakis, M. Lezius, F. Krausz, D. B. Milošević, W. Becker and G. G. Paulus, *Double-slit experiment in time domain and attosecond interferometry* (2004), in preparation.
- [Liu04] X. Liu, E. Eremina, H. Rottke, W. Sandner, E. Goulielmakis, K. O’Keeffe, M. Lezius, F. Krausz, F. Lindner, M. Schätzel, G. G. Paulus and H. Walther, *Steering non-sequential double ionization at the few-optical-cycle limit* (2004), in preparation.
- [Maine88] P. Maine, D. Strickland, P. Bado, M. Pessot and G. Mourou, *Generation of ultrahigh peak power pulses by chirped pulse amplification*, IEEE J. Quantum Electron., **24**, 398 (1988).
- [McGowan00] R. W. McGowan, R. A. Cheville and D. Grischkowsky, *Direct observation of the Gouy phase shift in THz impulse ranging*, Appl. Phys. Lett., **76**, 670 (2000).

-
- [McPherson87] A. McPherson, G. Gibson, H. Jara, U. Johann, T. S. Luk, I. A. McIntyre, K. Boyer and C. K. Rhodes, *Studies of multiphoton production of vacuum-ultraviolet radiation in the rare gases*, J. Opt. Soc. Am. B, **4**, 595 (1987).
- [Merli76] P. G. Merli, G. F. Missiroli and G. Pozzi, *On the statistical aspect of electron interference phenomena*, Am. J. Phys., **44**, 306 (1976).
- [Milošević03] D. B. Milošević, G. G. Paulus and W. Becker, *High-order above-threshold ionization with few-cycle pulse: a meter of the absolute phase*, Optics Express, **11**, 1418 (2003).
- [Milošević04] D. B. Milošević, G. G. Paulus and W. Becker, *Metering the absolute phase of a few-cycle pulse via its high-order above-threshold ionization spectrum*, Laser Phys. Lett., **1**, 93 (2004).
- [Moshhammer00] R. Moshhammer, B. Feuerstein, W. Schmitt, A. Dorn, C. D. Schröter, J. Ullrich, H. Rottke, C. Trupp, M. Wittmann, G. Korn, K. Hoffmann and W. Sandner, *Momentum distributions of Ne^{n+} ions created by an intense ultrashort laser pulse*, Phys. Rev. Lett., **84**, 447 (2000).
- [Moshhammer01] R. Moshhammer, B. Feuerstein, D. Fischer, A. Dorn, C. D. Schröter, J. Deipenwisch, J. R. C. Lopez-Urrutia, C. Hohl, P. Neumayer, J. Ullrich, H. Rottke, C. Trupp, M. Wittmann, G. Korn and W. Sandner, *Non-sequential double ionization of Ne in intense laser pulses: a coincidence experiment*, Optics Express, **8**, 358 (2001).
- [Nisoli96] M. Nisoli, S. D. Silvestri and O. Svelto, *Generation of high energy 10 fs pulses by a new pulse compression technique*, Appl. Phys. Lett., **68**, 2793 (1996).
- [Nisoli97] M. Nisoli, S. D. Silvestri, O. Svelto, R. Szipöcs, K. Ferencz, C. Spielmann, S. Sartania and F. Krausz, *Compression of high-energy laser pulses below 5 fs*, Opt. Lett., **22**, 522 (1997).
- [Nisoli02] M. Nisoli, E. Priori, G. Sansone, S. Stagira, G. Cerullo, S. D. Silvestri, C. Altucci, R. Bruzzese, C. de Lisio, P. Villoresi, L. Poletto, M. Pascolini and G. Tondello, *High-brightness high-order harmonic generation by truncated Bessel beams in the sub-10-fs regime*, Phys. Rev. Lett., **88**, 033902 (2002).
- [Nisoli03] M. Nisoli, G. Sansone, S. Stagira, S. D. Silvestri, C. Vozzi, M. Pascolini, L. Poletto, P. Villoresi and G. Tondello, *Effects of carrier-envelope phase differences of few-optical-cycle light pulses in single-shot high-order-harmonic spectra*, Phys. Rev. Lett., **91**, 213905 (2003).

- [Paulus94a] G. G. Paulus, W. Becker, W. Nicklich and H. Walther, *Rescattering effects in above-threshold-ionization: a classical model*, J. Phys. B: At. Mol. Opt. Phys., **27**, L703 (1994).
- [Paulus94b] G. G. Paulus, W. Nicklich, H. Xu, P. Lambropoulos and H. Walther, *Plateau in above threshold ionization spectra*, Phys. Rev. Lett., **72**, 2851 (1994).
- [Paulus95] G. G. Paulus, W. Becker and H. Walther, *Classical rescattering effects in two-color above-threshold ionization*, Phys. Rev. A, **52**, 4043 (1995).
- [Paulus98] G. G. Paulus, F. Zacher, H. Walther, A. Lohr, W. Becker and M. Kleber, *Above-threshold ionization by an elliptically polarized field: quantum tunneling interferences and classical dodging*, Phys. Rev. Lett., **80**, 484 (1998).
- [Paulus00] G. G. Paulus, F. Grasbon, A. Dreischuh, H. Walther, R. Kopold and W. Becker, *Above-threshold ionization by an elliptically polarized field: interplay between electronic quantum trajectories*, Phys. Rev. Lett., **84**, 3791 (2000).
- [Paulus01a] G. G. Paulus, F. Grasbon, H. Walther, R. Kopold and W. Becker, *Channel-closing-induced resonances in the above-threshold ionization plateau*, Phys. Rev. A, **64**, 021401(R) (2001).
- [Paulus01b] G. G. Paulus, F. Grasbon, H. Walther, P. Villorosi, M. Nisoli, S. Stagira, E. Priori and S. D. Silvestri, *Absolute-phase phenomena in photoionization with few-cycle laser pulses*, Nature, **414**, 182 (2001).
- [Paulus03] G. G. Paulus, F. Lindner, H. Walther, A. Baltuška, E. Goulielmakis, M. Lezius and F. Krausz, *Measurement of the phase of few-cycle laser pulses*, Phys. Rev. Lett., **91**, 253004 (2003).
- [Paulus04] G. G. Paulus, F. Lindner, D. B. Milošević and W. Becker, in *Proceedings of the XXIII International Conference on Photonic, Electronic and Atomic Collisions (ICPEAC), Stockholm, 2003* (2004).
- [Poppe01] A. Poppe, R. Holzwarth, A. Apolonski, G. Tempea, C. Spielmann, T. W. Hänsch and F. Krausz, *Few-cycle optical waveform synthesis*, Appl. Phys. B, **72**, 373 (2001).
- [Reichert99] J. Reichert, R. Holzwarth, T. Udem and T. W. Hänsch, *Measuring the frequency of light with mode-locked lasers*, Opt. Comm., **172**, 59 (1999).
- [Ruffin99] A. B. Ruffin, J. V. Rudd, J. F. Whitaker, S. Feng and H. G. Winful, *Direct observation of the Gouy phase shift with single-cycle terahertz pulses*, Phys. Rev. Lett., **83**, 3410 (1999).

- [Salières95] P. Salières, A. L’Huillier and M. Lewenstein, *Coherence control of high-order harmonics*, Phys. Rev. Lett., **74**, 3776 (1995).
- [Salières98] P. Salières, P. Antoine, A. de Bohan and M. Lewenstein, *Temporal and spectral tailoring of high-order harmonics*, Phys. Rev. Lett., **81**, 5544 (1998).
- [Salières99] P. Salières, A. L’Huillier, P. Antoine and M. Lewenstein, *Study of the spatial and temporal coherence of high-order harmonics*, Advances in atomic, molecular, and optical physics, **41**, 83 (1999).
- [Salières01] P. Salières, B. Carré, L. L. Déroff, F. Grasbon, G. G. Paulus, H. Walther, R. Kopold, W. Becker, D. B. Milošević, A. Sanpera and M. Lewenstein, *Feynman’s path-integral approach for intense-laser-atom interactions*, Science, **292**, 902 (2001).
- [Shen84] A. E. Shen, *The Principles of Nonlinear Optics* (Wiley-Interscience, New York, 1984).
- [Siegman86] A. E. Siegman, *Lasers* (University Science Books, Sausalito, 1986).
- [Steinmeyer99] G. Steinmeyer, D. H. Sutter, L. Gallman, N. Matuschek and U. Keller, *Frontiers in ultrashort pulse generation: pushing the limits in linear and nonlinear optics*, Science, **286**, 1507 (1999).
- [Strüder00] L. Strüder, *High-resolution imaging X-ray spectrometers*, Nucl. Instrum. Methods Phys. Res. A, **454**, 73 (2000).
- [Svelto98] O. Svelto, *Principles of lasers* (Plenum Press, New York and London, 1998).
- [Telle99] H. R. Telle, G. Steinmeyer, A. E. Dunlop, J. Stenger, D. H. Sutter and U. Keller, *Carrier-envelope offset phase control: A novel concept for absolute optical frequency measurement and ultrashort pulse generation*, Appl. Phys. B, **69**, 327 (1999).
- [Tonomura89] A. Tonomura, J. Endo, T. Matsuda, T. Kawasaki and H. Ezawa, *Demonstration of single-electron build-up of an interference pattern*, Am. J. Phys., **57**, 117 (1989).
- [Udem99] T. Udem, J. Reichert, R. Holzwarth and T. W. Hänsch, *Absolute optical frequency measurement of the Cesium D_1 line with a mode-locked laser*, Phys. Rev. Lett., **82**, 3568 (1999).
- [Ullrich97] J. Ullrich, R. Moshhammer, R. Dörner, O. Jagutzki, V. Mergel, H. Schmidt-Böcking and L. Spielberger, *Recoil-ion momentum spectroscopy*, J. Phys. B: At. Mol. Opt. Phys., **30**, 2917 (1997).

- [vLvdH88] H. B. van Linden van den Heuvell and H. G. Muller, *Multiphoton Processes, Cambridge Studies in Modern Optics*, 25 (Cambridge Univ. Press, Cambridge, 1988).
- [Weiner00] A. M. Weiner, *Femtosecond pulse shaping using spatial light modulators*, Rev. Sci. Instrum., **71**, 1929 (2000).
- [Yakovlev03] V. S. Yakovlev and A. Scrinzi, *High harmonic imaging of few-cycle laser pulses*, Phys. Rev. Lett., **91**, 153901 (2003).
- [Yudin01] G. L. Yudin and M. Y. Ivanov, *Nonadiabatic tunnel ionization: looking inside a laser cycle*, Phys. Rev. A, **64**, 013409 (2001).
- [Zacher98] F. Zacher, *Mehrphotonenionisation und Erzeugung hoher Harmonischer mit intensiven Femtosekundenlaserpulsen*, Phd thesis, Ludwig-Maximilians-Universität München (1998).
- [Zeidler00] D. Zeidler, T. Hornung, D. Proch and M. Motzkus, *Adaptive compression of tunable pulses from a noncollinear-type OPA to below 16 fs by feedback-controlled pulse shaping*, Appl. Phys. B, **70**, S125 (2000).

Acknowledgements

Although this is the last page of this work, it is likely to be one of the most often read, as it is the case for the bibliography in any publication. Let me apologize in advance if some names are unintentionally omitted.

First of all I'd like to thank Prof. H. Walther, for allowing the carrying-out of this work under excellent scientific and personal conditions. I wouldn't know where to start in thanking Gerhard Paulus for the careful scientific supervision of my work during these three years: it is probably easier to mention just his contribution to my running training, which made possible taking part (and concluding) three marathons. Thanks to the whole femtosecond group, which I first saw growing and afterwards decreasing: Felix Grasbon for introducing me to the laser and for his continuous support, Sascha Dreischuh for permitting a smooth beginning in the lab with his extraordinary politeness, Wolfgang Stremme for the sometimes confused but always exciting and brilliant theoretical understanding developed together during more than one year, Michael Schätzel for the endless tips around computers and his contribution during the last campaigns in Vienna. Finally, I'd like to thank all members of Prof. Walther's group, for the friendly climate which made these three years at MPQ enjoyable.

The major part of the experimental results presented in this work were obtained at the Vienna University of Technology. I am particularly grateful to Prof. F. Krausz for supporting this successful collaboration and for his enthusiastic interest in our experiments. I had the chance of working with several of his coworkers, of whom I could appreciate scientific and human qualities: thanks in particular to Sascha Apolonski, Andrius Baltuška, Peter Dombi, Eleftherios Goulielmakis, Matthias Lezius and others for their work and for the pizzas, Wienerschnitzels and beers often at crazy hours, before and after both successful and unsuccessful experiments.

Finally, the biggest thank to those who shared with me during these last three years part of my life outside the lab, which remains for me by far the most important: friends close and far (geographically) and of course my family and Laura, at the first place.

Resume

PERSONALS

Date of birth: 21.05.1974
Place of birth: Milan (Italy)
Citizenship: Italian
Marital status: married

EDUCATION

07.1993: Maturità Scientifica (School-leaving Certificate) at Liceo Scientifico P. Frisi (Monza, Italy). Final mark 60/60.
09.1993 - 07.1999: Faculty of Nuclear Engineering at Politecnico di Milano (Milan, Italy).
01.1998 - 07.1998: Admittance and attendance of the last year of Ecole Polytechnique (Paris, France). Final mark A.
07.1999: Degree in Nuclear Engineering at Politecnico di Milano (Milan, Italy). Final mark 100/100 cum laude (first-class honors).
04.2001 - 06.2004: PhD at the Max-Planck-Institut für Quantenoptik (Garching, Germany).

EXPERIENCE

04.1998 - 07.1998: Internship at the Laboratoire d'Optique Appliquée of the Ecole Polytechnique-ENSTA (Paris, France). Mark A.
10.1998 - 07.1999: Degree thesis at the Laboratoire d'Optique Appliquée of the Ecole Polytechnique-ENSTA (Paris, France) on the subject *High-intensity femtoseconds laser chains: thermal effects*.
09.1999 - 12.1999: Internship at Pirelli Cables & Systems S.p.A. (Milan, Italy).
01.2000 - 03.2001: Engineer Officer (Lieutenant) of the Army (ABC Division, Civitavecchia, Rome, Italy).

ADDITIONAL

Languages: Italian (native), English (fluent), French (fluent), German (good).
IT: Standard Microsoft SW packages. Matlab, Labview, Labwindows, Turbopascal, C++.
Affiliations: Italian Physical Society (SIF), European Physical Society (EPS).
Awards: First prize for the best seminar at the Annual Congress of the Italian Physical Society (2003).
Sports: Running (marathon), ski (cross-country and alpine), football.
Other interests: Cinema, classic music, meteorology.